Longitudinal and Transverse Mixing in Open-Channel Flows(Dissertation_全文)

AUTHOR(S):

Aya, Shirou

CITATION:

Aya, Shirou. Longitudinal and Transverse Mixing in Open-Channel Flows. 京都大学, 1991, 博士(工学)

ISSUE DATE:

1991-07-23

URL:

https://doi.org/10.11501/3057618

Longitudinal and Transverse Mixing in Open-Channel Flows

April 1991

Shirou Aya

Longitudinal and Transverse Mixing in Open-Channel Flows

April 1991

Shirou Aya

Longitudinal and Transverse Mixing in Open–Channel Flows

Abstract

The transport and mixing of mass, momentum, and heat in turbulent flows is of important research topics in many fields of engineering and science. It has a long history, and has been investigated in terms of various aspects, while this report studies only the longitudinal and the transverse mixing of conservative and passive materials in the confined, and uniform turbulent shear-flows. The work focuses on the basic studies, but aims to apply its results to actual problems in river engineering, because the longitudinal and the transverse mixing of fine particles and contaminants discharged into a river is quite interested in terms of environmental aspects in the field of river hydraulics.

The report consists of three portions. The **Part I** is concerned with the longitudinal dispersion coefficient which is the most important parameter for describing the longitudinal mixing in open-channel. The **Part II** studies the other topics related with the longitudinal mixing in open-channel flows, that is, concentration distributions and the mixing in the flows on permeable boundaries. The **Part III** is the investigation of the transverse mixing in an actual river by use of the numerical modeling.

In **Part I**, the longitudinal dispersion in confined turbulent shear flows was theoretically studied by the both method of Lagrangian modeling and Eulerian modeling. It was also investigated by the Lagrangian numerical experiments, laboratory experiments, and reviewing and examining the previous field-measured data. Theoretical results were successfully verified by the numerical and laboratory experiments, and field measured data. Finally it was concluded that:

1. Both of results by the Lagrangian and Eulerian modeling can describe the 1-D longitudinal mixing in not only laboratory flumes but also rivers.

2. The longitudinal dispersion in open-channel flows is 3-D. It can be decomposed into three components: the Eulerian turbulent diffusion: the dispersion caused by the vertical non-uniformity of the velocity distributions: the dispersion caused by the lateral non-uniformity of the velocity distributions.

3. The vertical and the lateral non-uniformity of the velocity distribution and the turbulent mixing in both directions mainly cause the longitudinal dispersion.

4. The intensity of the vertical non-uniformity is commonly larger than the lateral one in laboratory flumes and rivers, but the mixing time/length scale in the lateral direction is much larger than that in the vertical direction in ordinary open-channel flows in laboratory and rivers.

5. Therefore, both are effective on the longitudinal dispersion in laboratory, but the influence of the vertical non-uniformity of the velocity distributions becomes relatively smaller with increase of the width to depth ratio, and it can be commonly neglected in the dispersion in rivers.

6. The dispersion coefficient in open-channel flows is dependent on the width to depth ratio, because the mixing time scale in the lateral direction is in proportion to the square of the width to depth ratio in the lateral direction, and commonly larger than that in the vertical direction in open-channel flows.

The **Part II** is also investigations on the longitudinal mixing in open-channel flows, but in views of the dispersion by discontinuous movements, and the mass transport in the flows on pervious beds. The probability density function (**PDF**) of a particle location was presented by use of the **PDF** of the Lagrangian turbulent velocity, and the approaching processes to the Gaussian distribution for concentration distribution were clarified. On the mixing in the flows over permeable boundary, the experimental and theoretical results disclosed the important roles of the mass exchange between the surface and sub-surface flows in the longitudinal mass transport; the convective velocity of the concentration is the weighted average of the velocities in two flows, and the dispersion coefficient is the sum of the weighted average of the dispersion coefficients in two flows and the dispersion caused by the velocity difference between two flows.

The Lagrangian analyses presented in **Part I** and **Part II** disclosed the notable features of the longitudinal mixing in open channel flows as:

1. The non-linear growth of the variance observed in "Pulse Tracer Test" is caused by the dispersion by continuous movements. The required travel length/time for the linear growth of the variance are determined by the mixing time scale in the lateral direction in open-channel flows.

2. The skewed concentration distribution commonly measured in the longitudinal dispersion experiments in laboratory and natural streams is peculiar to the phenomena in shear flow dispersion, and the fundamental feature, because the **PDF** of the Lagrangian turbulent velocity is commonly different from the normal distribution. The required travel time for the convergence on the Gaussian is dependent on the **PDF** of the Lagrangian turbulent velocity, and its order of the magnitude is longer than $20T_l$, in case the **PDF** of v_l' is described by the exponential distribution.

The **Part III** dealt with the longitudinal and transverse mixing of mass in the actual river system which has complicated geometry by numerical analysis. The basic mathematical models in the generalized curvilinear coordinate system were derived and their numerical models with use of FDM were presented. Flow behaviors and concentration distributions at/below the confluence of the Yodo River system obtained by numerical analyses were successfully compared with the observed data, and the validity of the models was verified. The mechanism of the transverse mixing in the Yodo River system is explained as;

1. The riverbed is not uniform and the river water mainly flows down in the lower part of the riverbed.

2. The main stream meanders within the channel in accordance with riverbed topography, that is, the momentum flux vector distributions in the transverse direction have the longitudinal variations in accordance with the riverbed topography.

3. This meandering/longitudinal variation of the momentum flux distributions causes spreading and convergence of flows/tracer cloud and makes concentration distributions more uniform.

4. In case the total discharge is larger or the cross-section of channel is rectangular, the longitudinal variation of the transverse distribution of the momentum flux vectors is smaller and the transverse mixing is also smaller.

The convective transport is more dominant than the turbulent and dispersion transport in the actual river which has the non-uniform riverbed elevation in the longitudinal and the transverse directions, but the dispersion transport is more important in the uniform channel.

Acknowledgments

The research work described herein was conducted in River Hydraulics Laboratory, Department of Civil Engineering, Kyoto University. Professor and Doctor Yoshiaki Iwasa chairs the laboratory and has been the writer's supervisor throughout his research life in Kyoto University. The writer expresses his deepest gratitude and sincere thanks to Dr. Iwasa, who suggested the writer this research topics, and provided guidance, constant and kind advice, and encouragement throughout the research.

The writer's heartfelt gratitude is also extended to Dr. Yoshio Muramoto, Dr. Hirotake Imamoto, Dr. Kazuya Inoue, and Dr. Shuichi Ikebuchi for their kind assistance, useful advises, and the discussions in various phases of the study.

The writer also wishes to thank Dr. Yoshiaki Tsunematsu and Dr. Nobukazu Tanaka, who laid out foundations of the writer's knowledge in the numerical analysis.

The writer enjoyed the discussions on the research topics as well as other topics with my colleagues and friends: Dr. Masato Noguchi, Dr. Naoki Matsuo, Dr. Yuzuru Matsuoka, Dr. Takashi Hosoda, Mr. Akihide Tada, Dr. Keiichi Toda, and Ms Etsuko Nishide. They were very helpful, useful and joyful. The writer extends to them his sincere gratitude.

The writer expresses his deep appreciation to the graduate and under-graduate students in River Hydraulics Laboratory, Kyoto University. They assisted in preparing and performing the experiments, analyzing the much of the data, and preparing the drawings.

Perhaps the most deserving of the writer's gratitude is his wife, Yoshiko, and his son, Kousuke. This work could not be completed without their constant support, help and encouragement.

Contents

Longitudinal and Transverse Mixing in Open–Channel Flows

Chapter 1

INTRODUCTION

1.1 Preliminaries

The transport and mixing of mass, momentum, and heat in turbulent flows is of important research topics in many fields of engineering and science. It has a long history, and has been investigated in terms of various aspects, while this report studies only the longitudinal and the transverse mixing of conservative and passive materials in the confined turbulent shear flows. The work focuses on the basic studies, but aims to apply its results to actual problems in river engineering, because the longitudinal and the transverse mixing of fine particles and contaminants discharged into a river is quite interested in terms of environmental aspects in the field of river hydraulics.

Our environment is surrounded by various turbulent fluids as turbulent atmosphere, ocean, and coastal, lake and river waters. One of the oldest descriptions on the turbulent fluid was made by Leonard da Vinci in the 15th century, but the first step of the scientific research on turbulence and turbulent diffusion was made by Hagen (1839), Boussinesq (1877), Reynolds (1883), et al. The modern developments in this research field were started in 1920's by Taylor (1921), Prandtle (1925), Karman (1930), and so on. At present, the 2-D or 3-D turbulence and turbulent flows/mixing are being investigated by the turbulence models represented by "k–ϵ model" and "LES Model", or by the "Direct Simulation" by use of the highly developed electronics computer and software as well as experimental studies in laboratory.

The mixing of mass in shear flows, which includes the main research topics concerned with in this report was initially investigated by Taylor (1953) for the longitudinal mixing in laminar flows in a tube. Taylor's paper described the importance of the shear on the mass transport in the flow direction; the non-uniform velocity distribution and the mixing perpendicular to the flow direction contributes to the longitudinal mixing much more than the molecular or turbulent transport. Thus, the

mechanism of the mass transport in shear flows is quite different from the traditional turbulent diffusion, and it is called "Dispersion", "Shear Diffusion", or "Convective Diffusion/Dispersion" After his paper, the "Dispersion" in various shear flows has been investigated by various methods; the longitudinal dispersion in confined unidirectional flows has been done by Taylor (1954), Elder (1956), Fischer (1966), and so on by use of Taylor (1953)'s modeling based on the turbulent diffusion equation, and by Aris (1956), Saffamn (1962), Sayre (1969), and so on by use of the "Moment Transform" of the turbulent diffusion equation. "Dispersion" is not limited in confined flows, but also observed in unconfined flows as clearly shown in Novikov (1958). The Lagrangian modeling developed by Taylor (1921) for the diffusion in uniform turbulent flows is also useful for the longitudinal dispersion, and it was done by Taylor (1954), Batchelor (1956), Fischer (1966), and so on, but it was less successful, because the measurement of the Lagrangian auto-correlation function was quite difficult especially under natural environments. These classic investigations and other works are summarized in detail in Monin and Yaglom (1971), Tennekes and Lumley (1972), and so on. Recent developments in the longitudinal/lateral mixing in open-channel flows are summarized in Fischer et al (1979).

1.2 Objectives of Study

Focusing the topics on the longitudinal and lateral mixing in open-channel flows, which is one of the most interested topics for hydraulicians and river engineers, the investigation looked be over, because the longitudinal or transverse mixing/dispersion coefficient in rivers can practically been estimated after the active works conducted in U.S. in 1960's and '70's by Fischer (1966), Okoye (1970), Yotsukura and Sayre (1976) and so on. It is said that the research activity and the requirement in this research field are in slowdown at present.

The one-dimensional equations commonly used in one-dimensional hydraulic analysis are mathematically described more simply than the 2-D or 3-D mathematical models, and can be solved more easily. They are derived by the volumetric integration and/or averaging (Iwasa, 1976), and the complicated 3-D flow characteristics under actual environments are condensed into the parameters introduced in the 1-D models. Therefore, the parameter estimation for 1-D models has not yet clearly been resolved, and the writer has following questions on the longitudinal mixing:

1. Why is the dispersion coefficient measured in wide rectangular cross-section flumes larger than Elder's result?

2. What kinds of relationship exist between Elder's theory for 2-D open-channel flows and Fischer's theory for natural streams?, or
   How can we interpolate the dispersion between 2-D open-channel flows and natural streams?

3. What kinds of relationship does the dispersion coefficient have with the hydraulic variables?

4. Why are the concentration distribution curves measured in natural streams and laboratory skewed? or
   Do they converge on the normal distribution?

5. Which modeling is more rigorous for the longitudinal mixing in rivers, the "Dispersion Model" or the "Dead Zone Model"?

Part I and **Part II** are investigations for solving the questions above.

Reviewing the environmental problems, the period of 1960's and '70's, during which the investigations on the longitudinal/lateral mixing in open-channel flows were the most active, was the "First Age of the Environmental Pollution" in developed western countries. Now, we are living in the worlds of the "Global Environmental Problems", and of "High Technology", by which the super computer can commonly be available at reasonable cost. Much better environments are required in view of global aspects as well as close-at-home aspects. **Part III** is hoped to be useful for solving such kinds of problems as well as the basic study on the transverse mixing in actual rivers.

1.3 Scope of Study

The report consists of three parts. The **Part I** is concerned with the longitudinal dispersion coefficient which is the most important parameter for describing the longitudinal mixing in open-channel. The **Part II** focuses on the other topics related with the longitudinal mixing in open-channel flows, that is, concentration distributions, and the mixing in the flows on permeable boundaries, which is common under natural environment. The **Part III** is the investigation of the transverse mixing in an actual river by use of the numerical modeling. The constitutions of the present study are summarized bellow.

(1) Part I

In **Part I**, the one-dimensional longitudinal dispersion in confined turbulent shear flows is studied by theoretical, experimental and empirical methods. **Chapter 2** investigates the longitudinal dispersion by continuous movements of a particle by use of the method of Lagrangian modeling. The movements of a particle is stated by Lagrangian descriptions, and the theoretical models for the Lagrangian auto-correlation function in 3-D turbulent shear flows is presented and the longitudinal dispersion coefficient is obtained in **Section 2.2**. The 3-D numerical simulation models for a particle dispersion is developed in **Section 2.3**, and they are examined by 2-D numerical experiments, comparing the theoretical results obtained by the previous study in **Sections 2.4** and **2.5**. 3-D numerical experiments are conducted in **Section 2.6**, and the theoretical results and assumptions introduced in **Section 2.2** are examined by numerical experiments in **Sections 2.7** and **2.8**.

The longitudinal dispersion coefficient is theoretically investigated by the method of Eulerian modeling in **Chapter 3**. In **Section 3.2**, the previous theoretical studies on the dispersion coefficient based on the turbulent diffusion equation are reviewed, and the assumptions used are summarized. In **Section 3.3**, the 3-D turbulent diffusion equation, 1-D convective dispersion equation, and the definition of the longitudinal dispersion coefficient are stated in the orthogonal curvilinear coordinate system. The mathematical theory of the dispersion coefficient developed by the previous studies is presented in more general form by use of the 3-D turbulent diffusion equation in the orthogonal curvilinear coordinate system in **Section 3.4**. In **Section 3.5**, the locally time-averaged velocity and concentration are respectively decomposed into three components: the cross-sectional averaged values: the deviation of the depth-averaged values from the cross-sectional values: the deviation of the locally temporal averaged-values from the depth averaged values. The dispersion coefficient in 1-D models is also decomposed into three components, and theoretically investigated.

The longitudinal dispersion is also investigated by the detailed laboratory experiments in **Chapter 4**. The objectives of the experiment are to disclose the characteristics of time-dependent behaviors of the tracer cloud, and to verify the theoretical results in **Chapters 2** and **3**. The experimental apparatus and the method are stated in **Section 4.2**. The methods of data processing and analysis are described in **Section 4.3**, and the behaviors of the temporal moments for concentration distributions, the characteristics of the velocity distributions, and the dispersion coefficient are calculated. The results of the experiments are stated in **Section 4.4**, and the spreading of the tracer is investigated by the behaviors of the first, the second and the third temporal moments and the peak concentration. The difference of the temporal

moment behavior between the cross-sectional concentration and those measured at points in a section is also investigated. The experimental results are compared with the theoretical results obtained by use of the Lagrangian modeling in **Chapter 2**, and the Eulerian modeling in **Chapter 3**. The dimensional analysis is also conducted to disclose the relationship of the dimensionless dispersion coefficient with the hydraulic variables.

In **Chapter 5**, the applicability of the three formulae presented in the previous chapters is examined to river flows as well as to the various flows in laboratory flumes made by other researchers. The relationship between the dispersion coefficient and the hydraulic variables in rivers is also investigated by use of the screened data. The results of the previous measurements for the longitudinal dispersion coefficient in various laboratory flumes and actual rivers are collected and carefully reviewed in **Sections 5.2** and **5.3**. In **Sub-section 5.4.1**, the dispersion coefficient and the characteristics of the velocity distributions in rivers in terms of one-particle analysis described in **Chapter 2** is examined and investigated by use of field measured data in **Sub-section 5.4.1**. In **Sub-section 5.4.2**, the dispersion coefficient in terms of Eulerian analysis described in **Chapter 3** is also examined by use of field measured data. The dimensional analysis of the dispersion coefficient is conducted in **Sub-section 5.4.3**, and the relationship between D/du_* and the hydraulic variables is examined by using collected data in laboratory and rivers.

(2) Part II

The **Part II** also investigates the longitudinal mixing in open-channel flows, but focuses on different topics from the dispersion coefficient: the particle dispersion by discontinuous movement: concentration distributions in "Pulse Tracer Tests" in rivers and laboratory: the mass transport in the flows on pervious beds.

In **Chapter 6**, the convective dispersion processes in the longitudinal direction in confined flows are studied in view of the discontinuous movement of a particle. The probability density distribution of a particle location is presented by use of the probability density function (**PDF**) of the Lagrangian turbulent velocity in **Section 6.2**, and the approach to the normal distribution is described. In **Section 6.3**, the **PDF** of the Lagrangian turbulent velocity v_1' in the longitudinal dispersion phenomena is studied; the **PDF** of v_1' in 2-D open-channel flows under the logarithmic velocity distribution is described by the exponential distribution, and the concentration distributions during the asymptotic processes approaching the Gaussian distribution is described by the gamma distribution. The models describing the concentration

distributions in 3-D flows are presented in **Section 6.4**. The gamma distribution approximation is examined by use of the concentration distributions and the velocity distribution measured in the rectangular cross-section laboratory flume in **Section 6.5**.

The actual concentration distributions observed in "Pulse Tracer Test" observed in laboratory and natural streams are investigated in **Chapter 7**. They are commonly skewed from the Gaussian distribution, and the possibility of the gamma (Pearson's Type Ⅲ) distribution approximation is widely examined for not only cross-sectional averaged concentrations but also point-measured ones in laboratory and natural streams in **Section 7.2**. The main descriptors of the distribution: the first moment: the variance: the modal value, and so on at each of measuring points are investigated with relation to the hydraulic variables of flows in **Section 7.3**. The gamma distribution approximation for point-measured concentration distributions at a center of flow-section in natural streams is also demonstrated in **Section 7.4**.

The vertical and longitudinal mass transports in the flows over permeable boundary, which are common in natural environment, are investigated in **Chapter 8**. The results of preliminary dye tracer study presents the features of the vertical mass transport between the surface and the sub-surface flows, and its magnitude in **Section 8.2**. By using the mathematical models similar to those in "Dead Zone Modeling" for the longitudinal mixing in natural streams, the longitudinal mass transport in the surface and the sub-surface flows is theoretically investigated in **Section 8.3** and **8.4**. The theoretical results disclose that the mass exchange between the surface and the sub-surface flows play an important role in the longitudinal mass transport, and they are examined by use of the experimental results in **Section 8.5**.

(3) Part Ⅲ

The **Part Ⅲ** deals with the longitudinal and lateral mixing in the actual river which has complicated geometry by two-dimensional numerical analysis.

In **Chapter 9**, the mathematical models and their finite difference forms are presented in the generalized curvilinear coordinate system. They are applied to an actual river system, and their validity is examined. In **Section 9.2**, the 2-D mathematical models for flows and the associated longitudinal and transverse mixing of mass are derived in the generalized curvilinear coordinate system from the common 2-D mathematical models for shallow waters in the Cartesian coordinate system. The finite difference forms of the mathematical models are presented by the integration method in **Section 9.2**, and the numerical models are developed. The proposed models are

applied to the confluence of the Yodo River System case study and its validity is examined by comparing field measured data in **Section 9.3**. The mixing processes of the waters from Katsura River or Kizu River below the confluences are discussed in detail with the relation to the flow behavior.

In **Chapter 10**, the mechanism of the lateral mixing at/below the confluence in the Yodo River system are investigated by use of the mathematical models developed in **Chapter 9** as well as the simple physical model. The characteristics of the flow behavior and the associated mixing are investigated by numerical experiments under various hydraulic conditions in **Section 10.2**. The mechanism of the mixing in the Yodo River System is also investigated by the numerical experiments under the various channel geometries, the dispersion coefficient, and the discharge conditions in **Section 10.3**. The features obtained by numerical experiments is examined by the simplified hydraulic experiments in **Section 10.4**. The convective transport is disclosed to be more dominant than the turbulent/dispersion transport in an actual river which has the non-uniform riverbed elevation in the longitudinal and the transverse directions.

The last **Chapter 11** summarizes the contributions of each chapter to the longitudinal and transverse mixing in open-channel flows, and its mechanism.

References in Chapter 1

Aris, R. (1956). On the dispersion of a solute in a fluid flowing through a Tube, *Proc. Royal Society*, A235, No. 1200, 67–77.

Batchelor, G. K., and Townsend, A. A. (1956). Turbulent diffusion, in "Surveys in Mechanics", edited by Batchelor, G. K. and Devious, R. M., The Cambridge University Press, London, 352–399.

Boussinesq, J. (1877). Essai sur la theorie des eaux courantes, *Memoires presente par divers savants a l'Academie des Sciences*, Vol. 23, No. 1, 1–680.

Elder, J. W. (1959). The dispersion of marked fluid in turbulent shear flow, *J. Fluid Mechanics*, Vol. 5, 544–560.

Fischer, H. B. (1966). Longitudinal dispersion in laboratory and Natural streams, Report No. KH-R-12, California Institute of Technology, Pasadena, California.

Fischer, H. B. et al (1979). "Mixing in Inland and Coastal Waters", Academic Press, New York.

Hargen, G. (1839). Uber die Bewegung des Wassers in engen zylindrichen Rohren, *Poggendorf Annal. Phys. Chemie*, Vol. 46, 423–442.

Iwasa, Y. (1976). Mathematical aspect of one-dimensional equations of unsteady flows in open channels, *Proc. Int'l Symp. on Unsteady Flow in Open Channels*, BHRA-IAHR, D2-13–D2-24.

Karman, T. von (1930). Mechanische Ahnlichkei und Turbulenz, *Nachr. Ges. Wiss. Gottingen*, Math-Phys. KL., 58–76.

Monin, A. S., and Yaglom, A. M. (1971). "Statistical Fluid Mechanics" translated from the Russian by Scripta Technica, Inc., and edited by J. L. Lumley, MIT Press, Cambridge, Massachusetts.

Novikov, Ye, A. (1958). Turbulent diffusion in a shear flow, *Prikl. Matem. Mekh.*, Vol. 22, No. 3, 412–414..

Okoye, J. K. (1970). Characteristics of transverse mixing in open-channel flows, Report No. KH-R-23, California Institute of Technology, Pasadena, California.

Prandtle, L. (1925). Bericht uber Untersuchungen zur ausgebildeten Turbulenz, *Zs. angew. Math. Mech.*, Vol. 5, No. 2, 136–139.

Reynolds, O. (1883). An experimental investigation of the circumstances which determine whether the motion of water shall be direct or sinuous, and the law of resistance in parallel channels, *Phil. Trans. Royal Soceity of London*, Vol. 174, 935–982.

Saffman, P. G. (1960). The effect of wind shear on horizontal sread from instantaneous groud source, *Quart. J. Royal Met. Society*, Vol. 88, No. 378, 382–393.

Sayre, W. W. (1969). Dispersion of silt particles in open channel flow, *J. Hydraulic Division, Proc. ASCE*, Vol. 95, No. HY3, 1009–1039.

Taylor, G. I. (1921). Diffusion by continuous movements, *Proc. London Mathematical Society*, Series 2–20, 196–211.

Taylor, G. I. (1953). Dispersion of soluble matter in solvent flowing slowly through a tube, *Proc. Royal Society of London*, Series A, Vol. 219, 186–203.

Taylor, G. I. (1954). The dispersion of matter in turbulent flow through a pipe, *Proc. Royal Society of London*, Series A, Vol. 223, 446–468.

Tennekes, H., and Lumley, J. L. (1972). "A first course in turbulence", The MIT Press, Cambridge, Massachusetts.

Yotsukura, N., and Sayre, W. W. (1976). Transverse mixing in natural streams, *Water Resources Research*, Vol. 12, No. 4, 695–704.

PART I:

LONGITUDINAL DISPERSION COEFFICIENT IN OPEN–CHANNEL FLOWS

Chapter 2

LONGITUDINAL DISPERSION IN TURBULENT SHEAR FLOWS IN VIEW OF ONE–PARTICLE ANALYSIS

2.1 Introduction

A pioneer study of Taylor (1921) for the turbulent diffusion in a uniform turbulent flows shows that the variance of displacement for a fluid particle $[X'^2(a,t)]$ is an integral of the Lagrangian auto-correlation function $B_L(\tau)$ and that the turbulent diffusion coefficient D is a product of the square of Lagrangian turbulent intensity $[v'^2]$ and the Lagrangian integral time scale T_L;

$$[X'^2(a,t)] = 2\int_0^t (t-\tau)B_L(\tau)d\tau \tag{2.1.1}$$

$$D \equiv \frac{1}{2}\frac{d}{dt}[X'^2(a,t)] = \int_0^t B_L(\tau)d\tau \tag{2.1.2a}$$

$$D = [v'^2]T_L \qquad (t \to \infty) \tag{2.1.2b}$$

where $X(a,t)$ is the displacement of the particle at time $t = t$ which started at a point a at $t = 0$, $X'(a,t)$ is the fluctuation from the mean displacement of the particle, τ the time-lag, $v(a,t)$ the Lagrangian velocity of the particle, $v'(a,t)$ the fluctuation from the mean Lagrangian velocity of the particle and [ ] denotes the ensemble mean. $B_L(\tau)$ and T_L are respectively defined by:

$$B_L(\tau) = [v'(t)v'(t+\tau)] \tag{2.1.3}$$

$$T_L = \frac{1}{[v'^2]}\lim_{t\to\infty}\int_0^t B_L(\tau)d\tau \tag{2.1.4}$$

Introducing the Lagrangian auto-correlation coefficient $R_L(\tau)$ by:

$$R_L(\tau) \equiv \frac{1}{[v'^2]} B_L(\tau) \tag{2.1.5a}$$

and assuming:

$$R_L(\tau) = \exp(-\tau/T_L) \tag{2.1.5b}$$

the variance σ_x^2 is stated as:

$$\sigma_x^2(t) \equiv [X'^2(a,t)] = [v'^2] T_L^2 \left\{ \exp\left(-\frac{t}{T_L}\right) + \frac{t}{T_L} - 1 \right\} \tag{2.1.6}$$

and

$$\sigma_x^2 = \begin{cases} \propto t^2 & \text{for} \quad t \ll T_L \\ \propto Dt & \text{for} \quad t > (3 \sim 6) T_L \end{cases} \tag{2.1.7}$$

It is suggested that this classical theory can also be applied to a longitudinal mixing phenomenon in a confined turbulent shear flow by Taylor (1954), Batchelor and Townsend (1956) and Tennekes and Lumley (1972). The applications of this theory to the open-channel turbulent shear flow were made by Fischer(1966) and Sullivan(1971). Fischer(1966) proposed the formula predicting the integral time scale T_{Fi} in turbulent shear flows in the form of

$$T_{Fi} = \frac{1}{14.8} \frac{l_i^2}{\varepsilon_i} \qquad (i = 2, 3) \tag{2.1.8}$$

where l_i is the characteristic length (a half width for natural streams and the depth for two-dimensional flows) and ε_i the turbulent diffusion coefficient in the x_i direction. The subscript i denotes the variables concerned with the x_i direction and $x_i (i = 1, 2, 3)$ is the space coordinate in the flow direction ($i = 1$), the vertical direction ($i = 2$) and the lateral direction ($i = 3$). He also proposed the formula predicting the longitudinal dispersion coefficient D_L based on one-particle analysis as:

$$D_L = \frac{1}{A} \int_A (\bar{u}_1 - U)^2 dA \frac{1}{14.8} \frac{(B/2)^2}{\varepsilon_3} \tag{2.1.9}$$

where $\bar{u}_1$ is the local temporal-averaged velocity, U the cross-sectional-averaged velocity, A the cross-sectional area and B the surface width. Sullivan (1971) observed the Lagrangian characteristics of the velocity in the two-dimensional turbulent flow through both methods of the experiment in laboratory flumes and the numerical simulation. He concluded that the Lagrangian auto-correlation coefficient for a two-dimensional flow is represented as the exponential function. Matsuoka(1986) obtained $B_L(\tau)$ by making the detailed Eulerian velocity measurement in a rectangular cross-section laboratory flume and the idea of the transition probability for the particle location, and he showed that T_L is quite long in open-channel flow. Hosoda and

Yokoshi (1985) investigated the relationship between the Lagrangian and the Eulerian turbulence and obtain the dispersion coefficient in the two-dimensional flows, of which the velocity distributions are represented by the power-law. They also show the dispersion coefficient by the Lagrangian method has the fine agreement with analytical results by the Eulerian method by numerical procedures.

So far as the author concerns, detailed and reliable information of the autocorrelation function in a 3-D turbulent shear flows has not yet been obtained, and the study results of the Lagrangian characteristics in 2-D and 3-D steady turbulent shear flows which is uniform in the longitudinal direction will be shown and discussed in this chapter, while some parts of this chapter have already presented in Iwasa, Aya, Motita and Nishikawa (1982) and Iwasa and Aya (1985).

2.2 Lagrangian Description of Dispersion of a Particle in Shear Flows

2.2.1 Movements of a Fluid Particle

Assuming the confined turbulent flow which is uniform in the flow direction but non-uniform in the vertical and the lateral directions, the Eulerian velocity vector is written in the form of

$$u(x_i, t) = \bar{u}(x_2, x_3) + u'(x_i, t) \tag{2.2.1}$$

where $\bar{u}(x_2, x_3)$ is the mean Eulerian velocity vector and $u'(x_i, t)$ the Eulerian turbulent velocity, and overbars denote the temporal-averaged values hereafter. The definition sketch of the coordinate system is shown in Fig. 2.2.1. Denoting the displacement of the particle at time $t = t$ released from $x = a$ at $t = 0$ by $x = \boldsymbol{X}(a, t)$, $\boldsymbol{X}$ is written as:

$$\boldsymbol{X}(a, t) = \int_0^t v(a, t')dt' + a \tag{2.2.2}$$

where $v(a, t)$ is the Lagrangian particle velocity vector, which is stated with the Eulerian velocity vector $u(x_i, t)$ as:

$$v(a, t) = \bar{u}\,(\boldsymbol{Y}(a, t)\,) + u'\,(\boldsymbol{X}(a, t),\, t\,) \tag{2.2.3}$$

where $\boldsymbol{Y}(\,a, t) = (X_2(a, t),\, X_3(a, t)\,)$ is the 2-D displacement vector of the marked particle in a cross section. The mean longitudinal Lagrangian velocity $[v_1]$ defined by

$$[v_1] = \frac{1}{V_a} \int\int\int v_1 da_1 da_2 da_3 \tag{2.2.4}$$

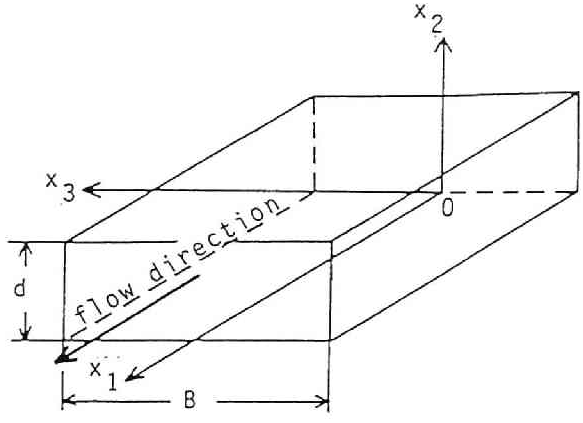

Figure 2.2.1: Definition of coordinate system.

is equal to the cross-sectional mean longitudinal Eulerian velocity U which is defined by

$$U \equiv \frac{1}{A}\int_A \bar{u}_1(x_1, x_2)dA$$

(Tennekes and Lumley, 1972). Therefore the longitudinal Lagrangian turbulent velocity $v_1'(a,t)$ can be written in the form of

$$v_1'(a,t) = u_1'(\,\boldsymbol{X}(a,t),\,t) + \bar{u}_1(\,Y(a,t)\,) - U \tag{2.2.5}$$

In 3-D flows, $\bar{u}_1(x_2, x_3)$ can be decomposed into two components;

$$\bar{u}_1(x_2, x_3) = \bar{u}_1^{x_3}(x_3) + u_{23}''(x_2, x_3) \tag{2.2.6}$$

where $\bar{u}^{x_3}(x_3)$ is the depth-averaged velocity and $u_{23}''(x_2, x_3)$ the fluctuation from $\bar{u}^{x_3}(x_3)$, and they are respectively defined by

$$\bar{u}^{x_3} \equiv \frac{1}{d}\int_{-z_b}^{\zeta} \bar{u}_1 dx_2 \qquad\qquad (d = \zeta + z_b) \tag{2.2.7}$$

and

$$u_{23}'' \equiv \bar{u} - \bar{u}^{x_3} \tag{2.2.8}$$

where $-\zeta$ is the water surface elevation, z_b the bottom of the channel, and d the depth.

Fig. 2.2.2 illustrates the mean velocity distributions of 3-D turbulent shear flows and the definition of these three kinds of velocity components in a rectangular cross-section flume.

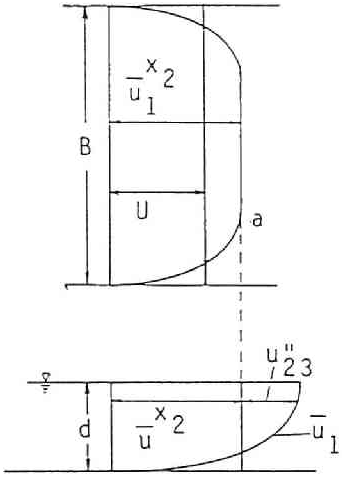

Figure 2.2.2: Definition of $u''_{23}, \bar{u}^{x_2}$ and U, and a velocity distribution. (a) The cross-sectional averaged velocity U and a distribution of the depth-averaged velocity $\bar{u}^{x_2}$, and (b) distributions of the locally temporal averaged velocity $\bar{u}_1$, the depth averaged velocity $\bar{u}_1^{x_2}$, and the deviation u''_{23}.

By substituting Eq. 2.2.6 into Eq. 2.2.5, $v'_1(a,t)$ can be rewritten in the form of

$$v'_1(a,t) = u'_1(\boldsymbol{X}(a,t),\, t) + u''_{23}(\boldsymbol{Y}(a,t)) + \bar{u}^{x_2}(\boldsymbol{Z}(a,t)) - U \tag{2.2.9}$$

where $\boldsymbol{Z}(a,t) = (X_3(a,t))$ is the 1-D displacement vector of a particle in the lateral direction. Introduction of the new Lagrangian velocities of

$$v'_t(a,t) = u'_1(\boldsymbol{X}(a,t),\, t) \tag{2.2.10}$$

$$v'_v(a,t) = u''_{23}(\boldsymbol{Y}(a,t)) \tag{2.2.11}$$

$$v'_l(a,t) = \bar{u}^{x_2}(\boldsymbol{Z}(a,t)) - U \tag{2.2.12}$$

can transform Eq.2.2.9 into the following Eq. 2.2.13.

$$v'_1(a,t) = v'_t(a,t) + v'_v(a,t) + v'_l(a,t) \tag{2.2.13}$$

where the subscript t, v and l denote the three Lagrangian velocity components referring to the Eulerian turbulent velocity, the vertical non-uniformity of the Eulerian local mean velocity, and its lateral one respectively.

Note following facts;

1. In the shear flow, $\bar{u}^{x_2}(x_2, x_3)$ is the local mean velocity and not random, however the displacement $\boldsymbol{Y}(a,t)$ and $\boldsymbol{Z}(a,t)$ are random in a section by particle migrations.

2. Therefore, both $u''_{23}(\boldsymbol{Y}(a,t))$ and $\bar{u}^{x_2}(\boldsymbol{Z}(a,t))$ are random.

3. Hence, the longitudinal Lagrangian turbulent velocity $v'_1(a,t)$ is random and quite different from the longitudinal Eulerian turbulent velocity $\bar{u}'_1(x_i,t)$.

In case the 2-D flows of which the velocity distributions are shown in Fig. 2.2.3(a), positions of particles started at a point $a(X_0, Y_0)$ at $t = t_0$ and t'_0 is illustrated as shown in Fig. 2.2.3(b). The two particles of which the heights at $t = t_0 + \Delta t$, $t = t_0 + 2\Delta t$ and $t = t_0 + 3\Delta t$ were the same each other, are denoted by solid and open circles respectively. Their displacements in the longitudinal direction are however different each other because of $v'_i(a,t)$, that is, the Eulerian turbulent velocity $u'_1((a,t),t)$ and this displacement difference causes the turbulent diffusion. In case the particle started at $x = a$ at $t = t_0$ moved to different heights from the former two in $t > t_0$, the difference of the longitudinal displacement between them is much larger than that by the Eulerian turbulence because of $v'_v(a,t)$, and the difference of the height causes the longitudinal dispersion in shear flows. Open square in Fig. 2.2.3(b) shows the movement of this particle. Fig. 2.2.3(c) schematically illustrates the time series of the Lagrangian velocity of the two particles. The velocity difference at the same travel time is very small and this is caused by the Eulerian turbulence, however the Lagrangian velocity fluctuation from the mean $[v_1] = U$ is much bigger than the Eulerian turbulence.

2.2.2 Longitudinal Dispersion in Shear Flows

Under the flow condition that the velocity characteristics are uniform in the longitudinal direction, $v'_1(a,t)$ is a stationary random time series and Taylor's classical turbulent diffusion theory, that is, Eqs. 2.1.1 to 2.1.4 can be used to analyze the concerned problem, when we use $v'_1(a,t)$ defined by Eq.2.2.13 as the Lagrangian turbulent velocity. The analogy of the longitudinal dispersion in confined turbulent shear flows with the turbulent diffusion in homogeneous turbulent flow is shown in details in Tennekes and Lumley (1972). Iwasa, Aya and Mitsuishi (1985) explains the analogy of the longitudinal dispersion of particles released at a section in confined turbulent shear flows in a uniform channel with the dispersion of particles released at a point in a homogeneous turbulent flow field.

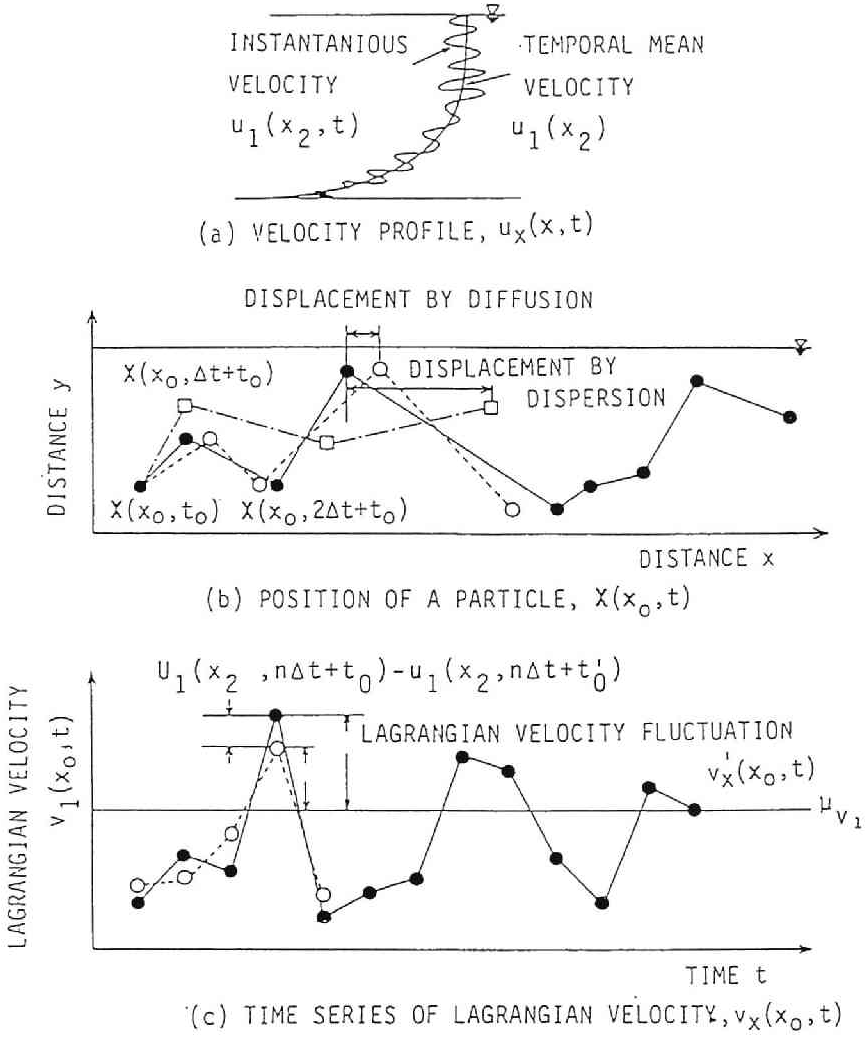

Figure 2.2.3: Movements of fluid particles and their Lagrangian velocity in 2-D turbulent shear flows. (a) Distributions of the velocity $\bar{u}_1$ in 2-D turbulent flows, (b) positions of particles in 2-D space released at $\boldsymbol{X}(\boldsymbol{x}_o, 0)$, and (c) time series of Lagrangian velocity, $v_1(a,t)$.

Suppose the mean location of particles at time $t = 0$ is $x_1 = 0$, then, a mean displacement of particles $[X_1(\boldsymbol{a}, t)]$ at $t = t$ is

$$[X_1(\boldsymbol{a}, t)] = Ut \tag{2.2.14}$$

and a displacement fluctuation from the mean $X'(\boldsymbol{a}, t)$ is obtained as:

$$X_1'(\boldsymbol{a}, t) = \int_0^t v'(\boldsymbol{a}, t')dt' \tag{2.2.15}$$

The square of the Lagrangian turbulent intensity $[v_1'^2]$ can be obtained by

$$\left[v_1'^2\right] = \left[v_t'^2\right] + \left[v_v'^2\right] + \left[v_l'^2\right] \tag{2.2.16}$$

in which

$$\left[v_t'^2\right] = \frac{1}{A}\int_A u_1'^2 dA \tag{2.2.17}$$

$$\left[v_v'^2\right] = \frac{1}{A}\int_A u_{23}''^2 dA \tag{2.2.18}$$

$$\left[v_l'^2\right] = \frac{1}{B}\int_{b_2}^{b_1} (\bar{u}^{x_2} - U)^2 dx_3 \tag{2.2.19}$$

Using Eq. 2.2.13, the auto-correlation function $B_L(\tau)$ can be divided into nine components and they are written in the form of

$$B_L = \sum_{i,j} B_{Li,j}(\tau) \qquad (i, j = t, v, l) \tag{2.2.20}$$

where

$$B_{Li,j}(\tau) = [v_i'(t)v_j'(t + \tau)] \tag{2.2.21}$$

The ample knowledge for $B_L(\tau)$ has not yet obtained. Asano (1980) estimates $B_{Ltt}(\tau)$ by the Eulerian turbulence measurement in open-channel flows by using the assumption made by Hay and Pasquill (1959) at

$$B_{Ltt}(\tau) = [v_t'^2]\exp(-\tau/T_L) \tag{2.2.22}$$

$$T_L = 0.72d/u_* \tag{2.2.23}$$

Fischer(1968) obtains the integral time scale T_L in 2-D turbulent shear flows as

$$T_L = \frac{1}{14.8}\frac{d^2}{\varepsilon_2} \tag{2.2.24}$$

by using his Lagrangian dispersion theory and Elder's results (Elder, 1954). He also extends the results above to the longitudinal dispersion in natural streams and estimates

$$T_L = \frac{1}{14.8}\frac{(B/2)^2}{\varepsilon_3} \tag{2.2.25}$$

Sullivan (1971) gives

$$B_L(\tau) = [v_1'^2]\exp(-\tau/T_L) \tag{2.2.26}$$

by the direct measurement of the Lagrangian turbulence in the 2-D open-channel flows and the quasi-Lagrangian turbulence simulation in 2-D confined flows. Lumley(1972) estimates T_L in the two-dimensional confined channel as

$$T_L \approx h/u_* \tag{2.2.27}$$

where h is a half depth.

Introduction of the assumption,

$$B_{Lij}(\tau) = 0 \qquad (i \neq j) \tag{2.2.28}$$

derives

$$B_L(\tau) = B_{Ltt}(\tau) + B_{Lvv}(\tau) + B_{Ltt}(\tau) \tag{2.2.29}$$

The previous study stated above leads to the general form of $B_L(\tau)$ in the three-dimensional turbulent shear flow as:

$$B_L(\tau) = [v_t'^2]\exp(-\tau/T_t) + [v_v'^2]\exp(-\tau/T_v) + [v_l'^2]\exp(-\tau/T_l) \tag{2.2.30}$$

and

$$T_t = 0.72d/u_* \tag{2.2.31}$$

$$T_v = \frac{1}{14.8}\frac{(d)^2}{\theta_2 d u_*} \tag{2.2.32}$$

$$T_l = \frac{1}{14.8}\frac{(B/2)^2}{\theta_3 d u_*} \tag{2.2.33}$$

where T_t is the integral time scale of the Eulerian turbulence, T_v the mixing time scale in the depth-wise direction, T_l the mixing time scale in the transverse direction, θ_i the dimensionless turbulent diffusion coefficient in the vertical direction ($i = 2$) and the lateral direction ($i = 3$).

Using Eqs. 2.2.30 to 2.2.33, the integral time scale T_{SL} in the three dimensional turbulent shear flows can be expressed by

$$T_{SL} = \frac{1}{[v_1'^2]}\left\{\left[v_t'^2\right]T_t + \left[v_v'^2\right]T_v + \left[v_l'^2\right]T_l\right\} \tag{2.2.34}$$

The dispersion coefficient D_L can be expressed by

$$D_L = [v_x'^2]T_{SL} = [v_t'^2]T_t + [v_v'^2]T_v + [v_l'^2]T_l \tag{2.2.35}$$

The first term of the right-hand side of Eq. 2.2.35 shows the effect of longitudinal turbulent diffusion on the longitudinal dispersion, the second term the effect of the non-uniform velocity distributions in the vertical direction and the third term the effect of that in the transverse direction.

The results above shows that small non-uniformity of the velocity distributions in the transverse direction has very big influence on the magnitude of the dispersion coefficient in wide channels as will be discussed in **Subsection 2. 2. 3.**

The assumptions introduced above and the validity of these results will be verified by the numerical simulation in the next section and the results obtained in the tracer dispersion study at the laboratory flume in **Chapter 3.**

2.2.3 Discussions on Theoretical Results

(1) Square of Lagrangian turbulent intensity: $[v_1'^2]$

The square of Lagrangian turbulent intensity of particles are expressed as the sum of the three components as shown in Eq. 2.2.13. The general discussion on the magnitude of each term is as follows;

Asano (1980) gives

$$[v_t'^2]/u_*^2 = 1.0 \quad \text{to} \quad 2.0$$

by the detailed measurement of Eulerian velocity by the hot-film anemometer in laboratory flumes and natural streams. Assuming the logarithmic velocity distribution in 2-D turbulent flows

$$\frac{[v_v'^2]}{u_*^2} = \begin{cases} 6.25 & \text{for} \quad \kappa = 0.40 \\ 11.0 & \text{for} \quad \kappa = 0.33 \end{cases}$$

The magnitude of $[v_l'^2]/u_*^2$ measured in laboratory flumes is reported as:

$$[v_l'^2]/u_*^2 \approx 10.0 \tag{2.2.36}$$

by Iwasa, Aya and Yakushiji (1984), and this is the function of the width to depth ratio B/d and decreases as B/d increases as will be shown in **4.4.5** in **Chapter 4.** The analysis of the field measurement data by Yakushiji (1983) shows that $[v_l'^2]/u_*^2$ is not always dominant over three terms in natural streams.

(2) Lagrangian Auto-Correlation Function and Coefficient: B_L and R_L

The proposed models for $B_L(\tau)$ described by Eq. 2.2.30 satisfies such basic features that

$$B_L(t) = \begin{cases} [v_1'^2] & \text{for} \quad t = 0 \\ 0 & \text{for} t \to \infty \end{cases}$$

and the Lagrangian Auto-Correlation Coefficient R_L defined by Eq. 2.1.5a satisfies

$$R_L(t) = \begin{cases} 1 & \text{for} \quad t = 0 \\ 0 & \text{for} \quad t \to \infty \end{cases}$$

(3) Integral Time Scale: T_{SL}

T_{SL} described by Eq. 2.2.34 is the weighted average of T_i with use of $[v_i'^2]$ $(i = t, v, l)$ as the weight. In 3-D turbulent shear flows, T_{SL} is quite different from the mixing time scale introduced by Fischer(1966). As represented by Eqs. 2.2.31, 2.2.32, and 2.2.33, the first and second term of Eq.2.2.34, that is, T_t and T_v are the function of the flow depth d and the shear velocity u_*, however the third term T_l is the function of the width to depth ratio, because T_l is written in the form of

$$\frac{T_l}{d/u_*} = \frac{1}{14.8\theta_3}(\frac{B}{d})^2 \tag{2.2.37}$$

In ordinary open channel flows in natural streams, the width to depth ratio is quite large and

$$T_l \gg T_t, \quad T_v$$

and Eq. 2.2.33 gives

$$T_l \gg T_{SL}$$

because the magnitude of the weight $[v_l'^2]/[v_1'^2]$ is small.

(4) Longitudinal Dispersion Coefficient: D_L

The longitudinal dispersion coefficient D_L is the sum of three components as shown in Eq. 2.2.35 and each term of Eq. 2.2.35 is a product of the square of turbulent intensity and the mixing time scale, respectively. As already discussed in **2.2.3 (1)**, the magnitude of $[v_l'^2]$ is not so large in 3-D turbulent flow in laboratory flumes and natural streams, however, the magnitude of T_l is quite larger than the other two and increases with increase of the width as discussed in **2.2.3 (3)**. Thus, the longitudinal dispersion coefficient in open channel flows is quite larger than that in 2-D turbulent flows in laboratory flumes as well as natural streams. This is also increases with the increase of the width or the width to depth ratio.

Fischer (1966) proposed the formula predicting the longitudinal dispersion coefficient based on the theory of one particle analysis as shown in Eq. 2.1.6, however the square of turbulent intensity and the Lagrangian integral time scale used in Eq. 2.1.6 may not be rigorous as described above.

(5) Time Dependent Behavior of the Variance

By substituting Eq. 2.2.30 into Eq. 2.1.1, the growth of the variance is written in the form of

$$\begin{aligned}[X'^2(a,t)] &= 2[v_t'^2]T_t^2\{\exp(-t/T_t)+t/T_t-1\}+ \\ &\quad 2[v_v'^2]T_v^2\{\exp(-t/T_v)+t/T_v-1\}+ \\ &\quad 2[v_l'^2]T_t^2\{\exp(-t/T_l)+t/T_l-1\}\end{aligned} \tag{2.2.38}$$

In a short travel time, $[X'^2]$ is proportional with the square of the travel time t

$$[X'^2] \propto t^2 \qquad \text{for} \quad t \approx 0$$

and with increase of the travel time, $[X'^2]$ is proportional with the travel time,

$$[X'^2] \propto t \qquad \text{for} \quad t > (3 \sim 6)T_l \qquad \text{or} \quad x > (3 \sim 6)T_l U \tag{2.2.39}$$

These relationships are equivalent to Fischer's criterion for Taylor's period (Fischer, 1966). This criterion will be used in measuring the longitudinal dispersion coefficient in the laboratory flume experiment described in Chapter 5.

(6) Applications of the Models to Different Kinds of Turbulent Fields

a. Homogeneous turbulent field

In the homogeneous turbulent field in which the velocity distribution is uniform in the vertical and lateral directions, $[v_v'^2]$ and $[v_l'^2]$ are equal to 0.0, therefore, the proposed models gives:

$$[v_1'^2] = [v_t'^2] \tag{2.2.40a}$$

$$B_L(\tau) = [v_t'^2]\exp(-\tau/T_t) \tag{2.2.40b}$$

$$T_{SL} = T_t \tag{2.2.40c}$$

and

$$D_L = [v_t'^2]T_t \tag{2.2.40d}$$

b. 2-D turbulent shear flows

In case 2-D turbulent flow in which the velocity distribution is uniform in the lateral direction, $[v_l'^2]$ is equal to 0.0 and the proposed models gives:

$$[v_1'^2] = [v_t'^2] + [v_v'^2] \tag{2.2.41a}$$

$$B_L(\tau) = [v_t'^2]\exp(-\tau/T_t) + [v_v'^2]\exp(-\tau/T_v) \tag{2.2.41b}$$

$$T_{SL} = \frac{1}{[v_1'^2]}\left\{\left[v_t'^2\right]T_t + \left[v_v'^2\right]T_v\right\} \tag{2.2.41c}$$

and

$$D_L = [v_t'^2]T_t + [v_v'^2]T_v \qquad (2.2.41d)$$

Therefore, the proposed models includes the application to the diffusion in homogeneous turbulent fields and the longitudinal dispersion in 2-D turbulent shear flows as well as the 3-D turbulent shear flows in laboratory flumes and natural streams.

2.3 Numerical Simulation Procedures

2.3.1 Simulation Models

In the following, assume that the turbulent shear flows are confined within the rectangular cross-section and uniform in the longitudinal direction, and that the local mean velocity is:

$$\bar{u}_1(x_2, x_3) = \bar{u}^{x_2}(x_3) + u''_{23}(x_2, x_3) \qquad (2.3.1a)$$

$$\bar{u}_2(x_2, x_3) = 0 \qquad (2.3.1b)$$

$$\bar{u}_3(x_2, x_3) = 0 \qquad (2.3.1c)$$

The displacement vector $\boldsymbol{X}(\boldsymbol{a}, (n+1)\Delta t)$ at $t = (n+1)\Delta t$ of a particle released at $\boldsymbol{a} = 0$ and $t = 0$ can be evaluated by:

$$\boldsymbol{X}(\boldsymbol{a}, (n+1)\Delta t) = \boldsymbol{X}(\boldsymbol{a}, n\Delta t) + \boldsymbol{v}(\boldsymbol{a}, n\Delta t)\,\Delta t \qquad (2.3.2)$$

Each component of the Lagrangian velocity $\boldsymbol{v}(\boldsymbol{a}, n\Delta t)$ can also be evaluated by:

$$v_1(\boldsymbol{a}, n\Delta t) = \bar{u}_1\left\{\frac{Y^n + Y^{n+1}}{2}, \frac{Z^n + Z^{n+1}}{2}\right\} + u_1'(X^n, Y^n, Z^n, n\Delta t) \qquad (2.3.3a)$$

$$v_i(\boldsymbol{a}, n\Delta t) = u_i'(X^n, Y^n, Z^n, n\Delta t) \qquad (i = 2, 3) \qquad (2.3.3b)$$

In the numerical simulation procedure, $\boldsymbol{u}'(\boldsymbol{X}(\boldsymbol{a}, t), t)$ is simulated using the "Turbulon Theory" initiated by Inoue (1952) and the "Random Number Models" developed by Hino (1965). The model has been used for the analysis of the turbulent diffusion by Hino (1965), and Hayashi and Iwasaki (1975), and for the analysis of the longitudinal dispersion in two-dimensional turbulent shear flows by Sumitomo (1976).

The outlines of the simulation procedures are as follows:

1. Turbulence v' is represented by the sum of its component v_k',

$$v' = v_0' + v_1' + \ldots + v_k' + \ldots + v_n' \qquad (2.3.4)$$

where v_k' is the k-th rank component.

2. Each rank component has its own turbulent intensity A_k.

$$v_k' = A_k R_k \tag{2.3.5}$$

where R_k is the random number of which the ensemble average is equal to zero and the standard deviation is unity, and the subscript k denotes the variables related with the k-th rank component.

3. Each rank component also has its own life time τ_k, and by using the geometric progression models it is written as:

$$\tau_k = \tau_0(1/2)^k \tag{2.3.6}$$

where the proportional constant of the geometric progression is a half.

R_k can be generated by electronic computer and the movement of a particle can be simulated by use of Eq. 2.3.2 and the time series of Lagrangian velocity of a particle can be evaluated by Eq. 2.3.3.

Other noticeable features used in the numerical simulations are:

1. The number of the maximum rank of the turbulence is six, that is, k is equal to 0 to 5.

2. Turbulent intensity in the longitudinal direction used in the numerical experiments is

$$v_i'^2 = u_1'^2 = 2.50{u_*}^2 \tag{2.3.7}$$

which is obtained by averaging the universal function models proposed by Asano(1980) with respect to the flow depth. The turbulent intensities in the other directions are obtained by the relationship between the turbulent diffusivity and the turbulent intensity:

$$\varepsilon_i = v_i'^2 T_L \tag{2.3.8}$$

Different turbulent diuffusivities are used in each numerical experiment, however, the relationship proposed by Asano (1980):

$$T_L = 0.72\frac{d}{u_*} \tag{2.3.9}$$

is used in all the experiments. The details will be shown in each numerical experiments.

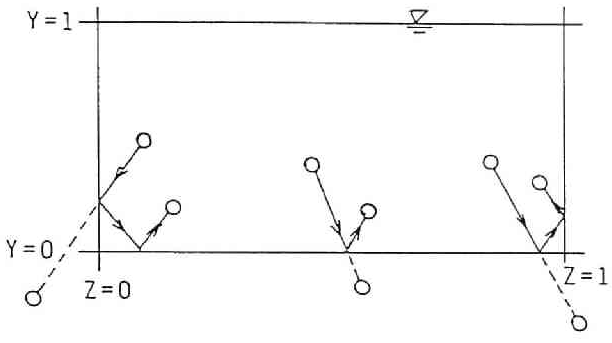

Figure 2.3.1: Reflections of particles at boundaries.

3. The time step Δt for the particle tracing is determined at:

$$\Delta t = 0.6\frac{d}{u_*} \tag{2.3.10}$$

by the results of the preliminary experiment described in **Subsection 2.5.2**. This Δt is also equal to the life time of the 5-th rank component of the turbulence.

4. Boundary condition used is "the complete reflection" of a particle at the boundaries, and the turbulent velocity v_i' and its each component v_{ik}' has the same absolute value but the opposite sign after the reflection.

2.3.2 Measuring Lagrangian Auto-Correlation Function in Shear Flows

(1) Definition of the Lagrangian Auto-Correlation Function

The longitudinal component of the Lagrangian turbulent velocity in shear flows of Eq. 2.2.9 is rewritten in the form of

$$v_1'(s; \boldsymbol{a}, t_0) = u_1(\boldsymbol{X}(s; \boldsymbol{a}, t_0), t) - U \tag{2.3.11}$$

where $\boldsymbol{a}$ is the displacement vector of a particle at the initial time $t = t_0$ and s the travel time from $t = t_0$. Introduce the new function

$$b_L(s_1, s_2; \boldsymbol{a}, t_0) \equiv v_1'(s_1; \boldsymbol{a}, t_0) v_1'(s_2; \boldsymbol{a}, t_0) \tag{2.3.12}$$

b_L is a product of the Lagrangian turbulent velocities at $t = t_0 + s_1$ and $t = t_0 + s_2$ of the particle released at $\boldsymbol{x} = \boldsymbol{a}$ and $t = t_0$ and the function of $s_1, s_2, \boldsymbol{a}$, and t_0 at

moment. The Lagrangian auto-correlation function is defined by the average of b_L and the following three kinds of averaging are practically possible.

a. Ensemble average: $< b_L >$

$$< b_L(s_1, s_2; \boldsymbol{a}, t_0) > \equiv \lim_{N\to\infty} \frac{1}{N} \sum_{i=1}^{N} v_1'(s_1; \boldsymbol{a}, t_{0i}) v_1'(s_2; \boldsymbol{a}, t_{0i}) \tag{2.3.13}$$

This method is realized by use of the time series of the Lagrangian velocity of N particles which are released at the same point $\boldsymbol{x} = \boldsymbol{a}$, but different time $t = t_{0i}$, where i ($= 1$ to N) denotes the i-th particle. This is initially used by Taylor(1921).

b. Volumetric average: $[b_L]$

$$[b_L(s_1, s_2; \boldsymbol{a}, t_0] \equiv \lim_{V_a\to\infty} \frac{1}{V_a} \iiint v_1'(s_1; \boldsymbol{a}, t_0) v_1'(s_2; \boldsymbol{a}, t_0) da_1 da_2 da_3 \tag{2.3.14}$$

This is the average of $b_L(s_1, s_2; \boldsymbol{a}, t_0)$ with respect to the box V_a in which the particles were located at time $t = t_0$.

c. Temporal average: $\overline{b_L}$

$$\overline{b_L}(s_1, \sigma; \boldsymbol{a}, t) \equiv \lim_{T\to\infty} \frac{1}{T} \int_0^T v_1'(s_1; \boldsymbol{a}, t_0) v_1'(s_1 - \sigma; \boldsymbol{a}, t_0) ds_1 \tag{2.3.15}$$

where σ is the lag time. This averaging method is commonly used in the analysis of the turbulent motion and realized by averaging a time series of observed Lagrangian velocity of a particle released at a point $\boldsymbol{x} = \boldsymbol{a}$ at time $t = t_0$ with respect to the travel time s_1.

The flow field concerned is 3-D turbulent shear flows which is confined, uniform in the longitudinal direction and stationary. Therefore, the ensemble average with respect to the particles released at $\boldsymbol{x} = \boldsymbol{a} = (a_1, a_2, a_3)$ at different time is equal to the average with respect to the particles which were located on the line parallel to the x_1 coordinate and through the point $\boldsymbol{a} = (a_1, a_2, a_3)$ at the time $t = t_0$. That is,

$$< b_L >= \lim_{L\to\infty} \frac{1}{L} \int_0^L v_1'(s_1; \boldsymbol{a}, t_0) v_1'(s_2; \boldsymbol{a}, t_0) da_1 \tag{2.3.16}$$

Therefore, the volumetric average $[b_L]$ is equivalent to the cross-sectional average of $< b_l >$, that is,

$$[b_L] = \frac{1}{A} \iint < b_L > da_2 da_3 \tag{2.3.17}$$

$[b_L]$ is also independent on the time when the particles are released, because $[b_L(s_1, s_2; \boldsymbol{a}, t_0)]$, the volumetric average at $t = t_0$ is also equivalent to

$[b_L(s_1', s_2'; \boldsymbol{a}'(s_1; \boldsymbol{a}, t_0), t_0 + s_1)]$, the average with respect to the volume in which the particles are located at the arbitrary time $t = t_0 + s_1$, because the flow field is uniform and stationary.

In case the travel time of a particle is long enough that the probability of the particle location in a cross-section is uniform, $\overline{b_L}$ is independent on the initial location of a particle.

Thus, three kinds of the averaging methods are theoretically equivalent each other and they are the function of only the lag time $\sigma = s_1 - s_2$ as described in details in Iwasa, Aya and Mitsuishi (1985). Note the following features of the Lagrangian turbulent velocity:

1. The Eulerian turbulent velocity is uniform in the longitudinal direction but non-uniform in the vertical and lateral directions, and the longitudinal component of the Eulerian locally averaged velocity is steady and three-dimensional,

2. Therefore, the longitudinal component of the Lagrangian velocity is stationary and random, because the particle migrates in a cross-section and gets the stationary random turbulent velocity in the longitudinal direction.

The Lagrangian auto-correlation function is quite influenced by the initial location of the particle during the short travel time. Fig. 2.3.2 illustrates $[b_L]$ and $< b_L >$ obtained in the numerical experiments for 2-D dispersion studies. In a short travel time, $< b_L >$ are quite dependent on the releasing point of particles, however, it converges into $[b_L]$ with increase of the travel time. In the following sections, Lagrangian auto-correlation function will be calculated by use of the definitions of Eqs. 2.3.14 to 2.3.17.

2.4 Preliminary Numerical Experiments

2.4.1 Objectives and Design of Experiments

The numerical study on the particle dispersion in 2-D turbulent shear flows has been conducted before making the numerical experiments in 3-D turbulent shear flows. The objectives of the study are:

1. Calibrating the simulation codes developed,

2. Verifying the assumptions introduced in the theory and the theoretical results obtained in Section 2.2,

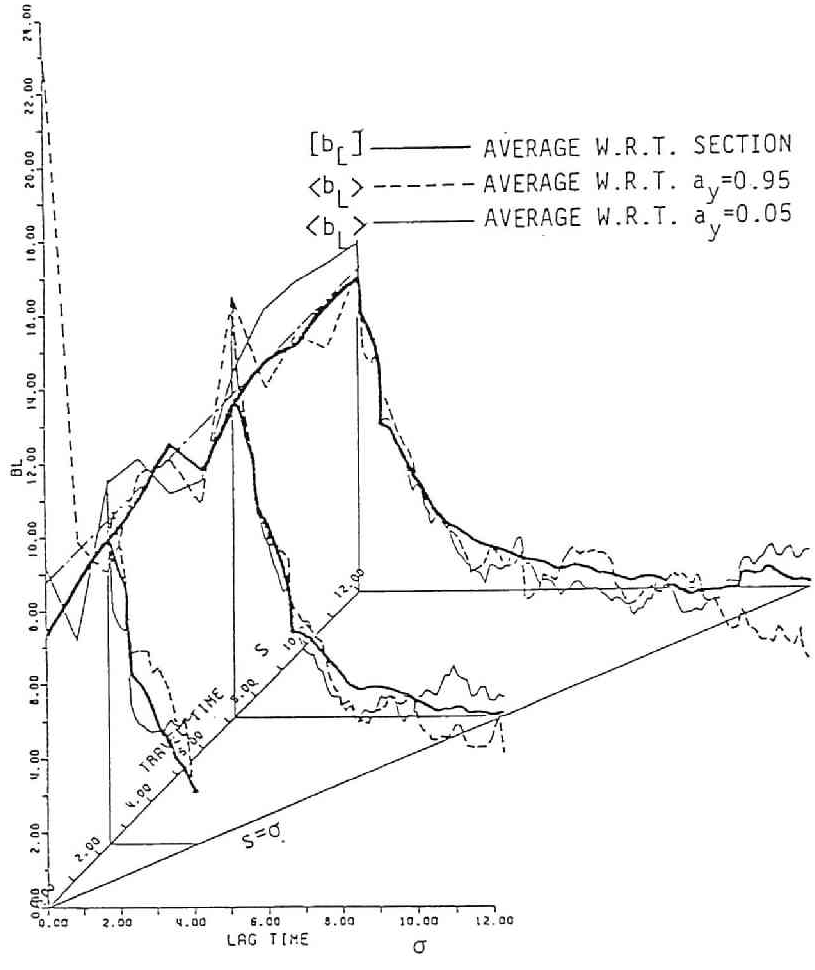

Figure 2.3.2: $< b_l >$ and $[b_L]$ obtained at some travel time in 2-D turbulent shear flow simulation. Particles are released at some points in a cross-section.

3. Verifying the theoretical results for the dispersion coefficient based on 2-D turbulent diffusion equation developed by Taylor(1954) and Elder(1956), and

4. Disclosing the Lagrangian characteristics on the particle dispersion in 2-D turbulent flows.

The strcuture of the 2-D turbulent shear flows are simpler than the 3-D turbulent flows, and it is much easier for handling the simulation codes, therefore numerical experiments in 2-D turbulent shear flows are preferable in view of the first and second objectives. The theoretical results based on the 2-D turbulent diffusion equation by Elder(1956) is very simple and clear, and looks rigorous, however, it also seems very difficult to realize the dispersion in 2-D turbulent shear flows by hydraulic experiments in laboratory flumes, because the particles disperse in the three-dimensional space and the actual velocity distribution is three-dimensional. Therefore the numerical study is required in view of the third and the forth objectives. The numerical experiments in 2-D turbulent shear flows have already been conducted by many researchers, that is, numerical study based on the 2-D turbulent diffusion equation by Yotsukura and Fiering (1964), and Tanaka (1979), the numerical study based on the "one-particle dispersion theory" by Sullivan (1971) and Sumitomo (1976) and so on. These results can be usable to examine the numerical results obtained by this study.

In order to cover the four objectives stated above, the four series of numerical experiments are designed, that is, the numerical experiments based on the 2-D turbulent diffusion equation (Run E Series), the Lagrangian numerical experiments in the uniform turbulent field (Run U Series), the Lagrangian numerical experiments in the 2-D turbulent flows (Run L Series and P Series). The details of experimental conditions in each series will be shown below.

2.4.2 Diffusion in Homogeneous Turbulent Field (Run U Series)

The flow field specified is the homogeneous and isotropic 2-D turbulent field in the infinite space, and the locally averaged velocity distribution is $u(x_2, x_3) = 0$. The number of particles released at $\boldsymbol{x} = \boldsymbol{a}$ is 2 000. The flow condition and results will be given in **Table 2.5.2 in Section 2.5.**

2.4.3 Dispersion Based on 2-D Turbulent Diffusion Equation (Run E Series)

The turbulent diffusion equation in 2-D uniform flows is:

$$\frac{\partial \bar{c}}{\partial t} + \bar{u}_i(x_2)\frac{\partial \bar{c}}{\partial x_i} = \frac{\partial}{\partial x_1}\left(\varepsilon_1 \frac{\partial \bar{c}}{\partial x_1}\right) + \frac{\partial}{\partial x_2}\left(\varepsilon_2 \frac{\partial \bar{c}}{\partial x_2}\right) \tag{2.4.1}$$

where $\bar{c}$ is the averaged concentration, ε_i the turbulent diffusion coefficient in the x_i direction, x_i the space coordinate ($i = 1$ and 2). The velocity distributions used is the logarithmic velocity distribution in the x_1 direction:

$$\frac{\overline{u}_1 - U}{u_*} = \frac{1}{\kappa}\left(\ln \frac{x_2}{d} + 1\right) \tag{2.4.2a}$$

and

$$\bar{u}_2 = 0 \tag{2.4.2b}$$

The basic equation is transformed into the non-dimensional form by use of the flow depth d and the shear velocity u_* and into the moving coordinate system $\xi = (x_1 - Ut)/d$. The boundary conditions specified is the "method of image" at the top and the bottom in accordance with the Lagrangian experiments and the length in the longitudinal direction is infinite. The initial condition is:

$$\bar{c} = C_0 \qquad \text{for} \quad -0.01 \leq \xi \leq 0.01 \tag{2.4.3}$$

Eq. 2.4.1, under such boundary conditions, and the initial condition of Eq. 2.4.3 can be solved by the finite difference method and the ADI scheme was used. The magnitude of the mesh size is selected as: $\Delta\xi$ = 0.01, 0.05 or 0.2 ($\xi = x_1/d$), $\Delta\eta$ = 0.025, 0.05 or 0.1 ($\eta = x_2/d$) and $\Delta\tau$ = 0.0002, 0.01 or 0.05 ($\tau = t/du_*$). The velocity on the bottom is adjusted so that the accumulated discharge in the moving coordinate system is equal to zero. The velocity distributions specified is shown in Fig. 2.4.1. The turbulent diffusion coefficient in the x_1 direction is ε_1/du_* = 1.80 and that in the vertical direction x_2 is:

$$\frac{\varepsilon_2}{du_*} = \kappa\eta(1-\eta) \tag{2.4.4}$$

or

$$\frac{\varepsilon_2}{du_*} = \frac{\kappa}{6} \tag{2.4.5}$$

The condition used and results will be summarized in Table 2.5.1.

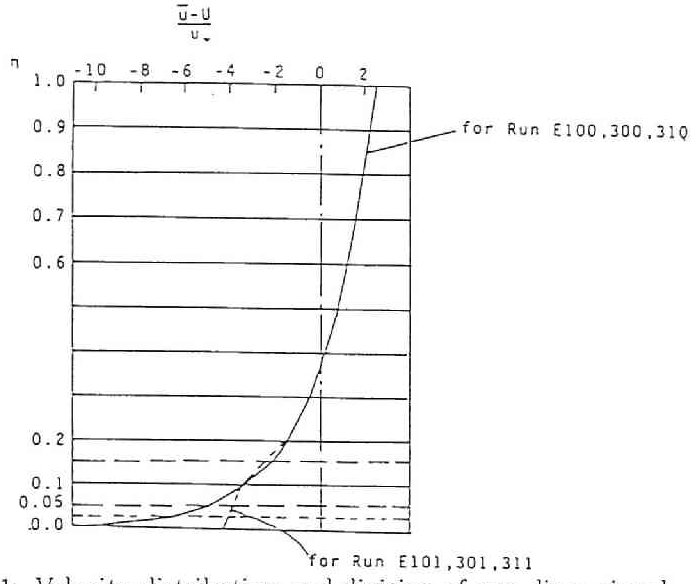

Figure 2.4.1: Velocity distribution and division of non-dimensional depth in 2-D simulation.

2.4.4 Particle Dispersion in 2-D Turbulent Shear Flows (Runs L and P Series)

Two kinds of velocity distributions are used, that is,

Logarithmic velocity distribution in Run L Series:

$$\frac{\overline{u}_1}{u_*} = \frac{1}{\kappa}\left(\ln\frac{x_2}{d} + 1\right) + \frac{U}{u_*} \tag{2.4.6}$$

In case $\overline{u}_1$ is negative, $\overline{u}_1$ is replaced by zero. The von Karman's constant κ is determined at 0.4 and the depth-averaged velocity $U = 20$.

Power law in Run U Series:

$$\frac{\overline{u}_1}{u_*} = 8.74 Re_*^{1/7}\left(\frac{x_2}{d}\right)^{1/7} \qquad \left(Re_* \equiv \frac{u_* d}{\nu}\right) \tag{2.4.7}$$

Re_* used is 836 which is equivalent to the averaged velocity $U/u_* = 20$ and $Re_* = 400$ is also used.

Some combinations of the turbulent intensities in the longitudinal and vertical directions are used after the results by Asano (1980) and Laufer (1954). Transformation between the turbulent intensity, the Lagrangian integral time scale and the turbulent diffusion coefficient was made by use of Eqs. 2.3.8 and 2.3.9 and they will be summarized in **Table 2.5.3** with the measured results in the numerical experiments.

The 200 particles start from each releasing point, and the 10 releasing points selected uniformly distributes on the line $x_1 = 0.0$. The duration of particle tracing is over $2000\Delta\tau_5$ and after completion of the traces of 200 particles from one releasing point, the releasing point is shifted to the next point. The statistical analysis of the time-series of Lagrangian velocity and locations of particles are made after the completion of 2000 particle tracings. In case of calculating the Lagrangian turbulent intensity and the auto-correlation function, 40 time series are selected as the sample and time-series analysis was made for each time-series and the ensemble average over 40 samples.

2.5 Results and Discussion on Preliminary Experiments

2.5.1 Results of Calibration Test

(1) Turbulent Diffusion Test (Run–U10)

One-dimensional turbulent diffusion of particles in homogeneous turbulent fields was examined. Its conditions specified and the dispersion coefficient measured will be summarized in Table 2.5.2. The variances of particle location σ_1^2/d^2 are plotted against the number of time step $n = t/\Delta t$ ($\Delta t = d/u_*$) in Fig. 2.5.1. The time-dependent growth of the variance is non-linear for $n < 100$, but becomes linear for $n > 200$ as described by Taylor (1921). The turbulent diffusion coefficient defined by Eq. 2.1.2a is calculated at :

$$D \equiv \frac{1}{2}\frac{d}{dt}[X'^2(a,t)] = 0.11\frac{d^2}{\Delta t} \tag{2.5.1}$$

By use of the specified condition:

$$[v'^2]/{u_*}^2 = 2.50$$

and

$$T_L/(d/u_*) = 0.72$$

the dispersion coefficient is calculated at

$$D = [v'^2]T_L = 1.80du_* \tag{2.5.2}$$

These two values obtained by Eqs. 2.5.1 and 2.5.2 should be equal each other, therefore Δt is calculated at

$$\Delta t = 0.061\frac{d}{u_*} \tag{2.5.3}$$

Eq. 2.5.3 will be used in the following analysis.

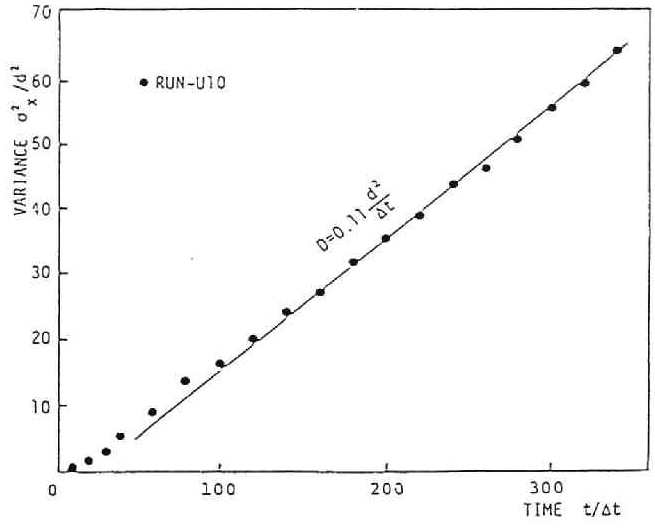

Figure 2.5.1: Time-dependent growth of variances in homogeneous turbulent field in Run U10.

(2) Longitudinal Dispersion Tests (Runs–E300, E310 and L30)

The longitudinal dispersion coefficient obtained by the particle dispersion test (Run–L30) and the Eulerian simulation (Runs–E300 and E310) based on the 2-D turbulent diffusion equation is summarized with the specified condition in Table 2.5.1. The vertical turbulent diffusion coefficient is uniform in Run–E300, however, it has a parabolic distribution in Run–E310. The longitudinal turbulent diffusion coefficient used is $\varepsilon_1/du_* = 1.80$ in Runs–E300 and 310. This value is derived from the results by Asano (1980), and he also measured the square of the longitudinal turbulent intensity

Table 2.5.1: Summary of conditions and results in experiments, Runs–E300, E310 and L30.

	CONDITION				DISPERSION COEFFICIENT	
	(1) ε_1/du_*	(2) ε_2/du_*	(3) $u_1'^2/u_*^2$	(4) $u_2'^2/u_*^2$	(5) D/du_*	(6) D/du_*
RUN-E300	1.80	$\kappa/6$	——	——	8.70	8.75
RUN-E310	1.80	$\kappa\eta(1-\eta)$	——	——	8.43	8.11
RUN-L30	——	——	2.50	0.0926	11.80	8.75
NOTATIONS: (5); Simulated, (6); Elder's Analysis						

at $u_1'^2/u_*^2 = 2.50$ in 2-D turbulent flows and this value is specified in Run–L30. This condition is equivalent to that used in Runs–E300 and E310. The square of the vertical turbulent intensity specified is $u_2'^2/u_*^2 = 0.0926$ and this is equivalent to the vertical turbulent diffusion coefficient $\varepsilon_2/du_* = \kappa/6$ and $T_L = 0.072d/u_*$.

The theoretical values of the dispersion coefficient calculated by Elder's formula (Elder, 1956)

$$D = d^2 \int_0^1 \frac{d\eta_1}{\varepsilon_2} \left\{ \int_0^{\eta_1} (\bar{u}_1 - U) d\eta \right\}^2 + \frac{1}{d} \int_0^1 \varepsilon_1 d\eta \tag{2.5.4}$$

are also listed in Table 2.5.1. They are little different from the dispersion coefficient in 2-D turbulent flows originally given by Elder

$$D = 6.01 du_* \tag{2.5.5}$$

because the turbulent diffusion coefficient in the longitudinal direction used here is larger than that used by Elder, and because the numerical integration was used in calculating Eq. 2.5.4.

The magnitudes of the longitudinal dispersion coefficient obtained in Runs–E300 and E310 have a good agreement each other. It is also disclosed that the longitudinal dispersion coefficient resulting from the condition of the constant turbulent diffusion coefficient is a little larger than those from the condition of the parabolic distribution, however the magnitude of the difference between two results is negligibly small and they are almost equal to the theoretical values respectively. Therefore, it is concluded that the assumption of the constant vertical diffusivity introduced in the Lagrangian simulation models is appropriate.

The magnitude of the longitudinal dispersion coefficient obtained by the Lagrangian simulation Run–L30 is a little larger than those measured in Runs–E300 and E310. The time-dependent growth of the variance measured in Run–L10 and Run-E300 is shown in Fig. 2.5.2 and the concentration distributions in Fig. 2.5.3. The variances measured in Run–L10 is also a little larger than those in Run–E300, however the concentration distributions are quite similar, therefore it is concluded that the Lagrangian simulation models proposed in **Section 2.3** is valid and useful for investigating the characteristics of the Lagrangian turbulence and the dispersion processes in shear flows.

2.5.2 Statistical Properties of the Lagrangian Turbulence in 2-D Turbulent Shear Flow (Run U and Run P Series)

The data measured in the eight numerical experiments are summarized with the conditions specified in each experiment in Table 2.5.2. The difference in each series

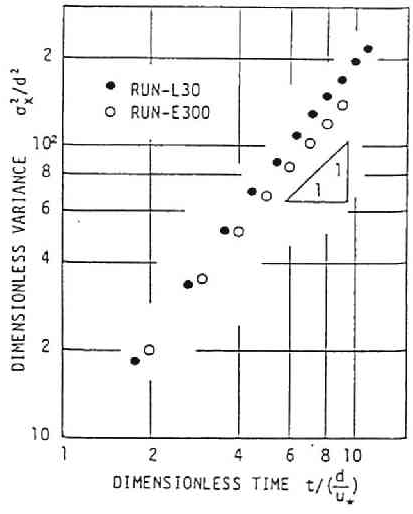

Figure 2.5.2: Comparison of time-dependent growth of variances in 2-D turbulent shear flows obtained by Lagrangian simulation Run L30, and Eulerian simulation Run E300.

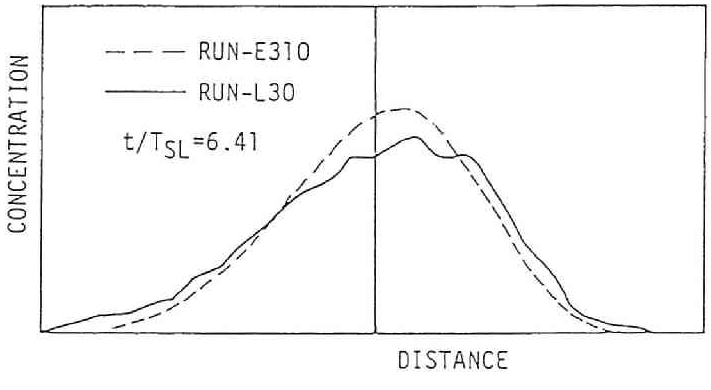

Figure 2.5.3: Comparison of concentration distributions obtained by Lagrangian simulation Run L30 and Eulerian simulation Run E310.

Table 2.5.2: Summary of conditions and results in 2–D Lagrangian simulations.

RUN NO.	FLOW CONDITION (1) $u_1'^2/u_*^2$	(2) $u_2'^2/u_*^2$	(3) $u_3'^2/u_*^2$	(4) U/u_*	THEORETICAL RESULTS (5) $\frac{1}{A}\int_A(u_1'^2+\overline{u_1''^2})/u_*^2 dA$	(6) $T_{SL}\sqrt{\frac{d}{U_*}}$	SIMULATED RESULTS (7) $[v_1'^2]/u_*^2$	(8) D/du_*	(9) $T_{SL1}/\frac{d}{U_*}$	(10) $T_{SL2}/\frac{d}{U_*}$
RUN-U10	2.50	——	——	0.0	——	——	2.50	1.80	0.720	——
RUN-L10	2.50	0.383	——	20.0	8.75	0.245	8.23	5.45	0.660	0.793
RUN-L20	0.00	0.383	——	20.0	6.25	0.245	5.82	3.61	0.625	0.692
RUN-L30	2.50	0.0926	——	20.0	8.75	1.013	8.41	11.80	1.403	1.878
RUN-L40	0.00	0.0926	——	20.0	6.25	1.013	6.40	10.00	1.560	1.655
RUN-L50	2.50	2.50	——	20.0	8.75	0.037	0.43	2.87	0.340	0.326
RUN-L60	2.50	0.276	——	20.0	8.75	0.338	7.84	6.05	0.770	0.507
RUN-P10	2.50	0.0802	——	20.0	8.85	1.17	8.31	13.90	1.670	——
RUN-P20	2.50	0.0891	——	18.0	7.64	1.05	7.23	11.70	1.620	——
RUN-3A	2.50	0.0926	0.208	19.0	12.68	31.7	11.1	102.0	9.19	6.26
RUN-3B	2.50	0.0926	0.417	19.0	12.68	15.8	11.1	65.0	5.86	4.42

NOTATIONS; U Series; Uniform Flow, L Series; Log-law(κ=0.4), P Series; Power-law(n=1/7)
3 Series; Three Dimensional Flow
(5); Lumley's Formula, (6); Fischer's Formula, (9); $T_{SL1}=D/[v_x'^2]$, (10); $T_{SL2}=\int_0^\infty R_L(\tau)d\tau$

is made by the specified conditions for turbulent intensity in the longitudinal and/or the vertical direction.

(1) Lagrangian Turbulence and Its Intensity

The time series of the Lagrangian turbulent velocity measured in Run–L10 is illustrated in Figs. 2.5.4 (a) and (b). The vertical component v_2' in Fig. 2.5.4(b) was generated by electronic computer with use of the "Random Number Models" described earlier and looks rigorous. The longitudinal component v_1' in Fig. 2.5.4(a) is the sum of the Eulerian/Lagrangian turbulence generated and the turbulence which is resulting from the random movements of a particle migrating in the confined steady 2-D shear flows. Therefore, the magnitude of the turbulent intensity in the longitudinal direction is of the much larger order than that in the vertical direction and it looks that the turbulence has much lower frequency components, which is caused by the migration of the particle.

The square of the turbulent intensity in the longitudinal direction calculated by

$$\left[v_1'^2\right] = \frac{1}{A}\int_A u_1'^2 dA + \frac{1}{A}\int_A u_{23}''^2 dA \qquad (2.5.6)$$

is listed in the 4th column and the measured one in the 5th column in Table 2.5.2. These two results have a fine agreement each other and their magnitude is of the much larger order than those of Eulerian turbulence. It is also disclosed that the

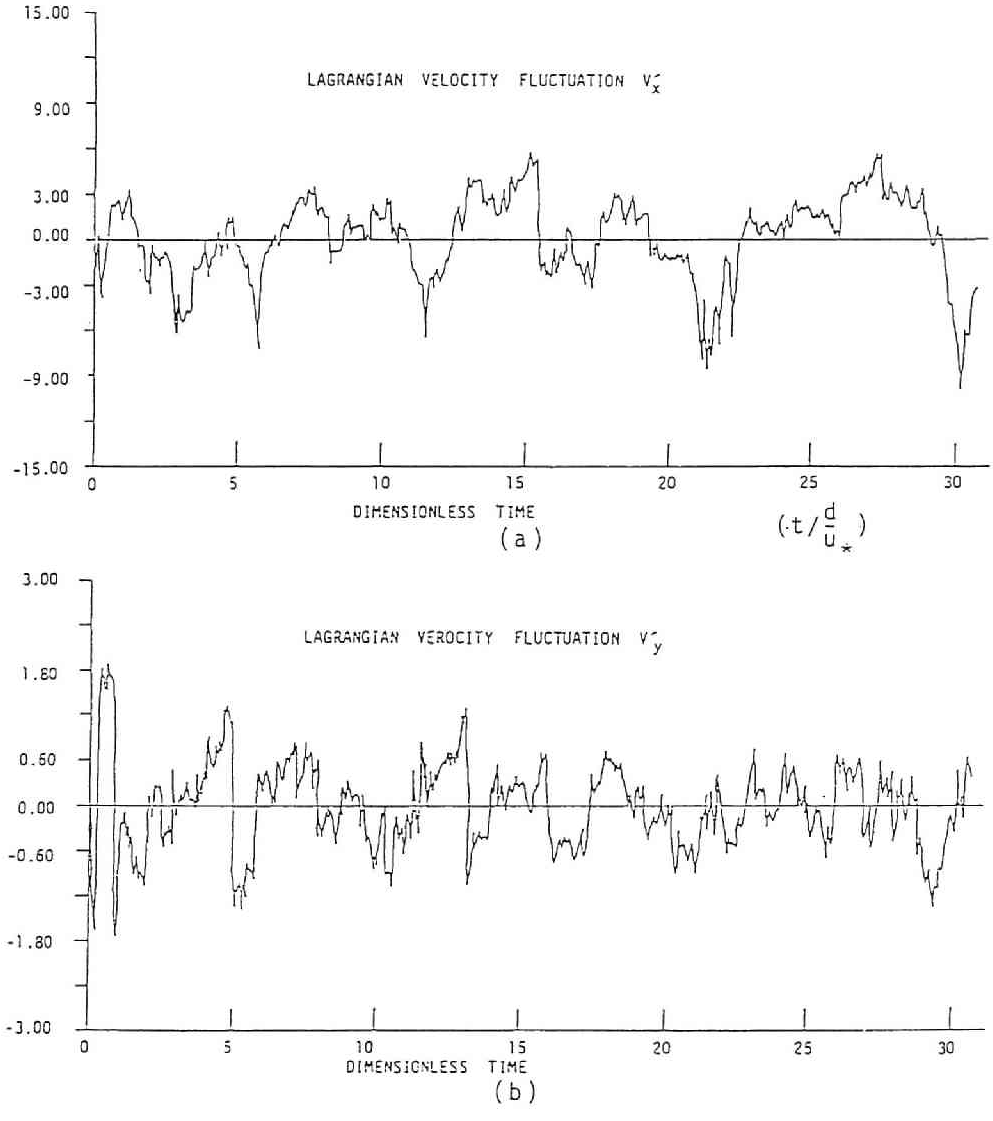

Figure 2.5.4: Time series of Lagrangian turbulent velocity in Run–L10. (a) Longitudinal component, and (b) vertical component

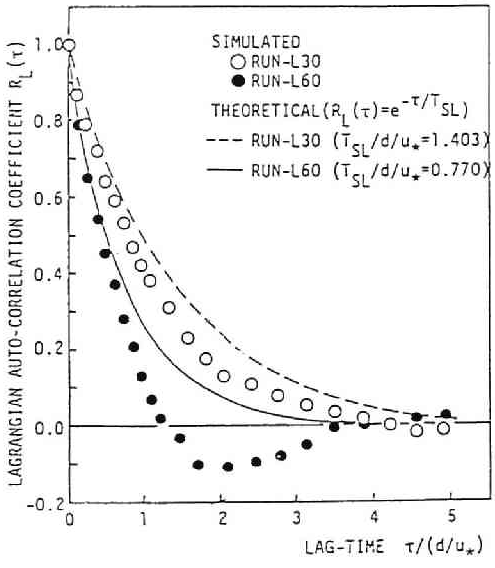

Figure 2.5.5: Lagrangian auto-correlation coefficients. Open and solid circles denote measured ones in Runs L30 and L60, and solid and dash-dotted lines denote predicted ones by Eq. 2.5.7.

Lagrangian turbulence can be observed even if the Eulerian turbulence in the x_1 direction did not exist.

Thus, the simulation results satisfy the theoretical relationship of Eq. 2.2.41a and the simulation models confirme to realize the random movement of particles.

(2) Lagrangian Auto-Correlation Coefficient

The auto-correlation function was calculated by the inverse-transform of the spectrum density function with use of FFT, and the sample size is 1024. The Lagrangian auto-correlation coefficient measured in Runs–L30 and L60 are shown in Fig. 2.5.5, and an example of the spectrum density function is illustrated in Fig. 2.5.6.

In Fig. 2.5.5, the auto correlation coefficient calculated by

$$R_L(\tau) = e^{-t/T_{SL}} \tag{2.5.7}$$

is also plotted and the integral time scale is determined by the measured turbulent intensity and the longitudinal dispersion coefficient by use of Eq. 2.5.9 bellow. Fig. 2.5.5 discloses that the Lagrangian auto-correlation function in 2-D turbulent shear flows can be estimated by Eq. 2.5.7.

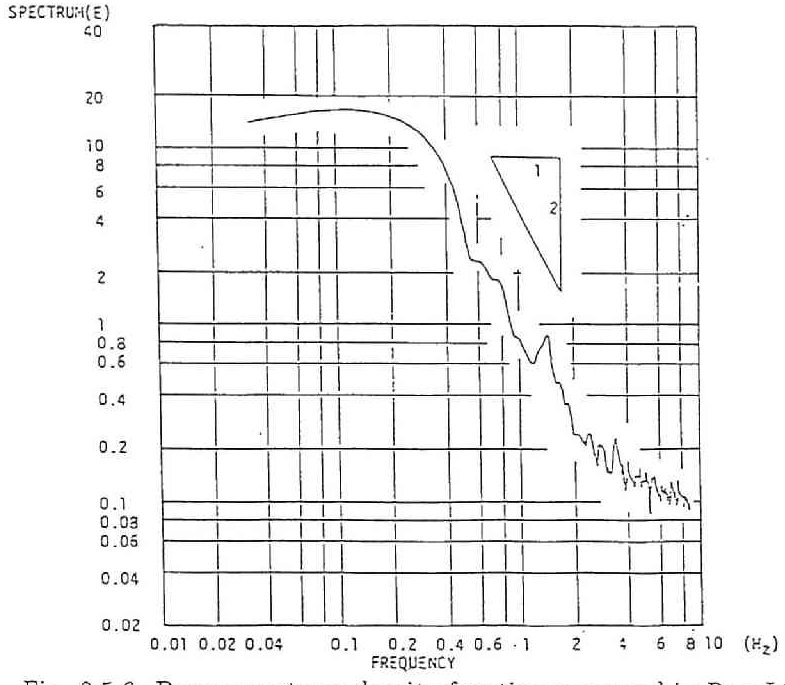

Fig. 2.5.6: Power spectrum density function measured in Run L10.

(3) Integral Time Scale

The integral time scale is calculated by both methods of

$$T_{SL} = \lim_{t\to\infty} \int_0^t R_L(\tau) d\tau \tag{2.5.8}$$

and

$$T_{SL} = D/[v'^2] \tag{2.5.9}$$

They are listed in the 8th and the 9th column in Table 2.5.2. The integral time scales obtained by the two different methods agree each other quite well and its magnitude is of the order of d/u_*. The estimated values by use of Fischer's equation

$$T_{Fv} = \frac{1}{14.8}\frac{d^2}{\varepsilon_2} \tag{2.5.10}$$

are also listed in the 7th column in Table 2.5.2. The estimated values are a little smaller than measured ones, but Eq. 2.5.10 gives good approximation for T_{SL}.

(4) Concentration Distributions

Examples of the concentration distribution in the vertical direction, that is, the probability density distributions of particle location in the vertical direction at different travel times are illustrated in Fig. 2.5.7.

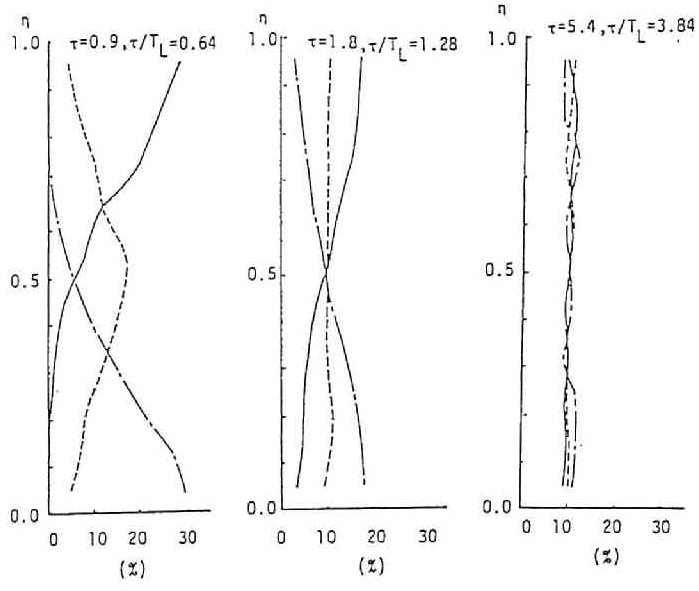

Figure 2.5.7: Probability density distributions in the vertical location of particles released from different points (Run–L30). Solid lines denote the distributions for line source, broken lines for a point source at $\eta = 0.9$, dash-dotted lines at $\eta = 0.5$, and dotted lines at $\eta = 0.1$. (a) $t/T_{SL} = 0.64$, (b) $t/T_{SL} = 1.28$ and (c) $t/T_{SL} = 3.84$.

The releasing points of particles are $\eta = 0.1$, 0.5, and 0.9. In the short travel time, the probability density distribution is influenced by releasing points, however, it becomes more uniform with increase of the travel time, and after t/T_{SL} is bigger than 3, it is almost uniform. This fact corresponds to the linear-growth of the variance of particle location described in Eq. 2.5.7. The longitudinal distributions of the particle location at different times are also presented in Fig. 2.5.8. The distributions and the mean travel time are also quite influenced by the releasing point of particles in short travel time. They slowly become similar each other with increase of the travel time, and even when t/T_{SL} is greater than 9, the distinguished difference is observed. It is also notable that the distributions are quite different from the Gaussian distribution.

(5) Longitudinal Dispersion Coefficient

The longitudinal dispersion coefficient calculated by

$$D \equiv \frac{1}{2}\frac{d}{dt}[X'^2(a,t)] \tag{2.5.11}$$

is listed in the 7th column in Table 2.5.2. The magnitude of the longitudinal dispersion coefficient is larger than that of the longitudinal diffusion coefficient estimated by $\varepsilon_1 = u_1'^2 T_L$=1.80. Comparing the magnitude of the dispersion coefficient between Runs–L10 and L20, and Runs–L30 and L40, it is disclosed that the longitudinal dispersion coefficient is the sum of the turbulent diffusion term and the shear dispersion term as described in Eqs. 2.2.41d and/or 2.5.6. It is also described that the magnitude of the dispersion coefficient increases with decrease of the turbulent intensity in the vertical direction by comparing the results between Runs–L10, L30, L50 and L60. This fact means that the larger vertical turbulent intensity accelerates the migration of the particles in the vertical direction, and the dispersion coefficient decreases. This effect is the most affective on the magnitude of the longitudinal dispersion coefficient in 2-D turbulent shear flows. The different velocity distribution of the log-low and the power-low give the nearly the same values of the dispersion coefficient.

The theoretical values of the dispersion coefficient calculated by the author's Eq. 2.2.41d and Elder's Eq. 2.5.6 have nearly the same magnitude in each run as expected, but the results obtained by the simulation is a little larger than theoretical ones as seen in **Subsection 2.5.1**, however the magnitude of the dispersion coefficient is of the same order each other and it is much smaller than those measured in laboratory flumes and natural streams. The variation of the vertical turbulent diffusivity causes nearly the same effect on the magnitude of the longitudinal dispersion coefficient as

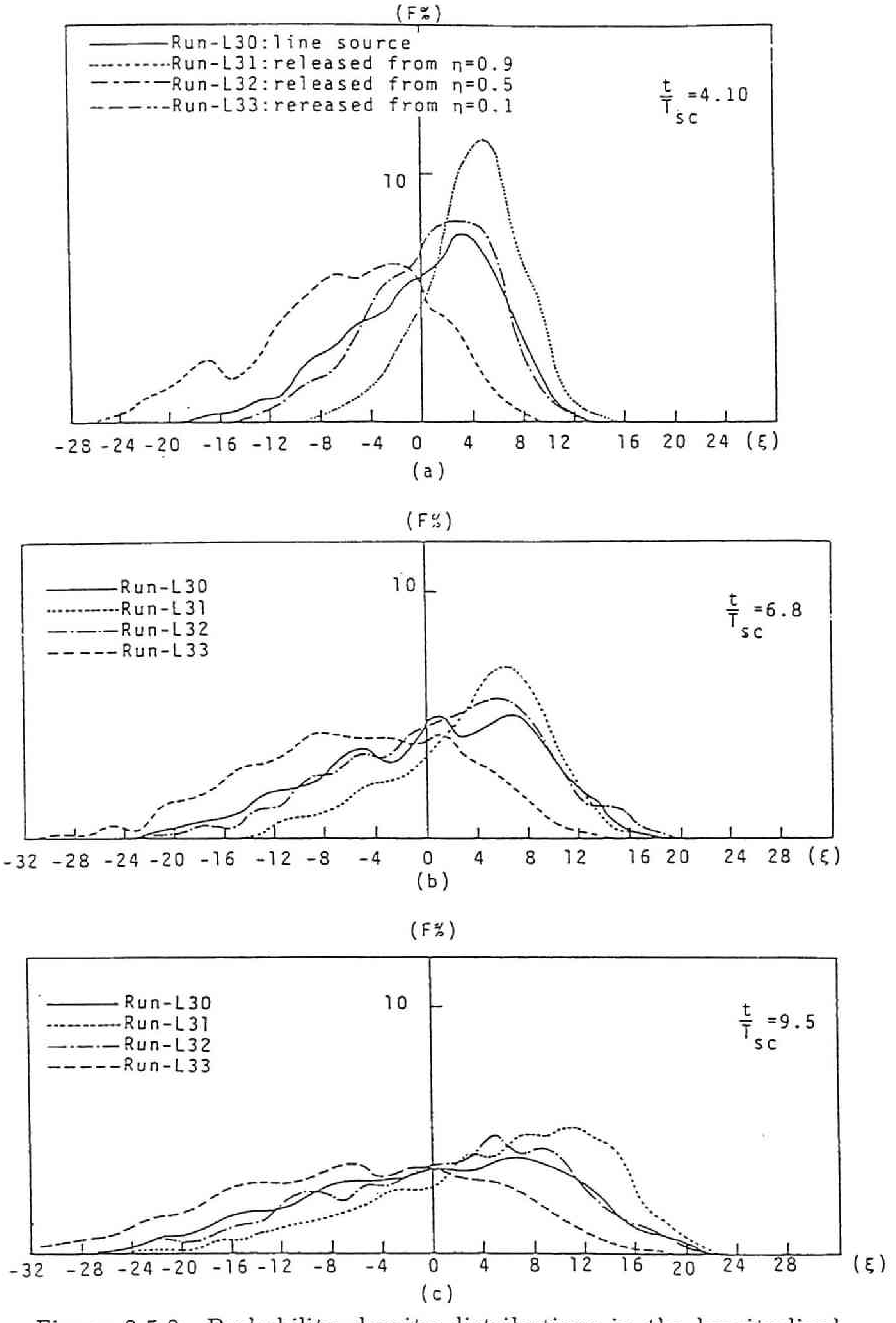

Figure 2.5.8: Probability density distributions in the longitudinal location of particles release from different points (Run–L30). Solid lines denote the distributions for line source, broken lines for a point source at $\eta = 0.9$, dash-dotted lines at $\eta = 0.5$, and dotted lines at $\eta = 0.1$. (a) $t/T_{SL} = 4.10$, (b) $t/T_{SL} = 6.80$, and (c) $t/T_{SL} = 9.50$.

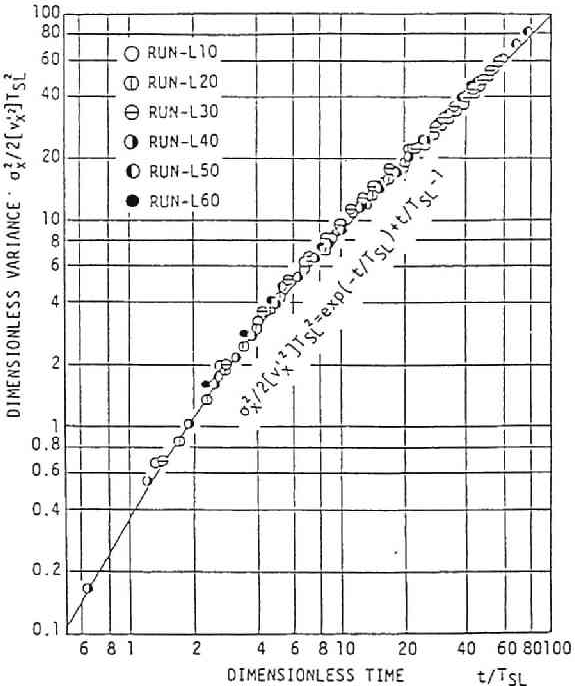

Figure 2.5.9: Time dependent growth of variances measured in simulation, and calculated by Eq. 2.5.2.

stated in the above paragraph.

(6) Time Dependent Growth of Variances

Time-dependent growth of the variances of particle locations is described by Eq. 2.1.1. By substituting Eq. 2.5.7 obtained in simulations into Eq. 2.1.1, the variances in non-dimensional form can be written in the form of

$$\frac{\sigma_1^2}{2[v_1'^2]T_{SL}^2} = \frac{t}{T_{SL}} - 1 + \exp(-\frac{t}{T_{SL}}) \tag{2.5.12}$$

In calculation of Eq. 2.5.12, $[v_1'^2]$ in the 7th column and T_{SL} in the 9th column of Table 2.5.2 is used. The comparison of the results calculated by Eq. 2.5.12 and measured one in experiments is made in Fig. 2.5.9. It is disclosed that Eq. 2.5.12 satisfactorily describes the time-dependent behavior of the variances in all experiments.

2.6 Three-Dimensional Experiment

2.6.1 Objectives and Design of Experiment

It is reported that the dispersion coefficient measured in the rectangular cross-section laboratory flumes is much larger than that predicted by Elder's formula of Eq. 2.5.4 and that observed ones in natural streams are much more larger. Fischer successfully proposed the formula predicting the longitudinal dispersion coefficient in natural streams. He also proposed the formula predicting the longitudinal dispersion coefficient based on the theory of one-particle analysis, but it is less successful. Matsuoka (1989) reported $B_L(\tau)$ has a long tail in the falling limb and T_{SL} in laboratory flumes is quite long. This report is only one which is concerned with the characteristics of the Lagrangian turbulence in 3-D confined turbulent shear flows, as far as the author knows. Therefore, it can be said that the mechanism of the longitudinal dispersion in the 3-D channel in view of one-particle analysis has not yet been disclosed. The numerical experiment in 3-D turbulent shear flows are planed in order to investigate the following objectives by use of the models proposed in **Section 2.2**, and numerical models developed in **Section 2.3** and verified in **Sections 2.4** and **2.5**;

1. Verifying the models proposed in **Section 2.2**,
2. Disclosing the characteristics of the Lagrangian turbulence in 3-D confined turbulent shear flows and their differences between 2-D and 3-D confined turbulent shear flows,
3. Making the mechanism of the longitudinal dispersion in 3-D confined turbulent shear flow more clear in view of the one-particle analysis, and
4. Examining the applicability of the models proposed to the actual flows

14 numerical experiments as shown in Table 2.6.1 were conducted in order to accomplish the objectives above. They are divided into two categories by the given local mean velocity distributions. The first simulation set of Run 3 Series: Run 3A to 3I was conducted under the first, second and third objectives and the hypothetical velocity distributions as will be shown in the next subsection are used. The 3-D velocity distributions and the intensity of the turbulence is specified so that their influence on the Lagrangian turbulence characteristics is made to be clear through the experiment. The second set of Run S Series: S921 to S222RC was made for the forth objectives and the velocity distributions measured in the laboratory dispersion experiments in **Chapter 4** are used, however the intensity of the turbulence is the same throughout the series. Conditions used for specifying the turbulent intensity are

Table 2.6.1: Summary of conditions and results in 3-D numerical experiment.

(1) Run No.	(2) $\bar{u}^{x_2}$	(3) κ	(4) $u_1'^2/u_*^2$	(5) $u_2'^2/u_*^2$	(6) $u_3'^2/u_*^2$	(7) B/d
3A	u_1	0.4	2.50	0.0926	0.208	16.8
3B	u_1	0.4	2.50	0.0926	0.417	16.8
3C	u_1	0.4	2.50	0.0926	0.278	16.8
3D	u_1	0.3	2.50	0.0926	0.278	16.8
3E	u_1	0.4	2.50	0.383	0.278	16.8
3F	u_1	0.4	2.50	0.276	0.278	16.8
3G	u_1	0.35	2.50	0.0926	0.278	16.8
3H	u_2	0.4	2.50	0.0926	0.278	16.8
3I	u_3	0.4	2.50	0.0926	0.278	16.8
S921	observed		2.50	0.0926	0.278	9.29
S221	observed		2.50	0.0926	0.278	7.78
S222	observed		2.50	0.0926	0.278	4.73
S221RC	observed		2.50	0.0926	0.278	7.56
S222RC	observed		2.50	0.0926	0.278	9.50

nearly the same as those in 2-D numerical experiments already described in Section 2.4 and the difference between them will be mentioned in the next subsection.

2.6.2 Conditions, Procedures and Data Processing Used in 3–D Numerical Experiments

(1) Velocity Distributions and Intensity of the Turbulence

a. Run 3 Series

The hypothetical velocity distributions described as:

$$\frac{u''_{23}(x_2)}{u_*} = \frac{1}{\kappa}\left(\ln\frac{x_2}{d}+1\right) \tag{2.6.1a}$$

$$\frac{\bar{u}^{x_2}(x_3)}{u_*} = \begin{cases} \dfrac{1}{\kappa_z}\ln\dfrac{B-2|x_3|}{B}+C_{x_3} & \text{for} \quad \dfrac{B-2|x_3|}{B} \le \zeta_1 \\ \dfrac{1}{\kappa_z}\ln\zeta_1 & \text{for} \quad \zeta_1 \le \dfrac{B-2|x_3|}{B} \le 1 \end{cases} \tag{2.6.1b}$$

are used, where κ_z is the coefficient, C_{x_3} the constant. The example of the velocity distributions is shown in Fig. 2.6.1. The vertical distributions of the temporal averaged velocity are expressed by the log-law as shown in Eq. 2.6.1a, however its average with respect to the flow-depth is constant in the core region but is expressed by the

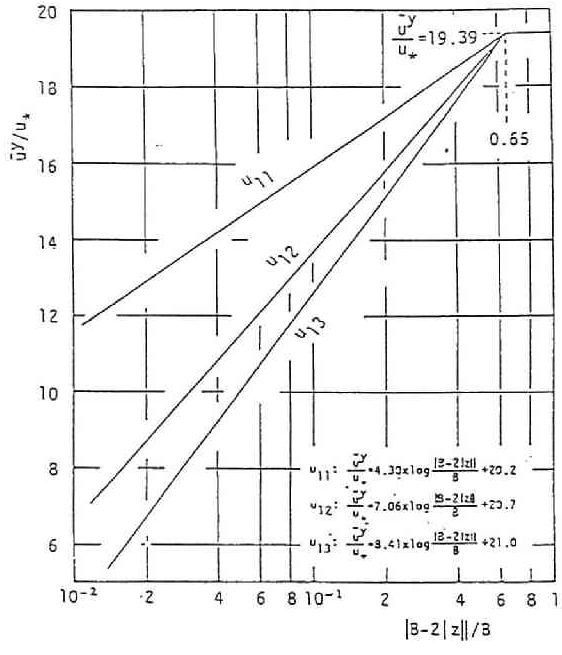

Figure 2.6.1: Example of velocity distributions used in Run 3 series.

log-law near the side boundary as Eq. 2.6.1b. The velocity distributions and/or the intensity of the Eulerian turbulence in the vertical and lateral directions are made to be different each other in the series by specifying the different parameters or the turbulent intensity. They are summarized in Table 2.6.1.

b. Run S Series

The measuring points for velocity distributions in laboratory experiments are coarse, and the interpolation described below was used. A cross-section was divided into 800 sub-cross-sections by 10 lines in the vertical direction and 80 lines in the lateral direction. In each sub-cross section, the velocity distributions are uniform and its magnitude is determined by the linear-interpolation with use of the measured velocity. The figures and characters following after "s" in each of the run numbers are corespondent with the run number for the laboratory experiments in Chapter 4. The specified turbulent intensities in the three directions are the same as those in Run-3C.

(2) Procedures of Experiments and Data Processing

a. Tracing particle locations

Procedures of releasing particles and tracing the particle locations are similar with those in 2-D numerical experiments described in **Subsection 2.4.4**, however the flow field is three-dimensional. Therefore, a cross-section is divided into sub-cross-sections by 10 × 20 lattices, and the 200 lattice points are used for the releasing point of particles. 2 particles were released from each lattice point and traced until 4050 time steps. The location of particles are recorded at every 200 time steps and the average $[X_1]$ and the variance $[X_1'^2]$ is calculated. The longitudinal dispersion coefficient is calculated by

$$D \equiv \frac{1}{2}\frac{d}{dt}[X'^2(a,t)]$$

b. Characteristics of Lagrangian Velocity

Time series of the Lagrangian velocity and its components are required in order to investigate the characteristics of the Lagrangian velocity

$$v_1'(a,t) = v_t'(a,t) + v_v'(a,t) + v_l'(a,t) \tag{2.2.13}$$

The measurement of the Lagrangian velocity and its components are made for the particle released from each point of 6 × 10 lattices in a cross-section. The flow conditions are specified as same as those in the test for "Tracing particle location". The sample size is 10001.

c. Lagrangian Auto-Correlation Function

The Lagrangian auto-correlation function

$$\overline{b_L}(s_1,\sigma;a,t) \equiv \lim_{T\to\infty}\frac{1}{T}\int_0^T v_1'(s_1;a,t_0)v_1'(s_1-\sigma;a,t_0)ds_1 \tag{2.3.15}$$

is calculated from the time series measured in the above, but the sampling frequency is 5 time steps, and the sample size is 1600 in case calculating the magnitude of each component. The maximum lag-time is one-tenth of the duration for the particle tracing.

In case investigating the features of the Lagrangian auto-correlation function and each component, different sampling method are used because the magnitude of the integral time scale for each component is quite different, that is, the sampling frequency is 10 time step and the sample size 1000 for $B_L(\tau)$ and $B_{Ll}(\tau)$, and the sampling frequency is 1 time step and the sample size 3000 for $B_{Lvv}(\tau)$ and $B_{Ll}(\tau)$. The condition for the maximum lag-time for them is the same as described in the paragraph above.

In calculating the integral time scale, B_L and B_{Lii} were numerically integrated from $\tau = 0$ to the maximum lag-time. The magnitude of the integral time scale at the maximum lag-time is not so small for $B_L(\tau)$ and B_{Ll} as shown in Fig. 2.6.2. Therefore, their falling limb is approximated by the exponential function and it is

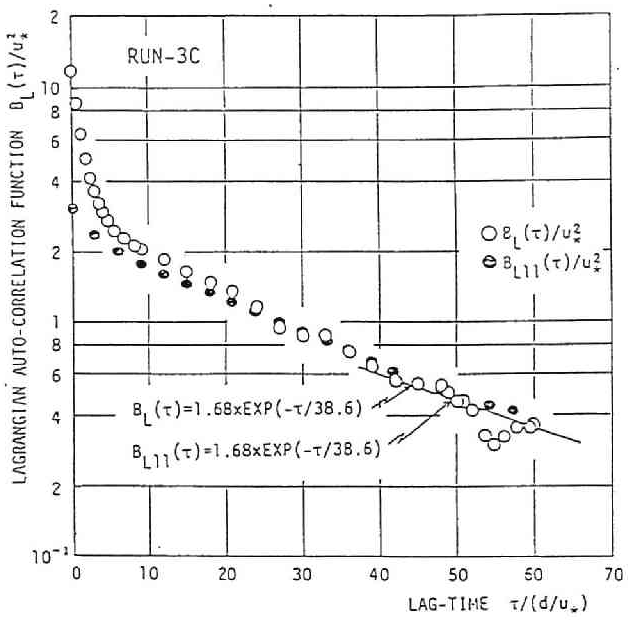

Figure 2.6.2: Example of the Lagrangian auto-correlation function and its component measured in Run 3C.

integrated to infinity. This value is added to the result obtained by the numerical integration.

2.7 Results of Three–Dimensional Numerical Experiments

2.7.1 Dispersion Processes Obtained in Simulations

Dispersion processes of particles starting from a point $x = a = (0.0, 0.05, 0.025)$ at $t = 0$ measured in Run-S921 are illustrated in Fig. 2.7.1. Fig. 2.7.1(a) is the bird's eye view of particle dispersion, Fig. 2.7.1(b) a plan view, and Fig. 2.7.1(c) a side view. It is disclosed that a period required for migrations of a particle in a lateral direction is much longer than that in a vertical direction by comparing Figs. 2.7.1(b) and (c).

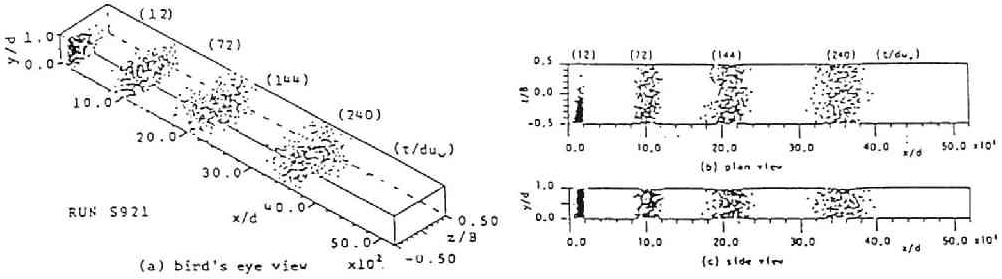

Figure 2.7.1: Dispersion processes of particles released at a = (0.0, 0.05, 0.025) in Run–S921. (a) a bird's eye view, (b) a plan view, and (c) a side view.

2.7.2 Lagrangian Turbulence and Its Intensity

Movement of a particle released in Run–3C are illustrated in Fig. 2.7.2. Positions of a particle in x_2–x_3 plane is illustrated in Fig. 2.7.2(a), that in x_1–x_2 plane in Fig. 2.7.2(b) and that in x_1–x_3 plane in Fig. 2.7.2(c) respectively. The associated Lagrangian velocity and its three components of a particle also measured in Run–3C are illustrated in Fig. 2.7.3. Fig. 2.7.3(a) shows the time-series of the Lagrangian velocity of a particle, Fig. 2.7.3(b) is the time-series of $v_l' + U$, Fig. 2.7.3(c) that of v_v', and Fig. 2.7.3(d) that of v_t respectively. v_t' is equivalent to the records generated by the "Complex Random Number Series Models", v_v' is caused by the random movements and the non-uniformity of the velocity distribution in the vertical direction, and v_l' are caused by the random movements and the non-uniformity of the velocity distributions in a lateral direction. Note the small turbulences recorded in Fig. 2.7.3 (b) are correspondent with the locations of a particle which migrates very near the side boundary as shown in Fig. 2.7.2 (a).

These two sets of figures disclose that the movement of a particle in a vertical direction is much stronger than that in the lateral direction. Therefore, it is suggested that the time series of v_l' has much lower frequency components and the time required for particle mixing in the lateral direction is much longer than those in the vertical direction.

The square of the Lagrangian turbulent intensity and its three components measured in numerical experiments are plotted against each of theoretical results calculated by Eqs. 2.2.16 to 2.2.19 respectively, in Fig. 2.7.4. Measured values have good

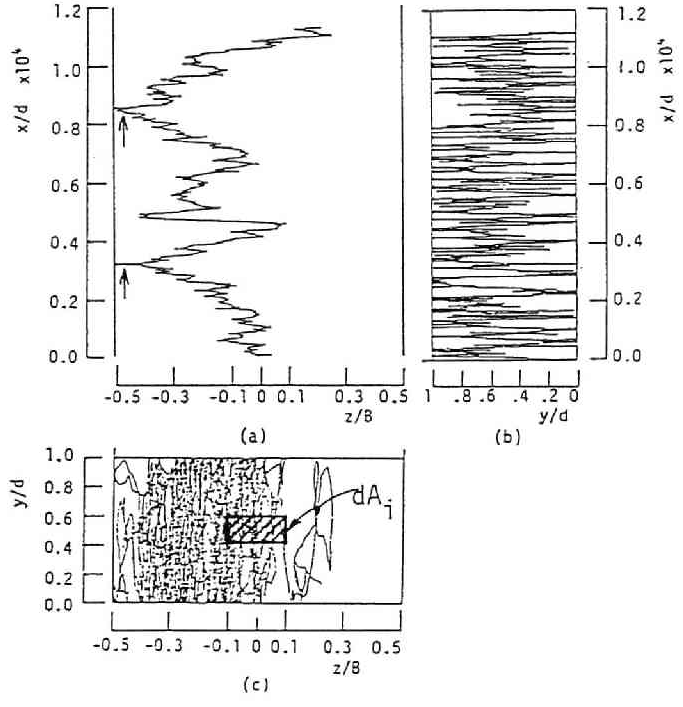

Figure 2.7.2.: Movements of a particle measured in Run-3C. (a) movements in a $x_2 - x_3$ plane, (b) movements in a $x_1 - x_3$ plane, and (c) movements in a $x_1 - x_2$ plane.

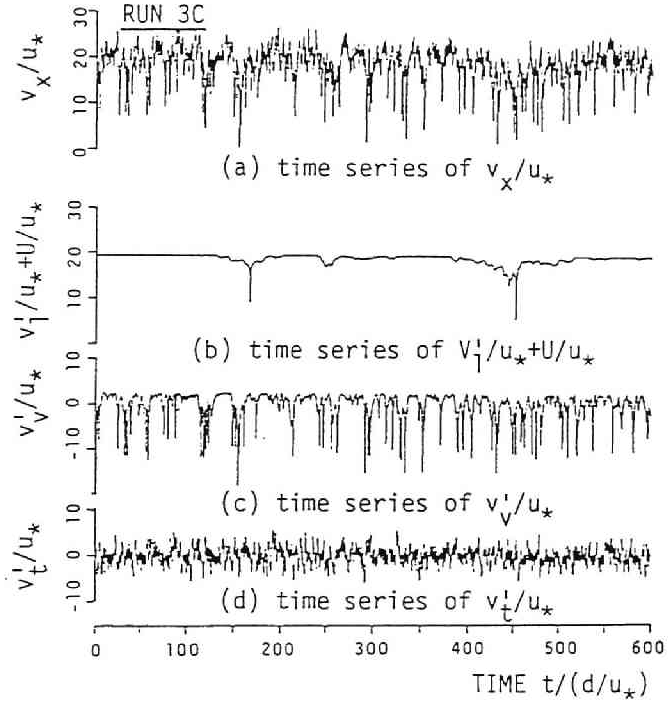

Figure 2.7.3: Time series of Lagrangian turbulent velocity and its components in Run–3C. (a) Lagrangian velocity in the longitudinal direction, (b) component of Lagrangian velocity $v_l' + U$, (c) component of Lagrangian velocity v_v' and (d) component of Lagrangian velocity v_t'

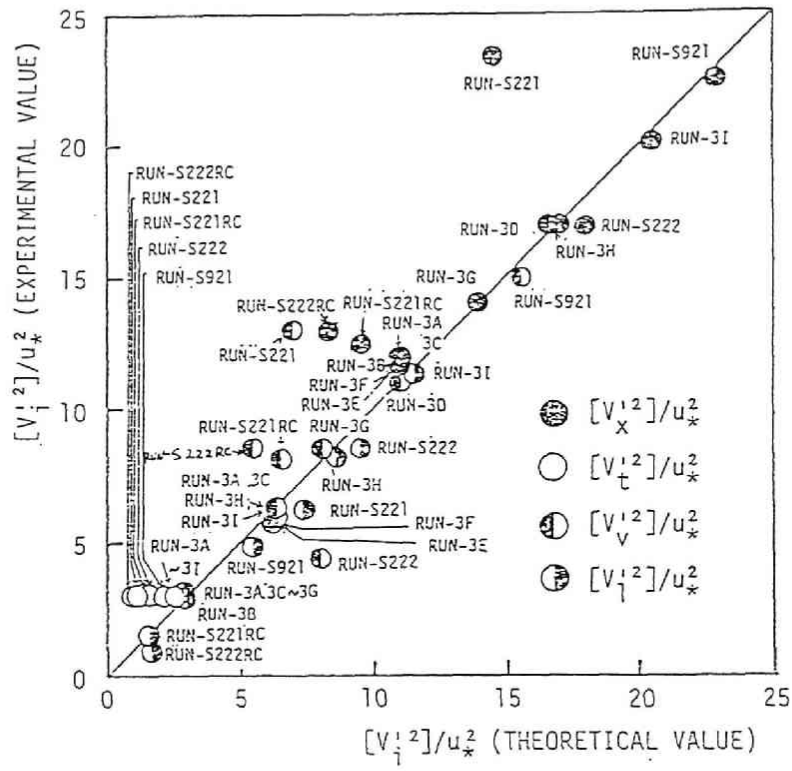

Figure 2.7.4: Comparison of the square of Lagrangian turbulence and its three components between measured and theoretical ones.

agreements with theoretical ones, however the theoretical values in Run S Series is a little smaller than measured ones, because the number of subsections used in calculating the theoretical values by the numerical integration is smaller than those used in the numerical experiments.

Thus, it is verified that the decomposition of the Lagrangian turbulent velocity into three components is rigorous and the generation of Lagrangian turbulence does in terms of the turbulent intensity and the particle movement.

2.7.3 Lagrangian Auto-Correlation Function

The examples of the auto-correlation function measured in Run–3C, S921 and S221RC on normal section papers are presented in Fig. 2.7.5, and those on a semi-logarithmic sheet in Fig. 2.7.6. Comparing the auto-correlation coefficient in 2-D turbulent shear flows described in Fig. 2.5.5, the auto-correlation function in 3-D turbulent shear flows has a quite long tail in the falling limb, and it is realized that plottings are not represented with a single straight line, but represented with a line having one or two bends. These bendings indicate that the decrease of the auto-correlation function is very fast for a range of short travel time, whereas for a range of long travel times, it decreases much slower. Thus, for different ranges of a travel time, different time scales are possible.

Fig. 2.7.7 illustrates the auto-correlation function and its nine components expressed by Eqs. 2.2.20 and 2.2.21. The three components $B_{Lii}(\tau)$ $(i = t, v, l)$ are dominant and the other six $B_{Lij}(\tau)$ $(i \neq j)$ are negligibly small. Thus, it is verified that the assumption introduced by Eq. 2.2.28

$$B_{Lij}(\tau) = 0 \qquad \text{for} \quad i \neq j \tag{2.2.28}$$

is appropriate.

The major three components have the comparable magnitude for the short lag-time, however they decrease slowly as the lag-time increases. The characteristic time scales of the three dominant components are different from each other, and that of B_{Lll} is much longer than other two, therefore B_L decreases rapidly for a short lag-time, and only B_{Lll} is prevailing over B_L for a long lag-time.

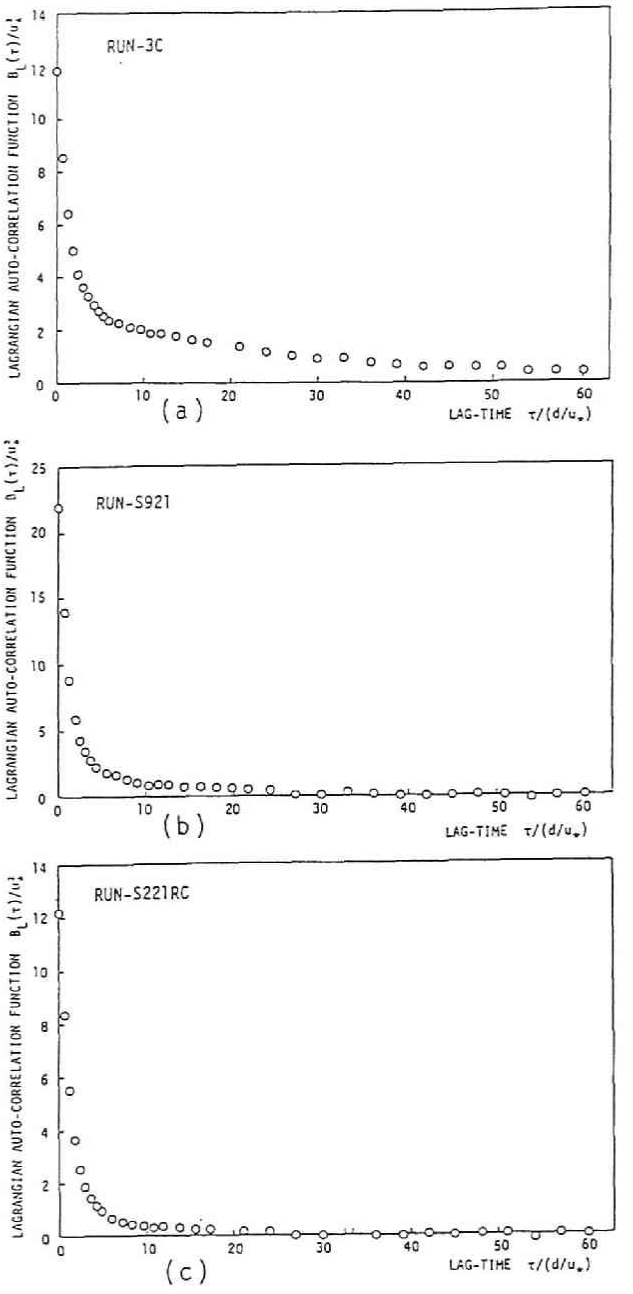

Figure 2.7.5: Lagrangian auto-correlation function measured in numerical experiment. Plottings are on normal section papers. (a) Run-3C, (b) Run-S921 and (c) Run-S221RC.

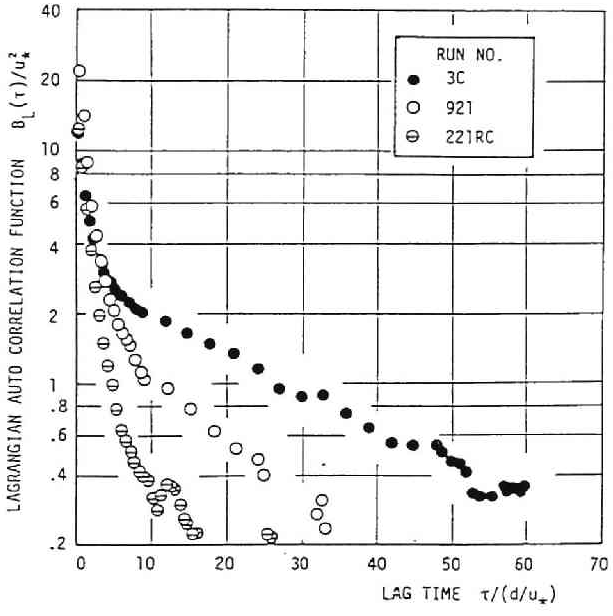

Figure 2.7.6: Lagrangian auto-correlation function measure in numerical experiment. Plottings are on a semi-logarithmic sheet. Solid circles denote the results for Run–3C, open circles for Run–S921, and circles with line for Run–S221RC.

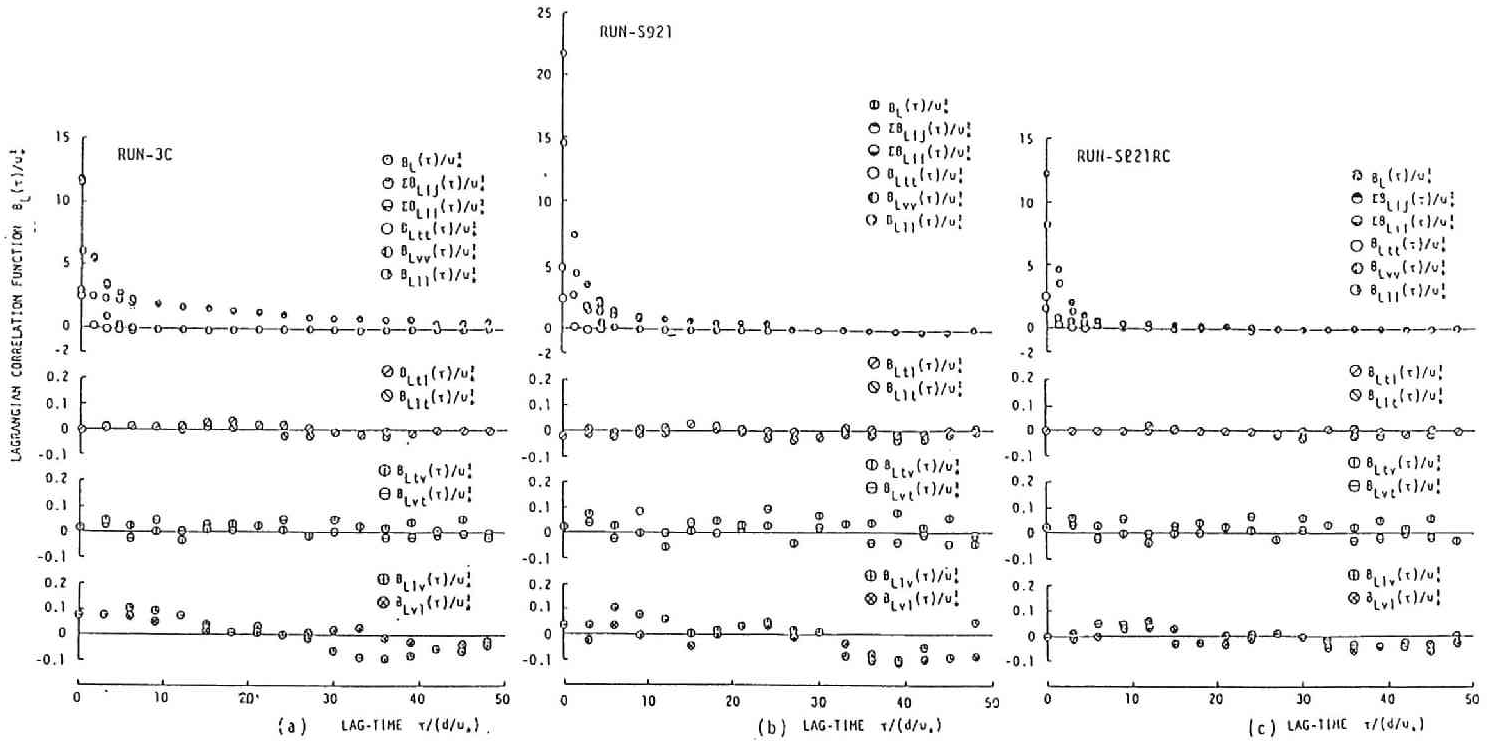

Figure 2.7.7: Lagrangian auto-correlation function and its nine components measured in numerical experiments. Plottings are on normal section paper; (a) Run-3C, (b) Run-S221 and (c) Run-S921RC.

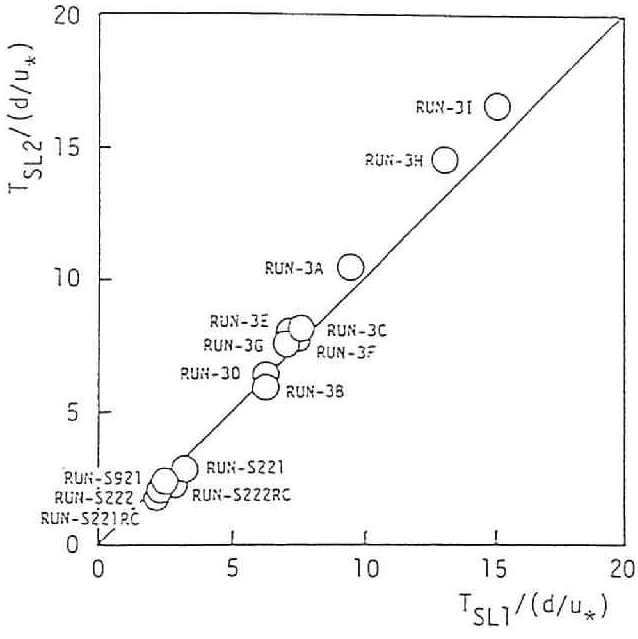

Figure 2.7.8: Comparison of two-kinds of the Lagrangian integral time scale measured in numerical experiments: T_{SL_1} by Eq. 2.7.1a and T_{SL_2} by Eq. 2.7.1b.

2.7.4 Integral Time Scale

Table 2.7.1 summarizes the characteristic features of Lagrangian turbulence obtained in the 3-D numerical experiments. The integral time scale calculated by Eq. 2.1.4 are listed in column (3) in Table 2.7.1. Fig. 2.7.8 shows the comparison of the integral time scales calculated by two methods of

$$T_{SL1} \equiv \frac{1}{[v_1'^2]} \lim_{t\to\infty} \int_0^t B_L(\tau)d\tau \qquad (2.7.1a)$$

and

$$T_{SL2} = \frac{D_L}{[v_1'^2]} \qquad (2.7.2b)$$

The fine agreement between two kinds of T_{SL} is demonstrated in Fig. 2.7.8. The magnitude of T_{SL} increases as the lateral turbulent intensity decrease, and as the lateral non-uniformity of depth-averaged velocity increase. The magnitude of the vertical turbulent intensity is less effective on T_{SL}. The magnitude of the integral time scale in Run 3 Series is much larger than that in a two-dimensional flow, however,

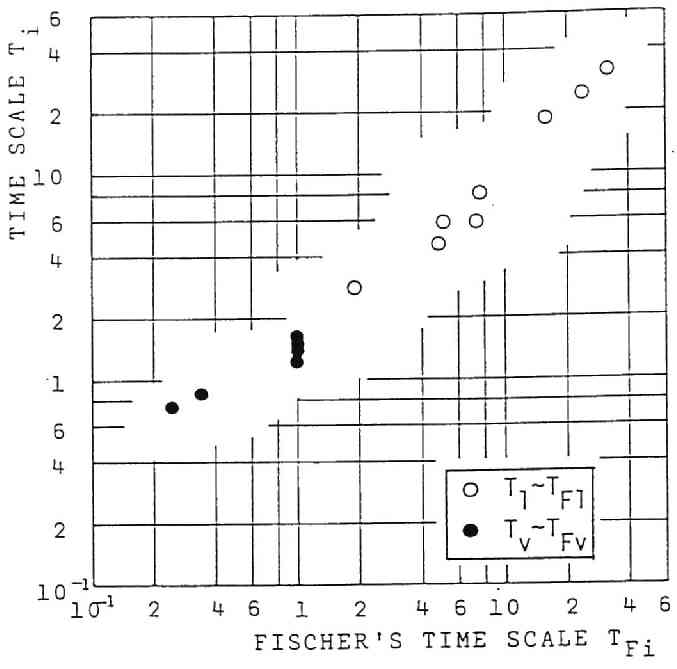

Figure 2.7.9: Comparison of the mixing time scale measured in numerical experiments by use of Eq. 2.7.3, and Fischer's integral time scale calculated by Eqs. 2.2.24 and 2.2.25.

that in Run S Series is about 3 and has the magnitude of the same order of that in 2-D flows.

$$T_{SL} \approx d/u_{\cdot} \tag{2.7.2}$$

Its reason will be disclosed by the models for the integral time scale, that is, Eqs. 2.2.31 to 2.2.34 in **Section 2.8**.

The time scale of three dominant components of the auto-correlation function is defined by

$$T_i \equiv \frac{1}{[v_i'^2]} \lim_{t\to\infty} \int_0^t B_{Lii}(\tau)d\tau \qquad (i = t, v, l) \tag{2.7.3}$$

T_l and T_v calculated by Eq. 2.7.3 are compared with Fischer's time scale T_{Fi} calculated by Eqs.2.2.24 and 2.2.25 in Fig. 2.7.9. Fischer's time scale T_{Fl} listed in the 4th column in Table 2.7.1 is 2 or 3 times larger than T_{SL} measured in numerical experiments, however as shown in Fig. 2.7.8, the respective comparison of T_{Fl} with T_l or T_{Fv} with T_v demonstrates that they have good a agreement each other. Therefore, it is concluded that T_{Fl} does not represent the integral time scale in 3-D turbulent

Table 2.7.1: Summary of the Lagrangian integral time scale obtained in 3-D numerical experiments.

RUN-NO.	(1) $T_{SL1}/(d/u_*)$ $\int R(\tau)d\tau/(d/u_*)$	(2) $T_{SL2}/(d/u_*)$ $D/[V_x'^2]/(d/u_*)$	(3) $T_{FL}/(d/u_*)$
RUN-3A	9.46	10.4	31.8
RUN-3B	6.22	5.94	15.8
RUN-3C	7.76	8.19	23.8
RUN-3D	6.29	6.42	23.8
RUN-3E	7.22	8.15	23.8
RUN-3F	7.58	8.01	23.8
RUN-3G	7.00	7.52	23.8
RUN-3H	12.9	14.5	23.8
RUN-3I	15.0	16.6	23.8
RUN-S921	2.63	2.20	7.29
RUN-S221	3.25	2.75	5.11
RUN-S222	2.36	1.95	1.89
RUN-S221RC	2.27	1.75	4.83
RUN-S222RC	2.81	2.23	7.62

shear flows, but T_{Fv} and T_{Fl} correspond to T_v and T_l proposed by Eqs. 2.2.32 and 2.2.33 in **Section 3.2** respectively. Thus, the models for the mixing time scale, that is, Eqs. 2.2.32 and 2.2.33 are verified to be appropriate.

2.7.5 Longitudinal Dispersion Coefficient

The dispersion coefficients calculated by its definition Eq. 2.1.2b in 3-D numerical experiments are listed in the column (4) in Table 2.7.1. The magnitude of the dispersion coefficient in three-dimensional flows are much greater than those obtained in the two-dimensional flow experiment. This big difference between results in 2-D and 3-D flows is mainly caused by the difference of the magnitude of the integral time scale between these two kinds of flows, because the magnitude of the turbulent intensity in both flows are of the same order but the integral time scale in 3-D flows are greater than that in 2-D flows.

The dispersion coefficients measured in the laboratory experiments which will be described in detail in **Chapter 4** are also listed in the 5th column in Table 2.7.1, and the calculated values by Fischer's equation:

$$D_{El} = \frac{1}{A}\int_{-b_1}^{b_2} \frac{dx_3'}{dD2_{33}} \left[\int_{-b_1}^{x_3'} u_{03}' dx_3\right]^2 \tag{3.5.43}$$

in the 6th column in Table 2.7.1. The dispersion coefficients measured in numerical experiments and laboratory experiments agree quite well each other, therefore, the numerical experiment is again verified to be valid in terms of the dispersion coefficient. The dispersion coefficients calculated by Fischer's equation, Eq. 3.5.43 have a little smaller values than those measured in numerical and/or laboratory experiments.

2.7.6 Time Dependent Growth of Variances

The examples of time-dependent behavior of variances measured in numerical experiments are presented in Fig. 2.7.9. Measured variances denoted by the open circle have a quite good agreement with the solid line calculated by Eq. 2.1.1 by use of the measured Lagrangian auto-correlation function. This result demonstrates that the application of Taylor's diffusion theory in the homogenous turbulent field to the longitudinal dispersion is valid and useful.

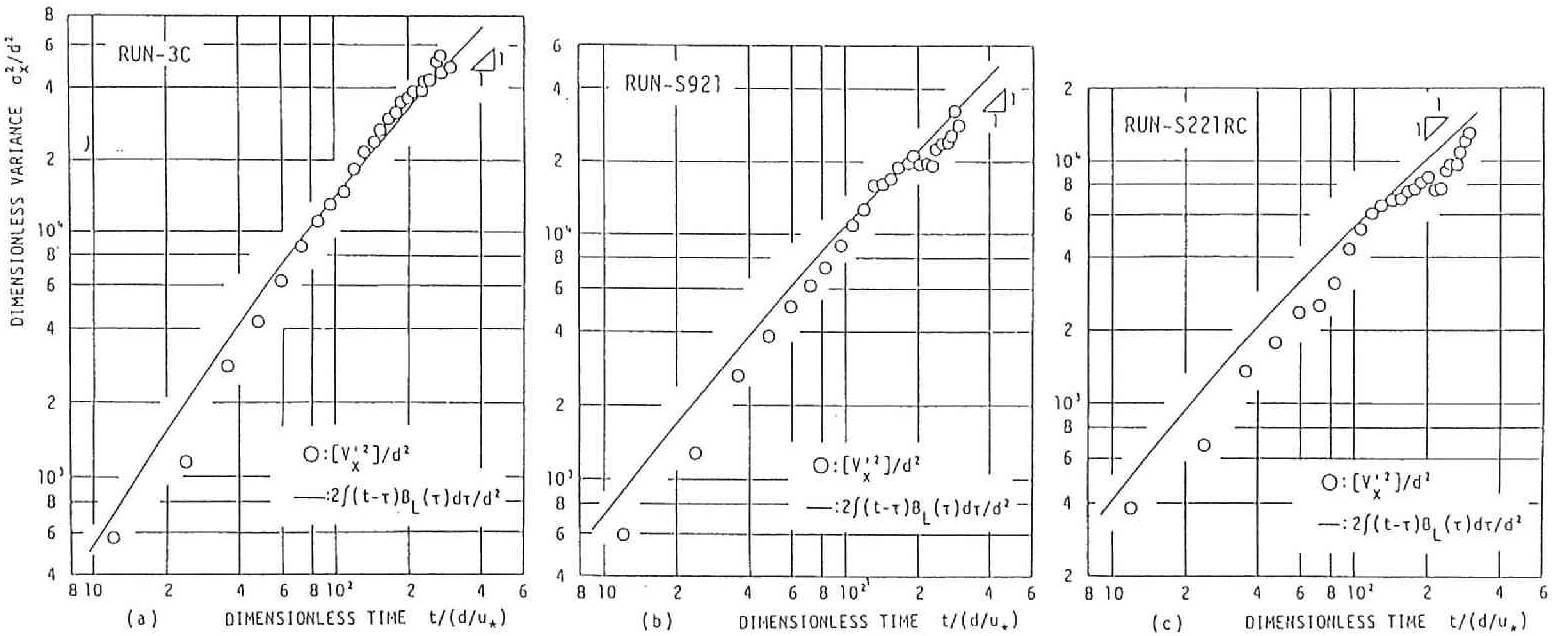

Figure 2.7.10: Time dependent growth of variances measured in numerical experiments. The open circles denote the measured variance and the solid line indicates the calculated results by use of Eq. 2.1.1 and the measured Lagrangian auto-correlation function; (a) Run-3C, (b) Run-S921, and (c) Run-S221RC.

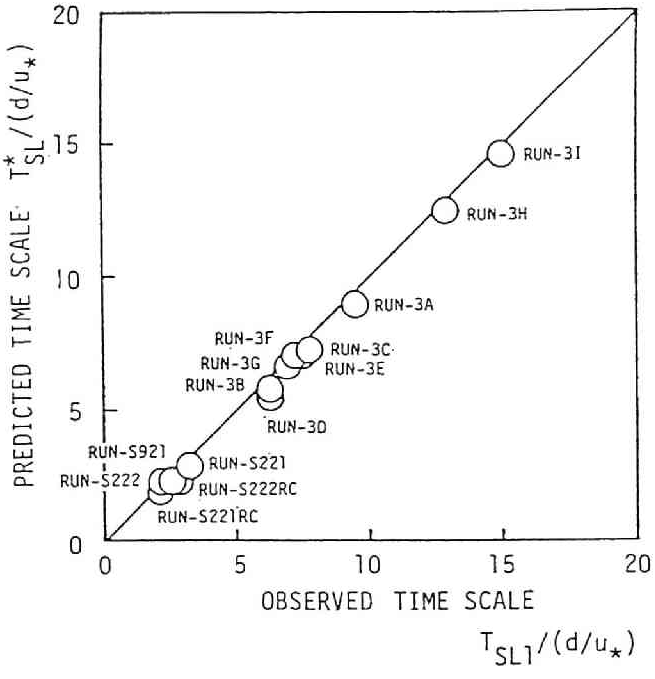

Figure 2.8.1: Comparison of Lagrangian time scale measured and predicted.

2.8 Discussions

2.8.1 Integral Time Scale

The time scales of three dominant components of the auto-correlation function are verified to be equivalent to Fischer's integral time scale in **Subsection 2.7.5**, that is it is concluded that T_{Fl} does not represent the integral time scale in 3-D turbulent shear flows, but T_{Fv} and T_{Fl} correspond to T_v and T_l proposed in **Section 3.2** respectively. The direct comparison of the integral time scale calculated by

$$T_L = \frac{1}{[v'^2]} \lim_{t\to\infty} \int_0^t B_L(\tau) d\tau \tag{2.1.4}$$

and the predicted ones by the proposed equation:

$$T_{SL} = \frac{1}{[v_1'^2]} \left\{ \left[v_t'^2\right] T_t + \left[v_v'^2\right] T_v + \left[v_l'^2\right] T_l \right\} \tag{2.2.34}$$

are made in Fig. 2.8.1. The definite agreement between two results verifies the usefulness of the proposed models Eq. 2.2.34.

2.8.2 Lagrangian Auto-Correlation Function

Fig. 2.8.2 illustrates the three dominant components, B_{Lii} ($i = t, v$ and l) in Lagrangian auto-correlation coefficient measured and calculated by Eqs. 2.2.30. The definite agreement between two results demonstrates that the proposed models of Eq. 2.2.30 for the Lagrangian auto-correlation function in 3-D turbulent shear flows are quite useful.

$$B_L(\tau) = [v_t'^2]\exp(-\tau/T_t) + [v_v'^2]\exp(-\tau/T_v) + [v_l'^2]\exp(-\tau/T_l) \qquad (2.2.30)$$

Eqs. 2.2.31, 2.2.32, and 2.2.33 predicting the mixing time scales in 3-D turbulent flows were used in calculating Eq. 2.2.29 and their validity has already be discussed in the subsection above.

2.8.3 Time-Dependent Behavior of the Variances

Fig.2.8.3 shows the time-dependent growth of variances measured and calculated by the proposed models

$$[X'^2] \propto t \quad \text{for} \quad t > (3-6)T_l \quad \text{or} \quad x > (3-6)T_l U \qquad (2.2.39)$$

The definite agreement between two results are demonstrated as well as those shown in the comparison of Lagrangian-auto correlation function.

The equations proposed in **Section 2.2** is directly applied to the results obtained in the Eulerian measurement in the laboratory which will be described in detail in **Chapter 4**. The variance in the time coordinate is transformed into that in the x_1 coordinate by

$$x = Ut$$

Fig. 2.8.4 shows the time-dependent growth of variances. In this figure, observed values in the laboratory experiments denoted by solid circles for Run 221 and open circles for Run 222RC and predicted values by Eq. 2.1.1 and 2.2.39 respectively denoted by solid and broken lines are presented. The good agreements observed in this figure demonstrates the usefulness of the proposed auto-correlation function models in **Section 2.2**.

2.8.4 Dispersion Coefficient

The dispersion coefficient measured in numerical experiments are compared with those predicted by proposed Eq. 2.2.35 in Fig. 2.8.5. The definite agreement between

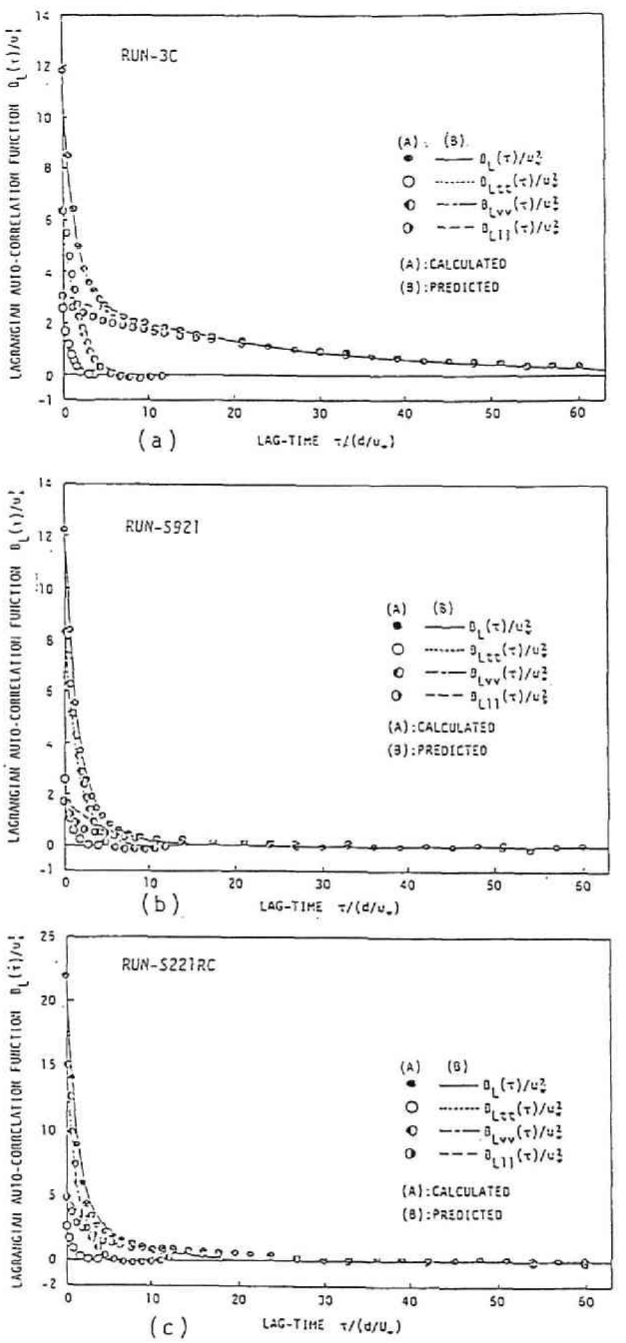

Figure 2.8.2: Lagrangian auto-correlation function and its three major components. Circles denote the measured auto-correlation functions and lines indicates the calculated results by use of Eq. 2.2.30 proposed. (a) Run–3C, (b) Run–S921, and (d) Run–S221RC.

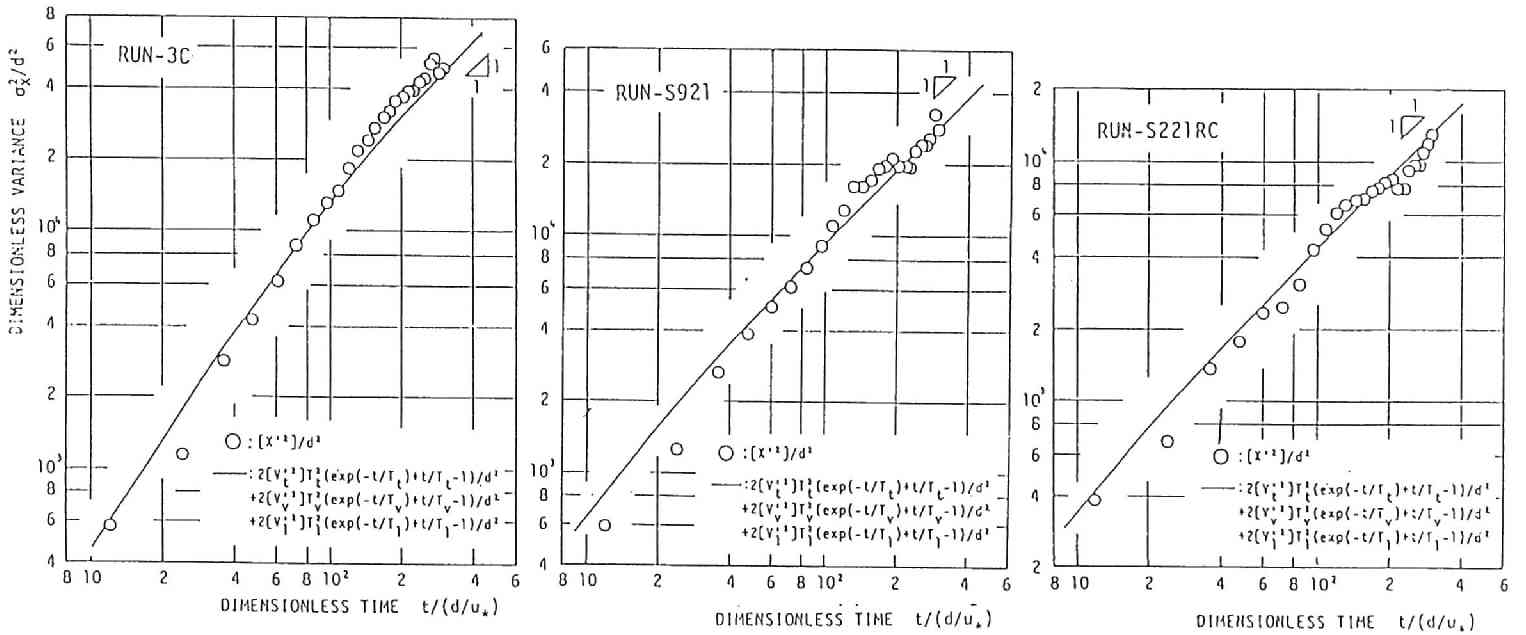

Figure 2.8.3: Time dependent growth of variances measured and predicted. The open circles denote the measured variance and the solid line indicates the predicted ones by use of Eq. 2.2.39 for (a) Run-3C, (b) Run-S921, and (d) Run-S221RC.

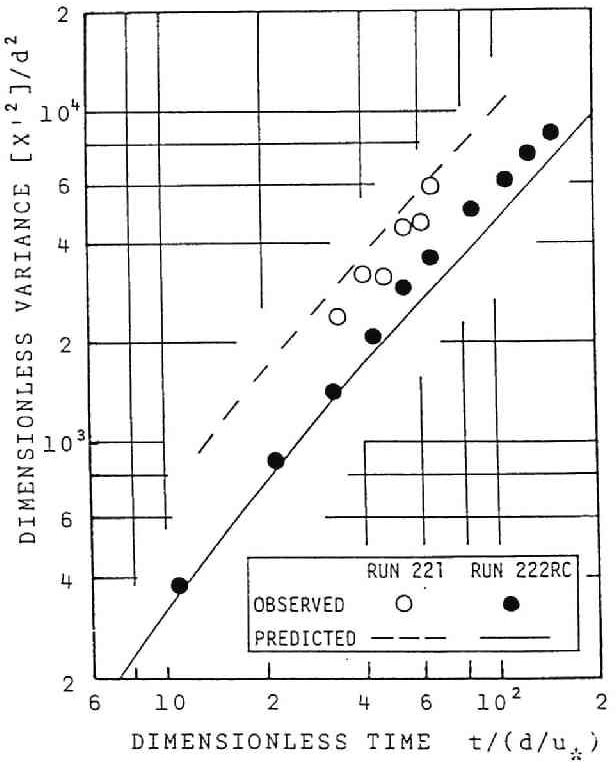

Figure 2.8.4: Time dependent growth of variances measured in laboratory experiments. The circles denote the measured variance and the lines indicates the calculated results by use of the proposed models of Eq. 2.2.39.

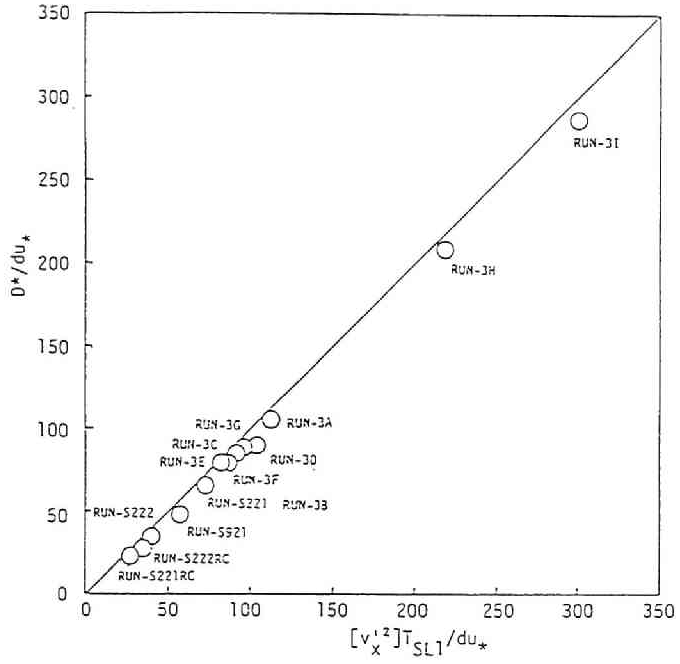

Figure 2.8.5: Dispersion coefficient measured in numerical experiments and predicted ones by proposed models.

two results verifies the validity of Eq. 2.2.35 for predicting the dispersion coefficient in 3-D turbulent shear flows. The dispersion coefficients predicted by Eq. 2.2.35 are also compared with those obtained in the laboratory experiments and field measurement in Fig. 2.8.6. The details of the laboratory measurement will be described in Chapter 4. The field measurement data are taken from Godfrey and Frederick (1970), and Fischer (1969). They will also be referred in Chapter 5. The fitness of data in the laboratory experiments to Eq. 2.2.35 shown in this figure is very good. Regarding the disagreements shown in the field observation data, they will result from few velocity measurements in a section and/or the irregularity of channel geometry.

Thus, the formula based on the Lagrangian one-particle analysis:

$$D_L = [v_x'^2]T_{SL} = [v_t'^2]T_t + [v_v'^2]T_v + [v_l'^2]T_l \qquad (2.2.35)$$

is verified to be valid and useful for predicting the longitudinal dispersion coefficient in 3-D turbulent shear flows.

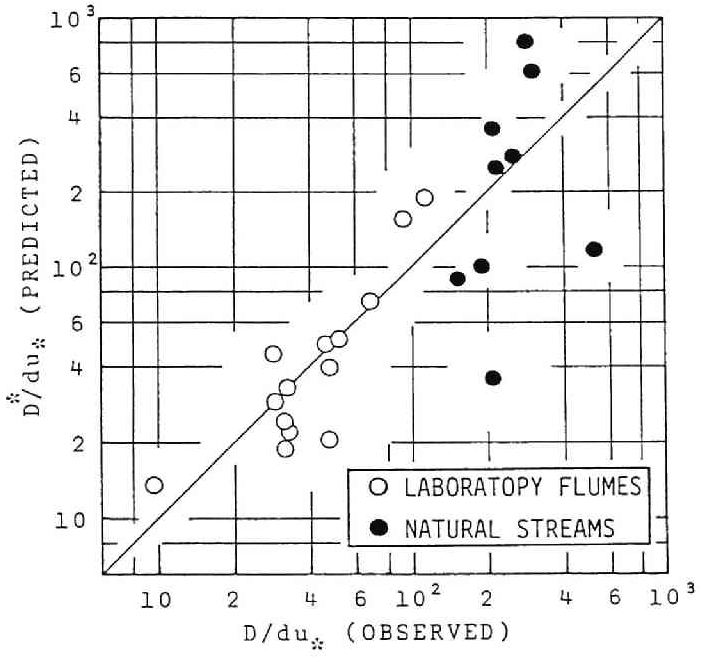

Figure 2.8.6: Dispersion coefficient measured in laboratory flumes and natural streams, and predicted ones by propose models.

2.9 Conclusions

The longitudinal dispersion in 3-D confined turbulent shear flows was investigated in terms of one-particle analysis in the uniform turbulent field. The study was focused on the Lagrangian auto-correlation function in a turbulent shear flow.

In **Section 2.1**, the turbulent diffusion theory in uniform turbulent flow by Taylor was summarized, and the previous applications to the longitudinal dispersion in confined turbulent shear flows were reviewed. In **Section 2.2**, continuous movements of a particle released in shear flows were described in terms of Lagrangian modeling. The Lagrangian particle velocity vector in shear flows is quite different from the Eulerian turbulent velocity vector, and its longitudinal component was decomposed into three components as:

$$v_1'(a,t) = v_t'(a,t) + v_v'(a,t) + v_l'(a,t) \tag{2.2.13}$$

where the first term is related with the Eulerian turbulent velocity, the second term with the vertical non-uniformity of the Eulerian local mean velocity, and the third term with its lateral one respectively. The Lagrangian auto-correlation function was proposed to be stated by

$$B_L(\tau) = [v_t'^2]\exp(-\tau/T_t) + [v_v'^2]\exp(-\tau/T_v) + [v_l'^2]\exp(-\tau/T_l) \tag{2.2.30}$$

and the integral time scale and the dispersion coefficient are respectively stated as

$$T_{SL} = \frac{1}{[v_1'^2]}\left\{\left[v_t'^2\right]T_t + \left[v_v'^2\right]T_v + \left[v_l'^2\right]T_l\right\} \tag{2.2.34}$$

$$D_L = [v_x'^2]T_{SL} = [v_t'^2]T_t + [v_v'^2]T_v + [v_l'^2]T_l \tag{2.2.35}$$

Numerical simulation models for a particle dispersion in confined 3-D turbulent shear flows were developed by use of "Complex random number models", and the data processing methods for the auto-correlation function were also discussed in **Section 2.3**.

Preliminary numerical experiments for the turbulent diffusion and for the longitudinal dispersion in 2-D turbulent shear flows were conducted before 3-D numerical experiments. The objectives and conditions for the preliminary experiments were described in **Section 2.4**. In **Section 2.5**, the magnitude of the time step in the numerical models was determined by the results of the turbulent diffusion test in uniform flows. The results of the longitudinal dispersion test in 2–D turbulent shear flows were successfully examined by being compared with results by Elder's theoretical work, and by 2–D numerical experiment based on 2–D turbulent diffusion

equation. Statistical properties of the 2–D Lagrangian turbulence and the longitudinal dispersion of particles were also investigated. They verified the theoretical results in **Section 2.2** useful, but the Lagrangian auto-correlation function and the growth of the variances were respectively modified as:

$$R_L(\tau) = e^{-t/T_{SL}} \tag{2.5.7}$$

and

$$\frac{\sigma_1^2}{2[v_1'^2]T_{SL}^2} = \frac{t}{T_{SL}} - 1 + \exp(-\frac{t}{T_{SL}}) \tag{2.5.12}$$

Sections 2.6 to 2.8 were concerned with the three–dimensional experiments. The objectives of 3–D experiments were stated in **Section 2.6**. The experiments mainly aimed to investigate the Lagrangian auto-correlation function in 3-D turbulent shear flows, and their conditions, procedures and the method of data processing were also described in **Section 2.6**. The results of experiments, that is, the particle dispersion, the intensity of the Lagrangian turbulence and its three components, the Lagrangian auto-correlation function, the integral time scale, the longitudinal dispersion coefficient and the time-dependent growth of the variances were presented in **Section 2.7**. The Lagrangian auto-correlation function in 3–D turbulent shear flows was disclosed to decrease very slowly in the course of the travel time, and possess two or three time scales. The three components $B_{Lii}(\tau)$ $(i = t, v, l)$ are dominant and the other six $B_{Lij}(\tau)$ $(i \neq j)$ are negligibly small, and it was verified that the assumption introduced by Eq. 2.2.28 was acceptable. The major three components have the comparable magnitude for the short lag-time, however they decrease as the lag-time increases. The characteristic time scales of the three dominant components are different from each other, and that of B_{Lll} is much longer than other two, therefore B_L decreases rapidly for a short lag-time, and only B_{Lll} is prevailing over B_L for a long lag-time. The Lagrangian integral time scale depends on a composition of the Lagrangian turbulent velocity which refers to the Eulerian local mean velocity and the turbulence, the channel geometry, and the turbulent diffusion coefficients in both vertical and lateral directions. It was also disclosed that Fischer's formula of Eq. 2.1.8 is equivalent to the characteristic time scale for vertical/lateral mixing, but quite different from the integral time scale in 3-D turbulent flow.

The proposed models of Eq. 2.2.30 for the Lagrangian auto-correlation function models have successfully been examined by the results of the numerical experiments, and the models for the integral time scale, the mixing time scale, the variance and the dispersion coefficient have respectively been verified in **Section 2.8**.

The mechanism of the longitudinal dispersion are summarized in terms of one-particle analysis as,

1. The non-uniformity of the velocity distributions in the lateral direction is the most important on the longitudinal dispersion in turbulent shear flows in rectangular cross-section laboratory flumes.

2. The dispersion processes in open–channel flows can be decomposed into three components, that is, the Eulerian turbulent transport, the dispersion caused by the vertical non-uniformity of the velocity distributions, and the dispersion by the lateral non-uniformity of the velocity distributions.

3. The intensity of the non-uniformity of the velocity distributions in the lateral direction is smaller than that in the vertical direction, but the mixing time scale in the lateral direction is much larger than that in the vertical direction.

4. Therefore, the dispersion coefficient described as a product of the three components of the intensity of the non-uniformity of velocity distributions and the three components of the integral time scale is quite larger in open-channel flows.

Chapter 3

LONGITUDINAL DISPERSION COEFFICIENT BASED ON 3–D TURBULENT DIFFUSION EQUATION

3.1 Introduction and Objectives

The Lagrangian analysis of a particle in **Chapter 2** demonstrated that the non-uniformity of the velocity distributions in the lateral direction is the most important on the longitudinal dispersion in turbulent shear flows in rectangular cross-section laboratory flumes.

In this chapter, the mechanism of the longitudinal dispersion phenomena in shear flows and the longitudinal dispersion coefficient will be investigated theoretically in view of the Eulerian turbulent diffusion equation by using the results obtained in **Chapters 2** and **4**. The flows mainly concerned are 3–D turbulent shear flows, and especially open-channel flows in wide rectangular cross-section laboratory flumes as well as natural streams, which may have the similar mechanism of the longitudinal dispersion to laboratory flumes. by using the results obtained in **Chapters 2** and **4**. At first, the previous theoretical studies on the dispersion coefficient based on the turbulent diffusion equation will be summarized. Next, the mechanism of the dispersion will be discussed, and the formula predicting the dispersion coefficient in 3–D turbulent shear flows will be derived. Theoretical results obtained will be examined in **Chapter 5** by comparing the experimental results described in **Chapter 4**.

3.2 Review of Taylor, Elder, and Fischer's Models

As far as the author knows, the first study on the longitudinal dispersion was made by Taylor (1953) for the laminar flows in a tube. Taylor (1954) also studied the longitudinal dispersion coefficient for turbulent shear flows in a pipe by using the same approach of the modeling as presented in his previous paper (Taylor, 1953). After Taylor's two papers, many research works on the longitudinal dispersion phenomena in various flows have been conducted by theoretical, experimental and empirical methods. Elder (1956) applied the Taylor's modeling to the open-channel flows which had the logarithmic velocity distribution. Fischer (1966) studied the longitudinal dispersion in natural streams. He pointed out the importance of the lateral velocity distributions on the longitudinal dispersion in natural streams, and presented the formula predicting the longitudinal dispersion coefficient by use of Taylor's modeling. He also studied the longitudinal dispersion coefficient in 2–D turbulent shear flows by tracer experiments in wide rectangular cross-section flumes, and concluded that Elder's results was varied. However, many researchers reported that magnitude of the dispersion coefficient in rectangular cross-section laboratory flumes is much larger than Elder's results (Michiue, Muramoto and Itami, 1978). Iwasa, Aya and Yakushiji (1983) showed that the longitudinal dispersion coefficient in rectangular cross-section flumes and natural streams depends on the width to depth ratio as will be shown in details in **Chapter 4**. Recently, Fukushima, Hayakawa and Sanjo (1984) theoretically studied the dispersion coefficient in turbulent shear flows in a lower-half of elliptic cross-section flumes and concluded that the dispersion coefficient asymptotes the Elder's results with increase of the width to depth ratio. The non-uniformity of the velocity distributions in the lateral direction is commonly much smaller than that in the vertical direction in ordinary wide open-channel flows, therefore, the direct application of the Fischer's results in natural streams to the flows in laboratory flumes should carefully be considered.

The mathematical theory of the dispersion coefficients initiated by Taylor will be presented in more general form in **Section 3.3**, and only the assumptions introduced in his theory and commonly used in other papers are summarized in followings:

1. The concerned flows are confined turbulent/laminar shear flows, which have the non-uniform cross-sectional distributions of the velocity in the longitudinal direction.

2. The flow is steady and uniform in the longitudinal direction.

3. The mass transport by the secondary current is negligibly small.

4. The mass transport by the turbulent diffusion in the longitudinal direction is additive to that by the convective transport by the averaged velocity in the longitudinal direction.

5. The time averaged concentration $\bar{c}(x_i, t)$ is able to be stated as the sum of two components, $C_\xi(x_1, t)$ and $c''(x_i, t)$:

$$\bar{c}(x_i, t) = C_\xi(x_1, t) + c''(x_i, t) \tag{3.2.1}$$

6.
$$\frac{\partial C_\xi}{\partial x_1} = Const. \quad \text{in} \quad \xi = x_1 - Ut, \ \tau = t \tag{3.2.2}$$
where U is the cross-sectional mean velocity.

7. c'' is not the function of ξ and
$$\frac{\partial c''}{\partial \tau} = 0 \tag{3.2.3}$$

8. The convective mass transport through the cross-section A in the moving coordinate ξ is defined by:
$$\dot{M} \equiv \int_A u_1'' \bar{c} dA \tag{3.2.4}$$
and this mass transfer can be stated by gradient type flux as:
$$\dot{M} = -AD_1 \frac{\partial C_\xi}{\partial \xi} \tag{3.2.5}$$
where u_1'' is the deviation from the cross-sectional mean velocity U and defined by Eq. 3.3.9, D_1 the proportional constant for the gradient type mass flux.

The 1-D convective dispersion equation can be derived for the confined 3-D turbulent flows by the one-dimensional method of hydraulics (Iwasa, 1976), therefore, assumptions 2 and 3 are not essential in the dispersion phenomena, however, nobody has succeeded to get the dispersion coefficient theoretically without these assumptions. The meaning of the assumptions 5, 6 and 7 was not so clear in Taylor (1954), and Fischer (1968) formulated these assumptions more clearly as:

$$C_\xi = C(x_1, t) \equiv \frac{1}{A} \int_A \bar{c} dA \tag{3.2.6}$$
$$c'' = c''(x_i, t) \equiv \bar{c} - C \tag{3.2.7}$$

Assumption 6, that is, Eq. 3.2.2 is rewritten in the following form:

$$\frac{\partial C_\xi}{\partial \xi} = \frac{\partial C}{\partial x_1} = Const. \tag{3.2.8}$$

by using $\xi = x_1 - Ut$. Fischer (1966) stated that c'' has the steady state solution in stead of introduction of the assumption 7, that is, Eq. 3.2.3. The definition of the dispersion coefficient, Eqs. 3.2.4 and 3.2.5 is also rewritten in the following form:

$$\dot{M} = \int_A u_1'' c'' dA = -AD_1 \frac{\partial C}{\partial x_1} \tag{3.2.9}$$

by using $\xi = x_1 - Ut$ and $\int_A u_1'' dA = 0$.

Note that there is one big difference between Taylor–Elder's models and Fischer's models. It is assumed that the concentration distributions in a cross-section is only the function of x_2, which is the only one coordinate describing the velocity distributions in Taylor–Elder's analysis. The constitutions of such coordinate system can always be possible in any channel, if the x_2 coordinate would be selected in accordance with the velocity distributions (Chiu, Lin, and Mizumura, 1978). Hayakawa, Fukushima, and Sanjo (1984) applied this method to the flows in the lower-half of elliptic cross-section flumes, and they assumed the velocity distributions is logarithmic in the elliptic coordinate system. On the contrary, Fischer (1966) assumed that the velocity distributions are three-dimensional, that is, $\bar{u}_1 = \bar{u}_1(x_2, x_3)$ but the concentration distributions are two-dimensional, that is, $c'' = c''(x_3, t)$, and only the function of the lateral coordinate x_3 in natural streams.

3.3 Longitudinal Dispersion in Turbulent Shear Flows

3.3.1 Basic Equations

The ordinary hydraulic phenomena are governed by the three principles of fluid mechanics; the conservation law for mass, the conservation law for momentum, and the conservation low of energy. Assuming the fluid is incompressible, and the density of fluid is constant, the governing law for the fluid and the low concentration solute are:

1. Conservation law for the volume of fluid,
2. Conservation law for the mass of solute or the concentration of solute,
3. Conservation law for the momentum, and
4. Conservation law for the mechanical energy.

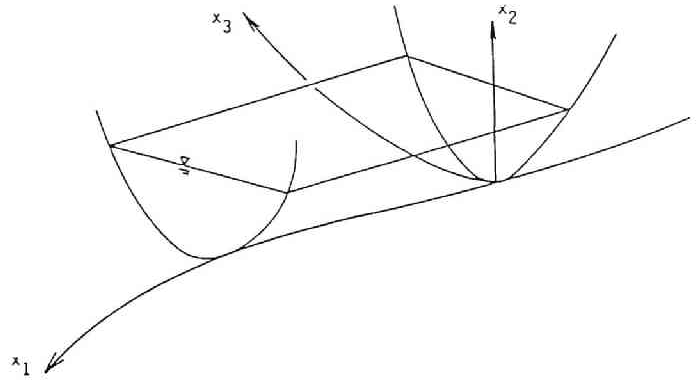

Figure 3.3.1: Definition of the orthogonal coordinate system.

These conservation laws are mathematically stated by using the control volume modeling in the specified coordinate system. Hereafter this modeling is called Eulerian Analysis. According to Rouse (1958), the conservation laws for the volume of water and the concentration in 3–D turbulent shear flows are written in the orthogonal curvilinear coordinate system as;
Continuity equation,

$$\frac{1}{g_1 g_2 g_3}\left\{\frac{\partial g_2 g_3 \bar{u}_1}{\partial x_1}+\frac{\partial g_3 g_1 \bar{u}_2}{\partial x_2}+\frac{\partial g_1 g_2 \bar{u}_3}{\partial x_3}\right\}=0 \tag{3.3.1}$$

Turbulent diffusion equation,

$$\begin{aligned}&\frac{\partial \bar{c}}{\partial t}+\frac{1}{g_1 g_2 g_3}\left\{\frac{\partial g_2 g_3 \bar{c}\bar{u}_1}{\partial x_1}+\frac{\partial g_3 g_1 \bar{c}\bar{u}_2}{\partial x_2}+\frac{\partial g_1 g_2 \bar{c}\bar{u}_3}{\partial x_3}\right\}\\ &\quad=\frac{1}{g_1 g_2 g_3}\left\{\frac{\partial}{\partial x_1}\left(\frac{g_2 g_3}{g_1}\varepsilon_1\frac{\partial \bar{c}}{\partial x_1}\right)+\frac{\partial}{\partial x_2}\left(\frac{g_3 g_1}{g_2}\varepsilon_2\frac{\partial \bar{c}}{\partial x_2}\right)+\frac{\partial}{\partial x_3}\left(\frac{g_1 g_2}{g_3}\varepsilon_3\frac{\partial \bar{c}}{\partial x_3}\right)\right\}\end{aligned} \tag{3.3.2}$$

where $\bar{u}_i$ is the Eulerian averaged velocity in the x_i coordinate, $\bar{c}$ concentration of solute, g_i the metric defined by

$$g_i=\sqrt{\left(\frac{\partial x}{\partial x_i}\right)^2+\left(\frac{\partial y}{\partial x_i}\right)^2+\left(\frac{\partial z}{\partial x_i}\right)^2}\quad(i=1,2,3)$$

x_i the space coordinate (i = 1, 2, 3), and t the time coordinate, and $\bar{}$ (over bar) denotes the ensemble or temporal average. The definition of the coordinate system is shown in Fig. 3.3.1. The molecular transport of mass is negligibly smaller than the turbulent transport in ordinary turbulent flows, and it is neglected in Eq. 3.3.2. The

turbulent mass transport is usually stated by gradient type flux, and it is written as:

$$-\overline{c'u_1'} = \frac{1}{g_1}\varepsilon_1\frac{\partial \bar{c}}{\partial x_1}, \quad -\overline{c'u_2'} = \frac{1}{g_2}\varepsilon_2\frac{\partial \bar{c}}{\partial x_2}, \quad -\overline{c'u_3'} = \frac{1}{g_3}\varepsilon_3\frac{\partial \bar{c}}{\partial x_3} \tag{3.3.3}$$

where ε_i is the turbulent diffusion coefficient. Eq.3.3.3 has already been introduced in Eq. 3.3.2.

3.3.2 1–D Convective Dispersion Equation and the Definition of Longitudinal Dispersion Coefficient

In usual analyses for low concentration solution, $\bar{u}_i$ is solved by the momentum equation and the continuity equation under certain boundary condition, and by using the velocity distributions obtained, the turbulent diffusion equation is solved independently. Since solving these equations in 3–D space is not so easy and requires a lot of time and computer resources at moment, simpler models which preserve the features of flow and concentration field are commonly used. In case of river flows which are almost uni-directional, and the length scale in the longitudinal/flow direction is much larger than those in the lateral and the depth-wise directions, one-dimensional models are commonly used. The one-dimensional models for Eq. 3.3.2 obtained by Iwasa (1976) are written as:

$$\int_A g_1\frac{\partial}{\partial t}\bar{c}g_2g_3dx_2dx_3 + \frac{\partial}{\partial x_1}\int_A \bar{c}\bar{u}_1g_2g_3dx_2dx_3 = \frac{\partial}{\partial x_1}\int_A \frac{g_2g_3}{g_1}\varepsilon_1\frac{\partial \bar{c}}{\partial x_1} \tag{3.3.4}$$

in which it is assumed that the mass of solute is not transported through the channel-bottom, the channel-side, and the free surface, and the assumption

$$\int_B \bar{c}_s\frac{\partial h}{\partial t}g_3dx_3 - \bar{c}_s\frac{\partial A}{\partial t} = 0$$

is introduced, where $\bar{c}_s$ is the concentration at the surface, ζ the water surface elevation, and B the surface width. The cross-sectional mean concentration C, and the cross-sectional mean velocity U are respectively defined as:

$$C \equiv \frac{1}{A}\int_A \bar{c}g_2g_3dx_2dx_3 \tag{3.3.5}$$

$$U \equiv \frac{1}{A}\int_A \bar{u}_1g_2g_3dx_2dx_3 \tag{3.3.6}$$

where A is the cross-sectional area and defined as:

$$A \equiv \int_A g_2g_3dx_2dx_3 \tag{3.3.7}$$

The deviations from the cross-sectional mean values are also introduced as:

$$c''(x_i,t) \equiv \bar{c}(x_i,t) - C(x_1,t) \tag{3.3.8}$$

$$u_1''(x_i,t) \equiv \bar{u}_1(x_i,t) - U(x_1,t) \tag{3.3.9}$$

Hereafter, assume

$$g_1 = g_1(x_1)$$

Introduce D_{Et} by the following relationship:

$$\int_A \frac{g_2 g_3}{g_1} \varepsilon_1 \frac{\partial \bar{c}}{\partial x_1} dx_2 dx_3 = \frac{A D_{Et}}{g_1} \frac{\partial C}{\partial x_1} \tag{3.3.10}$$

Eq. 3.3.10 assumes the Eulerian turbulent mass transport through the cross-section A is also stated as the gradient type mass transport and its proportional constant is D_{Et}. By using Eqs. 3.3.5 to 3.3.10, Eq. 3.3.4 is written in the form of:

$$\frac{\partial}{\partial t} AC + \frac{1}{g_1} \frac{\partial}{\partial x_1} \dot{M} = \frac{1}{g_1} \frac{\partial}{\partial x_1} \left(\frac{1}{g_1} A D_{Et} \frac{\partial C}{\partial x_1} \right) \tag{3.3.11}$$

where

$$\dot{M} \equiv \int_A \bar{c} \bar{u}_1 g_2 g_3 dx_2 dx_3 = AUC + \int_A u_1'' c'' g_2 g_3 dx_2 dx_3 \tag{3.3.12}$$

Assuming the second term of the right-hand side of Eq. 3.3.12 is also stated as the gradient type mass flux and its proportional constant is D_{Evl},

$$\dot{Q} \equiv \int_A u_1'' c'' g_2 g_3 dx_2 dx_3 = -\frac{1}{g_1} A D_{Evl} \frac{\partial C}{\partial x_1} \tag{3.3.13}$$

It will be shown in the next section that the definition of D_{Evl}, Eq. 3.3.13 is equivalent to the definition of the longitudinal dispersion coefficient D_1 by Taylor (1954).

Note that the energy coefficient (Coriolise) α and the momentum coefficient (Boussinesq) β are introduced in the one-dimensional equations of energy and momentum respectively, and that they are connected with the cross-sectional mean velocity U, however in case of the concentration equation, the correction term is connected with the gradient of the cross-sectional mean concentration $\partial C / \partial x_1$.

Substituting Eqs.3.3.12 and 3.3.13 into Eq. 3.3.11, Eq. 3.3.11 is written:

$$\frac{\partial}{\partial t} AC + \frac{1}{g_1} \frac{\partial}{\partial x_1} AUC = \frac{1}{g_1} \frac{\partial}{\partial x_1} \left(\frac{1}{g_1} A D_E \frac{\partial C}{\partial x_1} \right) \tag{3.3.14}$$

where D_E is the longitudinal dispersion coefficient in view of the Eulerian analysis and defined as:

$$D_E \equiv D_{Et} + D_{Evl} \tag{3.3.15}$$

By using one-dimensional continuity equation:

$$\frac{\partial A}{\partial t} + \frac{1}{g_1} \frac{\partial}{\partial x_1} AU = 0 \tag{3.3.16}$$

Eq. 3.3.14 is rewritten in the form of:

$$\frac{\partial}{\partial t} C + \frac{1}{g_1} U \frac{\partial C}{\partial x_1} = \frac{1}{A} \frac{1}{g_1} \frac{\partial}{\partial x_1} \left(\frac{1}{g_1} A D_E \frac{\partial C}{\partial x_1} \right) \tag{3.3.17}$$

Eq. 3.3.14 or Eq. 3.3.17 is called the "Convective Dispersion Equation"

3.4 Theory of Longitudinal Dispersion Coefficient

3.4.1 Equation for $c'' = \bar{c} - C$

The longitudinal dispersion coefficient is defined by Eq. 3.3.15. Assuming u_1'' is given as the solution of the momentum and the continuity equations, the longitudinal dispersion coefficient D_E is theoretically calculated by use of Eqs. 3.3.10, 3.3.13 and 3.3.15, if the distributions of c'' in a cross-section can be obtained. The governing equation for c'' is obtained by subtracting Eq. 3.3.17 from the equation which results from substituting Eqs. 3.3.8 and 3.3.9 into Eq. 3.3.2, and the result is:

$$\begin{aligned}
&\frac{\partial c''}{\partial t} + \\
&\frac{1}{g_1 g_2 g_3}\frac{\partial}{\partial x_1}\left(g_2 g_3 c''(U+u_1'')\right) - \frac{1}{g_1}\frac{1}{A}\frac{\partial}{\partial x_1}\left(\frac{1}{g_1}\int_A u_1'' c'' g_2 g_3 dx_2 dx_3\right) - \\
&\frac{1}{g_1 g_2 g_3}\frac{\partial}{\partial x_1}\left(\frac{g_2 g_3}{g_1}\varepsilon_1\frac{\partial c''}{\partial x_1}\right) + \\
&\frac{1}{g_1 g_2 g_3}\frac{\partial}{\partial x_2}\left\{\frac{g_3 g_1}{g_2}\left(g_2 c''\bar{u}_2 - \varepsilon_2\frac{\partial c''}{\partial x_2}\right)\right\} + \\
&\frac{1}{g_1 g_2 g_3}\frac{\partial}{\partial x_3}\left\{\frac{g_1 g_2}{g_3}\left(g_3 c''\bar{u}_3 - \varepsilon_3\frac{\partial c''}{\partial x_3}\right)\right\} + \\
= \; &-\frac{1}{g_1 g_2 g_3}\frac{\partial}{\partial x_1}\left\{\frac{g_2 g_3}{g_1}\left(C\left(U+u_1''\right) - \varepsilon_1\frac{\partial C}{\partial x_1}\right)\right\} - \\
&\frac{1}{g_1 g_2 g_3}\frac{\partial\left(g_3 g_1 C\bar{u}_2\right)}{\partial x_2} - \frac{1}{g_1 g_2 g_3}\frac{\partial\left(g_1 g_2 C\bar{u}_3\right)}{\partial x_3}
\end{aligned} \tag{3.4.1}$$

Eq. 3.4.1 could be solved under certain boundary conditions if the distributions of $C, U, u_1'', \bar{u}_2, \bar{u}_3, \varepsilon_1, \varepsilon_2$, and ε_3 would be known, however it is very difficult. Therefore, the simplification of Eq. 3.4.1 will be made by introducing following assumptions; for the transport of c'' in the longitudinal direction, assume:

$$O(c''U) \gg O\left(c''u'' - \frac{1}{A}\int_A u_1'' c'' g_2 g_3 dx_2 dx_3\right) \tag{3.4.2}$$

and

$$O(c''U) \gg O\left(\frac{1}{g_1}\varepsilon_1\frac{\partial c''}{\partial x_1}\right) \tag{3.4.3}$$

for the transport of C in the longitudinal direction, assume:

$$O(Cu_1'') \gg O\left(\frac{1}{g_1}\varepsilon_1\frac{\partial C}{\partial x_1}\right) \tag{3.4.4}$$

and

$$\frac{\partial}{\partial x_1}UC - U\frac{\partial C}{\partial x_1} \simeq 0 \tag{3.4.5}$$

Then, Eq. 3.4.1 can be written as:

$$
\begin{aligned}
&\frac{\partial c''}{\partial t} + \\
&\frac{1}{g_1 g_2 g_3}\frac{\partial}{\partial x_1}\left(g_2 g_3 c'' U\right) + \\
&\frac{1}{g_1 g_2 g_3}\frac{\partial}{\partial x_2}\left\{\frac{g_3 g_1}{g_2}\left(g_2 c''\bar{u}_2 - \varepsilon_2\frac{\partial c''}{\partial x_2}\right)\right\} + \\
&\frac{1}{g_1 g_2 g_3}\frac{\partial}{\partial x_3}\left\{\frac{g_1 g_2}{g_3}\left(g_3 c''\bar{u}_3 - \varepsilon_3\frac{\partial c''}{\partial x_3}\right)\right\} + \\
= \quad & -\frac{1}{g_1 g_2 g_3}\frac{\partial}{\partial x_1}\left(g_2 g_3 C u_1''\right) - \\
& \frac{1}{g_1 g_2 g_3}\frac{\partial\left(g_3 g_1 C\bar{u}_2\right)}{\partial x_2} - \frac{1}{g_1 g_2 g_3}\frac{\partial\left(g_1 g_2 C\bar{u}_3\right)}{\partial x_3}
\end{aligned}
\tag{3.4.6}
$$

Recent turbulence measurements in uniform flows in rectangular cross-section laboratory flumes by LDV discloses the existence of the complex longitudinal vortex and the secondary current (Tominaga, Nezu, Ezaki, 1989), however assuming that the convective transport of c'' and C by the secondary current is negligibly smaller than that of turbulent transport:

$$
O\left(\frac{1}{g_2}\varepsilon_2\frac{\partial c''}{\partial x_2}\right) \gg O(c''\bar{u}_2) \tag{3.4.7}
$$

$$
O\left(\frac{1}{g_3}\varepsilon_3\frac{\partial c''}{\partial x_3}\right) \gg O(c''\bar{u}_3) \tag{3.4.8}
$$

and the convective transport of C by u_1'' prevails over those by $\bar{u}_2$ and $\bar{u}_3$:

$$
O\left(\frac{\partial}{\partial x_1}\left(g_2 g_3 C u_1''\right)\right) \gg O\left(\frac{\partial}{\partial x_2}\left(g_3 g_1 C\bar{u}_2\right)\right) \tag{3.4.9}
$$

$$
O\left(\frac{\partial}{\partial x_1}\left(g_2 g_3 C u_1''\right)\right) \gg O\left(\frac{\partial}{\partial x_3}\left(g_1 g_2 C\bar{u}_3\right)\right) \tag{3.4.10}
$$

(The assumptions of Eqs. 3.4.9 and 3.4.10 are not necessary in case of the uniform flows in straight channel, in which $\bar{u}_2$, and $\bar{u}_3$ is assumed to be zero.)
These assumptions leads Eq. 3.4.6 to the following equation:

$$
\begin{aligned}
&\frac{\partial c''}{\partial t} + \frac{1}{g_1 g_2 g_3}\frac{\partial}{\partial x_1}\left(g_2 g_3 c'' U\right) - \\
&\frac{1}{g_1 g_2 g_3}\frac{\partial}{\partial x_2}\left(\frac{g_3 g_1}{g_2}\varepsilon_2\frac{\partial c''}{\partial x_2}\right) - \frac{1}{g_1 g_2 g_3}\frac{\partial}{\partial x_3}\left(\frac{g_1 g_2}{g_3}\varepsilon_3\frac{\partial c''}{\partial x_3}\right) \\
= \quad & -\frac{1}{g_1 g_2 g_3}\frac{\partial}{\partial x_1}\left(g_2 g_3 C u_1''\right)
\end{aligned}
\tag{3.4.11}
$$

Assuming that c'' is convected by the cross-sectional mean velocity U without any deformation of its distribution in a cross-section ("Frozen tracer cloud" hypothesis), Eq. 3.4.11 is rewritten in the from of:

$$\frac{1}{g_1 g_2 g_3}\left\{\frac{\partial}{\partial x_2}\left(\frac{g_3 g_1}{g_2}\varepsilon_2\frac{\partial c''}{\partial x_2}\right)+\frac{\partial}{\partial x_3}\left(\frac{g_1 g_2}{g_3}\varepsilon_3\frac{\partial c''}{\partial x_3}\right)\right\}=\frac{1}{g_1 g_2 g_3}\frac{\partial}{\partial x_1}\left(g_2 g_3 C u_1''\right) \quad (3.4.12)$$

According to Fischer (1966), c'' in Eq. 3.4.11 has the steady state solution in $\xi = x - Ut$, and $t = \tau$ coordinate system after enough long travel time/length, and it satisfies Eq. 3.4.12. Eq. 3.4.12 is the Poisson's partial differential equation of the second order, in which c'' is the unknown variable, and $\partial C u_1''/\partial x_1$ the non-homogeneous term. The boundary condition for c'' is:

$$\frac{\partial c''}{\partial n} = 0 \quad (3.4.13)$$

3.4.2 Solution of c'' Equation and Calculating Dispersion Coefficient in 2-D Uniform Flows

D_{Evl} will be obtained by substituting c'' into Eq. 3.3.13 after solving Eq.3.4.12 under the boundary condition, Eq. 3.4.13. The independent variables of Eq. 3.4.12 are x_2 and x_3, and Eq. 3.4.12 can numerically be solved by using electronics computers, but it is difficult to get the analytical solution. In case the velocity and concentration distributions are two dimensional, and the second coordinate is selected at x_2, Eq. 3.4.12 is reduced to the ordinary differential equation, and becomes much easier to be solved.

Assuming that c'' and ε_2 are only the function of the x_2 coordinate, and referring Fig. 3.4.1, Eq. 3.4.12 can be integrated with respect to x_3 as:

$$\frac{d}{dx_2}\left(\varepsilon_2 s\frac{dc''}{dx_2}\right)=\frac{\partial C}{\partial x_1}\frac{dA_1(x_2)}{dx_2}u_1''(x_2) \quad (3.4.14)$$

where

$$s(x_2) \equiv \int_{x_{3a}}^{x_{3b}} g_3 dx_3 \quad (3.4.15)$$

$$A_1(x_2) \equiv \int_0^{x_2} dx_2 \int_{x_{3a}}^{x_{3b}} g_2 g_3 dx_3 \quad (3.4.16)$$

Integrating Eq. 3.4.14 with respect to x_2, the following equations can be obtained:

$$\frac{dc''}{dx_2}=\frac{\partial C}{\partial x_1}\frac{1}{\varepsilon_2 s}\int_0^{x_2} u_1''(x_2')\frac{dA_1}{dx_2}dx_2' \quad (3.4.17)$$

under the boundary condition:

$$\left[\varepsilon_2 s\frac{dc''}{dx_2}\right]_{x_2=0} = 0 \quad (3.4.18)$$

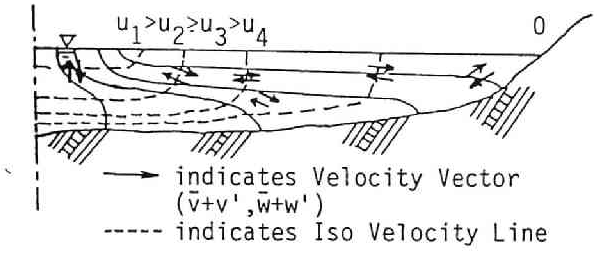

Figure 3.4.1: Definition of the coordinate system $x_2 - x_3$. Solid lines denote x_2 lines equivalent to the iso-velocity contour lines, and broken lines x_3 lines.

Eq. 3.4.17 can again be integrated with respect to x_2, and the result is:

$$c''(x_2) = \frac{\partial C}{\partial x_1} \int_0^{x_2} \frac{dx_2'}{\varepsilon_2 s} \int_0^{x_2'} u_1''(x_2'') \frac{dA_1}{dx_2} dx_2'' + c''(0) \tag{3.4.19}$$

Substituting Eq. 3.4.19 into Eq. 3.3.13, the final result is:

$$D_{Evl} = \frac{1}{A} \int_{x_{2a}}^{x_{2b}} \frac{dx_2}{\varepsilon_2 s} \left[\int_0^{x_2} u_1''(x_2') \frac{dA_1}{dx_2} dx_2' \right]^2 \tag{3.4.20}$$

Applying Eq. 3.4.20 to the Poiseuilli flow in a tube of which the diameter is a, and assuming the molecular diffusivity $D_m = \varepsilon_2$, the dispersion coefficient is calculated at,

$$D_{Evl} = \frac{a^2 U^2}{48 D_m} \tag{3.4.21}$$

under the assumption of the parabolic distribution of the velocity $u_1''(x_2)$. Eq. 3.4.21 is the same as the result in Taylor (1953). Assuming the logarithmic distribution of the velocity and the Reynolds analogy for turbulent diffusion coefficient ε_2, the application of Eq. 3.4.20 to the turbulent shear flows in a pipe calculates the dispersion coefficient at:

$$D_{Evl} = \frac{0.327}{\kappa^3} a u_* \tag{3.4.22}$$

where a is the diameter of a pipe, u_* the shear velocity and κ von Karman's constant. Assuming $\kappa = 0.32$ after the tables used in the calculation in Taylor (1954), Eq. 3.4.22 gives:

$$D_{Evl} = 9.98 a u_*$$

and it is very close with $D_1 = 10.1au_*$ obtained by Taylor (1954).

In case of the 2-D plain turbulent flows in which the velocity distribution is logarithmic, the phenomena is uniform in the lateral direction x_3, therefore variations of c'' and $\bar{u}_1$ in the x_3 coordinate can be negligible, and Eq. 3.4.12 is written in the form of:

$$\frac{d}{dx_2}\left(\varepsilon_2 \frac{dc''}{dx_2}\right) = u_1''(x_2)\frac{\partial C}{\partial x_1} \tag{3.4.23}$$

and under the assumption of Reynolds analogy for the turbulent diffusivity ε_2 the dispersion coefficient is calculated at:

$$D_{Evl} = \frac{0.404}{\kappa^3} du_* \tag{3.4.24}$$

where d is the flow depth. Eq. 3.4.24 is the same as the theoretical result obtained by Elder (1956).

Hayakawa, Fukushima and Sanjo (1984) applied the same modeling to the turbulent flows in the lower-half of the elliptic cross-section channel, assuming the velocity is the logarithmic in the x_2 coordinate, and the concentration distributions are also the function of the x_2 coordinate. Their theoretical results describe the behavior of D_{Evl} with respect to the width to depth ratio B/d as:

$$D_{Evl} = \begin{cases} \dfrac{0.404}{\kappa^3} du_*, & \text{for } B/d \to 0 \quad \text{or} \quad \infty \\ 10.1 du_*, & \text{for } B/d = 1.0 \end{cases} \tag{3.4.25}$$

Fischer (1966) assumed that the concentration distribution is dependent on only the lateral coordinate z in the Cartesian coordinate system for the river flows, because the length scale in the z direction is much larger than that in the depth-wise direction y in the ordinary river flows, therefore, Eq. 3.4.12 is written as:

$$\frac{\partial}{\partial z}\left(\varepsilon_z \frac{\partial c''(z)}{\partial z}\right) = u_1''(y,z)\frac{\partial C}{\partial x} \tag{3.4.26}$$

Integrating Eq. 3.4.26 with respect to the depth, and integrating the result with respect to the width two-times, c'' distribution is obtained as:

$$c'' = \int_0^z \frac{dz'}{\varepsilon_z} \int_0^{z'} q'(z'')dz'' \frac{\partial C}{\partial x} + c''(0) \tag{3.4.27}$$

where

$$q'(z) = \int_{-z_b}^{\eta} u_{yz}'' dy, \quad (d = \eta + z_b)$$

and D_{Evl} is finally obtained as:

$$D_{Evl} = \frac{1}{A}\int_{-b_1}^{b_2} \frac{dz}{\varepsilon_z d}\left[\int_0^z q'(z')dz'\right]^2 \tag{3.4.28}$$

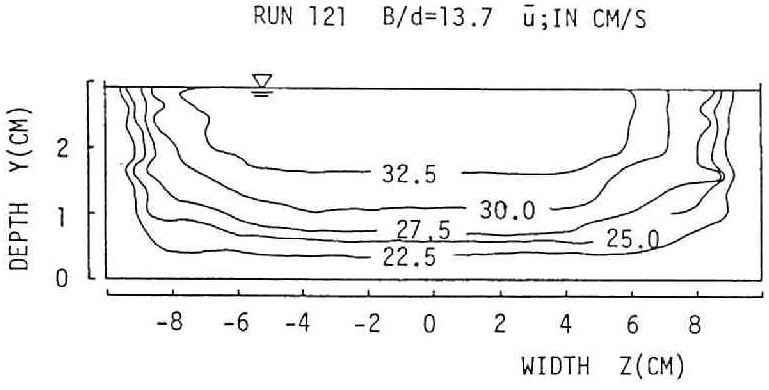

Figure 3.4.2: Iso-velocity contour map measured in Run 121 in a rectangular cross-section flume.

He also demonstrated the validity of Eq. 3.4.28 by comparison of the theoretical results with the dispersion coefficient measured in the tracer study in the trapezoidal cross-section flumes with the stone roughness at the side boundaries as well as in natural streams.

As described above, the dispersion coefficients D_1 in the five different kinds of flow were obtained from the same basic equation, Eq. 3.4.12. The difference between the former four results by Taylor (1953 and 1954), Elder (1956) and Hayakawa, Fukushima and Sanjo (1984), and Fischer (1966) should be notable. It is assumed that the concentration distributions in a cross-section is only the function of x_2, which is the only one coordinate describing the velocity distributions in Taylor-Elder's analysis. The construction of such coordinate system is always possible in any channel, if the x_2 coordinate would be selected in accordance with the velocity distributions (Chiu, Lin, and Mizumura, 1978). This assumption for concentration distributions may be acceptable in case of the flows in a pipes or 2-D open-channel flows, because the characteristics length of the flows is only the diameter a or the depth d respectively, and the flow and concentration fields is two-dimensional, however this assumption may not be acceptable for the flows in arbitrary cross-section channels by following reasons.

Referring Fig. 3.4.2 which describes an example of the iso-velocity contours of the turbulent flows in the rectangular cross-section flumes, consider the dispersion of the tracer cloud injected as a plain source at the section $x_1 = 0$ at $t = 0$. The injected

tracer is transported by the convective velocity $\bar{u}_1(x_2, x_3)$ in the x_1 direction and also disperses in the x_1, x_2, and x_3 directions by the turbulent transport. Therefore, the concentration distributions are similar to the velocity distributions for the short travel time. The two different sets of the combination for the principal directions are possible for the diffusive transport of the tracer in the cross-section for longer travel time. The first set is the combination of x_2 which describes the velocity distributions and x_3 orthogonal to x_2, and the second combination is the depth-wise direction y and the lateral direction z orthogonal to the depth-wise direction. In cases of the axi-symmetric two-dimensional flows considered by Taylor (1953, and 1954), and of the 2-D open-channel flows considered by Elder (1956), the first combination is natural and varied, because the flow field is uniform in the x_3 direction and has only one characteristic length a or d and also the concentration field does.

In case of the flows in rectangular cross-section flumes, the constitutions of the coordinate system x_2 and x_3 is possible, but the concentration distributions would be quite different, because it has two different length scales, that is, the depth d for the length scale in the depth-wise direction, and the width B or $B/2$ for the length scale in the lateral direction. Therefore, the characteristic time scale for the depth-wise directional mixing T_{Ey} is:

$$T_{Ey} = d^2/\varepsilon_y \tag{3.4.29}$$

where ε_y is the turbulent diffusion coefficient in the vertical direction. The characteristic time scale for the lateral directional mixing T_{Ez} is:

$$T_{Ez} = (B/2)^2/\varepsilon_z \tag{3.4.30}$$

where ε_z is the turbulent diffusion coefficient in the lateral direction. Therefore the ratio T_r of T_{Ez} to T_{Ey} is written as:

$$T_r \equiv \frac{T_{Ez}}{T_{Ey}} = \frac{1}{4}\left(\frac{B}{d}\right)^2 \left(\frac{\varepsilon_y}{\varepsilon_z}\right) \tag{3.4.31}$$

In ordinary open-channel flows,

$$\frac{\varepsilon_z}{\varepsilon_y} \approx 3 \quad \text{to} \quad 4 \tag{3.4.32}$$

and

$$\frac{B}{d} \begin{cases} > 10, & \text{for 2-D laboratory flumes} \\ \gg 100, & \text{for natural streams} \end{cases} \tag{3.4.33}$$

and the magnitude of T_r is very huge in ordinary open-channel flows. Therefore, the mixing in the lateral direction is much slower than those in the vertical direction, and the iso-concentration contour lines are almost parallel to the depth-wise coordinate for

long travel time and independent on the velocity contour lines. Fig. 4.4.1 in Chapter 4 describes the concentration distributions measured in the time coordinate, and demonstrates the non-uniformity of the concentration in the depth-wise direction is much smaller than those in the lateral direction for the long travel time. Fig. 3.4.3 shows the concentration distributions calculated by Eq. 3.4.12 by use of the velocity distributions measured in a rectangular laboratory flumes and the numerical method of FEM (Hosoda, 1980). This figure also demonstrates that the non-uniformity of the concentration in the depth-wise direction is much smaller than those in the lateral direction, and that concentration distributions in the depth-wise direction is almost similar each other, and the depth-averaged concentration distributions are slightly varied in the longitudinal direction. Thus, the concentration distributions in wide open-channel flows can be described to be rather uniform in the depth-wise direction, and the iso-concentration contour limes are not parallel to the iso-velocity contour lines.

3.5 Dispersion Coefficient in Open-Channel Flows

This section will study the longitudinal dispersion coefficient in steady turbulent open-channel flows. The coordinate system used in this chapter is the Cartesian as:

$$x_1 = x, \quad x_2 = y, \quad \text{and} \quad x_3 = z \tag{3.5.1}$$

and

$$g_1 = g_2 = g_3 = 1 \tag{3.5.2}$$

where x, y, and z is the Cartesian coordinate in the flow direction, the depth-wise direction, and the lateral direction respectively and the definition sketch of the coordinate system and symbols is shown in Fig. 3.5.1.

3.5.1 Decomposition of Variables

The locally average velocity $\bar{u}_1$ in the flow direction and concentration $\bar{c}$ can mathematically be decomposed into the following forms:

$$\bar{u}_i(x_i) = \bar{u}_i^{x_2}(x_1, x_3) + u_{i23}''(x_1, x_2, x_3) \quad (i = 1, 3) \tag{3.5.3}$$

$$\bar{c}(x_i) = \bar{c}^{x_2}(x_1, x_3) + c_{23}''(x_1, x_2, x_3, t) \tag{3.5.4}$$

where $\bar{a}^{x_2}$ denotes the depth-averaged values of $\bar{a}$ defined by:

$$\bar{a}^{x_2} \equiv \frac{1}{d} \int_{-z_b}^{\eta} \bar{a} dx_2$$

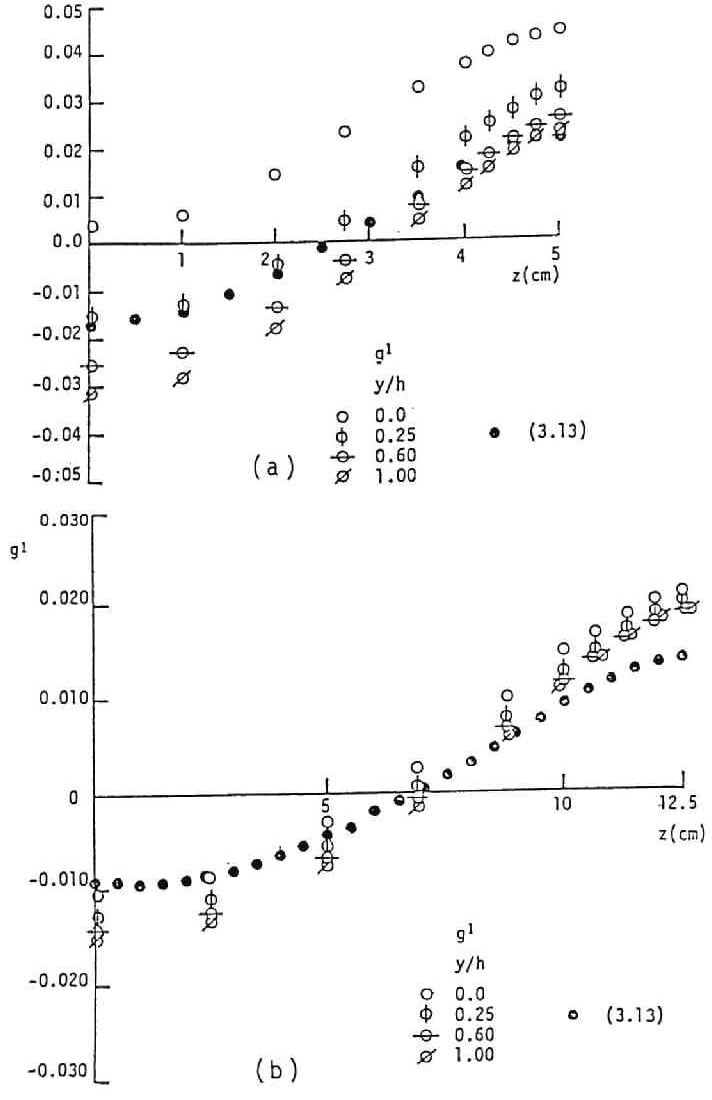

Figure 3.4.3: Concentration distributions at some heights calculated by Hosoda (1980). Open-circles denote the results of 3-D calculation, and solid circles the results of 2-D calculation. (a) $B/d = 3.12$, and (b) $B/d = 8.50$.

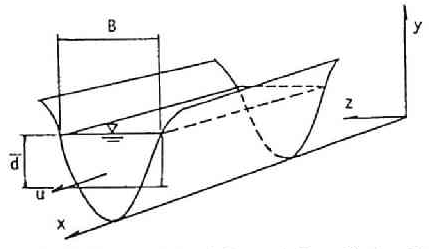

Figure 3.5.1: Definition of the Cartesian coordinate system and symbols.

in which $d(=\eta+z_b)$ is the flow depth, η the water surface elevation from the reference level, and $-z_b$ the elevation of the bottom. a''_{23} is the deviation from the depth averaged value $\bar{a}^{x_2}$ and defined by:

$$a''_{23} \equiv \bar{a} - \bar{a}^{x_2}$$

Introduction of the cross-sectional mean values defined by Eqs. 3.3.5 and 3.3.6 again decomposes $\bar{u}_1$ and $\bar{c}$ as,

$$\bar{u}_1(x_i) = U + (\bar{u}_1^{x_2} - U) + u''_{123} \tag{3.5.5}$$

$$\bar{c}(x_i,t) = C + (\bar{c}^{x_2} - C) + c''_{23} \tag{3.5.6}$$

In Eqs. 3.5.5 and 3.5.6, the locally time-averaged value $\bar{a}$ is decomposed into the cross-sectional averaged value A, the deviation of the depth-averaged value from the cross-sectional averaged value $\bar{a}^{x_2} - A$, and the deviation of the locally averaged value from the depth-averaged value a''_{23}. (See Fig. 2.2.2.)

Substituting Eqs. 3.5.5 and 3.5.6 into Eq. 3.3.12, the total mass flux transported by the locally averaged velocity $\bar{u}_1$ through the cross-sectional area A can be rewritten in the form of:

$$\dot{M} = AUC + \int_{-b_1}^{b_2} (\bar{u}^{x_2} - U)(\bar{c}^{x_2} - C)ddx_3 + \int_{-b_1}^{b_2} dx_3 \int_{-z_b}^{\eta} u''_{123} c''_{23} dx_2 \tag{3.5.7}$$

where $-b_1$ and b_2 is the x_3 coordinate at left/right boundary of the water surface respectively, and $B = (b_2+b_1)$ the surface width. The mass transport $\dot{M}' = \dot{M} - AUC$ which is the mass transport in the moving coordinate $\xi = x - Ut$ is decomposed into two components in Eq. 3.5.7, that is, the second term of the right-hand side of Eq. 3.5.7 indicates the product of the deviations of the depth-averaged value from the

cross-sectional value, and the third term does the product of the deviations of the locally averaged value form the depth-averaged value. Since the assumption is made that the distribution of $\bar{u}_1$ is given, $\dot{M}$ can be calculated if the distribution of $\bar{c}^{x_2}$ and c''_{23} are obtained. Assuming the following expressions:

$$\int_{-b_1}^{b_2}(\bar{u}^{x_2}-U)(\bar{c}^{x_2}-C)ddx_3 \equiv -AD_{El}\frac{\partial C}{\partial x} \tag{3.5.8}$$

$$\int_{-b_1}^{b_2}dx_3\int_{-z_b}^{\eta}u''_{123}c''_{23}dx_2 = -\int_{-b_1}^{b_2}(\eta+z_b)D2_{1i}\frac{\partial \bar{c}^{x_2}}{\partial x_i}dx_3 \equiv -AD_{Ev}\frac{\partial C}{\partial x} \tag{3.5.9}$$

$$\int_{-z_b}^{\eta}u''_{123}c''_{23}dx_2 \equiv -(\eta+z_b)D2_{1i}\frac{\partial \bar{c}^{x_2}}{\partial x_i} \tag{3.5.10}$$

By using Eqs. 3.5.8 to 3.5.10, Eq. 3.3.15 can be rewritten as:

$$D_E = D_{Et} + D_{Ev} + D_{El} \tag{3.5.11}$$

The first term of the right hand-side of Eq. 3.5.11 describes the turbulent transport by Eulerian turbulence, the second one the dispersion caused by the vertical non-uniformity of the velocity distribution, and the third one the dispersion caused by the lateral non-uniformity of the velocity distribution.

The mathematical procedures to obtain D_{Ev} and D_{El} are illustrated in Fig. 3.5.2, comparing those for D_{Evl} described in **Section 3.4**. The author recently found that Yotsukura (1977) discussed and explain the dispersion phenomena by the similar approach.

3.5.2 Equation for c''_{23} and Calculation of $D2_{ij}$

The 3-D turbulent diffusion equation and the 3-D equation of continuity are written in the Cartesian coordinates system as:

$$\frac{\partial \bar{c}}{\partial t}+\frac{\partial \bar{c}\bar{u}_1}{\partial x_1}+\frac{\partial \bar{c}\bar{u}_2}{\partial x_2}+\frac{\partial \bar{c}\bar{u}_3}{\partial x_3} = \frac{\partial}{\partial x_1}\left(\varepsilon_1\frac{\partial \bar{c}}{\partial x_1}\right)+\frac{\partial}{\partial x_2}\left(\varepsilon_2\frac{\partial \bar{c}}{\partial x_2}\right)+\frac{\partial}{\partial x_3}\left(\varepsilon_3\frac{\partial \bar{c}}{\partial x_3}\right) \tag{3.5.12}$$

$$\frac{\partial \bar{u}_1}{\partial x_1}+\frac{\partial \bar{u}_2}{\partial x_2}+\frac{\partial \bar{u}_3}{\partial x_3}=0 \tag{3.5.13}$$

Integrating Eqs. 3.5.12 and 3.5.13 with respect to the vertical direction from the bottom z_b to the water surface η, the following two equations are obtained respectively:

$$\frac{\partial}{\partial t}\int \bar{c}dx_2+\frac{\partial}{\partial x_1}\int \bar{u}_1\bar{c}dx_2+\frac{\partial}{\partial x_3}\int \bar{u}_3\bar{c}dx_2 = \frac{\partial}{\partial x_1}\left(\int \varepsilon_1\frac{\partial \bar{c}}{\partial x_1}dx_2\right)+\frac{\partial}{\partial x_3}\left(\int \varepsilon_3\frac{\partial \bar{c}}{\partial x_3}dx_2\right) \tag{3.5.14}$$

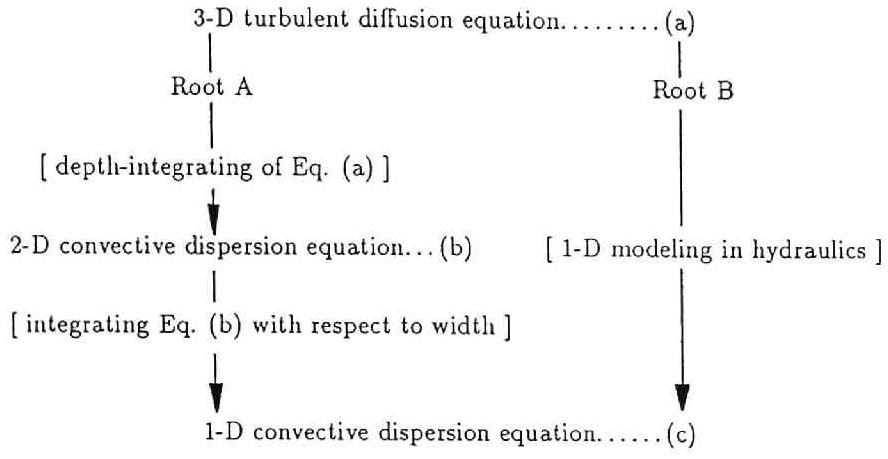

- Variables introduced in
  Eq. (a)..... $\bar{u}_i$, $\bar{c}$ and ϵ_i
  Eq. (b)..... $\bar{u}_1^{x_3}$, $\bar{u}_2^{x_3}$, $\bar{c}^{x_3}$, and $D2_{ij}$
  Eq. (c)..... U, C, and D_E

- Modeling in the present study: Root A
  · (a) — (b),
  equation of $c''_{23} \equiv \bar{c} - \bar{c}^{x_2}$, and $u''_{i23} \equiv \bar{u}_i - \bar{u}_i^{x_2}$
  defining $D2_{ij} \equiv D2_{tij} + D2_{vij}$
  · (b) — (c),
  equation of $c'_{03} \equiv \bar{c}^{x_2} - C$, and $u'_{03} \equiv \bar{u}_1^{x_3} - U$
  defining $D_E \equiv D_{Et} + D_{Ev} + D_{El}$

- Taylor, Elder, and Fischer's Modeling: Root B
  · (a) — (c),
  equation of $c'' \equiv \bar{c} - C$, and $u''_1 \equiv \bar{u}_1 - U$
  defining $D_E \equiv D_{Et} + D_{Evl}$

Figure 3.5.2: Decomposition of the dispersion processes in 1-D equation.

$$\frac{\partial}{\partial t}(\eta + z_b) + \frac{\partial}{\partial x_1}\int \bar{u}_1 dx_2 + \frac{\partial}{\partial x_3}\int \bar{u}_3 dx_2 = 0 \tag{3.5.15}$$

Substitution of Eqs. 3.5.3 and 3.5.4 into Eq. 3.5.14 leads the following equation:

$$\begin{aligned}
&\frac{\partial}{\partial t}\bar{c}^{x_2} + \bar{u}_1^{x_2}\frac{\partial \bar{c}^{x_2}}{\partial x_1} + \bar{u}_3^{x_2}\frac{\partial \bar{c}^{x_2}}{\partial x_3} + \\
&\frac{1}{d}\frac{\partial}{\partial x_1}\left(\int u''_{123}c''_{23}dx_2\right) + \frac{1}{d}\frac{\partial}{\partial x_3}\left(\int u''_{323}c''_{23}dx_2\right) \\
= \;& \frac{1}{d}\frac{\partial}{\partial x_1}\left(\int \varepsilon_1 \frac{\partial \bar{c}}{\partial x_1}dx_2\right) + \frac{1}{d}\frac{\partial}{\partial x_3}\left(\int \varepsilon_3 \frac{\partial \bar{c}}{\partial x_3}dx_2\right)
\end{aligned} \tag{3.5.16}$$

Eq. 3.5.16 is well known as 2-D convective dispersion equation commonly used in plain 2-D hydraulic analysis. The forth and fifth terms of the right hand-side of Eq. 3.5.16 represent the dispersion transport which are caused by the non-uniformity of the velocity distribution in the depth-wise direction and they are commonly stated as the gradient type mass flux as:

$$-\int u''_{i23}c''_{23}dx_2 = dD2_{vij}\frac{\partial \bar{c}^{x_2}}{\partial x_j} \quad (i,j = 1,3) \tag{3.5.17}$$

The integral of the turbulence transport terms in Eq. 3.5.16 are also assumed to be stated as the gradient type mass transport:

$$\int \varepsilon_{\underline{i}}\frac{\partial \bar{c}}{\partial x_{\underline{i}}}dx_2 = dD2_{tij}\frac{\partial \bar{c}^{x_2}}{\partial x_j} \quad (i,j = 1,3) \tag{3.5.18}$$

Then, Eq. 3.5.16 is written as:

$$\begin{aligned}
&\frac{\partial \bar{c}^{x_2}}{\partial t} + \bar{u}_1^{x_2}\frac{\partial \bar{c}^{x_2}}{\partial x_1} + \bar{u}_3^{x_2}\frac{\partial \bar{c}^{x_2}}{\partial x_3} \\
&\quad = \frac{1}{d}\frac{\partial}{\partial x_1}\left\{d\left(D2_{t1i} + D2_{v1i}\right)\frac{\partial \bar{c}^{x_2}}{\partial x_i}\right\} + \frac{1}{d}\frac{\partial}{\partial x_3}\left\{d\left(D2_{t3i} + D2_{v3i}\right)\frac{\partial \bar{c}^{x_2}}{\partial x_i}\right\}
\end{aligned} \tag{3.5.19}$$

The determination of the magnitude of the depth-averaged turbulent diffusion tensor $D2_{tij}$, and the 2-D dispersion tensor $D2_{vij}$ are generally very difficult. Assuming the principal axes of $D2_{tij}$ and $D2_{vij}$ are in the x_1 and x_3 directions, then,

$$D2_{tij} = D2_{vij} = 0 \quad \text{for} \quad i \neq j$$

and the previous studies on $D2_{tij}$ and $D2_{vij}$ in the uni-directional open-channel flows are summarized as:

$$D2_{t11} = \frac{\kappa}{6}du_* \tag{3.5.20}$$

by use of the logarithmic velocity distributions and the Reynolds analogy,

$$D2_{t11} = 1.1du_* \tag{3.5.21}$$

according to the estimation based on the Eulerian measurement of turbulence by Asano(1980). As for the lateral dispersion coefficient, many works have been done in the laboratory flumes as well as natural streams by Elder (1956), Okoye(1970), Hosoda(1990) and so on, and the magnitude of $D2_{t33} + D2_{v33}$ in laboratory flumes are estimated at of the order of:

$$D2_{t33} + D2_{v33} \approx 0.2du_* \tag{3.5.22}$$

$D2_{tij}$ and $D2_{vij}$ are expected to be closely related with the depth-wise velocity distributions and the result of Eq. 3.5.22 is limited. Theoretically, $D2_{vii}$ can be calculated by use of Eq. 3.5.17, if the distributions of c''_{23} can be obtained, and the governing equation of c''_{23} results from subtracting Eq. 3.5.14 from Eq. 3.5.12 and it written as:

$$\begin{aligned}
&\frac{\partial c''_{23}}{\partial t} + \\
&\bar{u}_1^{x_2}\frac{\partial c''_{23}}{\partial x_1} + u''_{123}\frac{\partial \bar{c}^{x_2}}{\partial x_1} + \left\{ u''_{123}\frac{\partial c''_{23}}{\partial x_1} - \frac{1}{d}\frac{\partial}{\partial x_1}\left(\int u''_{123}c''_{23}dx_2 \right) \right\} + \\
&\bar{u}_3^{x_2}\frac{\partial c''_{23}}{\partial x_3} + u''_{323}\frac{\partial \bar{c}^{x_2}}{\partial x_3} + \left\{ u''_{323}\frac{\partial c''_{23}}{\partial x_3} - \frac{1}{d}\frac{\partial}{\partial x_3}\left(\int u''_{323}c''_{23}dx_2 \right) \right\} + \\
&\bar{u}_2^{x_2}\frac{\partial c''_{23}}{\partial x_2} \\
= \; &\left\{ \frac{\partial}{\partial x_1}\left(\varepsilon_1 \frac{\partial \bar{c}^{x_2}}{\partial x_1} \right) - \frac{1}{d}\frac{\partial}{\partial x_1}\left(\int \varepsilon_1 \frac{\partial \bar{c}^{x_2}}{\partial x_1}dx_2 \right) \right\} + \\
&\left\{ \frac{\partial}{\partial x_1}\left(\varepsilon_1 \frac{\partial c''_{23}}{\partial x_1} \right) - \frac{1}{d}\frac{\partial}{\partial x_1}\left(\int \varepsilon_1 \frac{\partial c''_{23}}{\partial x_1}dx_2 \right) \right\} + \\
&\left\{ \frac{\partial}{\partial x_3}\left(\varepsilon_3 \frac{\partial \bar{c}^{x_2}}{\partial x_3} \right) - \frac{1}{d}\frac{\partial}{\partial x_3}\left(\int \varepsilon_3 \frac{\partial \bar{c}^{x_2}}{\partial x_3}dx_2 \right) \right\} + \\
&\left\{ \frac{\partial}{\partial x_3}\left(\varepsilon_3 \frac{\partial c''_{23}}{\partial x_3} \right) - \frac{1}{d}\frac{\partial}{\partial x_3}\left(\int \varepsilon_3 \frac{\partial c''_{23}}{\partial x_3}dx_2 \right) \right\} + \\
&\frac{\partial}{\partial x_2}\left(\varepsilon_2 \frac{\partial c''_{23}}{\partial x_2} \right)
\end{aligned} \tag{3.5.23}$$

Eq. 3.5.23 describes the conservation lows for c''_{23}, but looks very difficult to be solved. The only solution has been obtained under the condition that the velocity and concentration fields are uniform in the lateral direction, however this conditions are hypothetical as will be described in **Chapter 4**. Elder's solution under such conditions was already described in **Section 3.4** as:

$$D2_{v11} = \frac{0.404}{\kappa^3}du_* \tag{3.5.24}$$

$D = 0.404/\kappa^3 du_*$ is clearly depends on the velocity distributions, that is, the magnitude of κ. If the non-uniformity of the velocity distributions are stronger, the

$D2_{v11}$ becomes larger, on the contrary, it becomes smaller, if the velocity distributions becomes more uniform. In case of the uniform turbulent flows in rectangular cross-section laboratory flumes where von Karman's constant is at $\kappa = 0.4$, $D2_{v11}$ is calculated at:

$$D2_{v11} = 6.31 du_* \tag{3.5.25}$$

3.5.3 Equation for c'_{03} and Calculation of D_{El}

Mass transport caused by the lateral non-uniformity of the velocity and concentration $\dot{Q}$ is evaluated by:

$$\dot{Q} = \int_{b_1}^{b_2} u'_{03} c'_{03} dx_2 = -A D_{El} \frac{\partial C}{\partial x_1}. \tag{3.5.26}$$

where u'_{03} and c'_{03} are respectively defined by:

$$u'_{03} = \bar{u}_1^{x_2} - U \tag{3.5.27}$$

$$c'_{03} = \bar{c}^{x_2} - C \tag{3.5.28}$$

The mass conservation equation for c'_{03} is obtained by following procedures. The one-dimensional equations of the convective dispersion equation and the continuity equation of Eqs. 3.3.1 and 3.3.2 are written in the Cartesian coordinate system as:

$$\frac{\partial}{\partial t}\int_A \bar{c} dx_2 dx_3 + \frac{\partial}{\partial x_1}\int_A \bar{c}\bar{u}_1 dx_2 dx_3 = \frac{\partial}{\partial x_1}\int_A \varepsilon_1 \frac{\partial \bar{c}}{\partial x_1} dx_2 dx_3 \tag{3.5.29}$$

$$\frac{\partial A}{\partial t} + \frac{\partial}{\partial x_1} AU = 0 \tag{3.5.30}$$

Substituting Eqs. 3.5.5 and 3.5.6 into Eq. 3.5.29 and using Eq. 3.5.30, Eq. 3.5.29 is rewritten in the form of:

$$\frac{\partial C}{\partial t} + U\frac{\partial C}{\partial x_1} + \frac{1}{A}\frac{\partial}{\partial x_1}\left(\int_{-b_1}^{b_2} u'_{03} c'_{03} dx_3\right) + \frac{1}{A}\frac{\partial}{\partial x_1}\left(\int_A u''_{123} c''_{23} dA\right) = \frac{1}{A}\frac{\partial}{\partial x_1}\left(\int_A \varepsilon_1 \frac{\partial \bar{c}}{\partial x_1} dA\right) \tag{3.5.31}$$

The mass conservation equation for c'_{03} is obtained by subtracting Eq. 3.5.31 from Eq. 3.5.16 as:

$$\begin{aligned}
&\frac{\partial c'_{03}}{\partial t} + U\frac{\partial c'_{03}}{\partial x_1} + u'_{03}\frac{\partial c'_{03}}{\partial x_1} - \frac{1}{A}\frac{\partial}{\partial dx_1}\left(\int_{-b_1}^{b_2} u'_{03} c'_{03} dx_3\right) + \bar{u}_3^{x_2}\frac{\partial c'_{03}}{\partial x_3} \\
= \;& -u'_{03}\frac{\partial C}{\partial x_1} \\
&+\frac{1}{d}\frac{\partial}{\partial x_1}\left\{d(D2_{t1i} + D2_{v1i})\frac{\partial C}{\partial x_i}\right\} - \frac{1}{A}\frac{\partial}{\partial x_1}\left\{\int_{-b_1}^{b_2} d(D2_{t1i} + D2_{v1i})\frac{\partial C}{\partial x_i} dx_3\right\} \\
&+\frac{1}{d}\frac{\partial}{\partial x_1}\left\{d(D2_{t1i} + D2_{v1i})\frac{\partial c'_{03}}{\partial x_1}\right\} - \frac{1}{A}\frac{\partial}{\partial x_1}\left\{\int_{-b_1}^{b_2} d(D2_{t1i} + D2_{v1i})\frac{\partial c'_{03}}{\partial x_i} dx_3\right\} \\
&+\frac{1}{d}\frac{\partial}{\partial x_3}\left\{d(D2_{t3i} + D2_{v3i})\frac{\partial c'_{03}}{\partial x_i}\right\}
\end{aligned} \tag{3.5.32}$$

Simplifying Eq. 3.5.32 under the following assumptions;
for transport of C in the x_1 direction,

$$u'_{03}C \gg (D2_{t1i} + D2_{v1i})\frac{\partial C}{\partial x_i} - \frac{1}{A}\frac{\partial}{\partial x_1}\left\{\int_{-b_1}^{b_2} d(D2_{t1i} + D2_{v1i})\frac{\partial C}{\partial x_i}dx_3\right\} \tag{3.5.33}$$

for transport of c'_{03} in the x_1 direction,

$$\begin{aligned} U c'_{03} &\gg u'_{03}c'_{03} - \frac{1}{A}\int_{-b_1}^{b_2} u'_{03}c'_{03}ddx_3 \\ &\gg (D2_{t1i} + D2_{v1i})\frac{\partial c'_{03}}{\partial x_i} - \frac{1}{A}\frac{\partial}{\partial x_1}\int_{-b_1}^{b_2} d(D2_{t1i} + D2_{v1i})\frac{\partial C}{\partial x_i}dx_3 \end{aligned} \tag{3.5.34}$$

for transport of c'_{03} in the x_3 direction,

$$(D2_{t3i} + D2_{v3i})\frac{\partial c'_{03}}{\partial x_i} \equiv D2_{3i}\frac{\partial c'_{03}}{\partial x_i} \gg \bar{u}_3^{x_2}c'_{03} \tag{3.5.35}$$

leads to

$$\frac{\partial c'_{03}}{\partial t} + U\frac{\partial c'_{03}}{\partial x_1} = -u'_{03}\frac{\partial C}{\partial x_1} + \frac{1}{d}\frac{\partial}{\partial x_3}\left\{dD2_{3i}\frac{\partial c'_3}{\partial x_i}\right\} \tag{3.5.36}$$

where $D2_{ij} = D2_{tij} + D2_{vij}$. Assuming also the "Frozen Convection of c'_{03}" by the cross-sectional mean velocity U, Eq.3.5.36 is reduced to be:

$$\frac{1}{d}\frac{\partial}{\partial x_3}\left(dD2_{3i}\frac{\partial c'_{03}}{\partial x_i}\right) = u'_{03}\frac{\partial C}{\partial x_1} \tag{3.5.37}$$

Assuming the principal axes of the diffusion and 2-D dispersion coefficient tensor are in the x_1 and x_2 directions, the solution of Eq. 3.5.37 is obtained by integrating Eq. 3.5.37 with respect to x_3 twice as:

$$\left[dD2_{33}\frac{\partial c'_{03}}{\partial x_3}\right]_{x_3=-b_1}^{x_3=x_3} = \frac{\partial C}{\partial x_1}\int_{-b_1}^{x_3} u'_{03}ddx_3 \tag{3.5.38}$$

$$\frac{\partial c'_{03}}{\partial x_3} \Big/ \frac{\partial C}{\partial x_1} = \frac{1}{dD2_{33}}\int_{-b_1}^{x_3} u'_{03}ddx_3 \tag{3.5.39}$$

$$c'_{03} \Big/ \frac{\partial C}{\partial x_1} = \int_{-b_1}^{x_3}\frac{dx'_3}{dD2_{33}}\int_{-b_1}^{x'_3} u'_{03}ddx''_3 + \left[c'_{03} \Big/ \frac{\partial C}{\partial x_1}\right]_{x_3=-b_1} \tag{3.5.40}$$

Substituting Eq. 3.5.40 into Eq. 3.5.26, which is the definition of D_{El},

$$D_{El} \equiv -\int_{-b_1}^{b_2} u'_{03}c'_{03}dx_3 \Big/ A\frac{\partial C}{\partial x_1} \tag{3.5.26}$$

D_{El} is calculated as:

$$D_{El} = -\frac{1}{A}\int_{-b_1}^{b_2} u'_{03}dx_3\int_{-b_1}^{x_3}\frac{dx'_3}{dD2_{33}}\int_{-b_1}^{x'_3} u'_{03}ddx''_3 \tag{3.5.41}$$

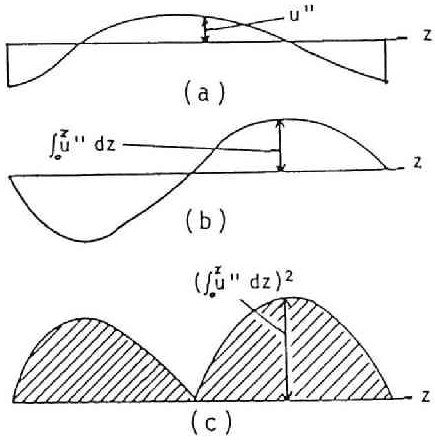

Figure 3.5.3: (a) The lateral distribution of the depth–averaged velocity, (b) $\int_0^z u'_{03}dz$, and (c) I_A

$$D_{El} = \frac{1}{A}\int_{-b_1}^{b_2} \frac{dx'_3}{dD2_{33}} \left[\int_{-b_1}^{x'_3} u'_{03} dx_3\right]^2 \tag{3.5.42}$$

Eq. 3.5.42 is rewritten in non-dimensional form as:

$$\frac{D_{El}}{\bar{d}u_*} \simeq \frac{I_A}{\theta_3}\left(\frac{U}{u_*}\right)^2\left(\frac{B}{\bar{d}}\right)^2 \tag{3.5.43}$$

$$I_A \equiv \frac{1}{B^3U^2}\int_{-b_1}^{b_2}\left[\int_0^z (\bar{u}_1^{x_2} - U)\,dz\right]^2 dx_3 \tag{3.5.44}$$

where $\bar{d} \equiv A/B$ and I_A represents the intensity of the lateral non-uniformity of the distributions of $\bar{u}^{x_2}$ (See Fig. 3.5.3), and the assumption of $D2_{33} = \theta_3 du_*$ is introduced.

As shown in Eq. 3.5.43, D_{El} is the function of the velocity factor U/u_*, the width to depth ratio B/d and the average turbulent diffusion coefficient θ_3.

Thus, the dispersion coefficient D_E is obtained as:

$$\begin{aligned} D_E &= D_{Et} + D_{Ev} + D_{El} \\ &= \frac{1}{A}\int_A \varepsilon_1 \frac{\partial \bar{c}}{\partial x_1} \Big/ \frac{\partial C}{\partial x_1} + \frac{1}{A}\int_{-b_1}^{b_2} dD2_{33}\frac{\partial \bar{c}^{x_2}}{\partial x_3} dx_3 \Big/ \frac{\partial C}{\partial x_1} + \end{aligned}$$

$$\frac{1}{A}\int_{-b_1}^{b_2}\frac{dx_3'}{dD2_{33}}\left[\int_{-b_1}^{x_3'}u_3'ddx_3\right]^2 \tag{3.5.45}$$

The estimated value for D_{Ev} is

$$D_{Ev}\approx 5 \text{ to } 15 \tag{3.5.46}$$

and that for D_{Et}

$$D_{Et}\approx 1.0 \tag{3.5.47}$$

3.6 Conclusions

In this chapter, the mechanism of the longitudinal dispersion phenomena in shear flows and the longitudinal dispersion coefficient was investigated theoretically in view of the Eulerian turbulent diffusion equation by using the results obtained in **Chapters 2** and **4**. The flows mainly concerned are 3–D turbulent shear flows, and especially open-channel flows in wide rectangular cross-section laboratory flumes and natural streams.

The objectives of the study in this chapter were stated in **Section 3.1**. In **Section 3.2**, the previous theoretical studies on the dispersion coefficient based on the turbulent diffusion equation were reviewed, and the assumptions used in Taylor, Elder, and Fischer's modeling were summarized. In **Section 3.3**, the 3-D turbulent diffusion equation, 1-D convective dispersion equation, and the definition of the longitudinal dispersion coefficient were stated in the orthogonal curvilinear coordinate system. The mathematical theory of the dispersion coefficient which was initiated by Taylor and applied to various flows by other investigators was presented in more general form by use of the 3-D turbulent diffusion equation in the orthogonal curvilinear coordinate system in **Section 3.4**. The major component of the dispersion coefficient D_{Evl} was derived as:

$$D_{Evl}=\frac{1}{A}\int_{x_{2a}}^{x_{2b}}\frac{dx_2}{\varepsilon_2 s}\left[\int_0^{x_2}u_1''(x_2')\frac{dA_1}{dx_2}dx_2'\right]^2 \tag{3.4.20}$$

It was proved that Eq. 3.4.20 gives the same (equivalent) result as (to) each of Taylor (1953), Taylor (1954), Elder (1956), and Fischer (1966). The distinguishable features of Fischer's modeling from others were also discussed in terms of the mixing time scale, and it was suggested that the longitudinal dispersion can be modeled in terms of 2-D plain phenomena in wide open-channel flows, but should be done in terms of 3-D phenomena in ordinary laboratory flumes.

In **Section 3.5**, the locally time-averaged velocity and concentration were respectively decomposed into three components, that is, the cross-sectional averaged values,

the deviation of the depth-averaged values from the cross-sectional values, and the deviation of the locally temporal averaged-values from the depth averaged values. The dispersion coefficient in 1-D models are also decomposed into three components,

$$D_E = D_{Et} + D_{Ev} + D_{El} \tag{3.5.45}$$

that is, the Eulerian turbulent diffusion term, the dispersion caused by the vertical non-uniformity of the velocity distributions, and the dispersion caused by the lateral non-uniformity of the velocity distribution. These three components of the dispersion coefficient were discussed and investigated in detail, and finally the dispersion coefficient in 1-D models was obtained. D_{El} is written as:

$$D_{El} = \frac{1}{A}\int_{-b_1}^{b_2} \frac{dx_3'}{dD2_{33}} \left[\int_{-b_1}^{x_3'} u_{03}' dx_3\right]^2 \tag{3.5.42}$$

$$\simeq \frac{I_A}{\theta_3}\left(\frac{U}{u_*}\right)^2 \left(\frac{B}{\bar{d}}\right)^2 du_* \tag{3.5.43}$$

and equivalent to Fischer's formula. D_{El} is dependent on B/d and the major component of Eq. 3.5.45 in wide open-channel flows in laboratory and natural streams, but the magnitude of D_{Ev} is estimated to be of the same order in ordinary laboratory flumes.

Chapter 4

EXPERIMENTAL STUDY ON LONGITUDINAL DISPERSION IN LABORATORY FLUMES

4.1 Introduction, Objectives and Design of Experiment

A lot of experimental works on the longitudinal dispersion coefficient in various flows have been made since Taylor (1953), however most of them were conducted with the flumes which had not enough length required for the complete transverse mixing. Fischer (1966) made excellent measurements of the dispersion coefficient in wide rectangular flumes and trapezoidal-section flumes, but his series of experiments with rectangular flumes do not satisfy the length scale of Eq. 2.2.39 required for the transverse mixing. His another series of experiments with trapezoidal flumes satisfies the length scale but velocity distributions were artificially distorted by stone roughness in channel sides. Therefore his two kinds of series of experiments do not give the enough information for verifying the theoretical results given in **Chapters 2** and **3**. Michiue, Muramoto and Itami (1978) made experiments with a rectangular cross-section flume of 150m in length. Their experiments satisfy the length scale and they showed that Elder's result of Eq. 3.4.24 is not acceptable in the open-channel flows, however they were not concerned with the influence of the hydraulic characteristics of flow, that is, the width to depth ratio, the bottom roughness, the lateral velocity distributions and so on.

It should also be noted that almost all experimental works directed to measure only the dispersion coefficient. And the time-dependent behavior of tracer clouds or the behaviors of the moment characteristics of the cross-sectional average concentration which are investigated in **Chapter 2** have not yet been verified. Therefore,

detailed measurements of cross-sectional averaged concentration at many sections in the flow direction are required in order to verify the theoretical results obtained in **Chapters 2** and **3**.

Experimental study of measuring the concentration-time curves at fixed points was conducted to investigate the three primary subjects:

1. to disclose the characteristics of time-dependent behavior of tracer clouds in the whole region from the insertion point of tracer to the fully developed region;

2. to disclose the behavior of the second central moment and the effect of flow characteristics on the dispersion coefficient which is closely related with the second moment and the most important parameter in the mixing phenomena, and

3. to verify the theoretical results for the dispersion coefficient obtained in **Chapters 2** and **3**.

The experiments of 19 runs were conducted with two flumes by adjusting the slope, the width, the bottom roughness and the discharge. The experiments have following notable characteristics to accomplish the subjective stated earlier:

1. Two rectangular cross section flumes of 10m or 37m in length are used: they have the large length to width ratio L/B which is more than 80, so that all series of experiments are satisfied with the length scale of the longitudinal mixing of Eq.2.2.39.

2. 19 series of the experiments are designed to cover the wide range of the width to depth ratio B/d and the velocity factor U/u_*.

3. Concentration is directly measured with a conductivity-meter by inserting the small sensors simultaneously in the flow at several selected points in a section and this is done at many sections in the flow direction. An average concentration-time curve is calculated by the weighted averaging method for concentration-time curves measured at the selected points in a section.

4. The velocity distributions also obtained by measuring the flow velocity at 40 to 100 points in a section by use of a propeller or a hot-film anemometer in the same flow condition of concentration measurement.

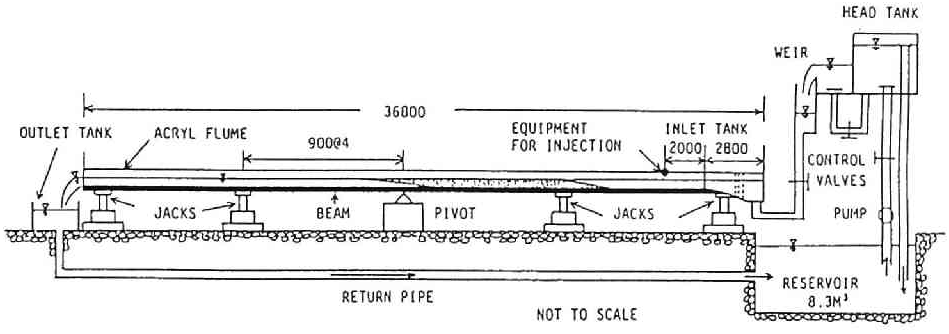

Figure 4.2.1: Schematic illustration of Flume B.

4.2 Experimental Apparatus and Method

4.2.1 Experimental Apparatus

(1) Flumes and Measuring the Basic Hydraulic Variables

Laboratory experiments were conducted in the Hydraulic Laboratory located at the basement of the Civil Engineering Building, Kyoto University. They were done in two recirculating rectangular cross-section flumes, identified as Flume A and Flume B. The slope of both flumes are adjustable by hinge and jack supporting systems.

Flume A:

Five preliminary series were conducted in Flume A made by duralumin and its dimensions are 10m in length and 0.25m in width. In experiments the width was made narrower at 0.1m in width using the painted plywood, so that it satisfies the length scale.

Flume B:

14 series were made in Flume B of 37m in length and 0.40m in width. It is made by lucid aclyl board, so that they can observe the dyed tracer behavior from its side and bottom. In experiments the width were adjusted at 0.10, 0.20 and 0.25m by painted square-lumber steel. A schematic diagram of Flume B is illustrated in Fig. 4.2.1.

Bottom roughness:

Both flumes have hydraulically smooth side and bottom. 13 runs were conducted in the flume with smooth bottom and 6 runs with rough bottom. Three kinds of the bottom roughness are adjusted by 0.001m diameter glass beads roughness in experiments identified as Run RA Series and two kinds of sand roughness in experiments

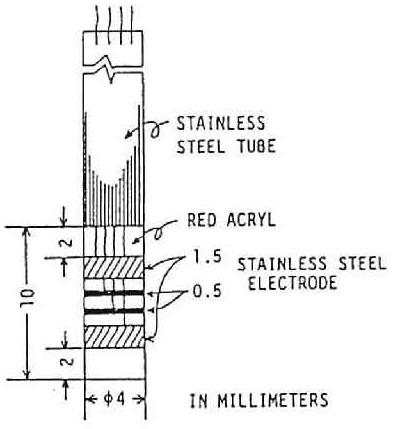

Figure 4.2.2: Conductivity-probe.

identified as Runs RB and RC Series. Equivalent roughness height is 0.001 m in Series RA. Roughness made by sand sorted out with 0.00314m and 0.00476m sieves was used in Run RB Series, and 0.00193m and 0.00314m sieves in Run RC Series. Each equivalent sand roughness height is 0.0025m in Run RB Series and 0.00149m in Run RC series. It was determined by the similar method used by Taylor(1954).

Flow discharge:

In both flumes, selected discharge is adjusted by the control valves situated at the upper part of a inlet tank. Discharge was measured by a triangular-shape weir or directly done.

Flow depth:

Flow depth was measured by a point gauge at three points in each section at every 0.5m to 1.0m in the flow direction. In case of determining the depth of the flow over rough bottom, an average depth was calculated by subtracting the equivalent roughness height from the results of direct depth measurements by a point gauge.

(2) Concentration Measurement

The tracer used for quantitative measurement in the laboratory was salt solution, whose density was adjusted to unity by addition of methanol. Concentration of salinity of tracer cloud was measured by the conductivity- meter (KENEK MA106), conductivity-probes (KENEK MTK-50-04) and a pen-recorder (WATANABE MC611). The system can simultaneously measure the concentration at six points.

Fig. 4.2.2 illustrates the design of the conductivity-probes. The main tube made by stainless steel is 0.5m long and its diameter 0.004 m. At the lower end of the main

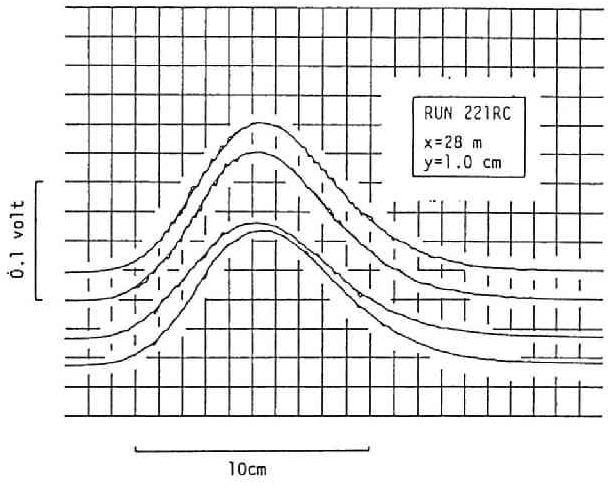

Figure 4.2.3: Examples of recorded out-put from the conductivity-meter.

tube, four electrodes were mounted on a cylinder made by aclyl plastic. Conductivity-probe can make in-place measurements with less effect on the flowing water, and is sufficiently sensitive and accurate in case they are located at 0.01m far each other and 0.005m far from channel side or bottom.

Typical examples of conductivity (voltage)-time curves recorded on the paper by use of this system are shown in Fig. 4.2.3. Paper speed and gain were adjusted, so that enough resolution for the time and the out-put voltage were obtained for digitizing them by the direct method. They have fluctuations caused by concentration fluctuation associated with turbulent motion of the flow, therefore original curves were manually transformed into smooth ones and digitized at more than 30 points. The time interval for digitizing was constant in a sub-run at a selected section, but different between sub-runs at different sections. It was decided by the valid period of conductivity-measurements.

The values of conductivity were transformed into salinity concentration through calibration curves, which were made in a calibration test in beakers before or after in-place measurement.

(3) Velocity Measurement

The local time-averaged velocity was measured by the anemometer of 0.005m diameter propeller (KENEK VA403) identified as Anemometer P or a hot-film anemometer

(DISA 55M System) with use of a conical type probe (55R42) or cylindrical probe (55R41) identified as Anemometer H. Both velocity measurement systems were calibrated in the velocity calibration tank located at Ujigawa Hydraulic Laboratory, Disaster Prevention Research Institute, Kyoto University.

4.2.2 Experimental Method

Tracer was inserted at 1.m downstream from the inlet end of the flume in Flume A and 3.m downstream in Flume B by rotating the trough filled with the salt solution of constant volume. The trough length is little smaller than the width of flume and by this procedure a line source of solution would drop onto the flow in the stream and instantaneous plane insertion of the tracer would be made possible. The volume of tracer solution is adjusted to get enough out-put voltage from the conductivity meter and changed by the flow discharge. The effect of insertion on the stream would be negligibly small.

In one run of experiments for the selected flow condition, concentration was measured at 4 to 5 sections in the flow direction. One sub-run of tracer experiment at a selected section and a selected probe height has more than three times tracer insertions and concentration measurements. The concentration distribution is not uniform in the both depth-wise and transverse directions in the near region from the insertion section, therefore it was measured at three different probe heights in the vertical direction, and more than 9 times tracer insertions were made in one sub-run and the number of measuring position was 15 at maximum. Traveling along the flow direction, the tracer cloud is developed and fully mixed in the depth-wise direction, and therefore it was measured at a half of depth in a section after confirming the concentration distribution is almost uniform in the vertical direction. In all sub-runs, three conductivity-time curves for each probe were selected and used for data processing.

In 14 runs, the three-dimensional velocity distributions were measured by either one of anemometers immediately after concentration measurements or in the similar flow condition on the next day. A measuring section was selected at downstream part from the tracer insertion section. Velocity measurement points were selected in the area of 0.002 to 0.003m above the bottom and 0.003m inner from the channel sides, and the measurement were conducted 3 to 7 points in the vertical direction and 13 to 22 points in the transverse direction. Measuring period is 60. to 120. seconds for each point. Output voltage from the amplifier was recorded on the paper and curves containing the effect of turbulence were manually made smooth ones and directly digitized and converted to the local time-averaged velocity by use of

calibration curves.

4.3 Data Processing and Method of Analysis

4.3.1 Concentration Measurement

In data processing, original curves on the recording paper were made smooth ones and digitized directly at more than 30 points in the time coordinate. Digitized values of conductivity were put into the computer at Data Processing Center, Kyoto University and transformed into concentration-time curves at each measuring point after averaging the values obtained in more than three times tracer insertions. Obtained concentration-time curves contain the effect of background, that is, the conductivity of recirculating water in channels, and this values were subtracted from measured ones. Concentration-time curves observed are quite different from the Gaussian distribution and skewed. They have long tails in falling limb. This part would be quite effective on the magnitude of temporal moments, and the part which has less than 1% of the highest concentration in falling limb was truncuated in the analysis.

(1) Cross-Sectional Averaged Concentration

Cross-sectional averaged concentration was obtained by the weighted averaging method from the concentration obtained at each measuring point in a section and the control area ΔA_i for each point i was used for weight.

$$C(t;x_1) \equiv \frac{1}{A}\int_A \bar{c}(t;x_1,x_2,x_3)dA = \frac{1}{\sum_{i=1}^{n}\Delta A_i}\bar{c}_i\Delta A_i \tag{4.3.1}$$

where $C(t;x_1)$ is the cross-sectional averaged concentration, $\bar{c}_i(t;x_1,x_2,x_3)$ the concentration at a point $\boldsymbol{x}_i(x_1,x_2,x_3)$, ΔA_i the weight(= the control area of the i-th probe), A the sum of weight (= the cross-sectional area), i the probe number ($i=1$ to n), n the total number of measuring points in a section, x_1 the distance from the insertion point, t the time from the tracer insertion.

Normalized concentration-time curves $C_n(t;x_1)$ are commonly used. They are calculated by:

$$C_n(t;x_1) \equiv C \Big/ \int_0^\infty C(t;x_1)dt \tag{4.3.2}$$

and the area under the normalized-concentration-time curve is equal to 1.

(2) Temporal Moment

The zero-th, first, second and third central moments in the time coordinate are defined and calculated by following equations.

a. The zero-th moment: M_0

The zero-th moment is defined and calculated by:

$$M_0(x_1) \equiv \int_0^\infty C(t;x_1)dt = \sum_{i=1}^{n} C(t_i;x_1)\Delta t \tag{4.3.3}$$

where Δt is the time interval equal to 0.2 – 1.0 second. This value is used for calculating the normalized concentration-time curves in Eq. 4.3.2.

b. The first moment: M_1

The first moment is defined and calculated by

$$M_1(x_1) \equiv \int_0^\infty C_n(t;x_1)tdt = \frac{1}{M_0}\sum_{i=1}^{n} C(t_i;x_1)t_i\Delta t \tag{4.3.4}$$

M_1 means the concentration time of the centroid of the tracer cloud from the insertion point, and is sometimes denoted by $\bar{t}$ which indicates the average travel time of the tracer cloud from the insertion point $x_1 = 0$ to the measuring point $x_1 = x_1$.

c. The second central moment: M_2 or ${\sigma_t}^2$

The second central moment is defined and calculated by

$$M_2(x_1) \equiv \int_0^\infty C_n(t;x_1)(t_i - \bar{t})^2dt = \frac{1}{M_0}\sum_{i=1}^{n} C(t_i;x_1)(t - \bar{t})^2\Delta t \tag{4.3.5}$$

M_2 is sometimes denoted by σ_t^2, which is called the variance.

c. The third central moment and the skewness factor: M_3 and S_t

The third central moment M_3 is defined and calculated by

$$M_3(x_1) \equiv \int_0^\infty C_n(t;x_1)(t - \bar{t})^3dt = \frac{1}{M_0}\sum_{i=1}^{n} C(t_i;x_1)(t_i - \bar{t})^3\Delta t \tag{4.3.6}$$

and the skewness factor S_t by

$$S_t \equiv M_3 \Big/ (\sigma_t^2)^{3/2} \tag{4.3.7}$$

In the analysis following, the statistical values for the concentration-time curves $\bar{c}_c$ measured at a center of the flow section, that is, at the point of a half depth and a half width will be sometimes used. They are denoted by subscript c and calculated by Eqs. 4.3.1 to 4.3.7 in which $\bar{c}_c$ is replaced C with.

(3) Dispersion Coefficient

The dispersion coefficient is theoretically defined by

$$D \equiv \frac{1}{2}\frac{d\sigma_x^2}{dt} \tag{4.3.8}$$

as shown in Eq. 2.1.2a. The measurement of $\sigma_x^2(t)$ is quite difficult in hydraulic experiments and Fischer (1966) proposed three different methods determining the dispersion coefficient in experiments; that is, (a) Change of Moment Method, (b) Routing Procedure, and (c) Diffusive Transport Method. In this study, following two or three methods were used.

a. Change of moment method

This method is obtained by Glover (1964) and Fischer(1966) by the temporal moment analysis of the basic 3-D turbulent diffusion equation without any assumption.

$$D_M = \frac{1}{2}U^3\frac{d\sigma_t^2}{dx} \tag{4.3.9}$$

This equation is also obtained from Eq. 3.3.14 directly, assuming that the tracer cloud is convected at the same velocity as the cross-sectional averaged velocity without any deformation of concentration distribution ("Frozen cloud" hypothesis). Dispersion coefficient obtained by this method is denoted by D_M in this study.

b. Routing method

Fischer's Routing Procedure is derived under some assumptions. Therefore the following new routing method was used in this study (Iwasa, Aya, and Kokado, 1978). Assuming the flow is uniform, the convective-dispersion equation derived by the one-dimensional analysis is written (Iwasa, 1976)

$$\frac{\partial C}{\partial t} + U\frac{\partial C}{\partial x_1} = D_R\frac{\partial^2 C}{\partial {x_1}^2} \tag{4.3.10}$$

The solution of Eq. 4.3.10 under the boundary condition;

$$C(t;x_1) = \varphi(t) \quad \text{at} \quad x_1 = x_1' \tag{4.3.11}$$

and

$$\frac{\partial C}{\partial x_1} \to 0 \quad \text{when} \quad x_1 \to \infty \tag{4.3.12}$$

and the initial condition;

$$C(0;x_1) = 0 \quad \text{at} \quad t = 0 \tag{4.3.13}$$

is obtained as:

$$C(t;x_1 - x_1') = \frac{x_1 - x_1'}{2\sqrt{\pi D_R}}\int_0^t \varphi(t-t')\exp\left\{-\frac{(x_1 - x_1' - Ut')^2}{4D_R t'}\right\}\frac{1}{t'^{3/2}}dt' \tag{4.3.14}$$

Therefore, the dispersion coefficient can be determined by comparing the observed concentration-time curve $C_{observed}(t;x_1'')$ at $x_1 = x_1''$ with results $C_{Calculated}(t;x_1'' - x_1')$ calculated by Eq. 4.3.14 by use of $C_{observed}(t;x_1')$ and the dispersion coefficient D_R.

This method consists of two steps. In the first step, the convective velocity of tracer cloud U_c should be determined so that the first moment $\bar{t}$ should satisfy the following relationship

$$U_c = \frac{x_1'' - x_1'}{\bar{t}_2 - \bar{t}_1} \tag{4.3.15}$$

In the second step, the dispersion coefficient could be determined so that the peak concentration in calculated concentration-time curve is equal to that in the observed concentration-time curve. This method is called Routing Method and the dispersion coefficient determined is denoted by D_R. (Recently the author has known that Yotsukura and Kilpatrick (1973) proposed the same method).

c. Peak concentration method

The third method used in this study is called Peak Concentration Method (Iwasa, Aya, Kokado, 1978). In Eq. 4.3.14, the peak concentration C_{nP} is written in the form of

$$C_{nP}{}^2 = \frac{1}{4}\left(\frac{U^2}{\pi D}\right)\frac{1}{t_P} \qquad \text{when} \quad t \to \infty \tag{4.3.16}$$

where t_P is the time when the C_{nP} is observed at a measuring section. Therefore the dispersion coefficient D_P is given by

$$D_P = \frac{U^2}{4\pi}\frac{d}{dt_P}C_{nP}{}^2 \tag{4.3.17}$$

4.3.2 Velocity Measurement

From the locally time-averaged velocity at many points in a section, the cross-sectional averaged velocity U_i and the depth-averaged velocity $\bar{u}_1^{x_2}$ are obtained by following relationships.

Cross-sectional averaged velocity: U_i

$$U_i = \frac{1}{\sum_{i=1}^{n}\Delta A_i}\sum_{i=1}^{n}\bar{u}_{1i}(t; x_1, x_2, x_3)\Delta A_i \tag{4.3.18}$$

Depth averaged velocity: $\bar{u}_1^{x_2}$

$$\bar{u}_1^{x_2} = \frac{1}{\sum_{i=1}^{n}\Delta x_{2_i}}\sum_{i=1}^{n}\bar{u}_{1i}(t; x_1, x_2, x_3)\Delta x_{2_i} \quad \left(d = \sum_{i=1}^{n}\Delta x_{2_i} = \zeta - z_b\right) \tag{4.3.19}$$

The theories stated in **Chapters 2** and **3** disclose that following three parameters for velocity distribution characteristics in a section is closely related with the dispersion coefficient.

The first parameter: J_A

$$J_A \equiv \frac{1}{AU_i^2}\int_A (\bar{u}_1 - U_i)^2 dA \tag{4.3.20}$$

This parameter is related with the dispersion coefficient obtained by the Lagrangian view point in **Chapter 2** and also the momentum coefficient β commonly used in the one-dimensional hydraulic analysis (Fukuoka and Sayre, 1973) as,

$$J_A = \beta - 1 \tag{4.3.21}$$

The second parameter: J_{Al}

This parameter shows the characteristics of the lateral velocity distribution and is also related with the dispersion coefficient in view of the Lagrangian theory in **Chapter 2**.

$$J_{Al} \equiv \frac{1}{(BU_i)^2}\int_{-b_1}^{b_2} (\bar{u}_1^{x_2} - U_i)^2 dx_2 \quad (B = b_2 + b_1) \tag{4.3.22}$$

The third parameter: I_A

This parameter also shows the characteristics of the lateral velocity distribution, but it is related with the dispersion coefficient from the Eulerian view point in **Chapter 3**.

$$I_A \equiv \frac{1}{B^3 U_i^2}\int_{-b_1}^{b_2} \left\{\int_{-b_1}^{x_2} (\bar{u}_1^{x_2} - U_i) dx_2'\right\}^2 dx_2 \tag{4.3.23}$$

4.4 Results

4.4.1 Outlines of Results

Results obtained in all of the laboratory experiments are summarized in Tables 4.4.1, 4.4.2 and 4.4.3. Each experiment in a particular flume at a particular set of hydraulic conditions is termed as a "run"; each insertion of tracer for a selected measuring section under the same hydraulic conditions constitutes a "sub-run"; a sub-run has more than three times tracer insertions. Thus all of the sub-runs in a particular run are made at identical hydraulic conditions although the location of measuring probes may vary between sub-runs.

The first column of Table 4.4.1 shows the run number. 13 runs were made in flumes with smooth side and bottom; 6 runs were made in flumes with smooth side and rough bottom and they were identified by the two alphabetical characters following three numbers of runs. The second column shows the flume used in a series of experiment by A or B. The number of concentration measuring points in a section is shown in the

Table 4.4.1: Summary of experiment.

(1)	(2)	(3)		(4)	(5)	(6)	(7)	(8)	(9)	(10)	(11)	(12)	(13)
Run	Flume	No. of measurement in section		No. of sections	Dimensionless distance $x' = x/UT_{rl}$	Discharge Q (cm³/s)	Width B (cm)	Depth d (cm)	Slope I_e	Velocity U (cm/s)	Shear velocity u_* (cm/s)	Time scale T_{rl} (s)	Dispersion coefficient D_M (cm²/s)
		Max.	Min.										
911	A	1×5	1×5	8	2.23 –17.8	1000	10.0	3.12	1/500	32.2	1.94	1.40	175
912	A	4×5	4×5	5	2.98 –20.9	2210	10.0	5.02	1/500	44.1	2.21	.761	106
913	A	1×5	1×5	10	1.50 –10.5	562	10.0	2.05	1/500	27.4	1.69	2.44	165
111	B	3×3	1×3	13	1.66 –43.2	643	10.0	2.27	1/500	28.3	1.75	2.13	114
112	B	1×3	1×3	4	16.7 –26.3	294	10.0	1.37	1/500	21.5	1.45	4.25	137
921	B	4×5	1×5	15	.304– 8.83	2450	25.0	2.69	1/456	36.5	2.18	9.00	270
121	B	3×5	3×5	14	.247– 7.17	805	20.0	1.46	1/500	27.6	1.58	14.6	214
122	B	1×5	1×5	14	.429– 6.22	530	20.0	1.19	1/500	22.3	1.44	20.9	194
123	B	1×5	1×5	6	2.32 – 8.42	933	20.0	1.49	1/300	31.3	2.06	11.0	307
124	B	1×5	1×5	6	2.90 –10.5	1500	20.0	1.99	1/300	37.6	2.33	7.28	316
125	B	1×3	1×3	6	1.41 – 6.83	1470	20.0	1.43	1/150	51.4	2.86	8.26	585
221	B	3×5	1×5	12	.888–12.9	1760	20.0	2.57	1/514	34.3	1.97	6.57	266
222	B	3×4	1×4	8	7.75 –18.7	3960	20.0	4.23	1/514	46.8	2.38	3.31	328
111RA	A	1×3	1×3	4	12.5 –15.7	513	10.0	2.23	1/500	23.0	1.74	2.08	86.6
112RA	A	1×3	1×3	4	10.3 –12.9	169	10.0	1.31	1/500	12.9	1.43	4.51	170
121RB	B	3×5	1×5	7	3.18 –22.3	667	20.7	2.13	1/500	15.1	1.86	8.33	144
122RB	B	3×5	1×5	8	1.64 –19.7	1140	20.7	2.67	1/500	20.6	2.04	5.92	194
221RC	B	3×4	1×4	10	1.60 –22.3	1080	20.3	2.68	1/514	19.8	2.01	6.33	129
222RC	B	3×4	1×4	10	1.41 –19.8	699	20.3	2.13	1/504	16.2	1.85	8.74	122

(3) (No. in vertical direction)×(No. in lateral direction)

(10) $U = Q/A$

(11) $u_* = \sqrt{gRI_e}$

(12) $T_{rl} = B^2/(4.14.8 \cdot 0.4 u_*)$

3rd column and the number of sections selected for concentration measurements in a run in the 4th column. The number of concentration measuring points in a section may vary between sub-runs in a run and the maximum and minimum numbers of measuring points in a section are listed in the sub-columns of the 3rd column. In the near region from the insertion section the concentration was measured at more than one vertical positions, and in the far region it was done at only a half depth in almost all of runs. And in every sub-runs it was done at more than 3 points in the lateral direction. The longest and shortest distances of the measuring section from the insertion section are listed in the 5th column. They are shown in the non-dimensional form with use of the cross-sectional average velocity $U_d(= Q/A)$ and the time scale of transverse mixing defined by

$$T_l = \frac{1}{14.8\varepsilon_3}\left(\frac{B}{2}\right)^2 \tag{4.4.1}$$

where B is the width and ε_3 the transverse diffusion coefficient. Eq. 4.4.1 is equivalent to the Fisher's integral time scale as shown in Chapter 2. In all experiments, the transverse mixing coefficient was not measured, and the relationship of

$$\varepsilon_3 = 0.2du_* \tag{4.4.2}$$

is used. T_l is mainly influenced by the width, therefore it is much smaller in the runs conducted in the 10cm wide channel than those in the wider channels. The longest dimensionless distance of a measuring section in a run is more than 6 throughout runs. The selected width is 10.0, 20.0, and 25.0cm and the depth is adjusted by selecting the flow discharge but the slope of the flume is about 1/500 in most of all series. The shear velocity listed in the 11th column is calculated by

$$u_* = \sqrt{gRI_e} \tag{4.4.3}$$

where R is the hydraulic radius and I_e the energy slope. The dispersion coefficient obtained by the moment method D_M are listed in the 13th column.

Thus, the experiments in the hydraulic condition of the wide range of the width to the depth ratio and the velocity factor could be made. These non-dimensional hydraulic variables and the dispersion coefficient obtained by the three method stated earlier are summarized in Table 4.4.2.

The width to depth ratio varies from 1.99 up to 16.8 and the velocity factor from 8.1 to 20.0. The non-dimensional dispersion coefficient varies from 9.56 up to 126., and it is not constant even in a rectangular cross-section flume but widely varies according to the hydraulic conditions.

Table 4.4.2: Dimensionless hydraulic variables and dispersion coefficient.

(1)	(2)	(3)	(4)	(5)	(6)		
Run	Aspect Ratio B/d	Velocity Factor U/u_*	Reynolds Number $Re.$	Froude Number $Fr.$	Dispersion Coefficient D_x/du_*	D_*/du_*	D_r/du_*
911	3.21	16.5	9560	.580	28.9	13.2	18.0
912	1.99	20.0	19400	.630	9.56	3.60	8.5
913	4.88	16.2	4700	.710	47.6	14.4	26.4
111	4.41	16.2	4420	.600	28.6	25.0	26.6
112	7.30	14.8	2320	.586	69.0	45.3	53.4
921	9.29	16.7	8380	.710	46.0	27.2	36.6
121	13.7	17.4	3090	.642	92.8	43.4	62.0
122	16.8	15.5	2360	.652	113.	69.9	92.0
123	13.4	15.2	4070	.819	100.	52.1	75.9
124	10.1	16.2	6270	.856	68.1	51.7	61.6
125	14.0	18.0	6430	1.37	126.	45.2	201.
221	7.78	17.4	8820	.683	52.5	—	—
222	4.73	19.7	19800	.727	32.6	—	—
111RA	4.48	14.1	3540	.492	22.3	12.8	18.6
112RA	7.63	11.3	1340	.360	90.7	34.7	56.0
121RB	9.71	8.12	3220	.331	36.3	—	—
122RB	7.75	10.5	5500	.403	35.6	—	—
221RC	7.56	9.85	5310	.382	23.9	—	—
222RC	9.50	8.75	3450	.355	31.0	—	—

4.4.2 Concentration Distribution

Figs. 4.4.1 (a), (b) and (c) show the typical examples of the concentration-time curves measured in Run 121.

Figs. 4.4.1 (a)(1) and (2) are results measured in the section 4.00m downstream from the tracer insertion section. Fig. 4.4.1 (a)(1) shows the depth-averaged concentration curves in three vertical lines and a cross-sectional averaged one. Fig. 4.4.1 (a)(2) shows the concentration-time curves at three points in the vertical direction near the center line of the flume. The features of concentration distributions are described as:

–the concentration distribution in the vertical direction is rather uniform, and

–a little bit variation from the depth-averaged mean concentration is observed, however,

–the concentration distribution in the transverse direction is non-uniform, and the spatial variation from the cross-sectional mean concentration is quite larger.

It is also known that all concentration-time curves observed is neither symmetrical nor Gaussian but skewed; the travel time of peak concentration t_P is shorter than the mean travel time of tracer cloud $\bar{t}$ in each curve. The mean travel time in the depth-averaged concentration-time curve is different each other; the one measured

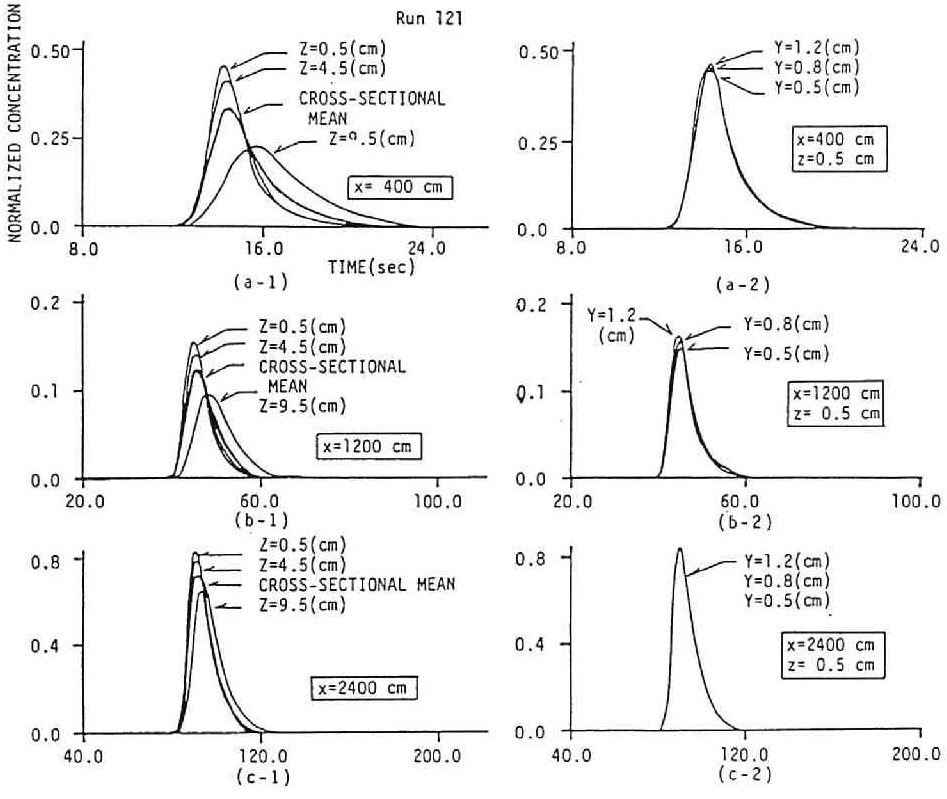

Figure 4.4.1: Concentration distributions measured at several points in Run 121. (a)(1) Depth/cross-sectional-averaged concentrations at a section x_1 = 400cm, (2)Concentrations at several points in a line at x_1 = 400cm and x_3=0.5cm, (a)(1) Depth/cross-sectional-averaged concentrations at a section x_1 = 1200cm, (2)Concentrations at several points in a line at x_1 = 1200cm and x_3=0.5cm, (c)(1) Depth/cross-sectional-averaged concentrations at a section x_1 = 2400cm, (2)Concentrations measured at several points in a line at x_1 = 2400cm and x_3=0.5cm.

near the center of the flume is shorter than that near the channel side. It may reflect the velocity distribution.

In Figs. 4.4.1 (b)(1) and(2) showing the results at the section 12.00m downstream from the tracer insertion section, nearly the same description for the concentration distribution can be made as those from Figs. 4.4.1 (a)(1) and(2).

The concentration distribution in the section 24.00m downstream is a little different from those in the former two sections. The concentration distribution in the vertical direction is quite uniform as shown in Fig. 4.4.1 (c)(1), and that in the transverse direction is also uniform, but the distinguishable spatial variation still exists.

These results from the measured concentration-time curves, the observation and the photos taken during the experiment can make the following image sketches of Figs. 4.4.2 (a), (b), (c) and (d), and the descriptions for the development of tracer cloud.

1. The tracer injected at a insertion section is distributed uniformly in the entire section (Fig. 4.4.2 (a)).

2. The tracer is transported by the flow whose convective velocity is different and dependent on the position of tracer in a section. In this process, the high speed core region of the flow transports the tracer fast and the tracer near the channel bottom and sides is transported slowly. These spatial variation of velocity makes the tracer stretched and the concentration distribution three-dimensionally non-uniform (Fig. 4.4.2 (b)). In the earlier stage of this process, the transverse distribution of the concentration near the center region of the flow may be uniform, because the velocity distributions are two-dimensional and uniform in the transverse direction in the center region of the channel in a wide flume.

3. The turbulent mixing in the vertical direction causes the depth-wise concentration distribution uniform again (Fig. 4.4.2 (c)). The time scale of mixing in the vertical direction is much smaller than that in the transverse direction, therefore the concentration distribution becomes uniform in the vertical direction at first. Figs. 4.4.1 (a)(1) and (b)(1) show this process. This process can also be illustrated in the both of rising and falling edges of the developed tracer cloud in Fig. 4.4.2 (d).

4. The weak transverse variation of velocity can also stretch the tracer and make the transverse non-uniformity of the concentration distribution stronger. This

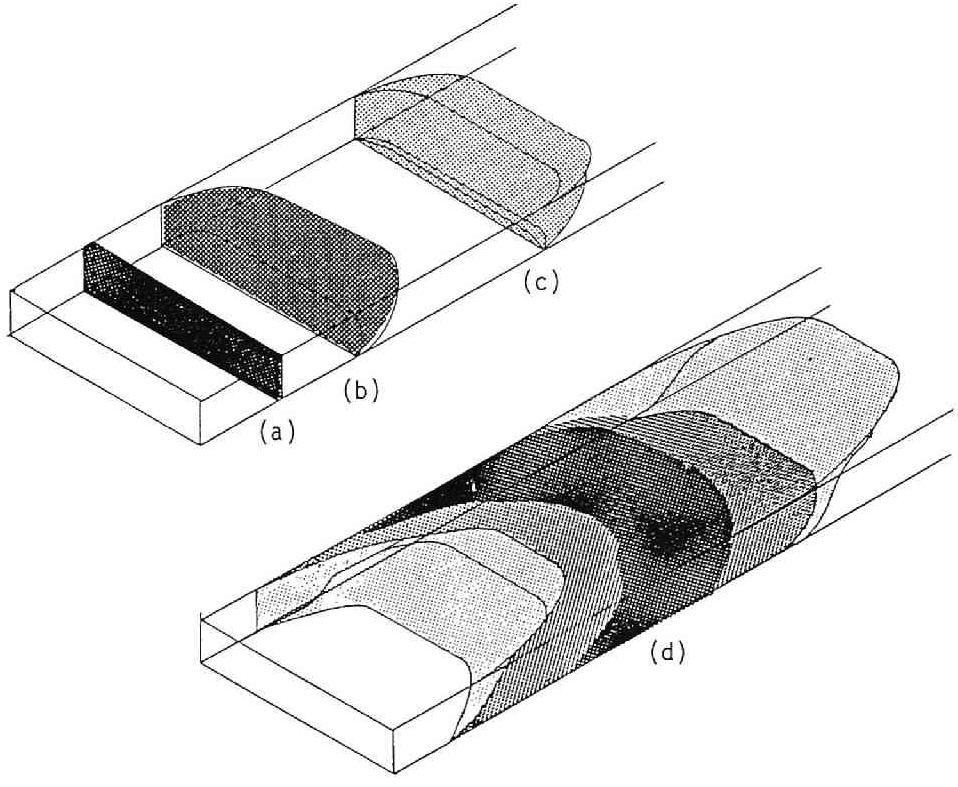

Figure 4.4.2: Development of tracer cloud dispersion instantaneously inserted in wide 3-D open-channel flows as a plane source. (a) Tracer cloud just after the insertion, (b) Tracer stretched by the velocity non-uniformly distributed; concentration distributions are quite three dimensional. (c) Development of tracer dispersion in early stage; 2-D concentration distribution is established in the vertical direction near the center region of the flows, (d) Fully developed tracer cloud in 3-D space; tracer is stretched in the vertical and lateral direction, and the concentration distributions in the the core of cloud becomes more uniform by vertical and lateral diffusion.

effect becomes more important as the tracer travels much farther from the insertion section, because it takes much time for the tracer to be stretched by this weak transverse velocity variation. Thus the concentration distribution becomes uniform in the vertical direction but non-uniform in the transverse direction. This process is shown in Figs. 4.4.1 (a) and (b).

5. Finally the concentration distribution becomes uniform in both of the vertical and the transverse directions by the effect of the transverse mixing as shown in Fig. 4.4.1 (c). The time scale of transverse mixing is much larger in a wide channel and the non-uniform distribution in the transverse direction disappears very very slowly.
   The image of fully developed tracer cloud is illustrated in Fig. 4.4.2 (d). Its concentration distribution can be described as follows; in the top and end edges of the tracer cloud, the concentration distribution is three dimensional; in inner parts from both edges it is uniform in the vertical direction but non-uniform in the transverse direction. Fig. 4.4.1 (c) describes the distribution only in inner parts and this parts becomes longer, as tracer flows down. .

4.4.3 Temporal Moments and Peak Concentration

(1) The First Moment

The transformation of the probability variable x to t by $x = Ut$ derives

$$\bar{t} = \bar{x}/U \tag{4.4.4}$$

Fig. 4.4.3 makes the comparison between observed and measured $\bar{t}$ on a logarithmic sheet and they are in non-dimensional form by use of T_l defined by Eq. 4.4.1. It is clear that Eq. 4.4.4 is established in all runs. Therefore, the convection velocity of the centroid of the tracer cloud is concluded to be equal to the discharge velocity U_d.

Thus, the theoretical result of Eq. 2.2.14 is verified, and it is disclosed that the transformation of the coordinate system:

$$\xi = x - Ut$$

used in the theory in **Chapter 3** is equivalent to describe the phenomena at the centroid which moves at the velocity U, and to describe the behavior of the central moments in view of the statistical movements of a particle in **Chapter 2**.

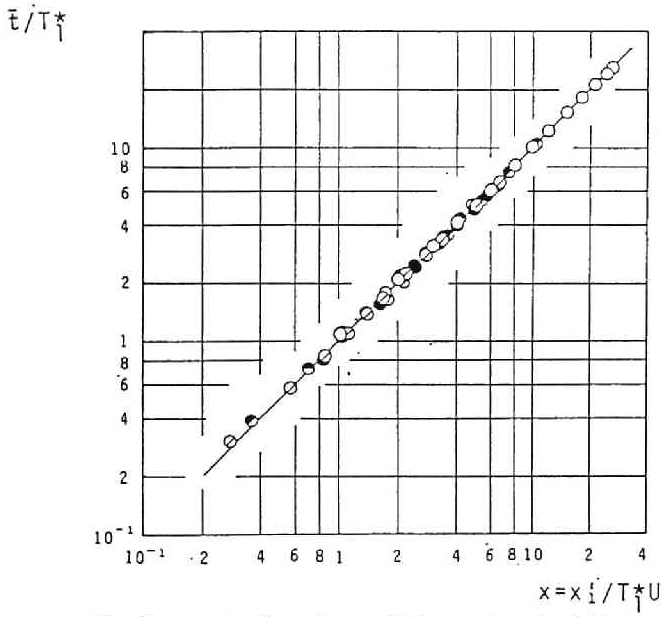

Figure 4.4.3: Concentration time of the centroid of the tracer cloud $\bar{t}/T_l^*$ and the distance x_1/T_l^*U.

(2) The Second Central Moment

As described in Eq. 2.1.1 in **Chapter 2**, σ_x^2 is stated by use of the turbulent intensity $[v_1'^2]$ and the Lagrangian auto-correlation function $R_L(t)$. Assuming $R_L(t) = \exp(-t/T_{SL})$, by use of the transformation of Eq. 4.4.4, σ_t^2 is written in the form of:

$$\frac{\sigma_t^2}{2J_A T_{SL}^2} = \exp(-\chi) + \chi - 1 \tag{4.4.5}$$

where χ is the non-dimensional distance defined by:

$$\chi \equiv x_1/UT_{SL} \tag{4.4.6}$$

and T_{SL} is determined by use of Eq. 2.2.35 as:

$$T_{SL} = D_M/J_A U^2$$

where the effect of Eulerian turbulence is neglected.

Observed σ_t^2 and those obtained by Eq. 4.4.5 are plotted against χ in Fig. 4.4.4 on a logarithmic sheet. It is disclosed that Eq. 4.4.4 gives smaller values than observed ones, but not-bad agreement with observed ones for $\chi > 40$. Further discussion on the behavior of the second central moment will be shown in **Section 4.5**.

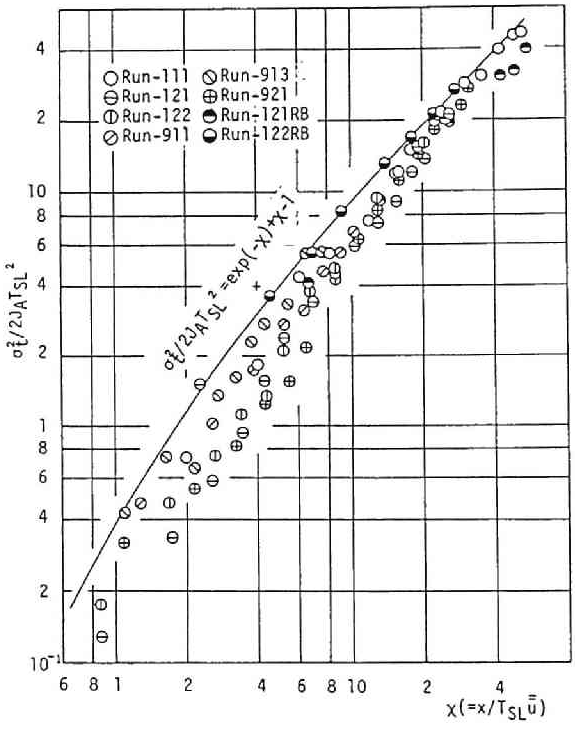

Figure 4.4.4: Variances measured and calculated by Eq. 4.4.5 at several sections.

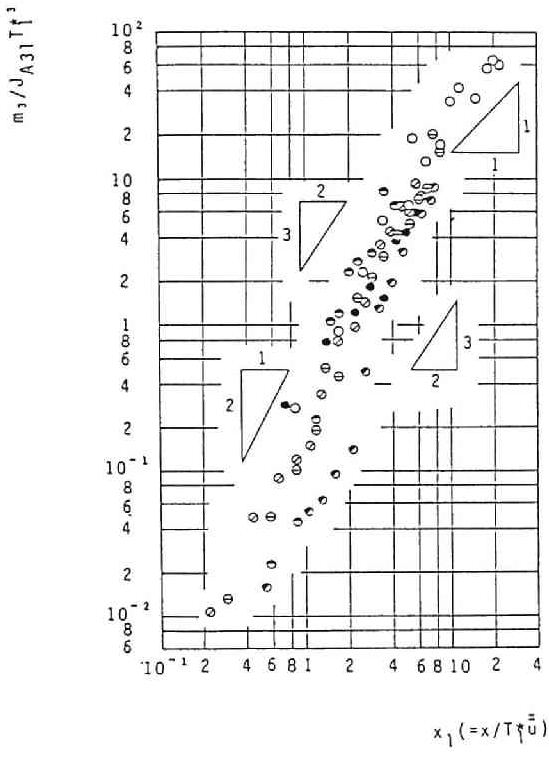

Figure 4.4.5: Third central moment measured at several sections.

(3)The Third Central Moment and Skewness Factor

The third central moment in non-dimensional form $M_3/J_{A3l}T_{SL}^3$ are plotted against χ on a logarithmic sheet in Fig. 4.4.5, where

$$J_{A3l} \equiv \frac{1}{A}\int_A \left(1 - \frac{\bar{u}_1^{x_2}}{U}\right)^3 dA \tag{4.4.7}$$

It is disclosed that

$$\frac{M_3}{J_{A3l}T_{SL}^3} \propto \begin{cases} \chi^2 & \text{for} \quad \chi < 1.5 \\ \chi^{1.5} & \text{for} \quad 1.5 < \chi < 8. \\ \chi & \text{for} \quad 8.0 < \chi < 1.5 \end{cases} \tag{4.4.8}$$

The skewness factor S_t is also plotted against χ on a logarithmic paper in Fig. 4.4.6, and it is disclosed:

$$S_t \begin{cases} \approx 1 \sim 3 & \text{for} \quad \chi < 8 \\ \propto \chi^{-1/2} & \text{for} \quad 8 < \chi \end{cases} \tag{4.4.9}$$

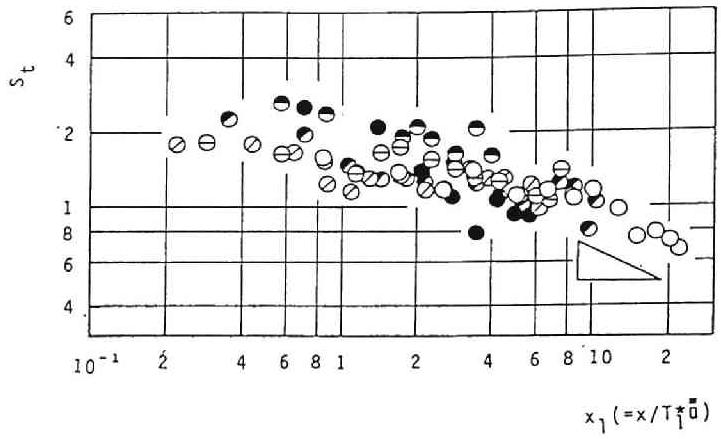

Figure 4.4.6: Skewness factor measured at several sections.

(4) Normalized Peak Concentration

The normalized peak concentration in non-dimensional form $C_{nP}/\left(1/T_{SL}\sqrt{4\pi J_{Al}}\right)$ after Iwasa, Aya, and Toda (1981) is plotted against t_P/T_{SL} on a logarithmic sheet in Fig. 4.4.7. It is also disclosed that:

$$\frac{C_{nP}}{1/T_{SL}\sqrt{4\pi J_{Al}}} \propto \begin{cases} (t_P/T_{SL})^{-1.0} & \text{for} \quad t_P/T_{SL} < 1.5 \\ (t_P/T_{SL})^{-0.5} & \text{for} \quad 8 < t_P/T_{SL} \end{cases} \tag{4.4.10}$$

The time difference between the concentration time for $\bar{t}$ and that for t_P is plotted against χ on a logarithmic sheet in Fig. 4.4.8. It is disclosed that:

$$\frac{\bar{t}-t_P}{T_{SL}} \begin{cases} \propto \chi & \text{for} \quad \chi < 1.5 \\ \propto \chi^{0.5} & \text{for} \quad 1.5 < \chi < 8 \\ = Const. & \text{for} \quad 8 < \chi \end{cases} \tag{4.4.11}$$

Thus, the distributions of the cross-sectional concentration is highly skewed, and its convergence to the Gaussian is very slow and requires very long travel time/distance. The temporal behavior of the tracer cloud injected as a plane source in open-channel flows is summarized as shown in Table 4.4.1.

(5) Temporal Behaviors of Concentration Measured in the Center Point of Flows

a. Second central moment: σ_{tc}^2

The variance σ_{tc}^2 for $\bar{c}_c$ and σ_t^2 measured in Run 121 are plotted against x_1 or χ on a normal sheet in Fig. 4.4.9.

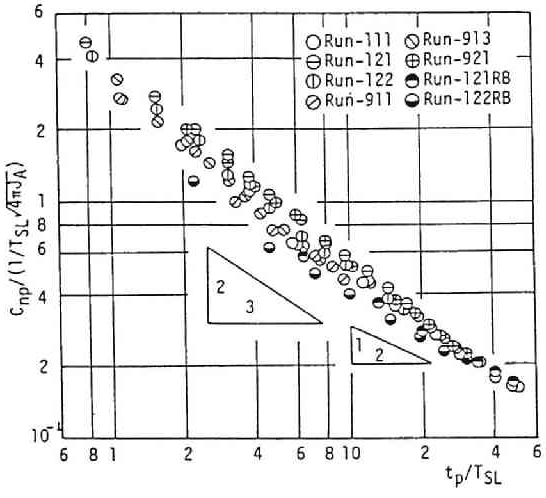

Figure 4.4.7: Normalized peak concentration measured at several sections.

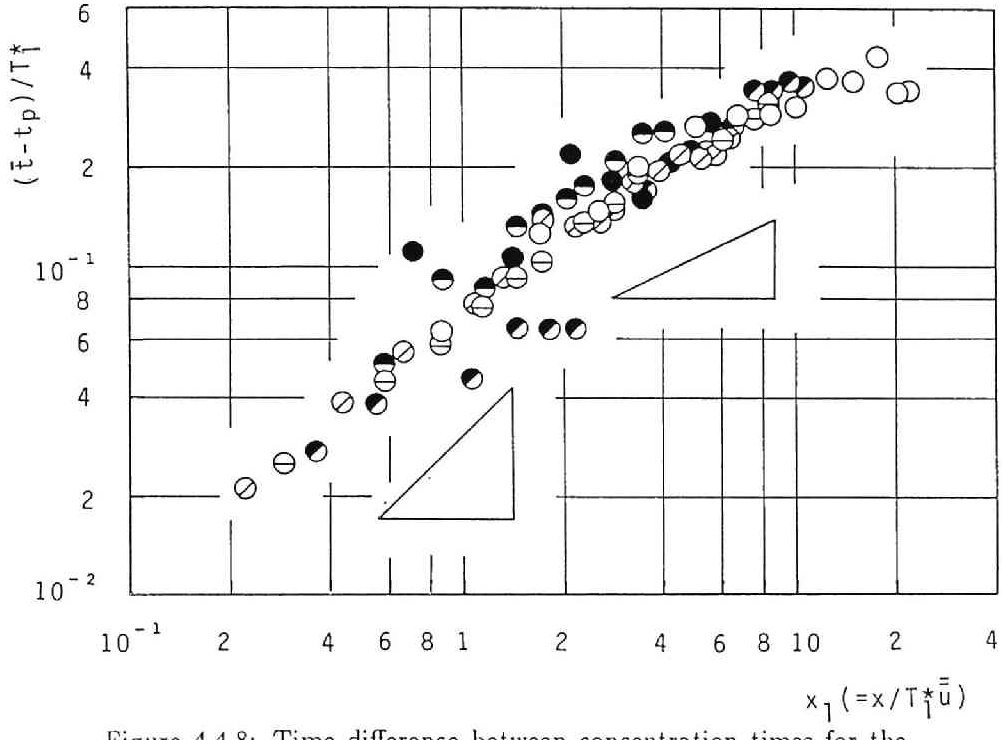

Figure 4.4.8: Time difference between concentration times for the centroid of the tracer cloud and for the peak concentration.

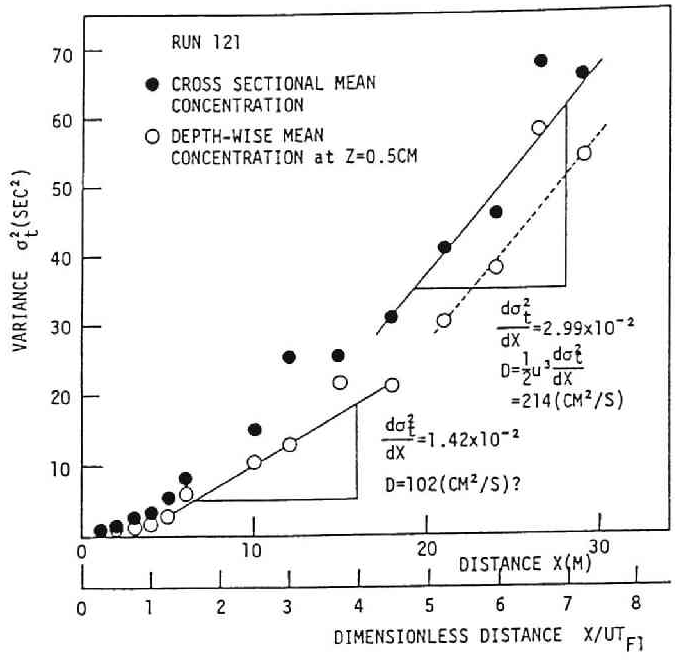

Figure 4.4.9: Variance σ_{tc}^2 for $\bar{c}_c$ and σ_t^2 for C measured in Run 121.

It is shown that the time-dependent growth of σ_{tc}^2 is slower than those for σ_t^2 and the required time for the linear growth of σ_{tc}^2 is larger than that for σ_t^2, however, the proportional constant for $\chi > 6$, which is equivalent to the dispersion coefficient, is the same as that for σ_t^2.

b. Peak concentration: $\bar{c}_{cnP}$

The relationships between the peak concentration for $\bar{c}_{cn}$ or C_n and the dimensionless concentration time for t_{cP} or t_P is presented in Fig. 4.4.10. $\bar{c}_{cnP}$ is always larger than C_{nP}, but have the nearly the same behavior as for C_{nP}.

Thus, it is disclosed that the behavior of $\bar{c}_c$ is a little different from those of C. Therefore the data analyses of $\bar{c}_c$ instead of C should carefully be done. The further discussion on $\bar{c}_c$ will be described in Chapter 7.

4.4.4 Dispersion Coefficient

The three kinds of dispersion coefficient obtained by (a) Change of Moment Method, (b) Routing Procedure, (c) Peak Concentration Method stated in **4.3.1 (3)** are listed in Table 4.4.2. They are shown in the non-dimensional form and hydraulic variables in the non-dimensional form are also listed.

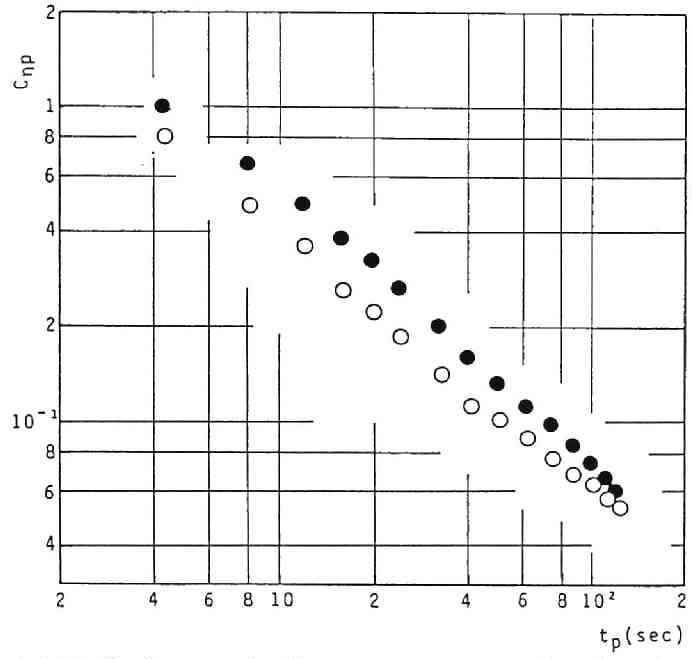

Figure 4.4.10: Peak concentration versus concentration time for $\bar{c}_{cn}$ and C_n

Comparing the magnitudes of dispersion coefficient by three methods, it is concluded that the Change of Moment Method gives the largest values of the coefficient D_M/du_* in almost all runs between the three methods. The Peak Concentration Method usually gives the second largest values D_P/du_*. The Routing Procedure gives the smallest values D_R/du_*, because the travel length of the tracer cloud is not so large enough as the one-dimensional equation can be applied to the analysis of the development of the tracer cloud injected as a plane source, and because D_R is selected so as to give the same peak concentration in the predicted curves as that in observed ones. D_R would be larger if D_R would be determined so as to give the least square error between predicted and observed curves.

The notable features on the dispersion coefficient are summarized as:

1. The values of the non-dimensional dispersion coefficient measured in the experiments is much larger than the theoretical and experimental values in Elder(1959) and experimental results in Fischer(1966).

2. The non-dimensional dispersion coefficient is quite dependent on hydraulic conditions. The relationship between D_M/du_* and B/d will be shown in Fig. 4.5.6.

3. According to Elder(1959) and its expansion made by Hayakawa, Fukushima

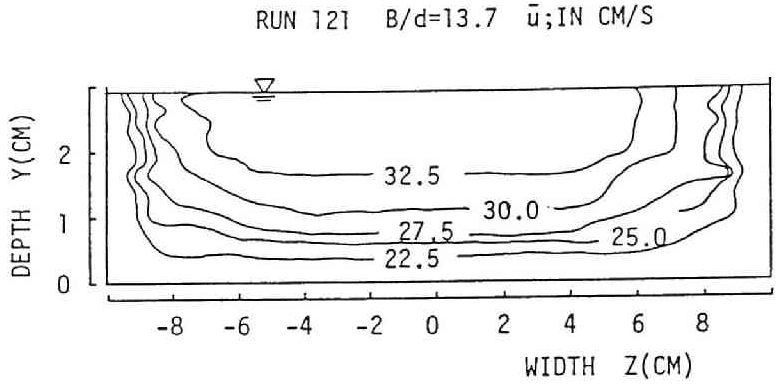

Figure 4.4.11: Iso-velocity contour map measured in Run 121

and Sanjyo (1984), D/du_* should be decrease to 5.93 with the increase of B/d, however experimental results shows that D/du_* becomes larger with increase of B/d.

The further discussion on the dispersion coefficient will be given in Section 4.5 and Chapter 5.

4.4.5 Velocity Distributions

(1) Average Velocity

A typical example of velocity distributions measured in Run 121 is presented as iso-velocity contour map in Fig. 4.4.11. Iso-velocity contour lines indicate that the flow is two-dimensional in the core region near the center line, however the velocity distributions are influenced by the channel sides and it is three-dimensional near the side region, therefore Elder's results in the two-dimensional flows are difficult to apply to the flows in the rectangular cross-section flumes.

Table 4.4.3 shows three kinds of the cross-sectional average velocity, that is, the discharge velocity defined by

$$U_d = Q/A \tag{4.4.12}$$

the accumulated velocity defined by

$$U_i = \sum_{i=1}^{n} \bar{u}_{1i} \Delta A_i / \sum_{i=1}^{n} \Delta A_i \tag{4.4.13}$$

Table 4.4.3: Cross-sectional average velocity measured by several methods

(1)	(2)	(3)	(4)
Run	Discharge velocity $U=Q/A$	Accumulated velocity $u_t=\Sigma\bar{u}dA/A$	Convective velocity $u_c=dx/d\bar{t}$
911	32.2	27.6	33.5
912	44.1	37.8	44.1
913	27.4	22.2	26.6
111	28.3	30.3	28.7
112	21.5	23.6	22.2
921	36.5	31.1	36.8
121	27.6	26.2	24.3
122	22.3	25.9	22.5
123	31.3	—	30.9
124	37.8	—	37.6
125	51.4	—	48.0
221	34.3	38.6	34.4
222	46.8	47.9	46.4
111RA	23.0	—	24.5
112RA	12.9	—	16.2
121RB	15.1	14.7	14.6
122RB	20.6	20.1	18.6
221RC	19.8	19.2	19.1
222RC	16.2	16.5	15.9

and the convective velocity defined by

$$U_c = \frac{dx}{d\bar{t}} \tag{4.4.14}$$

The discharge velocity has good agreement with the convective velocity as already shown in Fig. 4.4.3, and this experimental results confirm the theoretical results in Chapter 2.

(2) Characteristics of Velocity Distributions

Three kinds of characteristics of velocity distributions: J_A, J_{Al} and I_A, and the Lagrangian velocity fluctuation and its three components: $[v_x'^2]/u_*^2$, $[v_v'^2]/u_*^2$, $[v_l'^2]/u_*^2$, and $[v_t'^2]/u_*^2$ are listed in Table 4.4.4.

a. J_A and J_{Al}

J_A is the square of the coefficient of variation (COV) for the Eulerian velocity distributions and also the square of COV for the sum of two components of Lagrangian velocity fluctuation: $v_v' + v_l'$ in Chapter 2. The magnitude of J_A is of the order of 10^{-2} and J_A is not dependent on B/d as illustrated in Fig. 4.4.12. J_{Al} is the square of COV for $\bar{u}_1^{x_2}$ and the parameter showing the strength of the non-uniformity of $\bar{u}_1^{x_2}$ distributions in view of the Eulerian analysis and also the square of COV for v_l' in view of the Lagrangian Analysis. The magnitude of J_{Al} is of the order of 10^{-2} and it decreases with increase of B/d as illustrated in Fig. 4.4.13, and the relationship of

Table 4.4.4: Characteristics of velocity distributions and Lagrangian velocity fluctuation.

(1)	(2)	(3)		(4)	(5)	(6)	(7)	(8)	(9)	(10)
Run	Velocity meter	No. of velocity measurement in section		J_A	$J_{A1} \times 10^{-1}$	$I_A \times 10^{-3}$	$\frac{[v_1'^2]}{u_*^2}$	$\frac{[v_r'^2]}{u_*^2}$	$\frac{[v_v'^2]}{u_*^2}$	$\frac{[v_l'^2]}{u_*^2}$
		vertical	horizontal							
911	P	5	13	.172	.586	.621	30.5	1.39	19.2	9.91
912	P	6	13	.097	.600	.673	22.3	1.67	7.85	12.8
913	P	3	19	.227	.560	.465	32.2	1.35	23.4	7.41
111	H	5	13	.119	.445	.537	36.5	2.07	21.6	12.9
112	H	4	13	.127	.458	.569	33.6	1.87	20.3	11.5
921	P	5	17	.136	.246	.255	23.5	1.28	18.2	4.04
121	H	4	22	.125	.291	.373	35.8	1.92	26.0	7.88
122	H	4	22	.133	.234	.210	38.8	1.68	30.5	6.52
123	—	—	—	—	—	—	—	—	—	—
124	—	—	—	—	—	—	—	—	—	—
125	—	—	—	—	—	—	—	—	—	—
221	H	6	15	.067	.239	.357	21.6	1.19	13.2	7.24
222	H	7	15	.055	.251	.403	24.5	2.65	12.1	10.0
111RA	—	—	—	—	—	—	—	—	—	—
112RA	—	—	—	—	—	—	—	—	—	—
121RB	H	6	15	.212	.285	.352	11.9	.957	9.45	1.47
122RB	H	6	15	.141	.223	.205	12.0	1.36	10.9	2.05
221RC	H	6	15	.134	.215	.207	13.5	1.32	10.2	1.96
222RC	H	6	15	.150	.217	.275	13.1	1.20	10.2	1.72

(2) P: Propellers velocity meter, H: Hot film velocity meter

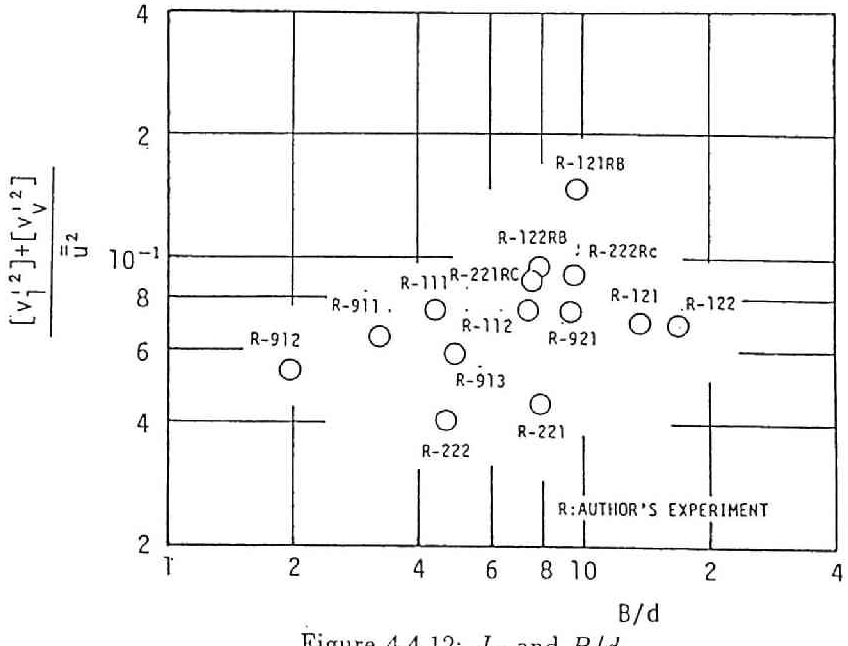

Figure 4.4.12: J_A and B/d

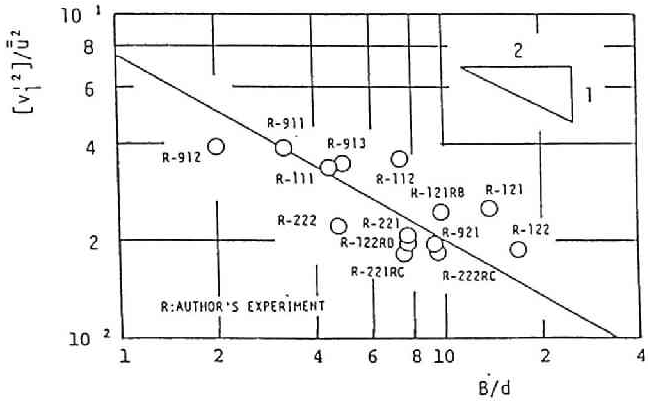

Figure 4.4.13: J_{Al} and B/d.

$$J_{Al} \propto (B/d)^{-0.5} \tag{4.4.15}$$

is obtained. The difference between the relationship of J_A to B/d and that of J_{Al} to B/d can be explained as follows:

The temporal-averaged velocity $\bar{u}_1(x_2, x_3)$ can be written as the sum of two components: $\bar{u}_1^{x_2}(x_3)$ and $\bar{u}_{23}''(x_2, x_3)$ as shown in Eq. 2.2.6, and u_{23}'' is defined by Eq. 2.2.8 as

$$u_{23}''(x_2, x_3) \equiv \bar{u}(x_2, x_3) - \bar{u}^{x_2}(x_3) \tag{2.2.8}$$

By using Eq. 2.2.8, J_A is written in the form of

$$J_A = J_{Al} + J_{Av} \tag{4.4.16}$$

where J_{Av} is defined by

$$J_{Av} \equiv \frac{1}{AU^2} \int_{-b_1}^{b_2} dx_3 \int_{-z_b}^{\zeta} {u_{23}''}^2 dx_2 \tag{4.4.19}$$

In case the flow is two-dimensional, assuming the logarithmic velocity distribution,

$$J_{Al} = 0.0 \tag{4.4.20}$$

$$J_{Av} = \frac{1}{\kappa^2} \left(\frac{\bar{u}_1^{x_2}}{u_*} \right)^{-2} \tag{4.4.21}$$

$$\bar{u}_1^{x_2} = U \tag{4.4.22}$$

where κ is von Karman's constant and U the depth-averaged velocity. The core region where the two-dimensional velocity distribution is established becomes wider

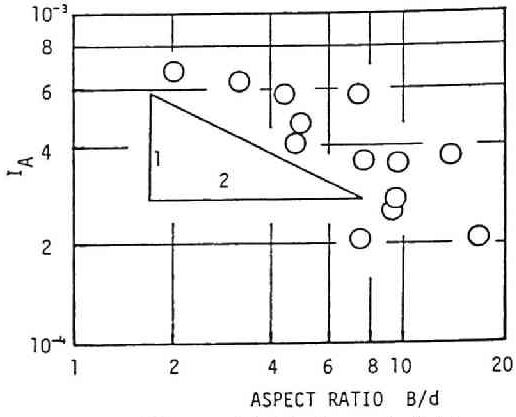

Figure 4.4.14: I_A and B/d

in a wider rectangular cross-section flume, however, the velocity distribution is still three-dimensional in whole of the cross-section. Therefore J_{Al} becomes smaller and J_A becomes equal to J_{Av} with increase of B/d.

b. I_A

The relationship of I_A with B/d is also illustrated in Fig. 4.4.14. In case the flow is two-dimensional, I_A is equal to zero and experimental results in the rectangular cross-sectional flumes lead the following relationship

$$I_A \propto (B/d)^{-0.5} \tag{4.4.23}$$

The relationship of these characteristics of velocity distributions with the dispersion coefficient will be discussed in the next section.

4.5 Discussions

4.5.1 Discussion Based on One-Particle Analysis

(1) Summary of Results in Chapter 2

The theoretical results based on one-particle analysis and verified by numerical experiments in Chapter 2 are again summarized for the convenience for discussion in this chapter, and they are as follows:

a. Turbulent intensity

$$\frac{[v_1'^2]}{u_*^2} = \frac{[v_t'^2]}{u_*^2} + \frac{[v_v'^2]}{u_*^2} + \frac{[v_l'^2]}{u_*^2} \tag{4.5.1}$$

$$\frac{[v_t'^2]}{u_*^2} = \frac{1}{A}\int_A \frac{u_1'^2}{u_*^2} dA \tag{4.5.2a}$$

$$\frac{[v_v'^2]}{u_*^2} = \frac{1}{A}\int_A \frac{u_{23}''^2}{u_*^2} dA = J_{Av}\left(\frac{U}{u_*}\right)^2 \tag{4.5.2b}$$

$$\frac{[v_l'^2]}{u_*^2} = \frac{1}{B}\int_{-b_1}^{b_2} \frac{(\bar{u}^{x_2} - U)^2}{u_*^2} dx_3 = J_{Al}\left(\frac{U}{u_*}\right)^2 \tag{4.5.2c}$$

b. Mixing time scale

$$T_t = 0.72\frac{d}{u_*} \approx \frac{d}{u_*} \tag{4.5.3a}$$

$$T_v = \frac{1}{14.8}\frac{d^2}{\theta_2 d u_*} \approx \frac{d}{u_*} \tag{4.5.3b}$$

$$T_l = \frac{1}{14.8}\frac{(B/2)^2}{\theta_3 d u_*} = \frac{1}{59.2\theta_3}\left(\frac{B}{d}\right)^2 \frac{d}{u_*} \tag{4.5.3c}$$

where T_t is the integral time scale of the Eulerian turbulence, T_v the mixing time scale in the depth-wise direction, T_l the mixing time scale in the transverse direction, θ_2 the turbulent dispersion coefficient($\approx \kappa/6$), θ_3 the turbulent dispersion coefficient in the transverse direction (≈ 0.2).

c. Lagrangian auto-correlation function

$$B_L(\tau) = [v_t'^2]\exp(-\tau/T_t) + [v_v'^2]\exp(-\tau/T_v) + [v_l'^2]\exp(-\tau/T_l) \tag{4.5.4}$$

d. Growth of variances

$$\begin{aligned}[X'^2(a,t)] \;=\; & 2[v_t'^2]T_t^2\{\exp(-\tau/T_t) + t/T_t - 1\} + \\ & 2[v_v'^2]T_v^2\{\exp(-\tau/T_v) + t/T_v - 1\} + \\ & 2[v_l'^2]T_l^2\{\exp(-\tau/T_l) + t/T_l - 1\}\end{aligned} \tag{4.5.5}$$

e. Integral time scale

$$\frac{T_{SL}}{d/u_*} = \frac{[v_t'^2]}{[v_1'^2]}\frac{T_t}{d/u_*} + \frac{[v_v'^2]}{[v_1'^2]}\frac{T_v}{d/u_*} + \frac{[v_l'^2]}{[v_1'^2]}\frac{T_l}{d/u_*} \tag{4.5.6}$$

f. Dispersion coefficient

$$\begin{aligned}\frac{D_L}{du_*} &= \frac{[v_1'^2]}{u_*^2}\frac{T_{SL}}{d/u_*} \\ &= \frac{1}{du_*}\left\{[v_t'^2]T_t + [v_v'^2]T_v + [v_l'^2]T_l\right\} \\ &= \frac{D_{Lt}}{du_*} + \frac{D_{Lv}}{du_*} + \frac{D_{Ll}}{du_*}\end{aligned} \tag{4.5.7}$$

$$\frac{D_{Lt}}{du_*} = 0.72\frac{[v_t'^2]}{u_*^2}\frac{1}{d/u_*} \approx 1. \tag{4.5.8a}$$

$$\frac{D_{Lv}}{du_*} = \frac{[v_v'^2]}{u_*^2}\frac{1}{d/u_*} \approx 10. \tag{4.5.8b}$$

$$\frac{D_{Ll}}{du_*} = \frac{1}{14.8}\frac{[v_l'^2]}{u_*^2}\frac{(B/2)^2}{\theta_3 du_*} = \frac{1}{59.2\theta_3}J_{Al}\left(\frac{U}{u_*}\right)^2\left(\frac{B}{d}\right)^2 \tag{4.5.8c}$$

The first term of Eq. 4.5.7 is the cross-sectional average of the turbulent diffusion coefficient in the flow direction, the second one the dispersion coefficient caused by the non-uniform distribution of the velocity in the depth-wise direction, and the third one caused by the non-uniform distribution of the velocity in the lateral direction.

(2) Lagrangian Auto-Correlation Function

The theory and the numerical experiment based on one-particle analysis presented in **Chapter 2** leads Eq. 4.5.4 for the Lagrangian auto-correlation function as stated above. The Lagrangian auto correlation coefficient $R_L(t)$ in turbulent flows is usually assumed as:

$$R_L(t) = e^{-t/T_{SL}} \tag{4.5.9}$$

and B_L is:

$$B_L(t) = [v_1'^2]e^{-t/T_{SL}} \tag{4.5.10}$$

Using velocity distributions measured in experiments and T_{SL} calculated by the first equation of Eq.4.5.7, two kinds of B_L for Run 122 calculated by Eqs. 4.5.4 and 4.5.10 are presented in Fig. 4.5.1. B_L by Eq. 4.5.4 decreases much more rapidly than those by Eq. 4.5.10 for short lag-time, but decreases much more slowly than those by Eq. 4.5.10 for longer lag-time. Thus, the approximation of exponential function for R_L commonly used in uniform turbulent flows is not acceptable for dispersion in the turbulent shear flows. The other possible relationship is

$$B_L{}^*(t) = [v_l'^2]e^{-t/T_l^*} \tag{4.5.11}$$

where T_l^* is defined by:

$$T_l^* \equiv \frac{D}{J_{Al}U^2} \tag{4.5.12}$$

B_L^* is not the auto-correlation function, because $B_L^*(0)$ is not equal to the Lagrangian turbulent intensity. However, $B_L^*(t)$ is good approximation for $B_L(t)$ for longer lag time as examined in Fig. 4.5.1.

(2) Growth of Variances

Growth of variance is obtained by integrating B_L, and they are shown in Eq. 4.5.5. For Eq. 4.5.10, the variance is calculated at:

$$\sigma_{x_1}^2 = 2[v_1'^2]T_{SL}{}^2(e^{-t/T_{SL}} + t/T_{SL} - 1) \tag{4.5.13}$$

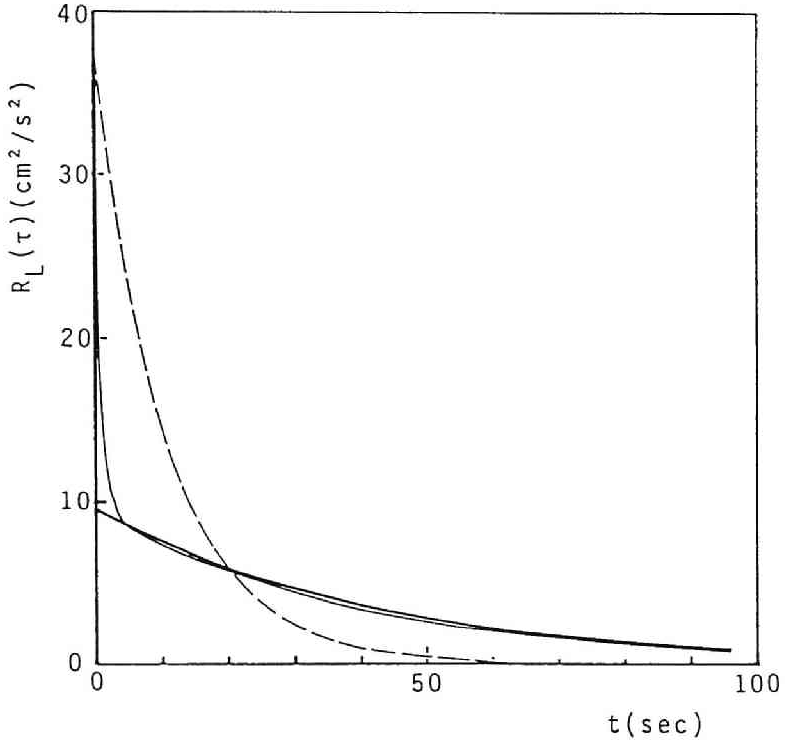

Figure 4.5.1: Lagrangian auto-correlation functions for Run 122. Solid line denotes Eq. 4.5.4, broken line Eq. 4.5.10, and thick solid line Eq. 4.5.11.

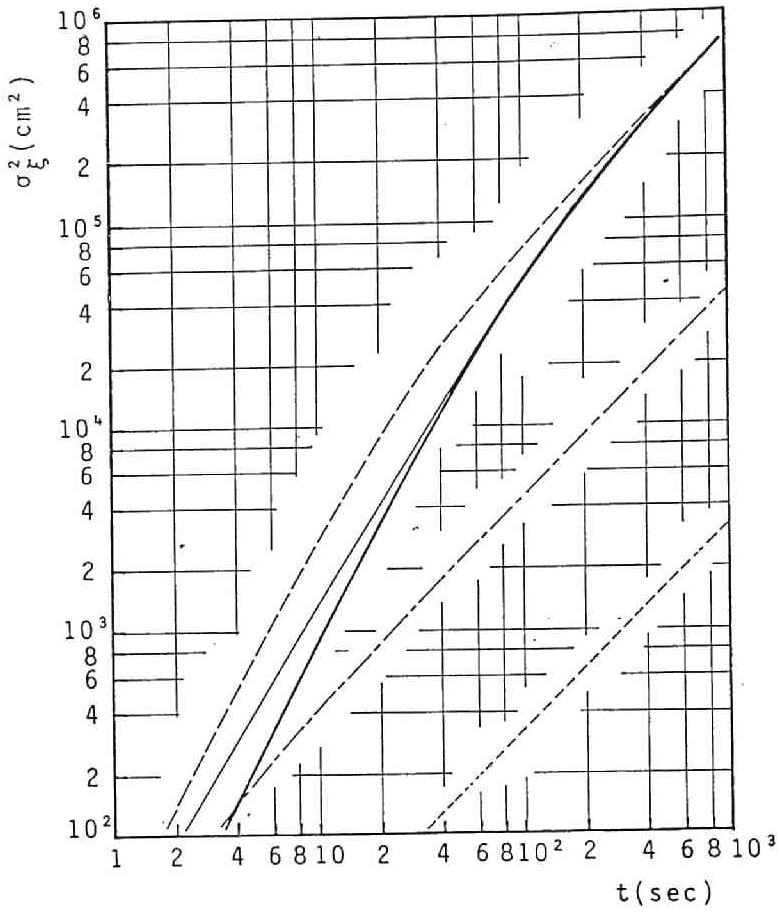

Figure 4.5.2: Growth of variances for Run122. Solid line denotes Eq. 4.5.4, broken line Eq. 4.5.10, and thick solid line Eq. 4.5.11.

and for $B_L^*(t)$, the variance is calculated at:

$$\sigma_{x_1}^2 = 2[v_1'^2]J_{AI}T_I^{*2}(e^{-t/T_I^*} + t/T_I^* - 1) \tag{4.5.14}$$

Eqs. 4.5.5, 4.5.13 and 4.5.14 are illustrated in Fig. 4.5.2. For a long lag-time, they converge the same values, but for a short lag-time, Eq. 4.5.13 gives larger values than those by Eqs. 4.5.5 and 4.5.14. Thus, the approximation of exponential function for R_L is again not acceptable for calculating the variance for dispersion in the turbulent shear flows, and this fact has already been shown in Fig. 4.4.4. The variance calculated by Eq. 4.5.14 is much better approximation for Eq. 4.5.5 for the longer period, and its failure is seen in only short travel time.

Fig.4.5.3 demonstrates that the variances observed in the experiments and calculated by Eq. 4.5.14 under the assumption of $x = Ut$ have fine agreement each other.

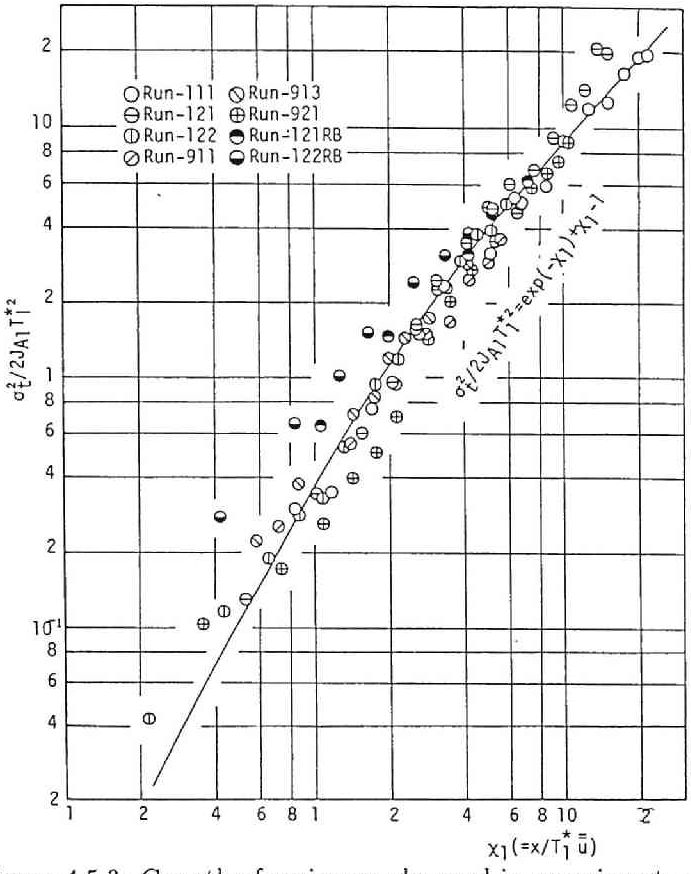

Figure 4.5.3: Growth of variances observed in experiments and calculated by Eq. 4.5.14.

It is also concluded that the growth of variance is linear for $\chi_l(= x_1/T_l^* U) \approx 2 \sim 3$.

(3) Integral Time Scale

The relationship between the integral time scale T_{SL} calculated by Eq. 4.5.7 and Fischer's time scale T_{Fl} equivalent to the mixing time scale T_l in the lateral direction are illustrated in Fig. 4.5.4. T_{SL} is not so large even in wider channels, but T_l is quite large, because $[v_l'^2]/[v_1'2] = J_{Al}$ becomes smaller with increase of B/d. Thus, it is disclosed that the mixing time scale is quite different idea from the integral time scale as described in Eq. 4.5.5 in 3-D turbulent shear flows. Fig. 4.5.5 shows the relationship between the mixing time scale T_l and T_l^* It is definitely demonstrated that T_l is good approximation for T_l^*.

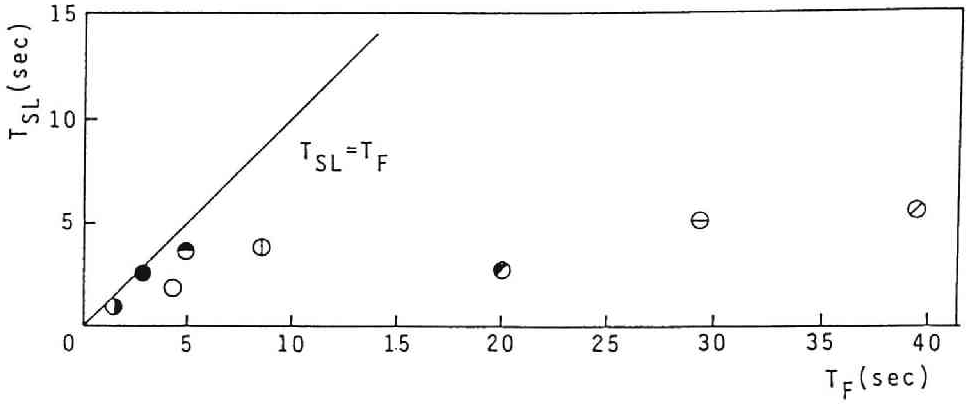

Figure 4.5.4: Lagrangian integral time scale and Fischer's time scale.

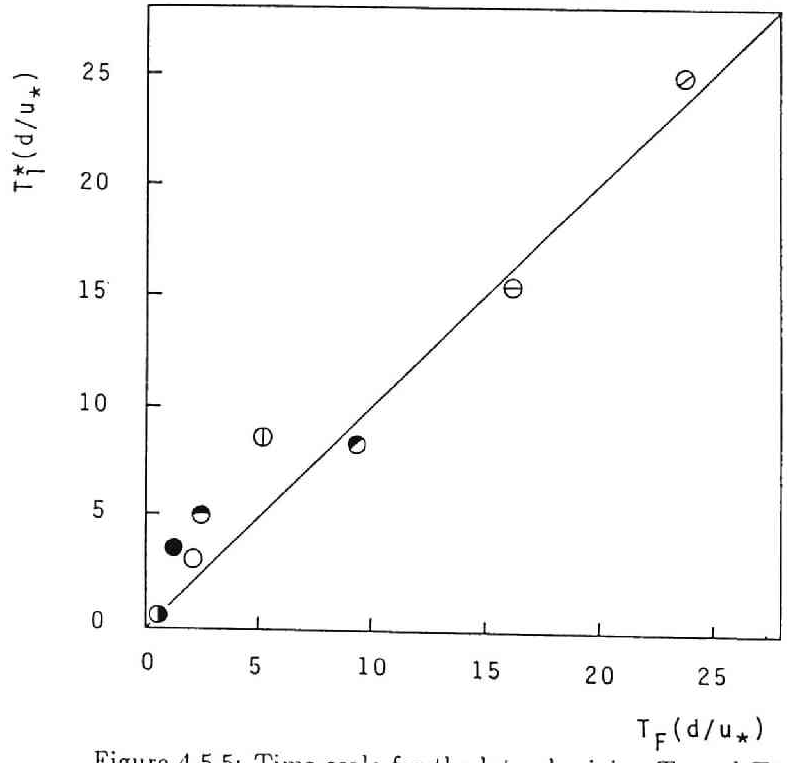

Figure 4.5.5: Time scale for the lateral mixing T_l, and T_l^*.

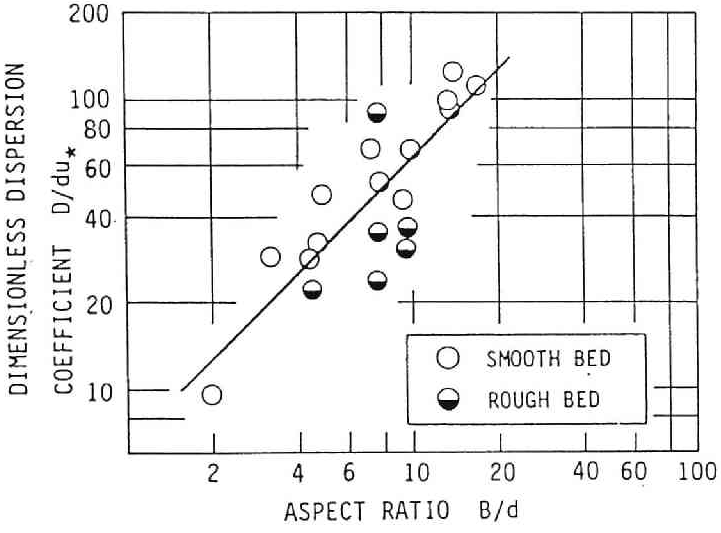

Figure 4.5.6: Relationship between non-dimensional dispersion coefficient and width to depth ratio.

4.5.2 Dispersion Coefficient

(1) Relationship with Hydraulic Characteristics

As listed in Table 4.4.2, the dimensionless form of dispersion coefficient in laboratory flumes looks dependent on the width to depth ratio B/d and the velocity factor U/u_*. Fig. 4.5.6 definitely demonstrates the dependence of D_M/du_* on B/d as:

$$D_M/du_* = 6.21\left(\frac{B}{d}\right)^{1.002} \qquad \text{for} \quad 2.0 < B/d < 20.0 \tag{4.5.15}$$

Another possibility examined is the relationship between D_M/du_* and U/u_*. As shown in Fig. 4.5.6 displayed above, D_M/du_* in rough-bottom channels are commonly smaller than those in smooth bottom channels. Fig. 4.5.7 plots $D_M/du_*(B/d)^{-1.03}$ against U/u_* and the following relationship is obtained:

$$\frac{D_M}{du_*(B/d)^{1.002}} = 0.38\left(\frac{U}{u_*}\right) \tag{4.5.16}$$

Finally we obtains:

$$\frac{D_M}{du_*} = 0.38\left(\frac{B}{d}\right)^{1.002}\left(\frac{U}{u_*}\right) \tag{4.5.17}$$

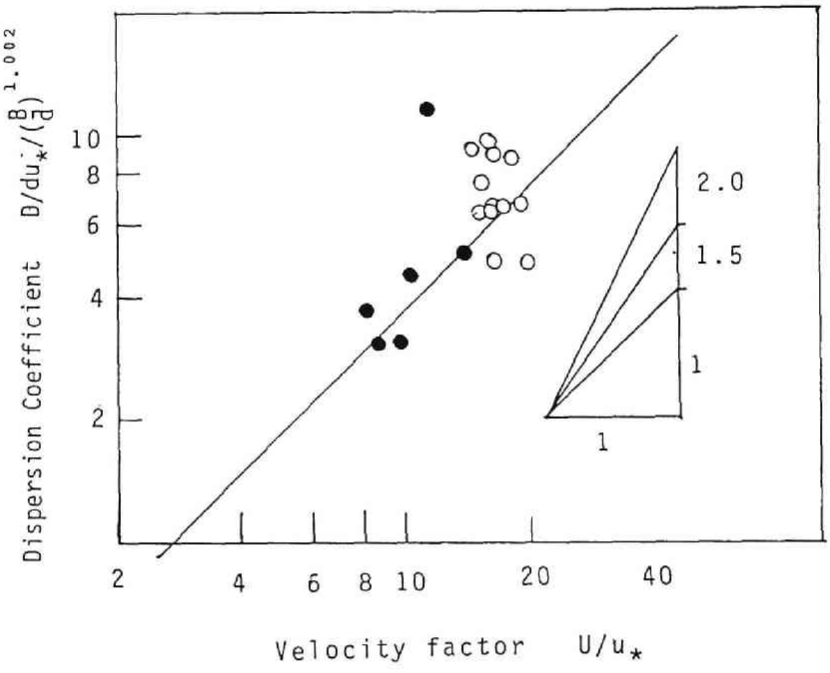

Figure 4.5.7: $D_M/du_*(B/d)^{-1.002}$ versus U/u_*

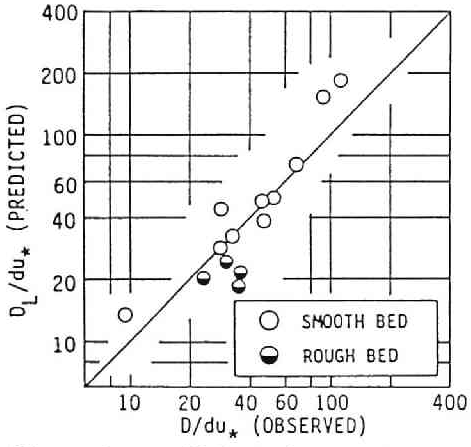

Figure 4.5.8: Dispersion coefficient observed in experiment and predicted by Eq. 4.5.7 in view of Lagrangian Analysis.

(2) Dispersion Coefficient in View of One-Particle Analysis

The values of the dispersion coefficient obtained in the laboratory experiments are plotted against the theoretical values by Eq.4.5.7 in Fig. 4.5.8. The definite agreement between observed and theoretical values are demonstrated. Thus, validity of Eq. 4.5.7 for predicting the dispersion coefficient in 3-D turbulent shear flows are verified.

(3) Dispersion Coefficient Based on 3-D Turbulent Diffusion Equation

The results obtained in **Chapter 3** are summarize as follows.

$$\frac{D_E}{du_*} = \frac{D_{Et}}{du_*} + \frac{D_{Ev}}{du_*} + \frac{D_{El}}{du_*} \tag{4.5.18}$$

$$\frac{D_{Et}}{du_*} = \frac{1}{A}\int_A \varepsilon_1 \frac{\partial \bar{c}}{\partial x} dA \Big/ \left(\frac{\partial C}{\partial x} du_*\right) \approx 1.0 \tag{4.5.19a}$$

$$\frac{D_{Ev}}{du_*} = -\frac{1}{A}\int_A u''_{23} c''_{23} dA \Big/ \left(\frac{\partial C}{\partial x} du_*\right) \approx 10.0 \tag{4.5.19b}$$

$$\frac{D_{El}}{du_*} = \frac{1}{A}\int_A (\bar{u}^{x_2} - U)(\bar{c}^{x_2} - C) dA \Big/ \left(\frac{\partial C}{\partial x} du_*\right) = \frac{I_A}{\theta_3}\left(\frac{U}{u_*}\right)^2 \left(\frac{B}{d}\right)^2 \tag{4.5.19c}$$

The first term of Eq. 4.5.18 is the cross-sectional average of the turbulent diffusion coefficient in the flow direction, the second one the dispersion coefficient caused by the non-uniform distribution of the velocity in the depth-wise direction, and the third one caused by the non-uniform distribution of the velocity in the lateral direction. The constitution of the dispersion coefficient based on 3-D turbulent diffusion equation is

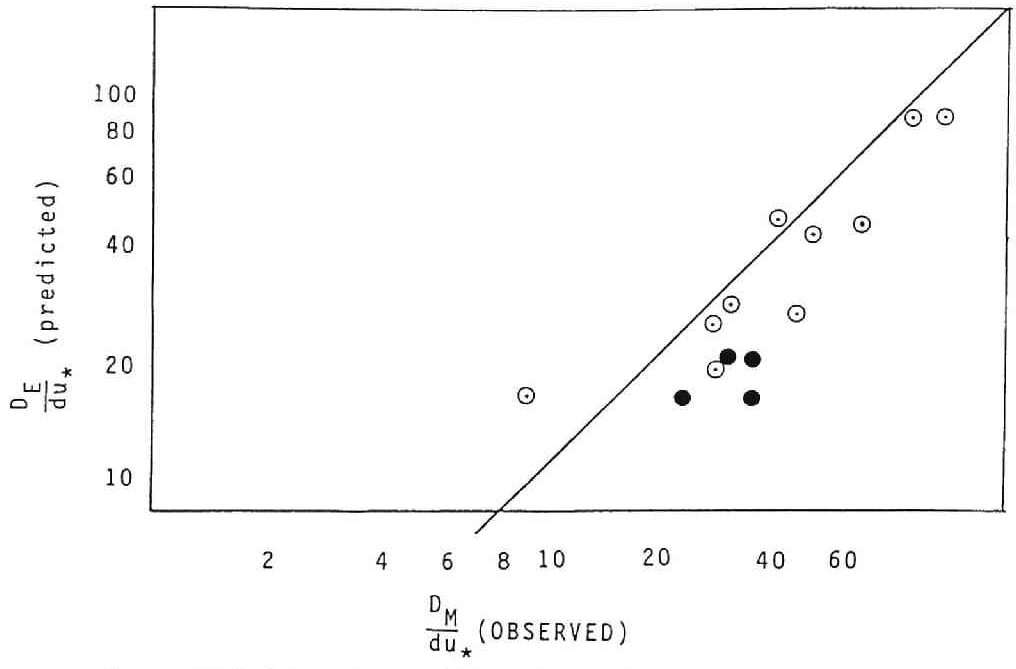

Figure 4.5.9: Dispersion coefficient observed in experiment and predicted by Eq. 4.5.18 in view of Eulerian Analysis.

the same as that based on one-particle analysis of Eq. 4.5.7, however, the expression is little different each other because the method of analysis is different.

The direct comparison of measured data in the laboratory flumes with those by Eq. 4.5.18 are illustrated in Fig. 4.5.9, and the fine agreement between observed and predicted dispersion coefficient is demonstrated. Thus, the validity of Eq. 4.5.18 for predicting the dispersion coefficient in 3-D turbulent shear flows are verified.

Fischer's theory (Fischer, 1966) for natural streams, which neglects the effects of the turbulent mixing in the flow direction and the non-uniform velocity distribution in the depth-wise direction is equivalent to Eq. 4.5.19. Therefore, Fischer's formula may give the smaller values than observed one in flows in narrow flumes, however, the width and/or the width to depth ratio in ordinary river channels is very large and the magnitude of the third term of Eq. 4.5.18 is much bigger than other two, therefore Eq. 4.5.19c may be applicable to predicting the dispersion coefficient in natural streams and rivers.

4.6 Conclusions

This Chapter investigated the longitudinal dispersion by the experimental method. The experiments were conducted by injecting the salt solution as the tracer in the rectangular cross-section laboratory flumes, and measuring its concentration at selected points in selected sections by use of the conductivity meter. The behavior of the temporal moments was calculated and the dispersion coefficient was determined by three different methods. The results disclosed the 3-D spreading of the tracer cloud inserted as a plane source into the flow, and verified the theoretical results obtained in **Chapters 2** and **3**. The dimensional analysis also disclosed the empirical relationship of the dimensionless dispersion coefficient with the width to depth ratio and the velocity factor.

The objectives and the design of the experiment were described in **Section 4.1**, and the experimental apparatus and the method in **Section 4.2**. The methods of data processing and analysis were stated in **Section 4.3**.

The results of the experiments were stated in **Section 4.4** and they were summarized as:

1. The spreading of the injected tracer in 3-D space was disclosed, and it is described as:

   (a) the tracer is stretched in the longitudinal direction by the longitudinal component of the flow velocity vector which has the strong non-uniform distribution in the vertical direction and the weak one in the lateral direction, and the concentration distributions becomes three-dimensionally non-uniform and highly skewed.

   (b) the vertical mixing makes the concentration distribution in the vertical direction uniform again.

   (c) the lateral mixing following the vertical mixing also makes the concentration distribution in the lateral direction uniform again, and the magnitude of the dispersion coefficient becomes much larger than that in 2-D shear flows.

2. The spreading of the tracer was also investigated by the behavior of the first, the second and the third temporal moments and the peak concentration. It describes the quite different concentration distributions from the Gaussian distribution, and highly skewed ones. The convergence to the Gaussian distribution is disclosed to be very slow. The difference of the temporal moment behavior

between the cross-sectional concentration and those measured at points in a section was also disclosed.

3. The velocity distributions were also measured in the experiment and the characteristics of the velocity distributions were disclosed.

4. The theoretical results obtained in **Chapter 2** were successfully examined by the experimental results.

   (a) the convective velocity of the centroid of the tracer cloud is equal to the cross-sectional averaged velocity.

   (b) the growth of the variance of the tracer cloud can be stated by

$$\begin{aligned}[X'^2(a,t)] &= 2[v_t'^2]T_t^2\{\exp(-\tau/T_t)+t/T_t-1\}+ \\ &\quad 2[v_v'^2]T_v^2\{\exp(-\tau/T_v)+t/T_v-1\}+ \\ &\quad 2[v_l'^2]T_l^2\{\exp(-\tau/T_l)+t/T_l-1\}\end{aligned} \tag{4.5.5}$$

   and can be approximated by

$$[X'^2(a,t)] \approx 2[v_1'^2]J_{Al}T_l^{*2}(e^{-t/T_l^*}+t/T_l^*-1) \tag{4.5.14}$$

   (c) The characteristics of the integral time scale in 3-D turbulent shear flows was also examined and it was verified that the mixing time scale in the lateral direction is quite different from the integral time scale, and also good approximation for T_l^*.

5. The empirical relationship of the dispersion coefficient with the hydraulic variables obtained by the dimensional analysis was stated as

$$\frac{D_M}{du_*} = 0.38\left(\frac{B}{d}\right)^{1.002}\left(\frac{U}{u_*}\right) \tag{4.5.17}$$

6. The definite agreement between the dispersion coefficient measured in the experiments and predicted by

$$\frac{D_L}{du_*} = \frac{1}{du_*}\left\{[v_t'^2]T_t+[v_v'^2]T_v+[v_l'^2]T_l\right\} \tag{4.5.7}$$

   was demonstrated.

7. The dispersion coefficient based on 3-D turbulent diffusion equation, presented in **Chapter 3**

$$\frac{D_E}{du_*} = \frac{D_{Et}}{du_*}+\frac{D_{Ev}}{du_*}+\frac{D_{El}}{du_*} \tag{4.5.18}$$

$$\frac{D_{El}}{du_*} = \frac{1}{A}\int_A (\bar{u}^{x_2} - U)(\bar{c}^{x_2} - C)dA \Big/ \left(\frac{\partial C}{\partial x}du_*\right) = \frac{I_A}{\theta_3}\left(\frac{U}{u_*}\right)^2\left(\frac{B}{d}\right)^2 \quad (4.5.19c)$$

was also successfully examined by the measured dispersion coefficient.

8. It was concluded that the dispersion coefficient in rectangular cross-section open-channel flows is not predicted by Elder's formula, but can be predicted by Eqs. 4.5.7, 4.5.17, and/or 4.5.18.

Chapter 5

PREDICTING LONGITUDINAL DISPERSION COEFFICIENT IN LABORATORY FLUMES AND RIVERS

5.1 Introduction and Objectives

In the field of the river hydraulics, various investigations on the longitudinal mixing in river flows were made especially in view of the spreading of the contaminants as radio active materials, or waste into rivers from various sources and so on. Elder's work (Elder, 1956)

$$\frac{D}{du_*} = \frac{0.404}{\kappa^3} \tag{3.4.24}$$

for 2-D turbulent shear flows was one of the most primitive ones and was found less useful for predicting the dispersion coefficient of rivers. Assuming the velocity distributions in rivers, some investigations were made in this direction (Thomas, 1958, Parker, 1961, Sooky, 1968 and so on), however, they were neither successful for predicting the dispersion coefficient in rivers. The theoretical and experimental works for the dispersion coefficient for natural streams made by Fischer (1966) were one of the most famous and successful works in this research field, that is,

$$D = \frac{1}{A}\int_{-b_1}^{b_2} \frac{dz}{\varepsilon_z d}\left\{\int_0^z q'(z')dz'\right\}^2 \tag{3.4.28}$$

Some variations of Fischer's formula have been proposed for the flows in various cross-section flumes or natural streams, assuming the relationships of the velocity distributions with the geometric characteristics of the cross-section (Jain, 1976, and Chiu, Lin and Mizumura, 1978). The effect of bends in channels on the dispersion was also investigated by Fukuoka and Sayre (1973). Empirical relationships of the dispersion coefficient in rivers with the geometrical features of the cross-sections and/or the

hydraulic variables have also been investigated by Liu (1977), Iwasa and Aya (1980) and others.

The quite different modeling for the dispersion in rivers is the dead zone modeling developed by Hay (1966), Thakston and Schnelle (1970), Valentine and Wood (1977), and Muramoto, Michiue and Nakagawa (1976) and others. They assumed that the dead zone which may be exist in the channel-bottom or channel-side in natural rivers causes the dispersion and the highly skewed concentration distributions.

In the previous chapters, the three different formulae for the dispersion coefficient of open-channel flows are presented. In **Chapter 2**, the author presented the formula predicting the dispersion coefficient in 3-D open-channel flows by being based on Taylor's turbulent diffusion theory in the uniform turbulent field as:

$$D_L = [v_1'^2]T_{SL} = [v_t'^2]T_t + [v_v'^2]T_v + [v_l'^2]T_l \tag{2.2.35}$$

In **Chapter 3**,

$$D_E = \frac{1}{A}\int_A \varepsilon_1 \frac{\partial \bar{c}}{\partial x_1} \Big/ \frac{\partial C}{\partial x_1} + \frac{1}{A}\int_{-b_1}^{b_2} dD2_{11}\frac{\partial \bar{c}^{x_2}}{\partial x_1}dx_3 \Big/ \frac{\partial C}{\partial x_1} + \frac{1}{A}\int_{-b_1}^{b_2}\frac{dx_3}{dD2_{33}}\left[\int_{-b_1}^{x_3} u'_{03}ddx'_3\right]^2 \tag{3.5.45}$$

was also presented by being based on the 3-D turbulent diffusion equation. **Chapter 4** disclosed the empirical relationships of

$$\frac{D_M}{du_*} = 0.38\left(\frac{B}{d}\right)^{1.002}\left(\frac{U}{u_*}\right) \tag{4.5.17}$$

by the dimensional analysis. Each of three formulae was successfully examined by comparing them with the experimental results made by the author in **Chapter 4**, however, not examined by previous measurements in laboratory flumes and natural streams, because theoretical works presented in **Chapters 2** and **3** are limited only for the flows in the rectangular cross-section straight flumes.

This chapter will demonstrate the applicability of the formulae presented in the previous chapters to river flows as well as to the various flows in laboratory flumes made by many investigators and the formulae presented by other investigators. The reason why the concentration distribution measured in open-channel flows is so skewed will be investigated in **Chapter 6**.

5.2 Review of Previous Measurements of Longitudinal Dispersion Coefficient in Laboratory Flumes

As described in **Chapters 2** and **4**, the variance of tracer clouds injected to the flows as an instantaneous plane source is proportional to the square of the travel time for the short travel time and to the travel time for the long travel time. The required travel time or length for the linear growth in flows in rivers as well as laboratory flumes is:

$$[X'^2] \propto t \quad \text{for} \quad t > (3 \sim 6)T_l \quad \text{or} \quad x > (3 \sim 6)T_l U \tag{2.2.39}$$

Assuming $\varepsilon_3 = 0.2du_*$, $B/d \simeq 10 \sim 20$, and $U/u_* \approx 20$ for flows in smooth laboratory flumes, the required length is approximately calculated at:

$$x/B \simeq 100 \sim 200 \tag{4.2.1}$$

As far as author can know, the previous laboratory measurements of the dispersion coefficient in open-channel flows which satisfy Eq. 2.2.39 or 4.2.1 are only 6 series summarized bellow. Adding to the author's experimental results presented in **Chapter 4**, they are used for examining the formulae of the dispersion coefficient in open-channel flows proposed in the previous chapters. They includes the measurements in rectangular cross-section flumes with smooth or rough bottoms, meandering flumes and the triangular cross-section flumes, therefore, they are useful for examining the applicability of the proposed models to various flows.

(1) Fischer (1966) 's Experiment

Fischer made 21 series of tracer studies in smooth or rough laboratory flumes of rectangular or trapezoidal cross-section. 11 series out of 21 series satisfy Eq. 4.2.1, however, the 6 series made in trapezoidal flumes with stone roughness at the side-boundary were exempted from the investigation in this chapter, because the velocity distributions were distorted by the stone roughness and not natural. The last 5 series of 0100, 0200, 0300, 0400 and 2500 were made in rectangular cross-section flumes and the bottom roughness was made by sand dunes or stone roughness. B/d is 2. to 7., and U/u_* 5. to 10.. Fischer conducted these experiment for verifying the Elder's theoretical work of Eq. 3.4.24, measuring the concentration distributions at a center of flows and reported that the dispersion coefficient determined by the "Moment method" are $D_M/du_* \simeq 5.17 \sim 7.17$.

(2) Michiue, Muramoto and Itami (1978) 's Experiment

They conducted 4 runs of dispersion measurements in the rectangular cross-section flume of 150m in length and 0.6m in width, therefore the dimensionless distance is quite long, however, B/d is 9. to 17., and U/u_* about 16.. The concentration measurement is made only a center of the flows except Run I. They determined the dispersion coefficient by the "Moment Method" and the "Routing Method" according to Fischer (1966). It is reported that the routed concentration distributions have the fine agreement with the observed ones and that the dispersion coefficient is $D_M/du_* \simeq 37.5 \sim 85.0$. The development of the tracer cloud was also discussed in their paper.

(3) Hayakawa, Fukushima and Sanjo (1984) 's Experiment

The measurements were conducted in the flows in rectangular cross-section flumes of 10.5m in length and 0.099m in width. The width to depth ratio is very small and $B/d \simeq 0.66 \sim 3.96$, and U/u_* about 12. The dispersion coefficient determined by the "Routing Method" were reported at $D_R/du_* \simeq 2.16 \sim 9.69$. They also measured the lateral diffusion coefficient in the similar hydraulic condition and they are $\varepsilon_3/du_* \simeq 0.20 \sim 0.30$.

(4) Glover (1964) 's Experiment

Fortcollins tests were exempted because of the requirement of Eq. 2.2.39, and only 3 runs in Allenspark experiments were used. They were done in a triangular cross-section flumes of 122m (400 ft.) in length; B/d is about 4., and U/u_* about 25.. Dispersion coefficient were determined by using the Gaussian distribution of the mathematical solution for the 1-D dispersion equation under the initial condition of Dirac's distribution, therefore its accuracy may be not so high, and $D/du_* \simeq 13.2 \sim 17.6$ was reported..

(5) Fukuoka and Sayre (1972) 's Experiment

He conducted the systematic experiments of measuring the dispersion coefficient in 25m sinuous channels. 13 runs were made in a smooth-bottom channel of 0.25m in width and 5 runs in a rough-bottom channel of 0.125m in width. The experiment covers B/d of 4. to 10. and U/u_* of 14. to 18. for the smooth-bottom channel, and B/d of 2. to 5. and U/u_* of 17. for the rough bottom channel. The measured concentration distributions were truncuated at 5% of the highest concentration, and they were used for determining the dispersion coefficient by the "Moment Method" and the "Routing Method". The objectives of the experiments were to investigate

the influence of meandering on the dispersion coefficient and $D_M/du_* \simeq 12.2 \sim 44.3$ for a smooth-bottom channel and $D_M/du_* \simeq 6.08 \sim 28.5$ for a rough-bottom channel are reported.

(6) Ikeya and Tamai (1984) 's Experiments

The dispersion coefficient in meandering channel of 3.0m in length and 0.30m in width was measured, and B/d is 10., and U/u_* 14.5. The concentration distributions were truncuated at 10% of the highest concentration and used for determining the dispersion coefficient by the "Routing Method". The dispersion coefficient reported was $D_R/du_* = 31.6$ and this value may be a little smaller because the dimensionless distance is not long enough.

5.3 Review of Previous Measurements of Longitudinal Dispersion Coefficient in Rivers

(1) Godfrey and Frederick (1970) 's Measurement

They measured the longitudinal dispersion coefficient under 10 different hydraulic conditions at 6 channel reaches in 4 natural streams, that is, Clinch River (Va.), Copper Creek (Va.), Powell River (Tenn.) and Coachella Canal (Calif.). They used Gold-198 solution as tracer injected as a line source at a water surface, and measured concentration distributions at a center of 5 to 6 cross-sections downstream. They also measured the velocity distributions at each section in detail. They will be used in Sub-sections 5.4.1 and 5.4.2. They investigated the convective velocity, and the dispersion coefficient by calculating the first, and the second temporal moments of tracer cloud. The concentration distributions were also examined by Gamma distributions.

The results of their measurements are often used by many investigators, because measurements of concentration distributions and velocity distributions as well as geometric features of channel was very detailed and reported in detail. Fischer (1968) used their data (Godfrey and Frederick, 1963) for verifying his formula of Eq. 3.4.28, and obtains the dispersion coefficient by the "Routing Method". He also referred the dispersion coefficient obtained by Thakston and Krenkel (1966). Iwasa, Aya and Toda (1981) reviewed their measured data in detail and calculated the convective velocity and the dispersion coefficient by themselves and reported that the magnitude of the dispersion coefficient obtained is 2 times more than Fischer's one in cases. The data used in the following analysis are 8 measurements referred by Fischer, but calculated

by Iwasa, Aya and Toda (1981). The magnitude of the dispersion coefficient reported by the authors is $D/du_* \simeq 122. \sim 514.$, $B/d \simeq 15.3 \sim 43.3$, and $U/u_* \simeq 1.36 \sim 15.4$. They are listed in Table 7.2.1 in **Chapter 7**.

(2) Yotsukura, Fischer and Sayre (1970) 's Measurement

They conducted the longitudinal and the transverse dispersion measurements in 141 miles reach between Sious City (Ia.) and Plattsmouth in Missouri River. The tracer used was Rhodamine WT solution and the direct sampling was made for measuring the concentration distribution. The magnitude of the dispersion coefficient has been the largest among those reported and is 16,000 ft^2/s by the Routing Method and 15,000 ft^2/s by the Moment Method.

(3) Data Summarized by Nordin and Sabol (1974)

Nordin and Sabol reported 51 results of the field measurement of tracer studies in 22 rivers in United States made by Geological Survey, U.S.. They includes the results by Godfrey and Frederick (1970), and Fischer, Yotsukura and Sayre (1970), therefore, 39 measurement results out of 51 were examined in this study. The procedures of examining data are as follows.

1. Plot $\bar{t}$ and σ_t^2 reported by Nordin and Sabol against the distance x on normal section papers, and the reach in which both of $\bar{t}$ and σ_t^2 are proportional to x is selected.
2. Calculate u_c, $\dfrac{d\sigma_t^2}{dx}$ and $D = \dfrac{u_c^3}{2}\dfrac{d\sigma_t^2}{dx}$.
3. Calculate the average hydraulic variables in the reach selected in the item 1. by use of the data listed in the tables in Nordin and Sabol.
4. Calculate the mixing time scale T_l by Eq. 2.2.37, and the required length scale by Eq. 2.2.39. θ_3 is assumed to be 0.2.
5. Select the data which satisfy Eq. 2.2.39

The 32 data measured in 17 rivers are finally used in the analysis in **Sub-section 5.4.3**. The magnitude of the dispersion coefficient by the author is $D/du_* \simeq 10. \sim 8,200$, the width to depth ratio $B/d \simeq 16. \sim 270.$, and the velocity factor $U/u_* \simeq 1.1 \sim 24.0$. Note that all the tracer insertion were not made as a line or plane source, therefore, Eq. 2.2.39 is not always varied for the criteria for the dispersion period, but the linear growth of $\bar{t}$ and σ_t^2 is assured by the first procedure.

(4) Data Summarized by McQuivey and Keefer (1974)

McQuivey and Keefer summarized the 41 field data measured in 18 rivers in United States by Geological Survey, U.S., and reported the average hydraulic variables as well as the dispersion coefficient determined by Fischer's Routing Method and the least square error method. They satisfy the conditions; 1) complete concentration distributions in the test reach are obtained, 2) concentration distributions are measured at least two sections, and 3) hydraulic variables are measured in the test reach.

Fischer discussed on their results, because the reported variables by McQuivey and Keefer are sometimes different from those by Nordin and Sabol. Therefore, the data included in Godfrey and Frederick, Yotsukura, Fischer and Sayre, and Nordin and Sabol are exempted from the following analysis, and 26 measured data in 15 rivers are finally used in the analysis. The magnitude of the dispersion coefficient reported by the writers is $D/du_* \simeq 120. \sim 5,700.$, the width to depth ratio $B/d \simeq 14. \sim 150.$, and the velocity factor $U/u_* \simeq 4.2 \sim 20.0$.

5.4 Predicting Longitudinal Dispersion Coefficient in Open-Channel Flows

5.4.1 Dispersion Coefficient in View of One–Particle Analysis

The dispersion coefficients as well as hydraulic conditions measured in laboratory flumes by the author and in natural streams by Godfrey and Frederick (1970) will be examined, because other papers do not include the detailed velocity distributions.

(1) Dispersion Coefficient

Fig. 5.4.1 compares the non-dimensional dispersion coefficient D/du_* measured by the author and calculated by Fischer (1969) for Godfrey and Frederick data with those predicted by use of Eq. 2.2.35, assuming the lateral mixing coefficient is equal to $0.2du_*$. The agreement of the measured and predicted dispersion coefficient in laboratory is very fine as already described in Section 4.5, but the measured ones in natural streams have not so fine agreement with predicted ones as those in laboratory flumes, because all the hydraulic conditions assumed in the theory were may be not satisfied. The magnitude of the turbulent diffusion term (the first term) in Eq. 2.2.35 is of the order of 1.0 and its contribution to dispersion coefficient is calculated at 10% for laboratory flumes and 1% for natural streams, therefore, it is negligibly small for calculating the dispersion coefficient in natural streams. The magnitude of the term

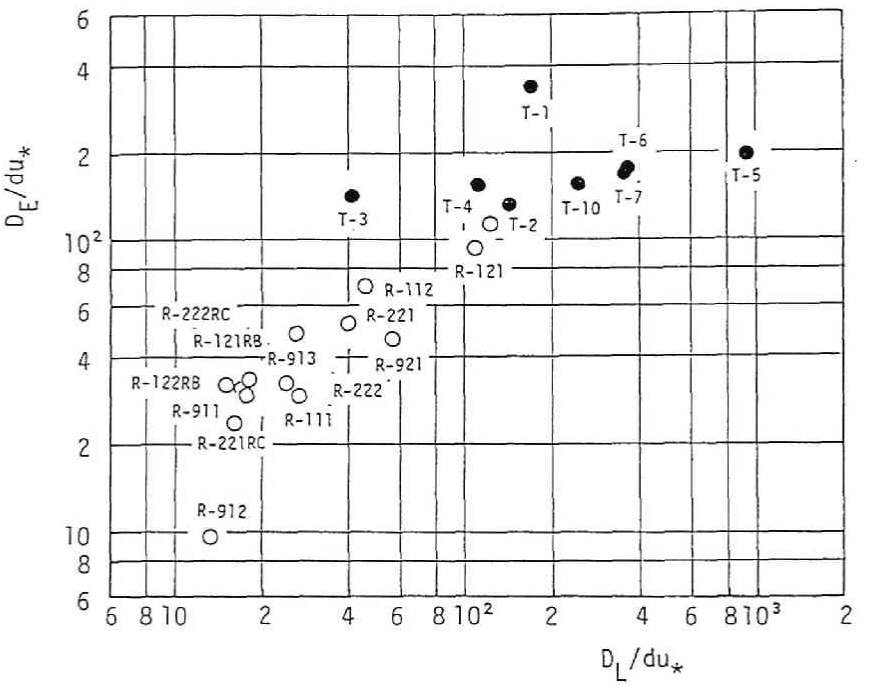

Figure 5.4.1: Dispersion coefficient measured in laboratory flumes and rivers against those predicted by Eq. 2.2.35 in view of one particle analysis. Open circles denotes the data measured in laboratory, and solid circles in rivers.

of the vertical non-uniformity of the velocity distributions (the second term) is of the order of 10. in laboratory flumes and 1. in natural streams. The contribution of the second term to the dispersion coefficient can not be negligible in laboratory, but is around 1% and negligibly small in natural streams, because the magnitude of the dispersion coefficient, which will be disclosed to be dependent on the width to depth ratio in **Sub-section 5.4.3**, increases with increase of the width to depth ratio. The magnitude of the third term, that is, the term of the lateral non-uniformity of the velocity distributions is 5.26 to 100. for laboratory flumes and 40.4 to 920. for natural streams. Therefore, the contributions of the second term is comparable to those of the third term in narrow laboratory flumes, but it is negligibly small for wide natural streams, and

$$\begin{aligned} D_L &\approx D_{Ll} = [v_l'^2]T_l \\ &\simeq \frac{1}{59.2\theta_3} J_{Al} \left(\frac{U}{u_*}\right)^2 \left(\frac{B}{d}\right)^2 du_* \\ &\qquad \text{for natural streams} \end{aligned} \tag{5.4.1}$$

Fig. 5.4.2 shows the relationship between D_L and D_{Ll}, and it is concluded that the dispersion in rivers can be approximated as the 2-D phenomena in the lateral direction.

(2) Lagrangian Turbulent Intensity

a. Eulerian turbulence term

According to the measurements in laboratory and rivers by Asano (1980), the magnitude of the cross-sectional average of the Eulerian turbulent intensity is estimated at of the order of:

$$\frac{[v_t'^2]}{u_*^2} = 1.0 \sim 2.0 \tag{5.4.2}$$

b. Turbulent intensity caused by the vertical non-uniformity of the velocity distribution

In case of the 2-D flows in which the logarithmic velocity distribution is established, the following relationship is obtained.

$$\frac{[v_v'^2]}{u_*^2} = \frac{1}{\kappa^2}$$

In case of the 3-D flows in laboratory and rivers, the following relationship is obtained.

$$\frac{[v_v'^2]}{u_*^2} = \begin{cases} 6.0 \sim 10.0 & \text{for laboratory flume} \\ 0.2 \sim 10.0 & \text{for rivers} \end{cases} \tag{5.4.3}$$

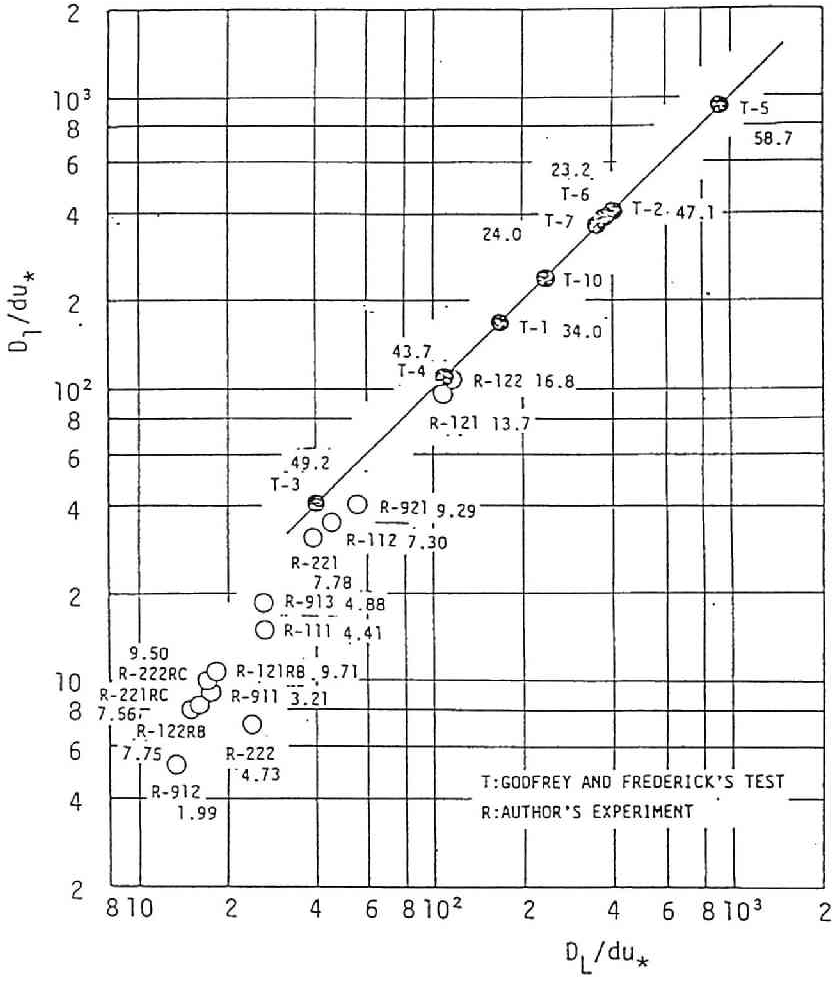

Figure 5.4.2: Dispersion coefficient calculated by Eq. 2.2.35 and those approximated by Eq. 5.4.1 for laboratory flumes and rivers. Open circles denotes the data measured in laboratory, and solid circles in rivers.

According to the data measured by Godfrey and Frederick, almost all of $[v_v'^2]/u_*^2$ has its magnitude of the order of 1.0, and not so strong.

c. Turbulent intensity caused by the lateral non-uniformity of the velocity distribution

As shown in Fig. 4.4.13, $J_{Al} = 20.0(B/d)^{-1/2}$ for laboratory flume, and therefore, the equivalent relationship is obtained as:

$$\frac{[v_l'^2]}{u_*^2} = 20.0\left(\frac{B}{d}\right)^{-0.5}\left(\frac{U}{u_*}\right)^2 \qquad \text{for laboratory flume} \qquad (5.4.4)$$

In case of the river flows, the relationship of $[v_l'^2]/u_*^2$ with B/d is presented in Fig. 5.4.3 (a), and the definite relationship is hardly obtained. Fig. 5.4.3 (b) shows the definite relationship of $[v_l'^2]/U^2$ with B/d, and its magnitude is of the order of 10.

(3) Lagrangian Integral Time Scale

In wide open-channel flows, the Lagrangian auto-correlation coefficient T_{SL} is able to be approximated as:

$$\frac{T_{SL}}{d/u_*} \equiv \frac{D/du_*}{[v_1'^2]/u_*^2} \qquad (5.4.5)$$

$$\approx \frac{[v_l'^2]}{[v_1'^2]}\frac{T_l}{d/u_*} \qquad (5.4.6)$$

Fig. 5.4.4 plots T_{SL} measured by Eq. 5.4.5 against the approximately calculated one by Eq. 5.4.6 on a logarithmic sheet, and the following relationship is obtained.

$$\frac{T_{SL}}{d/u_*} = 0.03\left(\frac{B}{d}\right)^2 \qquad \text{for} \qquad \frac{B}{d} > 10 \qquad (5.4.7)$$

Therefore, it is concluded that the dispersion can be approximated as the 2-D phenomena in the lateral direction for $B/d > 10$ in terms of the Lagrangian integral time scale. The little difference of the magnitude of the proportional constant between Eqs. 4.5.3 and 5.4.7 is cause by the magnitude of the lateral mixing coefficient and the characteristic length in rivers.

5.4.2 Dispersion Coefficient Based on Turbulent Diffusion Equation

The dispersion coefficient D_E calculated by Eq. 3.5.45 can also be approximated by D_{El} for wide open channel flows as:

$$D_E \approx D_{El} = \frac{1}{A}\int_{-b_l}^{b_l}\frac{dx_3}{dD2_{33}}\left[\int_{-b_l}^{x_3}u_{03}'dx_3'\right]^2 \simeq \frac{I_A}{\theta_3}\left(\frac{U}{u_*}\right)^2\left(\frac{B}{\bar{d}}\right)^2 du_* \qquad \text{for natural streams} \qquad (5.4.8)$$

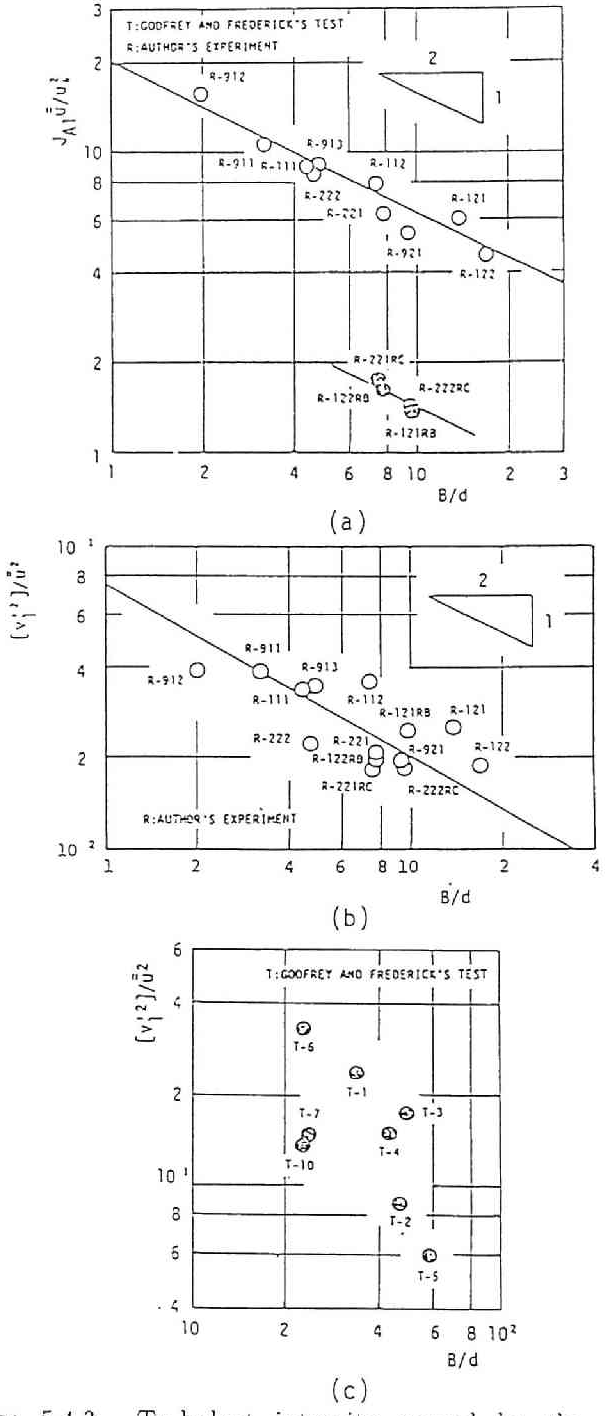

Figure 5.4.3: Turbulent intensity caused by the lateral non-uniformity of the velocity distribution. (a) $[v_l'^2]/u_*^2$ against B/d, (b) $[v_l'^2]/U^2$ against B/d in laboratory, and (c) $[v_l'^2]/U^2$ against B/d in rivers.

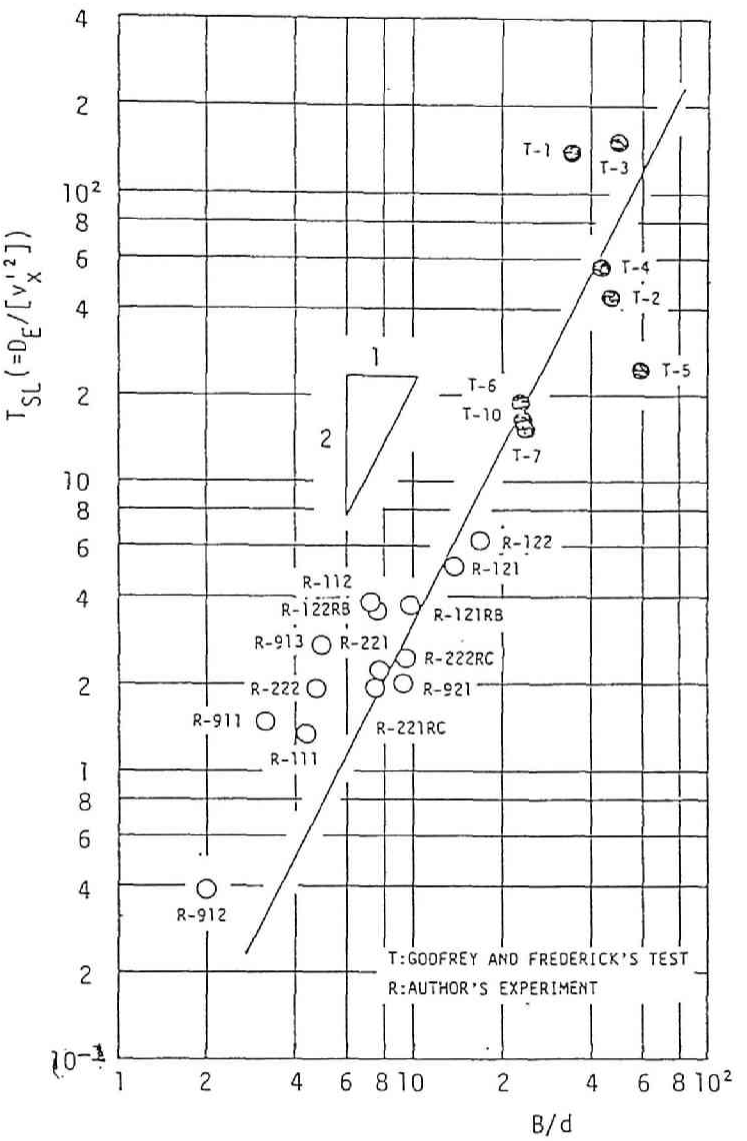

Figure 5.4.4: T_{SL} measured by Eq. 5.4.5 against the approximately calculated one by Eq. 5.4.6 on a logarithmic sheet. Open circles denotes the data measured in laboratory, and solid circles in rivers.

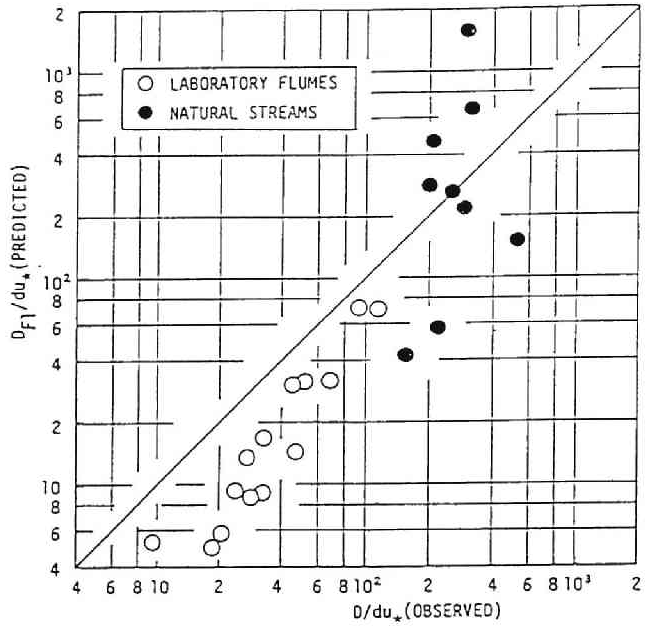

Figure 5.4.5: D/du_* measured by the author and calculated by Fischer (1969) for Godfrey and Frederick data against those predicted by use of Eq. 5.4.8, assuming the lateral mixing coefficient is equal to $0.2du_*$.

The dispersion coefficients measured in laboratory flumes by the author and in natural streams by Godfrey and Frederick (1970) were again examined. Fig. 5.4.5 compares the non-dimensional dispersion coefficient D/du_* measured by the author and calculated by Fischer (1969) for Godfrey and Frederick data with those predicted by use of Eq. 5.4.8, assuming the lateral mixing coefficient is equal to $0.2du_*$. The agreement of the measured one in natural streams with predicted ones is not so fine as those in laboratory flumes, because all the hydraulic conditions assumed in the theory were may be not satisfied.

Assuming the lateral mixing coefficient for rivers at $0.23du_*$, the dispersion coefficients calculated by Eqs. 2.2.35 and 5.4.8 by use of the velocity distributions measured in laboratory by the author and measured at each section in rivers by Godfrey and Frederick are plotted on Fig. 5.4.6. Eq. 2.2.35 gives a little larger values for laboratory flume data, because Eq. 2.2.35 includes the effects of the Eulerian turbulence and of the vertical non-uniformity of the velocity distribution, but Eq.

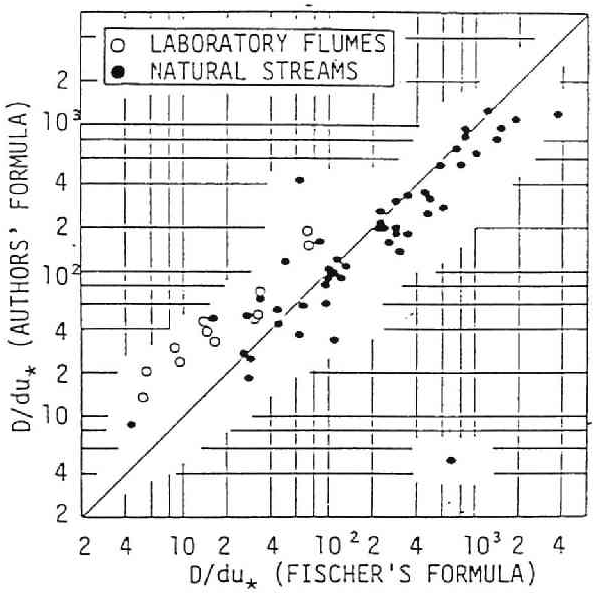

Figure 5.4.6: D_L/du_* calculated by Eq. 2.2.35 against D_{EI}/du_* by Eq. 5.4.8.

5.4.8 excludes them. As the width to depth increases, these effects becomes negligibly smaller than that of the lateral non-uniformity of the velocity distributions, the magnitude of these two kinds of dispersion coefficient becomes of the same order exempting one exceptional datum. Thus, Eq. 2.2.35 is concluded to give the same magnitude of the order as those by Eq. 5.4.8, which is equivalent to the Fischer's formula of Eq. 3.4.28 for the dispersion coefficient in rivers.

5.4.3 Dimensional Analysis of Longitudinal Dispersion Coefficient

Hydraulic conditions and the channel geometry are continuously changing from a section to a section in actual river flows. A practical way to estimate the dispersion coefficient is the application of the dimensional analysis. The mass transport processes and the mixing in open-channel flows are usually of meso- and macro-scales in hydraulic phenomena, and the hydraulic variables are then classified as

- dynamic: ρ, μ
- kinematics: $D, \varepsilon_i, U, u_*, \bar{u}_i, u_i', g$
- geometry: $B, d, \bar{d}, d_{max}, L$

where $\bar{d}$ is the hydraulic depth ($= A/B$), d_{max} the maximum local depth, L the characteristic length for the mixing, and g the gravitational acceleration. The Buckingham π theorem makes

$$\frac{D}{du_*} = \phi\left[\frac{B}{d}, \frac{d_{max}}{d}, \frac{L}{d}, \frac{U}{u_*}, \frac{\bar{u}_i}{u_*}, \frac{u_i'}{u_*(\bar{u}_i/u_*)^{1/3}}, Re, Fr\right] \tag{5.4.10}$$

where Re is the Reynolds number, and Fr the Froude number.

The functional form of ϕ and the phenomenological priority of all the dimensionless parameters consisting of ϕ have to be selected by the experimental procedures. All the experimental data come from the author described in **Chapter 4**, Fischer (1968), Muramoto et al (1978), Hayakawa et al (1984), Glover (1964), Fukuoka and Sayre (1973), and Ikeya and Tamai (1984) in laboratory measurements referred in **Section 5.2**, Godfrey and Frederick (1970), Yotsukura et al (1970), Nordin and Sabol (1974), and McQuivey and Keefer (1974) in field measurements referred in **Section 5.3**. In total, 62 different data in laboratory flumes from 7 sources, and 79 different data in actual rivers/canals from 4 sources are examined in this study.

All the data used in the study satisfy the required time/length scale of Eq. 2.2.39 for lateral mixing, and the dispersion coefficient is calculated by use of the "Moment method" or the "Routing Procedure" by the author or writers as described in **Sections 5.2** and **5.3**. The magnitude of the dispersion coefficient will be changed by the computation procedure itself.

The results obtained in **Sub-sections 5.4.1** and **5.4.2** describe the most important priority would be:

$$\frac{D}{du_*} = F\left(\frac{B}{d}, \frac{U}{u_*}\right) \tag{5.4.11}$$

which represents that the dimensionless dispersion coefficient D/du_*, as a bulk parameter of the dispersion processes is a function of the width to depth ratio B/d and the ratio of mean velocity to the shear velocity U/u_*.

Fig. 5.4.7 shows the relationship between D/du_* and B/d obtained in laboratory flumes and natural streams. Notable features seen from this figure are summarized as follows:

1. A distinct correlation of D/du_* with B/d is observed in laboratory data as well as in river/canal data.

2. A functional relationship of

$$\frac{D}{du_*} = 2.0\left(\frac{B}{d}\right)^{1.5} \tag{5.4.12}$$

can be obtained, exempting the data in laboratory flumes of small B/d, and the some data in actual rivers/canals.

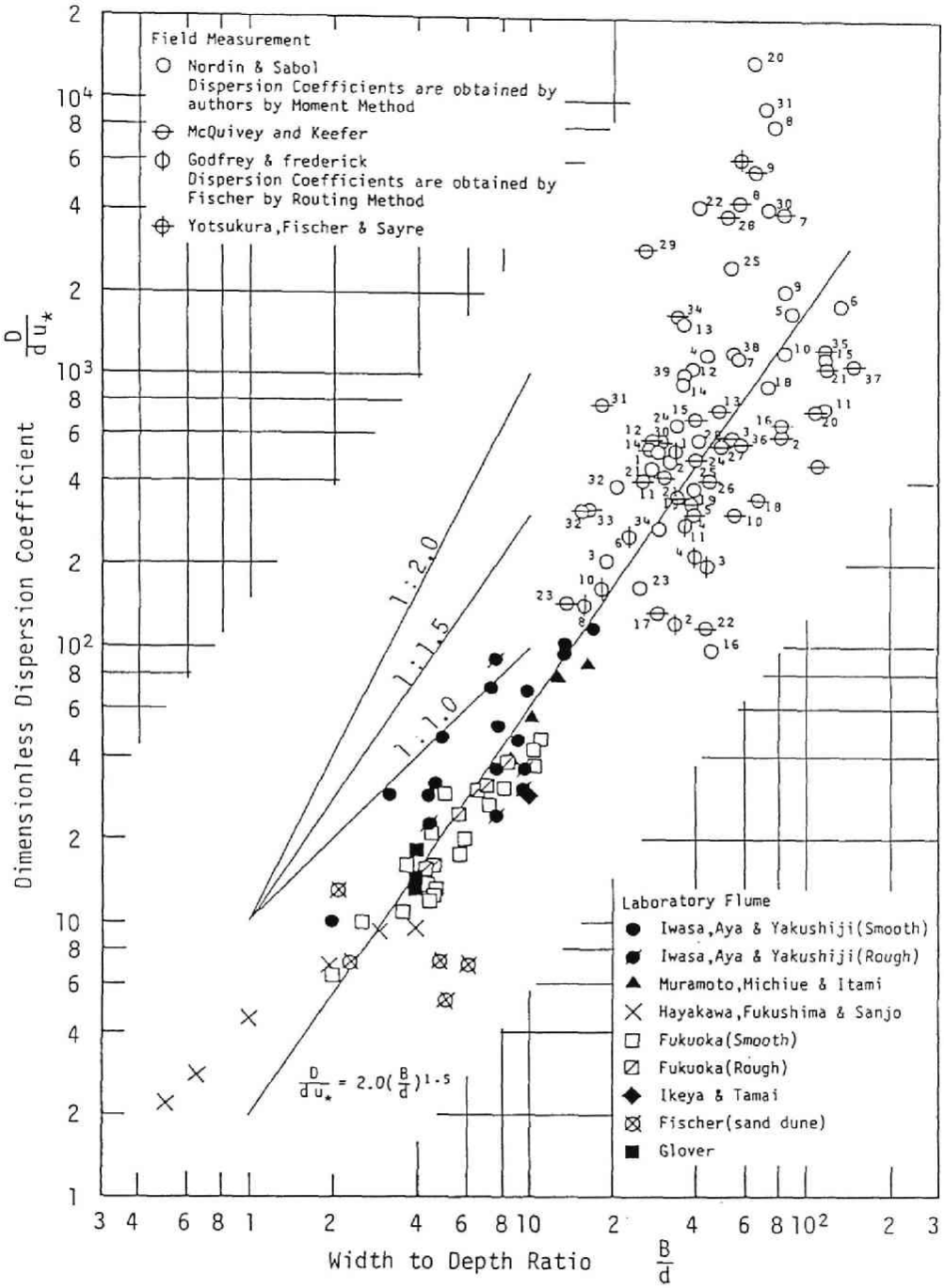

Figure 5.4.7: Dispersion coefficient measured in laboratory flumes and rivers against the width to depth ratio.

3. The influence of bends in flumes on the longitudinal dispersion is not so clear, comparing the data of the author, Muramoto et al, and Hayakawa et al in straight laboratory flumes to those of Fukuoka and Sayre, and Ikeya and Tamai in sinuous laboratory flumes.

4. The influence of bottom roughness on the longitudinal dispersion is not so large, comparing the data of the author and Fukuoka and Sayre in smooth and rough bottom flumes.

The results of the items 1. and 2. are similar to those obtained by Liu (1978) and Iwasa and Aya (1980) which mainly examined the data in rivers/canals. Eq. 5.4.12 is employed to describe the relationship of D/du_* with B/d in wide rage of the width to depth ratio in laboratory flumes as well as rivers/canals. Some data scatter around Eq. 5.4.12, and this fact suggests the influence of other parameters as described in Eq. 5.4.10, but Eq. 5.4.12 will be useful for predicting the dispersion coefficient in open-channel flows.

5.5 Conclusions

In this chapter, the applicability of the three formulae presented in the previous chapters was examined to river flows as well as to the various flows in laboratory flumes made by other investigators, and the dispersion coefficient in rivers was also investigated. The theoretical results developed in the former chapters were summarized and the objectives of this chapter were stated in **Section 5.1**. The short review of each of previous measurements in laboratory was described in **Section 5.2** and those in rivers, streams, and canals in **Section 5.3**.

The dispersion coefficient in rivers was examined in terms of one-particle analysis by use of Godfrey and Frederick's data in **Sub-section 5.4.1**. The applicability of the theoretical results described in **Chapter 2** was successfully examined to the longitudinal dispersion in rivers, though its agreement was not so fine as that in laboratory. The magnitude of the three components of the dispersion coefficient was also investigated by use of the velocity distribution data measured in rivers, and it was concluded that the 2-D approximation in the lateral direction can be possible for the dispersion in rivers. The characteristics of the velocity distributions in rivers were investigated in terms of Lagrangian dispersion theory, and it was concluded that the magnitude of the non-uniformity of the vertical direction is of the order of 1.0 to 10., and those of the lateral direction 10.. Therefore, they are comparable each other. The integral time scale and the mixing time scale were also studied, and the definite relationship of Eq. 5.4.7 for rivers was obtained.

The dispersion coefficient in rivers was also examined in terms of Eulerian analysis in **Sub-section 5.4.2**. The applicability of the theoretical results described in **Chapter 3** was successfully examined to the longitudinal dispersion in rivers, though its agreement was not so fine as that in laboratory. The dispersion coefficients calculated by Eqs. 2.2.35 and 5.4.8 by use of the velocity distributions measured in laboratory by the author and measured at each section in rivers by Godfrey and Frederick were compared, and it was concluded that the magnitude of the dispersion coefficient calculated by both of the Lagrangian method and the Eulerian method which is equivalent to Fischer's formula are of the same order in rivers.

The dimensional analysis of the dispersion coefficient was also conducted in **Sub-section 5.4.3**, and the definite relationship between D/du_* and B/d was obtained as,

$$\frac{D}{du_*} = 2.0 \left(\frac{B}{d}\right)^{1.5} \tag{5.4.12}$$

by using 62 data in laboratory and 79 data in rivers.

Thus, the conclusions in this chapter are summarized as:

1. The dispersion coefficient in rivers can be predicted by both of Lagrangian method described in **Chapter 2** and Eulerian method described in **Chapter 3** by use of the velocity distributions measured.

2. They are approximated by Eq. 5.4.1 or Eq. 5.4.8 respectively, and they give the same magnitude of the order.

3. The empirical relationship of Eq. 5.4.12 can be employed to describe the dispersion coefficient in ordinary laboratories and rivers, unless the detailed velocity distributions in a cross-section are obtained.

References in Part I

Asano, T. (1980). Study on the time-space structures of turbulence in open channel flows, Dissertation submitted to Kyoto University, in partial fulfillment of the requirements for the degree of Doctor of Engineering.

Batchelor, G. K., and Townsend, A. A. (1956). Turbulent diffusion, in "Surveys in Mechanics", edited by Batchelor, G. K. and Devious, R. M., The Cambridge University Press, London, 352–399.

Chiu, C. L., Lin. H. C., and Mizumura, K. (1978). Simulation of Hydraulic Processes in Open Channels, *J. Hydraulic Division, Proc. ASCE*, Vol. 102, No. HY5,

Elder, J. W. (1959). The dispersion of marked fluid in turbulent shear flow, *J. Fluid Mechanics*, Vol. 5, 544–560.

Fischer, H. B. (1966). Longitudinal dispersion in laboratory and Natural streams, Report No. KH-R-12, California Institute of Technology, Pasadena, California.

Fischer, H. B. (1968). Dispersion prediction in natural streams, *J. Sanitary Engineering Division, Proc. ASCE*, Vol. 94, No. SA5, 927–943.

Fukuoka, S., and Sayre, W. W. (1973). Longitudinal dispersion in sinuous channels, *J. Hydraulic division, Proc. ASCE*, Vol. 99, No. HY1, 195–217.

Glover, R. E. (1964). Dispersion of dissolved and suspended materials in flowing streams, Professional Paper 433–B, U. S. Geological Survey.

Godfrey, R. G., and Frederick, B. J. (1963). Dispersion in natural streams, Open file report, U. S. Geological Survey.

Godfrey, R. G., and Frederick, B. J. (1970). Stream dispersion of selected sites, Professional Paper 433-K, U. S. Geological Survey.

Hay, J. R., (1966). Mass transport mechanics in open channel flow, Dissertation presented to Vanderbilt University, Nashville, Tennessee., in partial fulfillment of the requirements for the degree of Doctor of Philosophy.

Hay, J. S., and Pasquill, F. (1957). Diffusion from a fixed source at a height of a few hundred feet in the atmosphere, *J. Fluid Mechanics*, 2, 299–310.

Hayakawa, N., Fukushima, Y., and Sanjo, (1984). Diffusion and dispersion in narrow open channel flow, *Proc. JSCE*, No. 342, 179–185.

Hayashi, T., and Iwasaki, M. (1975). Numerical simulation of turbulent diffusion, *Proc. 19th Japanese Conference on Hydraulics*, JSCE, 167–172, (in Japanese).

Hino, M. (1965). Digital computer simulation of random phenomena, *Trans. of JSCE*, No. 123, 33–43.

Hosoda, T. (1980). Mechanism of the longitudinal dispersion in open channel flows, Dissertation submitted to Kyoto University, in partial fulfillment of the requirements for the degree of Master of Engineering, (in Japanese).

Hosoda, T. (1990). Mechanism of the turbulent diffusion in open channel flows, Dissertation submitted to Kyoto University, in partial fulfillment of the requirements for the degree of Doctor of Engineering, (in Japanese).

Hosoda, T., and Yokoshi, S. (1985). Stochastic considerations on longitudinal dispersion, *Mem. Faculty of Eng.*, Hiroshima University, Vol. 9, No. 1, 73–75.

Ikeya, T., and Tamai, N. (1984). Dispersion in meandering channels of rectangular section, *Proc. 28th Japanese Conference on Hydraulics*, JSCE, 277–282, (in Japanese).

Inoue, E. (1952). On the structure of wind near the ground, *Bulletin of the National Institute of Agricultural Silences*, Series A, No. 2, (in Japanese).

Iwasa, Y. (1976). Mathematical aspect of one-dimensional equations of unsteady flows in open channels, *Proc. Int'l Symp. on Unsteady Flow in Open Channels*, BHRA-IAHR, D2-13–D2-24.

Iwasa, Y., and Aya, S. (1980). Dispersion coefficient of natural streams, *Proc. of the 3rd International Symposium on Stochastic Hydraulics*, JSCE-IAHR, 527–538.

Iwasa, Y., and Aya, S. (1985). Lagrangian characteristics of longitudinal mixing in free surface shear flows, *Proc. of the 21st IAHR Congress*, IEA-IAHR, Vol. 2, 180–185.

Iwasa, Y., Aya, S., and Kokado, T. (1978). Numerical Analysis of dispersive processes in natural streams, *Annuals*, Disaster Prevention Research Institute, Kyoto University, Vol. 21, B–2, 307–317, (in Japanese).

Iwasa, Y., Aya, S., and Mitsuishi, S. (1985). Lagrangian auto-correlation function in turbulent shear flow, *Annuals*, Disaster Prevention Research Institute, Kyoto University, Vol. 28, B–2, 417–427, (in Japanese).

Iwasa, Y., Aya, S., and Morita, Y., and Nishikawa, H. (1982). Lagrangian properties of mixing phenomena in bounded turbulent shear flows by means of numerical simulations, *Annuals*, Disaster Prevention Research Institute, Kyoto University, Vol. 25, B–2, 573–583, (in Japanese).

Iwasa, Y., Aya, S., and Toda, K. (1981). Analysis of some longitudinal experiments in natural streams, *Proc. 25th Japanese Conference on Hydraulics*, JSCE, 423-432, (in Japanese).

Iwasa, Y., Aya, S., and Yakushiji, K. (1984). Longitudinal dispersion coefficient of open channel flow in rectangular cross section flumes, *Annuals*, Disaster Prevention Research Institute, Kyoto University, Vol. 26, B–2, 445–460, (in Japanese).

Jain, S. (1976). Longitudinal dispersion coefficient for streams, *J. Environmental Eng. Division, Proc. ASCE*, Vol. 102, No. EE2, 465–474.

Laufer, J. (1954). The structure of turbulence in fully developed pipe flow, Report No. 1174, U. S. National Advisory Committee on Aeronautics.

Liu, H. (1977). Predicting dispersion coefficient of streams, *J. Environmental Eng. Division, Proc. ASCE*, Vol. 103, No. EE1, 59–69.

Matsuoka, Y. (1986). Modeling transport processes of water quality and its application, Dissertation submitted to Kyoto University, in partial fulfillment of the requirements for the degree of Doctor of Engineering, (in Japanese).

McQuivey, R. S., and Keefer, T. N. (1974). Simple method for predicting dispersion in streams, *J. Environmental Eng. Division, Proc. ASCE*, Vol. 100, No. EE4, 997–1010.

Michiue, M., Muramoto, Y., and Itami, M. (1978). The role of convective period in the longitudinal dispersion, *Proc. 22nd Japanese Conference on Hydraulics*, JSCE, 125–130, (in Japanese).

Muramoto, Y., Michiue, M., and Nakagawa, H. (1976). Longitudinal dispersion in open-channel flows, *Proc. 20th Japanese Conference on Hydraulics*, JSCE, 133-139, (in Japanese).

Nordin, C. F., and Sabol, G. V. C. (1974). Empirical data on longitudinal dispersion in rivers, Water Resources Investigations 20–74, U. S. Geological Survey.

Okoye, J. K. (1970). Characteristics of transverse mixing in open-channel flows, Report No. KH-R-23, California Institute of Technology, Pasadena, California.

Parker, F. L.(1961). Eddy diffusion in reservoirs and pipelines, *J. Hydraulics Division, Proc. ASCE*, Vol.87, No. HY3, 151–171.

Rouse, H. (1958). "Advanced Mechanics of Fluid", John Wiley & Sons, New York.

Sooky, A. A. (1969). Longitudinal dispersion in open channels, *J. Hydraulic Division, Proc. ASCE*, Vol. 95, No. HY4, 1327–1346.

Sullivan, P. J. (1971). Longitudinal dispersion within a two-dimensional turbulent shear flow, *J. Fluid Mechanics*, Vol. 49, Part 3, 551–576.

Sumitomo, H. (1976). Water quality management, in "Water Quality Engineering", edited by T. Goda, Maruzen, Tokyo, (in Japanese).

Tanaka, M. (1979). Numerical experiments on the dispersion process at the initial time stage in the open channel flow, –Studies on the dispersion process in open channel flow (I)–, *Trans. JSIDRE*, Vol. 84, 44-51, (in Japanese).

Taylor, G. I. (1921). Diffusion by continuous movements, *Proc. London Mathematical Society*, Series 2–20, 196–211.

Taylor, G. I. (1953). Dispersion of soluble matter in solvent flowing slowly through a tube, *Proc. Royal Society of London*, Series A, Vol. 219, 186–203.

Taylor, G. I. (1954). The dispersion of matter in turbulent flow through a pipe, *Proc. Royal Society of London*, Series A, Vol. 223, 446–468.

Tennekes, H., and Lumley, J. L. (1972). "A first course in turbulence", The MIT Press, Cambridge, Massachusetts.

Thakston, E. L. and Schnelle, K. B., (1970). Predicting Effects of Dead Zones on Stream Mixing, *J. Sanitary Engineering Division, Proc. ASCE*, Vol. 96, No. SA2, 319-331.

Thakston, E. L. and Krenkel, P. A. (1966). Longitudinal mixing and reaeration in natural streams, Technical Report No. 7, Sanitary and Water Resources Engineering, Vanderbilt University, Nashville, Tennessee.

Thomas (1958). Dispersion in open channel flow, Dissertation submitted to Northwestern University, in partial fulfillment of the requirements for the degree of Doctor of Philosophy.

Tominaga, A., Nezu, I., Ezaki, K., and Nakagawa, H. (1989). *J. Hydraulic Research*, IAHR, Vol. 27, No.1, 149–173.

Valentine, E. N., and Wood, I. R. (1977). Longitudinal dispersion with dead zones, *J. Hydraulic Division, Proc. of ASCE*, Vol. 103, No. HY. 9, 975–990.

Yakushiji, K. (1983). Longitudinal mixing and dispersion coefficient in open-channel flows, Dissertation submitted to Kyoto University, in partial fulfillment of the requirements for the degree of Master of Engineering, (in Japanese).

Yotsukura, N., and Fiering, M. (1964). Numerical solution to a dispersion equation, *J. Hydraulics division, Proc. ASCE*, Vol. 90, No. HY5, 83–104.

Yotsukura, N., Fischer, H., and Sayre, W. W. (1970). Mixing characteristics of the Missouri river between Sioux city Iowa, and Plattsmouth Nebraska, Water–supply paper, 1899–G, U. S. Geological Survey.

Yotsukura, N., and Kilpatrick, F. A. (1973). Tracer simulation of soluble waste concentration, *J. Environmental Eng. Division, Proc. ASCE*, Vol. 99, No. EE4, 499–515.

PART II:

DISPERSION PROCESSES IN OPEN–CHANNEL FLOWS

Chapter 6

DISPERSION BASED ON DISCONTINUOUS MOVEMENTS OF A PARTICLE

6.1 Introduction and Objectives

On the longitudinal concentration distributions, Taylor (1953) initially pointed out the importance of the convective transport by the longitudinal component of the Eulerian velocity, and described the longitudinal dispersion coefficient in laminar flows in a tube. McQuivey and Keefer (1976) proposed the "Convective Models" which was based on the logarithmic distribution of the temporal averaged velocity. They successfully applied their models to the field measurement data for the longitudinal dispersion in natural streams. Sayre (1977) discussed that McQuivey and Keefer's models should be modified in its application to natural streams, because the velocity distributions are 3-D in natural streams. Shimada (1980) studied the longitudinal dispersion in turbulent shear flows in pipes and 2-D open-channel flows by the stochastic approach and succeeded to explain the skewed concentration distributions by the statistical properties of the velocity distribution.

This chapter will investigate the concentration distributions in open-channel flows in view of the discontinuous movements of a particle. Studying the concentration distributions is equivalent to doing the probability density distribution of the location of a particle as discussed in detail in Monin and Yaglom (1965). The normalized three-dimensional concentration distribution $\bar{c}_n(x_i;t)$ is equivalent to the probability density distribution of the location of a particle $P'(x_i,t)$, and the normalized one-dimensional concentration distribution in the longitudinal direction $C_n(x_1;t)$ is also equivalent to the one-dimensional probability density distribution of the location of

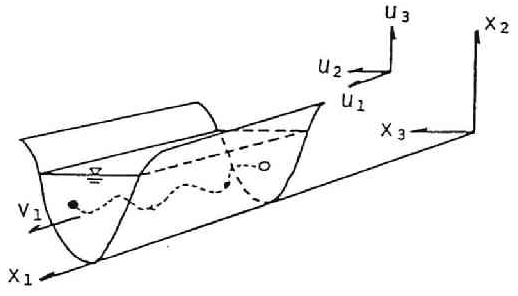

Figure 6.1.1: Definition of symbols and coordinate system.

a particle $P(x_1;t)$:

$$P(x_1;t) = \int_A P'(x_i;\, t)dx_2dx_3 \tag{6.1.1}$$

where x_i is the space coordinate, that is, x_1 the space coordinate in the longitudinal direction, x_2 the space coordinate in the vertical direction, and x_3 the space coordinate in the lateral direction.

The behaviors of the ensemble average and the variances of the location of a particle in turbulent shear flows have already been discussed in detail in view of continuous movements of a particle in **Chapter 2**, however, the probability density distributions and other information on the location of a particle has not yet been discussed. Therefore, this chapter will study the probability density distributions of the location of a particle, being based on Lagrangian movements of a particle in turbulent shear flows. In case that the probability density function (**PDF**) of the Lagrangian turbulent velocity of a particle is different from the normal (Gaussian) distribution, the higher moments are required to describe the **PDF** of the location of a particle, and it is a little complicated to know the behavior of the corresponding higher Lagrangian correlation in view of the continuous movements of a particle. Therefore, the movements of a particle will be modeled by the discontinuous movements and the **PDF** of the location of a particle in the longitudinal direction will be discussed in this chapter.

6.2 Displacement of a Particle by Discontinuous Movement

6.2.1 Mathematics of Probability and Statistics

The **PDF** of the random variable y is defined by

$$\int_a^b f(y)dy \equiv \mathbf{P}[a < y < b] = \frac{\partial F}{\partial y} \tag{6.2.1}$$

where $f(y)$ is the PDF of y, and $F(y)$ the cumulative distribution function (**CDF**) of y defined by

$$F(y) = \mathbf{P}[Y < y] \equiv \int_{-\infty}^{y} f(\eta)d\eta \tag{6.2.2}$$

The characteristic function $\phi(y)$ of a random variable y is defined by

$$\phi(k) \equiv \int_{-\infty}^{\infty} e^{jyk} f(y)dy, \qquad (j^2 = -1) \tag{6.2.3}$$

where k is the parameter, and the inverse-transformation of the characteristic function defined by

$$f(y) = \frac{1}{2\pi} \int_{-\infty}^{\infty} e^{-jyk} \phi(y)dk \tag{6.2.4}$$

gives the **PDF** of y. The derivative of the characteristic function with respect to the parameter k gives the moment as:

$$\phi^{(r)}(0) \equiv \left[\frac{d^r \phi(k)}{dk^r} \right]_{k=0} = j^r m'_r \tag{6.2.5}$$

where m'_r is the r-th moment around $y = 0$ defined by:

$$m'_r \equiv \int_{-\infty}^{\infty} y^r f(y)dy \tag{6.2.6}$$

6.2.2 Discontinuous Movements of a Particle

Stochastic approach for convective transport of the tracer cloud derived by Shimada (1980) can be rewritten in the following forms in view of the discontinuous movement of a particle based on the Lagrangian modeling.

Consider the behavior of the particle released at the position $\boldsymbol{x} = \boldsymbol{a} = (0, a_2, a_3)$ at time $t = 0$ in the confined 3-D turbulent shear flows, where $\boldsymbol{a}$ is an arbitrary position in a cross-section at $x_1 = 0$. Denoting the longitudinal component of the Lagrangian turbulent velocity of a particle which was located at $\boldsymbol{X}_{i-1}(\boldsymbol{a}, t_{i-1})$ at $t = t_{i-1}$ by

$$v'_{1i} \equiv v'_1(\boldsymbol{a}, t_{i-1})$$

and assuming

$$v'_{1i} = \text{Const.} \qquad \text{for} \quad \sum_{i=1}^{i-1} \Delta t_i \leq t < \sum_{i=1}^{i} \Delta t_i$$

the fluctuation of a particle displacement in the longitudinal direction $\Delta X'_i$ at $t = \Delta t_i$ from the mean displacement

$$[\Delta X'_i] = [v'_{1i} \Delta t_i] = 0$$

is calculated at

$$\Delta X'_i = v'_{1i} \Delta t_i \tag{6.2.7}$$

by use of Eq. 2.2.15.

After n time steps, the fluctuation of the longitudinal displacement of a particle X'_n is written as:

$$X'_n = \Delta X'_1 + \Delta X'_2 + \cdots + \Delta X'_i + \cdots + \Delta X'_n \tag{6.2.8}$$

assuming that a particle obtains different Lagrangian velocity $v'_{1i+1} = v'_1(\boldsymbol{a}, t_i)$ at a point $\boldsymbol{X}(\boldsymbol{a}, t_i)$ where a particle arrived after the migration period Δt_i from a point $\boldsymbol{X}(\boldsymbol{a}, t_{i-1})$, and t_n is calculated at:

$$t = t_n = \Delta t_1 + \Delta t_2 + \cdots + \Delta t'_i + \cdots + \Delta t'_n \tag{6.2.9}$$

The Lagrangian turbulent velocity in the longitudinal direction is defined by

$$v'_1(\boldsymbol{a}, t) = u'_1(\, \boldsymbol{X}(\boldsymbol{a}, t),\, t) + u''_{23}(\, \boldsymbol{Y}(\boldsymbol{a}, t)\,) + \bar{u}^{x_2}(\, \boldsymbol{Z}(\boldsymbol{a}, t)\,) - U \tag{2.2.9}$$

$$v'_1(\boldsymbol{a}, t) = v'_t(\boldsymbol{a}, t) + v'_v(\boldsymbol{a}, t) + v'_l(\boldsymbol{a}, t) \tag{2.2.13}$$

and a random variable, because a particle migrates in a cross-section, and therefore $\Delta X'_i$ is also random as already shown in **Chapter 2.**

Following notes are important. In the simulation models in **Chapter 2**, the movements of a particle is stated by the similar models, and the Lagrangian velocity is decided by a location of a particle in a cross-section as described:

$$v'_t(\boldsymbol{a}, t) = u'_1\,(\, \boldsymbol{X}(\boldsymbol{a}, t),\, t) \tag{2.2.10}$$

$$v'_v(\boldsymbol{a}, t) = u''_{23}\,(\, \boldsymbol{Y}(\boldsymbol{a}, t)\,) \tag{2.2.11}$$

$$v'_l(\boldsymbol{a}, t) = \bar{u}^{x_2}\,(\, \boldsymbol{Z}(\boldsymbol{a}, t)\,) - U \tag{2.2.12}$$

and a particle location in the three-dimensional space is decided by

$$\boldsymbol{X}(a,t) = \int_0^t v(a,t')dt' + a \tag{2.2.2}$$

That is, in the models in **Chapter 2**, a particle is given a random velocity v_t' and obtains a random velocity v_1' by the random movement of a particle in a section. On the contrary, in the models of Eqs. 6.2.7 to 6.2.9 presented in this chapter, the Lagrangian turbulent velocity v_{1i+1}' is assumed to be random and independent on v_{1i}', therefore, the location of a particle in a cross section at $t_l = \sum_{i=1}^{l} \Delta t_i$ is assumed not to be dependent on the particle location at $t_{l-1} = \sum_{i=1}^{l-1} \Delta t_i$. This assumption is equivalent to the complete mixing in a cross-section.

The **PDF** of the Lagrangian turbulent velocity fluctuation v_1' is defined by

$$\mathbf{P}[a < v_1' < b] \equiv \int_a^b f(v_1')dv_1' \tag{6.2.10}$$

By use of Eq. 6.2.10 and the transformation of the random variable v_1' to $\Delta X'$ by Eq. 6.2.7, **PDF** of $\Delta X'$ is written as

$$g(\Delta X') = \frac{f(\Delta X'/\Delta t)}{\Delta t} \tag{6.2.11}$$

where $g(\Delta X')$ is the **PDF** of $\Delta X'$.

The Lagrangian turbulent velocity v_1' is assumed to be independent each other in the sense of probability, therefore, the displacement $\Delta X'$ is also independent each other and the first and the second central moments of $\Delta X'$ is written as:

$$[\Delta X'] = \Delta t \int_{-\infty}^{\infty} v_1' f(v_1')dv_1' \tag{6.2.12}$$

and

$$[\Delta X'^2] = (\Delta t)^2 [v_1'^2] \tag{6.2.13}$$

because of $[v_1'] = 0$ and $[\Delta X'] = 0$, where [ ] denotes the ensemble average.

Since $\Delta X_i'$ is independent each other, the average and the variance of the location of the particle $X_n' = \sum_{1=1}^{n} \Delta X_i'$ at $t = \sum_{i=1}^{n} \Delta t_i$ are obtained as:

$$[X_n'] = \sum_{i=1}^{n} [\Delta X_i'] = 0$$

and

$$[X_n'^2] = \sum_{i=1}^{n} (\Delta t_i)^2 [\Delta v_1'^2] \tag{6.2.14}$$

where $[X_n']$ is the average of X_n', and $[X_n'^2]$ the variance of X_n' at $t = \sum_{i=1}^{n} \Delta t_i$.

In case that the time step n is not so large enough, the **PDF** of a particle location X_n' is influenced by and dependent on $g(\Delta X')$, that is, $f(v_1')$. In case n is large enough, the "Central Limit Theorem" assures that the variable defined by

$$Y_n' \equiv \frac{X_n'}{\sqrt{n \sum_{i=1}^{n} (\Delta t_i)^2 [v_1'^2]}} \tag{6.2.15}$$

is described by the standard normal distribution, even if the **PDF** of the turbulent velocity is not the normal distribution. (The Bessel's correction coefficient is ignored in Eq. 6.2.15.) The "Central Limit Theorem" is also established in case that the populations of ΔX_l at each time $t = \sum_{i=1}^{l} \Delta t_i$ are different each other. Therefore, in case that the **PDF** of $\Delta X'$ is varied in the longitudinal direction, that is, the **PDF** of v_1' is varied in the longitudinal direction, the concentration distribution becomes the Gaussian, if the time step n is large enough. Thus, the establishment of the convective dispersion equation is again verified in view of the statistical analysis of discontinuous movements of a particle.

6.2.3 Statistical Properties of the Location of a Particle

The **PDF** of v_{1_i}' is assumed not to be varied in the longitudinal direction in the following analysis, and this assumption is satisfied in the confined flows uniform in the longitudinal direction. Δt_i is also assumed to be constant hereafter.

The characteristic function $\phi(k)$ for the Lagrangian velocity fluctuation v_1' is defined by:

$$\phi(k) \equiv \int_{-\infty}^{\infty} e^{jv_1'k} f(v_1') dv_1', \qquad (j^2 = -1) \tag{6.2.16}$$

Since the Lagrangian turbulent velocity for $(i-1)\Delta t < t \leq i\Delta t$ is assumed to be independent on the Lagrangian turbulent velocity for other time steps, the characteristic function $\psi(k)$ for the sum X_n' of independent random variables $\Delta X_i'$

$$X_n' = (v_{11}' + v_{12}' + \cdots + v_{1_i}' + \cdots + v_{1_n}')\Delta t \tag{6.2.17}$$

is the product of each of the characteristic function:

$$\psi(k) = \{\phi(k)\}^n \tag{6.2.18}$$

The inverse-transformation of Eq. 6.2.18 gives the probability density distribution of the displacement of a particle as:

$$P(X_n') = \frac{1}{2\pi} \int_{-\infty}^{\infty} \exp(-j \frac{X_n'}{\Delta t} k) \{\phi(k)\}^n \, dk \tag{6.2.19}$$

and by denoting the operation of the convolution by $*$:

$$f(y) * g(y) \equiv \int_{-\infty}^{\infty} f(y')g(y-y')dy'$$

$P(X_n')$ can be rewritten in the form of

$$P(X_n') = P(X_{n-1}') * P(X_1') \tag{6.2.20}$$

The moments of $P(X_n)$ are obtained as:
the first moment

$$[X_n'] = 0 \tag{6.2.21}$$

the variance

$$[X_n'^2] = n[v_1'^2](\Delta t)^2 \tag{6.2.22a}$$

and since t is equal to $n\Delta t$, Eq. 6.2.22a can be written as

$$[X_n'^2] = \Delta t[v_1'^2]\, t \tag{6.2.22b}$$

the dispersion coefficient defined by Eq. 2.1.2a is derived as

$$D = \frac{1}{2}[v_1'^2](\Delta t) \tag{6.2.23}$$

By use of Eqs. 2.1.2b and 6.2.23, the magnitude of the time step should be

$$\Delta t = 2T_{SL} \tag{6.2.24}$$

6.3 Longitudinal Dispersion in Turbulent Shear Flows

6.3.1 Probability Density Distribution of Lagrangian Turbulent Velocity

As shown in Chapter 2, the longitudinal dispersion processes in 3-D turbulent shear flows can be decomposed into three components as:
Lagrangian turbulent velocity in the longitudinal direction

$$v_1'(a,t) = v_t'(a,t) + v_v'(a,t) + v_l'(a,t) \tag{2.2.13}$$

Dispersion coefficient

$$D_L = [v_x'^2]T_{SL} = [v_t'^2]T_t + [v_v'^2]T_v + [v_l'^2]T_l \tag{2.2.35}$$

Time-dependent behavior of the variance

$$B_L(\tau) = [v_t'^2]\exp(-\tau/T_t) + [v_v'^2]\exp(-\tau/T_v) + [v_l'^2]\exp(-\tau/T_l) \tag{2.2.30}$$

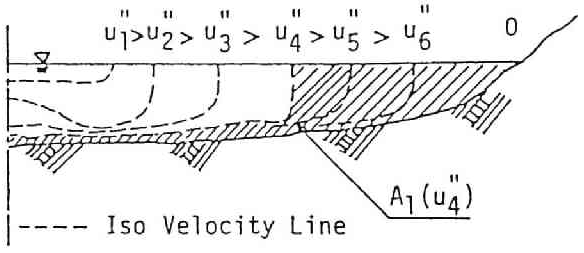

Figure 6.3.1: 3-D velocity distribution and the cummulative area A_1 where the Lagrangian turbulent velocity V_1' is less than $v_1' = u_1''$. The hatched area denotes $A_1(u_4'')$. CDF is equal to $F = A_1/A$.

and it was disclosed that the effect of the Eulerian turbulence is much smaller than those of the non-uniformity of the time-averaged velocity in the vertical and lateral directions.

Neglecting the effect of the Eulerian turbulence, and noting that the Lagrangian turbulence can be realized and be random by the random movements of a particle in a section, the cumulative distribution function CDF of the Lagrangian turbulence is:

$$F(v_1') = \mathrm{P}[V_1' < v_1'] = \frac{A_1(u_1'')}{A} \tag{6.3.1}$$

$$u_1'' \equiv \bar{u}_1 - U \tag{6.3.2}$$

where A is the cross-sectional area, A_1 the cumulative area in which Lagrangian turbulent velocity V_1' is less or equal to $v_1'(= u_1'')$, $\bar{u}_1$ Eulerian temporally averaged velocity, and U the cross-sectional averaged velocity equal to the average of Lagrangian velocity $[v_1]$. The relationship between $F(v_1')$ and the 3-D velocity distribution is presented in Fig. 6.3.1. By use of Eqs. 6.2.1 and 6.3.1, the PDF of the Lagrangian turbulence is obtained as:

$$f(v_1') = \frac{dF(v_1')}{dv_1'} = \frac{dF(u_1'')}{du_1''} = \frac{1}{A}\frac{dA_1(u_1'')}{du_1''} \tag{6.3.3}$$

6.3.2 Longitudinal Dispersion in 2-D Turbulent Shear Flows

In case of 2-D turbulent shear flows, let assume the logarithmic velocity distribution of Eq. 6.3.4 is established:

$$\frac{\bar{u}_1 - U}{u_*} = \frac{1}{\kappa}(\ln \frac{x_2}{d} + 1) \tag{6.3.4}$$

where u_* is the friction velocity, κ von Karman's constant, d the channel depth, and x_2 the depth-wise coordinate. By use of Eq. 6.3.3, the **PDF** of v_1' is written in the form of:

$$f(v_1') = f(u_1'') = \frac{\kappa}{u_*} \exp\left\{\frac{\kappa}{u_*}(u_1'' - \frac{u_*}{\kappa})\right\} \tag{6.3.5}$$

where

$$u_1'' = \bar{u}_1 - U = \frac{u_*}{\kappa}(\ln \eta + 1), \qquad (\eta = \frac{x_2}{d}) \tag{6.3.6}$$

and the **PDF** of $\Delta X' = v_1' \Delta t$ is:

$$g(\Delta X') = \frac{\kappa}{u_*} \exp\left\{\frac{\kappa}{u_*}(\frac{\Delta X'}{\Delta t} - \frac{u_*}{\kappa})\right\} \frac{1}{\Delta t} \tag{6.3.7}$$

Eqs. 6.3.5 and 6.3.7 show that the **PDF** of v_1' and the **PDF** of $\Delta X'$ is described by the exponential distribution:

$$g(\Delta\xi) = \lambda \exp(-\lambda \Delta\xi) \tag{6.3.8}$$

where

$$\lambda \equiv \frac{\kappa}{u_* \Delta t} \tag{6.3.9}$$

and

$$\Delta\xi \equiv \Delta X' - u_{1max}'' \Delta t \tag{6.3.10}$$

$$u_{1max}'' \equiv \bar{u}_1|_{\eta=1} - U = \frac{u_*}{\kappa}$$

The average μ is

$$\mu = \frac{1}{\lambda} \tag{6.3.11}$$

and the variance σ^2

$$\sigma^2 = \frac{1}{\lambda^2} \tag{6.3.12}$$

Therefore, the **PDF** of the displacement of a particle after n steps is described by the Earling distribution by use of Eqs. 6.2.16 to 6.2.19

$$P_n(\xi) = \frac{\lambda(\lambda\xi)^{n-1}}{(n-1)!} \exp(-\lambda\xi) \qquad \text{for} \quad \xi > 0 \tag{6.3.13}$$

where

$$\xi \equiv -(x - u_{1max}t) \tag{6.3.14}$$

and

$$u_{1max} = \bar{u}_1|_{\eta=1}$$

$$t = n\Delta t \tag{6.3.15}$$

and the average:

$$\mu_\xi = \frac{n}{\lambda} = (\frac{u_*}{\kappa})(n\Delta t) \tag{6.3.16}$$

and the variance:

$$\sigma_\xi^2 = \frac{k}{\lambda^2} = \left(\frac{u_*}{\kappa}\right)^2 n\Delta t^2 \tag{6.3.17}$$

Note the Earling distribution converges on the Gaussian distribution with increase of the parameter n.

The results obtained in **Sections 6.2 and 6.3** are almost equivalent to the results by McQuivey and Keefer (1976), Sayre (1977), and Shimada (1980). In their analysis, it is assumed that inserted dispersant is convected by the longitudinal velocity non-uniformly distributed, and completely mixed after $t = \Delta t$. In the models described here in this study, the dispersion phenomena is dealt with in view of the Lagrangian analysis of a particle, and the movement of a particle is modeled by the discontinuous movements. They deprive the phenomena of features of continuous movements disclosed in **Chapter 2**, but following results are obtained.

1. In the region near the releasing point, the **PDF** of the displacement of a particle is extremely dependent on the **PDF** of the Lagrangian velocity fluctuation of a particle. Its difference from the Gaussian distribution can cause the skewed distribution of the concentration.

2. When n is large enough, the concentration distribution converges on the Gaussian distribution by the "Central Limit Theorem", even if the **PDF** of the Lagrangian turbulent velocity is arbitrary.

3. In the 2-D open-channel flows, the concentration distribution will be approximated by the Earling distribution. The parameter n in the Earling distribution should be replaced by the real number k in view of the continuous movements of a particle, and the distribution should be the gamma distribution.

6.4 Longitudinal Dispersion in 3-D Turbulent Shear Flows

6.4.1 Period Required for Particle Migration

The **PDF** of the Lagrangian turbulent velocity v_1' is theoretically obtained by Eq. 6.3.3, however the direct use of Eq. 6.3.3 for 3-D turbulent shears flows should be carefully examined. The most important assumption introduced in the theory described in **Sections 6.2** and **6.3** is the independence of the random variable v_{1i}' in the sense of probability. This independence is established by the migration of a particle in view of the continuous movement of a particle. The order of the magnitude of the period required for the establishment of the independence of v_{1i}' is expected at T_{SL} by Eq. 6.2.24. However, the integral time scale is the different idea from the mixing time scale as discussed in **Chapter 2**. The migration period required for the independence of v_{1i}' in 3-D turbulent shear flows is dependent on the particle location and the width to depth ratio as will be discussed below.

As described in **Chapter 2**, T_{SL} in 3–D turbulent shear flows can be decomposed into three components:

$$T_{SL} = \frac{[v_t'^2]}{[v_1'^2]}T_t + \frac{[v_v'^2]}{[v_1'^2]}T_v + \frac{[v_l'^2]}{[v_1'^2]}T_l \tag{2.2.34}$$

$[v_t'^2]/[v_1'^2]T_t$ is negligibly small in ordinary 2-D or 3-D turbulent shear flows. Therefore, T_{SL} has only one component T_v, and the assumption that the required period does not have any relationships with the location a particle in a cross-section is valid in case of 2-D turbulent flows. On the contrary, this assumption is not acceptable for 3-D turbulent shear flows, because the required period for migration depends on the location of a particle. Let assume two particles locating at different positions in a channel, that is, "Particle A" near the channel side, and "Particle B", near the bottom in the center of the channel and that the both of Lagrangian velocity of two particles are the same. (Refer Fig. 6.4.1). The required time for the "Particle A" to get the maximum velocity is of the order of T_l, however, that is of the order of T_v for the "Particle B". Thus, the required time for migration between the maximum velocity point and the minimum velocity point is quite different and depends on the location of a particle. This is also explained by Eq. 2.2.34, which states the model for T_{SL}. T_{SL} has two components of $[v_v'^2]/[v_1'^2]T_v$ and $[v_l'^2]/[v_1'^2]T_l$ in 3-D turbulent flows, and the order of the magnitude of T_l which describes the mixing time scale in the lateral direction is much larger than that of T_v which describes the mixing time scale in the vertical direction in wide open-channel flows as demonstrated in

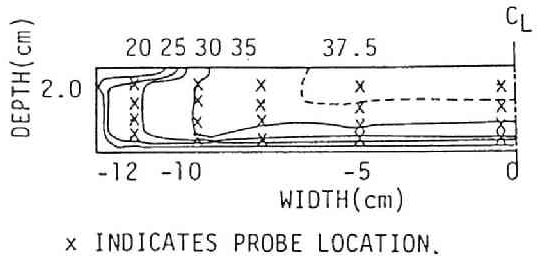

Figure 6.4.1: Iso-velocity contour map in Run 921, and the migration of a particle.

Chapter 2. Therefore, the discussion on the results of McQuivey and Keefer (1976) by Sayre (1977) should be re-considered carefully.

6.4.2 Modeling Dispersion Processes in 3-D Turbulent Shear Flows

In wide open-channel flows, the non-uniform distributions of the depth-averaged velocity in the lateral direction is dominant over the longitudinal dispersion processes. Assume that the Eulerian turbulence and the non-uniformity of the velocity distributions in the vertical direction is much less effective on the dispersion processes in 3-D turbulent shear flows than the non-uniformity of the velocity distribution in the lateral direction, then the theoretical results presented in **Sections 6.2** and **6.3** will be re-written as follows.

The Lagrangian turbulent velocity v_1' should be replaced with the Lagrangian turbulence component caused by the lateral non-uniformity of the depth-averaged velocity v_l':

$$v_1' \approx v_l' \tag{6.4.2}$$

where v_l' is defined by Eq.2.2.12 in **Chapter 2**. Therefore, **CDF** of v_l' is stated as:

$$F(v_l') = \mathrm{P}[V_l' < v_l'] = \frac{A_1(\bar{u}^{x_2})}{A} \tag{6.4.3}$$

where $\bar{u}^{x_2}$ is the depth-averaged velocity introduced in **Chapter 2**, and **PDF** of v_l' is written as:

$$f(v_l') = \frac{dF(v_l')}{dv_l'} = \frac{dF(\bar{u}^{x_2})}{d\bar{u}^{x_2}} = \frac{1}{A}\frac{dA_1(\bar{u}^{x_2})}{d\bar{u}^{x_2}} \tag{6.4.4}$$

The dispersion coefficient obtained in **Chapter 2** can be approximated by:

$$D_L \approx [v_l'^2]T_l \tag{6.4.5}$$

for wide open-channel flows, therefore, the relationship of Eq. 6.2.20 is rewritten as:

$$\Delta t = 2T_l \tag{6.4.6}$$

Other relationships are also obtained by replacing v_1' with v_l', and T_{SL} with T_l respectively.

As shown in Fig. 6.5.1 in the next section, the **PDF** of v_l' in rectangular cross-section laboratory flumes can be approximated by the exponential distribution, then the concentration distribution in rectangular cross-section laboratory flumes again can be represented by the Earling distribution as well as those in 2–D open-channel flows. However, the order of the magnitude of the dispersion coefficient and the required time scale for migration, that is, the order of the magnitude of the time step is much bigger than those in 2–D flows.

McQuivey and Keefer (1977) made simulations by means of their "Convective Model" through the series of the operation of the convolution. Their simulated results are compared with the results in laboratory flumes and the field-measurements, and they are quite agreed each other. In their analysis, the parameters are decided by the trial and error method, and it is concluded that the magnitude of the time step Δt should be equal to Fischer's time scale T_{Fl} of Eq. 2.1.8, which is equal to T_l. This result confirms the above consideration valid.

6.5 Concentration Distributions in Laboratory

Assuming the non-uniform velocity distributions in the lateral direction is dominant over the dispersion in 3-D open-channel flows, the longitudinal concentration distributions in 3-D open channel flows are theoretically discussed in **Section 6.4**. Fig. 6.5.1 shows the lateral distributions of the depth-wise averaged velocity measured in the author's experiment Run 921 on a log-normal sheet and it is disclosed that the logarithmic velocity distribution in the lateral direction is almost established. Therefore, the concentration distributions in Run921 are expected to be described by the gamma distribution. The measured concentration distributions were in the time coordinate, and the direct approximation for the concentration distributions by the **PDF** of the gamma distribution in the time coordinate will be examined in this

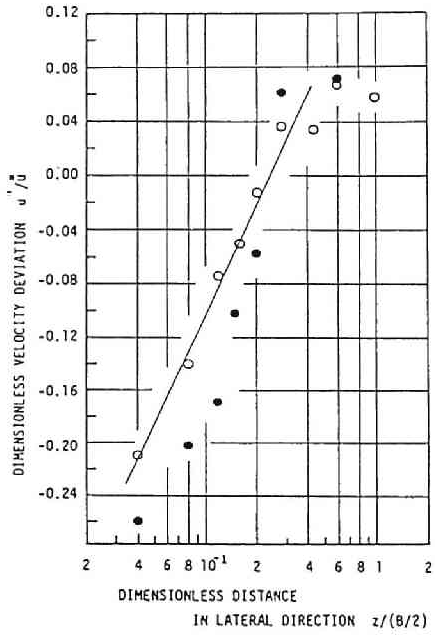

Figure 6.5.1: Lateral distribution of the depth-averaged velocity measured in Run 921.

section, because the gamma distribution is the expansion of the Earling distribution and the parameter n of an integer number is replaced with the real number k.

Normalized cross-sectional mean concentration is defined by:

$$C_n(t;x_1) \equiv C(t;\,x_1) \Big/ \int_0^\infty C(t;\,x_1)dt \tag{6.5.1}$$

Assuming $C_n(t;x_1)$ is able to be described by the **PDF** of the gamma distribution (See Fig. 6.5.2), it is written as:

$$C_n(t;x) = \frac{(\lambda k)^k}{\Gamma(k)}(t-t_i)^{k-1}\exp\{-\lambda k(t-t_i)\} \qquad \text{for} \quad t-t_i \geq 0 \tag{6.5.2}$$

where, $\Gamma(k)$ is the gamma function, and t_i , λ, and k is the three parameters of the gamma distribution, and they are related with the moments of the concentration distribution as:

$$\bar{t} - t_i = \frac{1}{\lambda k} \tag{6.5.3}$$

$$\sigma_t{}^2 = \frac{1}{(\lambda)^2 k} \tag{6.5.4}$$

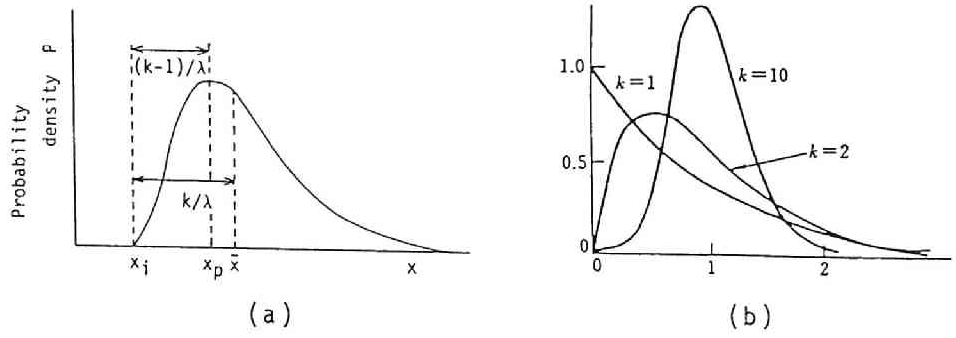

Figure 6.5.2: Schematic illustration of **PDF** of the gamma distribution. (a) Gamma distribution and its three parameters, and (b) Gamma distributions of which the mean is 1.0 but k is various.

where $\bar{t}$ is the first moment (the concentration time of the centroid of the dispersion cloud), t_i the concentration time of the top edge of the dispersion cloud, and ${\sigma_t}^2$ the variance and they are calculated from $C_n(t;x)$ as shown in **Chapter 4**.

Fig. 6.5.3 makes the comparison of the concentration distributions curves measured at selected points in a section and the cross-sectional averaged ones in Run 921 with the predicted ones which were calculated by use of $\bar{t}$ and σ_t^2 measured, and t_i which was determined by the trial and error method. The fine agreement between two kinds of results are demonstrated not only in the cross-sectional averaged concentrations but also point-measured concentration distributions. Figs. 6.5.2 (a), (b) and (c) respectively correspond to the data in the three different periods, that is, the convective period, the transition, and the Taylor's period defined by Fischer (1968). These three figures show the skewed concentration distributions, and the agreement of the calculated results with the observed ones is quite fine in three periods.

These results verifies that the cross-sectional mean concentration distributions in the time coordinate measured in the laboratory flumes are almost predicted by means of the **PDF** of the gamma distribution in the region from the beginning of the tracer insertion to the Taylor (dispersion) period.

The gamma distribution approximation are expected to state the concentration distributions under different conditions in laboratory as well as natural rivers, and its further applications will be examined in **Chapter 7**.

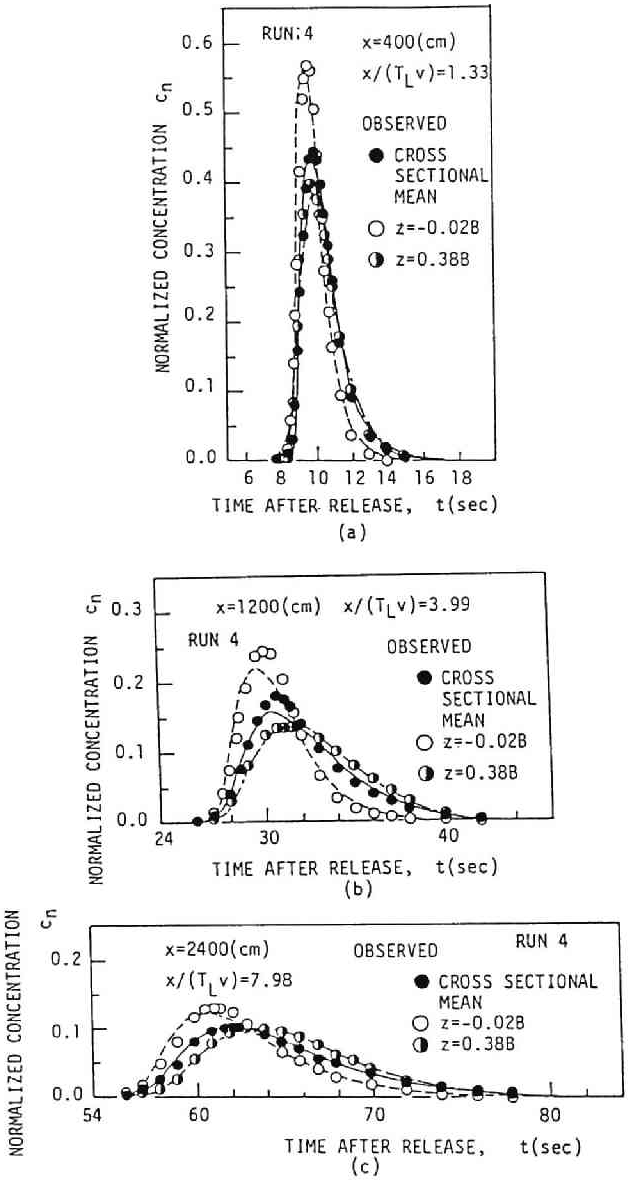

Figure 6.5.3: Concentration distributions in the time coordinate. The calculated distributions are compared with those observed in Run 921 in rectangular cross-section laboratory flumes. Closed circles denote the cross-sectional averaged concentration measured, and open and half closed circles point-measured concentration. Three kinds of line indicate the concentration calculated by use of the gamma distribution. (a) Convective period ($x_1/T_{SL}U = 1.33$), (b) Transition ($x_1/T_{SL}U = 3.99$), and (c) Taylor period ($x_1/T_{SL}U = 7.98$)

6.6 Conclusions

The convective dispersion processes in open-channel flows were studied in view of the discontinuous movements of a particle. The models for a particle movement are similar to those described in **Chapter 2**, however, it is assumed that the Lagrangian turbulent velocity v'_{1i} in the time step Δt_i is independent on v'_{1i-1} in the former time step Δt_{i-1}. Therefore the models in this chapter deprive the dispersion processes of the features described in **Chapter 2**, but following notable features are obtained in **Section 6.2**.

1. The probability density function **PDF** of a displacement of a particle, that is, the concentration distribution was described by use of the **PDF** of the Lagrangian turbulent velocity of a particle.

2. It was disclosed that the concentration distributions are influenced by the **PDF** of the Lagrangian velocity, and are different from the Gaussian distributions for a short travel time, if the **PDF** of the Lagrangian turbulent velocity distribution is different from the Gaussian distribution.

3. It converges on the Gaussian distribution by the "Central Limit Theorem" in the mathematics of probability and statistics for a longer travel time, even if the **PDF** of v'_1 is not described by the Gaussian distribution.

In **Section 6.3**, the **PDF** of the Lagrangian turbulent velocity v'_1 in the longitudinal dispersion phenomena was studied, assuming the influence of the Eulerian turbulent velocity is negligibly small. The **PDF** of v'_1 in 2-D open-channel flows under the logarithmic velocity distribution was disclosed to be described by the exponential distribution, and it was demonstrated that the concentration distributions during the asymptotic processes approaching the Gaussian distribution can be stated by the Earling/gamma distribution (Pearson Type III distribution). The parameter n of the integer number in the Earling distribution should be replaced by the real number k in this approximation in view of the continuous movements of a particle.

The concentration distribution in wide open-channel flows was studied in **Section 6.4**. The **PDF** of v'_1, and the magnitude of the time step Δt in the longitudinal dispersion in 3-D flows were discussed in view of the magnitude of the mixing time scale T_v in the vertical direction, and T_l in the lateral direction. The models for describing the concentration distributions in 3-D flows were presented, though they neglected the effects of the Eulerian turbulence and the vertical non-uniformity of the velocity distribution on the longitudinal dispersion.

The direct verification of the proposed models was not made, but the gamma distribution approximation was successfully examined by use of the concentration distributions and the velocity distribution measured in the wide rectangular cross-section laboratory flume in **Section 6.5**. The non-uniform lateral distribution of the depth-averaged velocity, which is dominant component over the longitudinal dispersion, was disclosed to be stated by the logarithmic distribution. That is, the **PDF** of v_l' is described by the exponential distribution, and the concentration distribution by the gamma distribution in wide open channel flows.

Thus, the skewed concentration distribution commonly measured in the longitudinal dispersion experiments in laboratory and natural streams was disclosed to be peculiar to the phenomena in shear flow dispersion, and the fundamental feature, because the **PDF** of the Lagrangian turbulent velocity is commonly different from the normal distribution. The skewed concentration distribution converges on the Gaussian distribution for a longer travel time by the "Central Limit Theorem", but the required travel time is dependent on the **PDF** of the Lagrangian turbulent velocity, and its order of the magnitude is longer than $20T_l$, in case the **PDF** of v_l' is described by the exponential distribution.

Chapter 7

CONCENTRATION DISTRIBUTIONS IN PULSE TRACER TESTS IN NATURAL STREAMS AND LABORATORY

7.1 Introduction, Objectives, and Outlines

The longitudinal dispersion coefficient can be experimentally measured and determined by the analysis of the behavior of the first and the second temporal moment of the concentration distributions, and/or distributions themselves, which are made by instantaneous injection of tracer into flow as a plain source, as described in **PART I**. (Hereafter this method is called "Pulse Tracer Test".) This method is very common, and has widely been used for the measurement of the longitudinal dispersion coefficient in laboratory as well as natural streams.

As reported by many researchers, and typically described in **Chapter 4**, the growth of the second temporal moment measured is commonly non-linear during a short travel time of the tracer cloud, and the concentration–time curves measured at the selected sections are usually very skewed, that is, the slope of a concentration distribution curve in the leading limb is steep, and that in the trailing limb is very mild, so that it is quite different from the Gaussian distribution:

$$C = \frac{1}{\sqrt{4\pi Dt}} \exp\{-\frac{(x-Ut)^2}{4Dt}\} \tag{7.1.1}$$

which is the fundamental solution of the 1-D convective-dispersion equation in infinite and uniform flows:

$$\frac{\partial C}{\partial t} + U\frac{\partial C}{\partial x} = D\frac{\partial^2 C}{\partial x^2} \tag{7.1.2}$$

under the initial condition:

$$C(x;t) = \delta(x) \qquad \text{at} \qquad t = 0 \tag{7.1.3}$$

where C is the cross-sectional averaged concentration, U the cross-sectional averaged velocity, D the longitudinal dispersion coefficient, δ Dirac's distribution, x the space coordinate in the flow direction, and t the time.

The skewed distribution was explained to be caused by some mechanisms such as: the effect of the laminar sub-layer (Elder, 1956), the effect of the dead zone, or the convective transport itself as described in **Chapter 6**. The difference from the Gaussian distribution are especially strongly observed in field measurements in natural rivers, and it leads to the development of another models for describing the longitudinal mixing in a river, that is, "Dead Zone Modeling" It was initiated by Hay (1966), and investigated by Thakston and Schnelle (1966), Valentine and Wood (1977), Muramoto, Michiue and Nakagawa (1978), and so on. They assume the existence of the dead zone in riverbed or bank-sides, because a cross-section of natural streams is irregular and a depth is also irregular by sedimentation. Assuming a river channel is uniform in the longitudinal direction, but has the dead zone, Bo Petersen (1977) described the non-linear behavior of the variance based on the following equations:

$$\frac{\partial C_a}{\partial t} + U' \frac{\partial C_a}{\partial x} - \frac{\partial}{\partial x}(D_F \frac{\partial C_a}{\partial x}) = \frac{Q_E}{V}(C_i - C_a) \qquad \text{for main stream} \qquad (7.1.4)$$

$$\Omega \frac{\partial C_i}{\partial t} = Q_E(C_a - C_i) \qquad \text{for dead zone} \qquad (7.1.5)$$

where C_a is the cross-sectional averaged concentration, C_i the average concentration in the dead zone, U' the cross-sectional average velocity in the main stream, D_F the Fischer's dispersion coefficient in the main stream, Q_E the exchange discharge per unit length, V the volume of main stream per unit length, and Ω the volume of the dead zone per unit length. According to him, the variance in a river with dead zone is stated as the sum of that caused by the non-uniform distribution of the velocity and that caused by the dead zone. He examined the 21 data by Godfrey and Frederick (1970), and verified his theoretical results. Muramoto, Michiue and Nakagawa (1978) obtained the longitudinal dispersion coefficient by use of the Fourier transformation of the mathematical models similar to those described by Eqs. 7.1.4 and 7.1.5.

The non-linear growth of the second moment was clearly explained by the Lagrangian theory of a particle dispersion by continuous movements described in **Chapter 2**, and the skewed distribution of the concentration-time curves by the Lagrangian theory of a particle by discontinuous movements described in **Chapter 6**. The skewed distribution results from the probability density function (**PDF**) of the Lagrangian velocity of a particle, therefore these two features are peculiar to the longitudinal dispersion in shear flows, and fundamental characteristics of the phenomena; however,

the variance has the linear relationship with the distance after $x > 6T_lU$ as shown in Eq. 2.2.39, and the concentration curves converges on the Gaussian distribution after the required travel time which is dependent on the **PDF** of the Lagrangian turbulent velocity.

Fischer (1966) proposed that the application of Eq. 7.1.2 to "Pulse Tracer Test" should be limited for the period:

$$t > 6T_{Fl} = 0.180\frac{l^2}{Ru_*} \tag{7.1.6}$$

where T_{Fl} is the Fischer's time scale, l the characteristic length (the half wide (= $B/2$)), R the hydraulic radius, and u_* the friction velocity. Eq. 7.1.6 is equivalent to Eq. 2.2.39. The convective dispersion equation of Eq. 7.1.2 is available to state the concentration distributions in the "Pulse Tracer Test" for the period above, if the concentration distribution at a certain time $t_0 > 6T_{Fl}$ is obtained. The concentration distributions for $t_0 < 6T_{Fl}$ is 3–D or 2–D, therefore they are numerically obtained as a solution of the 3-D turbulent diffusion equation under the specified boundary and initial conditions in various flows, if close distributions of the velocity field and the turbulent diffusion coefficient are available, but it will require a lot of time and computer resources. Therefore, the models describing cross-sectional averaged concentration distributions in the longitudinal direction are convenient and preferable to predict the concentration distributions in such a case of accidental influent of toxic materials or pollutants into a river as well as the measurement of the dispersion coefficient.

In this chapter, the skewed concentration distributions measured in natural streams and laboratory will be examined by the "Gamma (Pearson's Type III) Distribution Model":

$$f(t) = \frac{1}{\Gamma(k)}\lambda^k(t-t_i)^{k-1}\exp\{-\lambda(t-t_i)\}$$

The gamma distribution is commonly known to have three parameters, that is, k, λ, and t_i, while the Gaussian distribution has two parameters. Therefore, the parameter estimation methods will also be investigated as well as the approximate description of concentration distributions by the gamma distribution.

7.2 Approximation of Concentration Distributions by Gamma Distribution

It has already been realized that the gamma distribution can be employed to describe the concentration distribution measured in "Pulse Tracer Test" in natural streams

(Godfrey and Frederick, 1970, Sayre, 1969, and so on). The gamma distribution for concentration distribution can be obtained, if the **PDF** of the component of the Lagrangian turbulent velocity v_l' in open-channel flow, or that of the Lagrangian turbulent velocity v_1' in 2-D flow is described by the exponential distribution as shown in **Chapter 6**.

The theoretical approach to the concentration distributions will not be concerned any more, but the direct application of the gamma distribution approximation for concentration distributions in the time coordinate under various flow conditions will be examined in this chapter.

Assuming the probability variable t is described by the gamma distribution, it is written as

$$f(t) = \frac{1}{\Gamma(k)}\lambda^k(t-t_i)^{k-1}\exp\{-\lambda(t-t_i)\} \qquad \text{for} \qquad t \geq t_i \tag{7.2.1}$$

where t is the travel time of a particle which started at $x = 0$ at the time t=0, $\Gamma(k)$ the gamma function, and k, λ and t_i the three parameters of the distribution. The gamma distribution is equivalent to the exponential function for $k = 1$, and convergent on the Gaussian distribution for $k \to \infty$, assuming λ is constant. The relationships between these three parameters with the moment of the distribution are respectively given as

$$\mu_t = \bar{t} - t_i = k/\lambda \tag{7.2.2}$$

$$\sigma_t^2 = k/\lambda^2 \tag{7.2.3}$$

$$S_t = 2/\sqrt{k} \tag{7.2.4}$$

where μ_t is the first moment, σ_t^2 the second central moment and S_t the skewness factor, and t_i shifts the origin of the distribution. (See Fig. 7.2.1.) The maximum value of the distribution f_p at the modal value t_p can be stated as:

$$f_p(t_p) = \frac{\lambda}{\Gamma(k)}(k-1)^{k-1}\exp\{-(k-1)\} \qquad (k \geq 1) \tag{7.2.5}$$

at

$$t_p - t_i = \frac{1}{\lambda}(k-1) \tag{7.2.6}$$

and simultaneously

$$\bar{t} - t_p = 1/\lambda \tag{7.2.6}$$

Therefore, characteristic parameters which describe the concentration distributions will be:

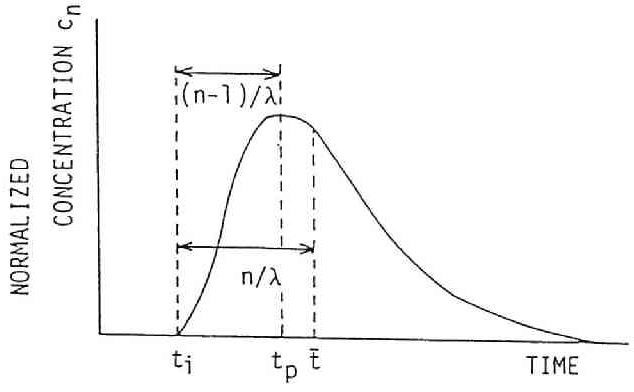

Figure 7.2.1: Gamma distribution in the time coordinate and its three parameters.

$\bar{t}$: the first moment of the distribution, and
the concentration (average travel) time for the centroid of the distribution.

σ_t^2 : the variance of the distribution.

t_P: the concentration time for the maximum value of the distribution, or
the time when the peak concentration is observed.

t_i: the concentration time for the top edge of the distribution, or
the time when the top edge of the distribution is transported at a measuring section and the concentration goes up.

$\bar{t}$ and σ_t^2 can be calculated by Eqs. 4.3.4, and 4.3.5 respectively, and t_p and t_i can be directly determined by use of the measured concentration-time curves. Therefore, the gamma distribution can practically be determined by either of following two sets of parameters.

- $\bar{t}$, σ_t^2, and t_i:

$$\lambda = \frac{\mu_t}{{\sigma_t}^2} = \frac{\bar{t} - t_i}{{\sigma_t}^2} \tag{7.2.7}$$

$$k = \frac{{\mu_t}^2}{{\sigma_t}^2} = \frac{(\bar{t} - t_i)^2}{{\sigma_t}^2} \tag{7.2.8}$$

- $\bar{t}$, σ_t^2, and t_p:

$$\lambda = (\bar{t} - t_p)^{-1} \tag{7.2.9}$$

$$k = {\sigma_t}^2\lambda^2 = \frac{{\sigma_t}^2}{(\bar{t} - t_p)^2} \tag{7.2.10}$$

$$t_i = \bar{t} - k/\lambda \tag{7.2.11}$$

The first set determines the distribution by use of the initiation time of the concentration distributions t_i, the first moment $\bar{t}$ and the variance σ_t^2, and the second set by use of the first moment $\bar{t}$, the variance σ_t^2 and the skewness factor S_t, because

$$S_t = 2(\bar{t} - t_p)/\sigma_t \tag{7.2.12}$$

is established.

In **Chapter 6**, it has already successfully been demonstrated that $C_n(t;x)$ could be approximated by the **PDF** of the gamma distribution for author's data of Run 921 by use of $\bar{t}, {\sigma_t}^2$, and t_i measured. The further possibility for the "gamma distribution approximation" will be examined for author's data (Run 921), Fischer's data (Series 2900 and 3400) in trapezoidal laboratory flumes (Fischer, 1966), and Godfrey and Frederick's data (Tests 1 and 8) in natural streams (Godfrey and Frederick, 1970).

Figs. 7.2.2 (a), (b), (c) compares the observed concentration distributions in Run 921 which are denoted by open circles, with the distributions calculated by use of the measured three parameters which were denoted by solid lines, as well as the distributions predicted by use of the following equations by dashed lines.

$$\bar{t} = x/U \tag{7.2.13}$$

$$\frac{{\sigma_t}^2}{T_{SL}} = \frac{2[{v_l'}^2]\{\exp(-\chi) + \chi - 1\}}{U^2}, \qquad (\chi \equiv \frac{x}{T_{SL}U}) \tag{7.2.14}$$

$$t_i = \frac{x_1}{\alpha u_{max}} \tag{7.2.15}$$

where α is the new parameter which links the distance x_1 and the concentration time of the top edge of the dispersion cloud t_i at $x_1 = x_1$ with the maximum velocity u_{max}, and it is selected at 1.1 in the following analysis. Eq. 7.2.14 is the empirically obtained relationship between the variance σ_t^2 and the distance x in **Chapter 4**. This relationship is used in stead of the theoretically obtained relationship, Eq. 2.2.30, because Eq. 2.2.30 is more complicated than Eq. 7.2.14. Figs. 7.2.2 (a), (b), and (c) respectively correspond to data in the three different regions proposed by Fischer (1966), namely, the convective period, the transition, and the Taylor's period. These figures show the skewed distributions, and the agreement of the calculated and predicted results with the observed ones is quite fine.

Fig. 7.2.3 show the results of the application of the proposed models to Fischer's data sets, Series 2900 (Fig.7.2.3 (a)) and Series 3400 (Fig. 7.2.3 (b)). In the simulation, the three parameters used are obtained from the measured cross-sectional mean concentrations, and t_i is estimated by Eq. 7.2.15. The concentration distributions routed by use of the 1-D convective dispersion equation by Fischer (1966), and those simulated by use of the "Convective Model" by McQuivey and Keefer (1976) are

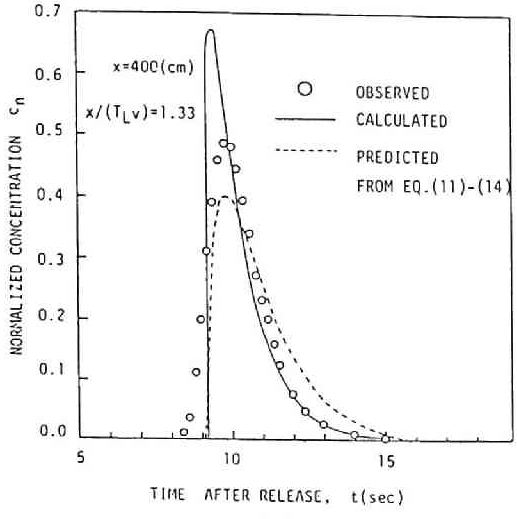

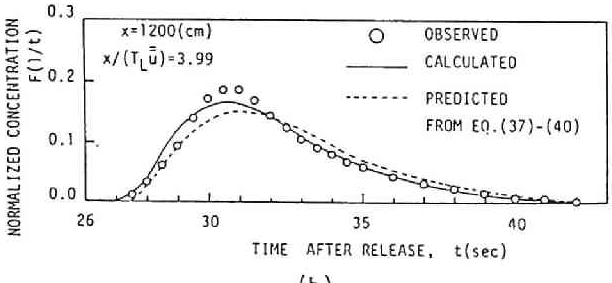

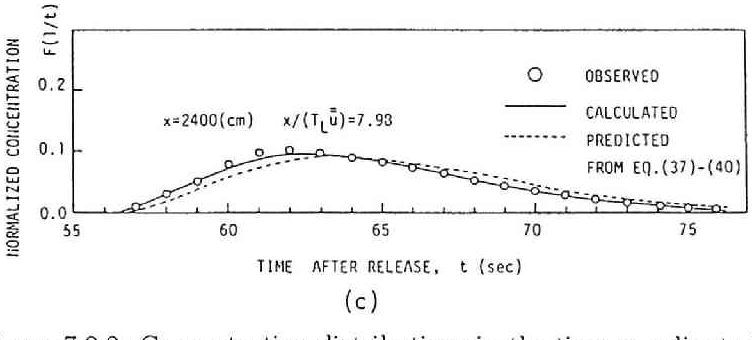

Figure 7.2.2: Concentration distributions in the time coordinate for Run 921. Open circles denote the distribution observed, solid lines the calculated distributions by use of the gamma distribution with parameter measured, and dashed lines the predicted distributions by use of the gamma distributions with Eqs. 7.2.13, 14, and 15. (a) x = 4.00 m, (b) x = 12.00 m, and (c) x = 24.00 m.

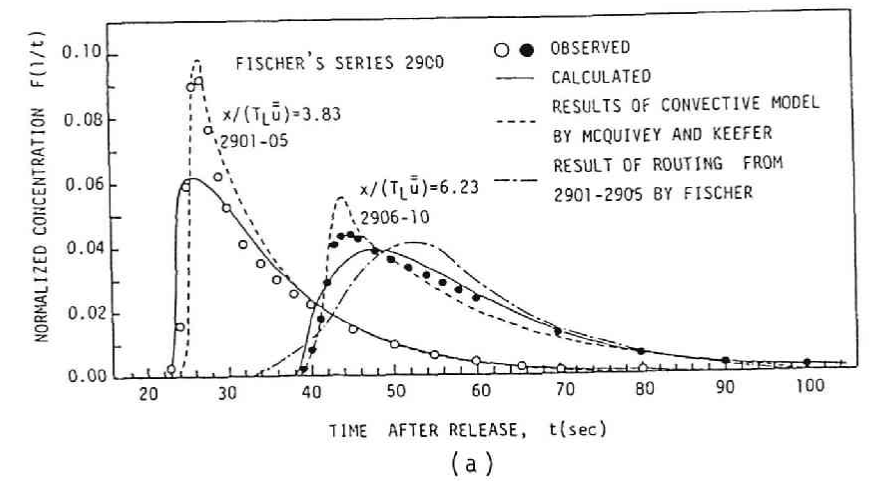

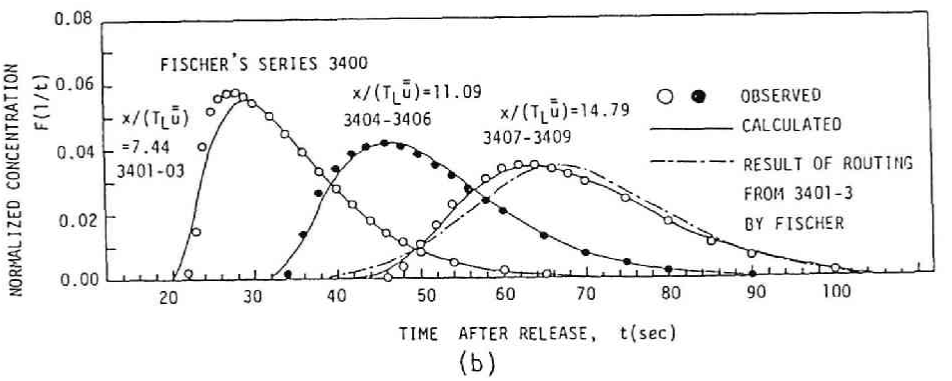

Figure 7.2.3: Concentration distributions in the time coordinate. Comparison of the calculated distributions by use of the gamma distribution, "Convective Models" and 1-D convective dispersion equation with the distributions measured in trapezoidal laboratory flumes are made. (a) Fischer's Series 2900, and (b) Fischer's Series 3400

also presented in Figs. 7.2.3. Author's, and McQuivey and Keefer's results represent the skewed concentration distributions, and both models are more acceptable than Fischer's models.

The calculated results for the tracer dispersion study made in two natural streams by Godfrey and Frederick (1970) are presented in Fig. 7.2.4 (a) for Test 1 in Copper Creek below gage near Gate City, Va., and Fig. 7.2.4 (b) for Test 8 in Coachella Canal near Hotvill, Calif.. Simulated results are also acceptable, though the concentration distributions used were not the cross-sectional averaged one, but measured at a center of the flow-section.

These results show that the cross-sectional averaged concentration distributions in the time coordinate in the laboratory flumes and natural streams are almost predicted by use of the **PDF** of the gamma distributions throughout any region, and suggest the **PDF** of v_i' is approximately described by the exponential distribution.

7.3 Parameters of Concentration Distributions

It was disclosed that the concentration distributions measured in "Pulse Tracer Test" under various hydraulic conditions was described by the **PDF** of the gamma distribution in the time coordinate in **Section 7.2**, though the general relationships of $\bar{t}$, σ_t^2, t_i and/or t_P with the distance x are required to describe the concentration distributions. The concentration times of the centroid $\bar{t}$, the peak concentration t_P and the top edge t_i, the variance σ_t^2, the peak concentration C_{nP} is very important and interested parameters of a concentration distribution in view of engineering aspects as well as the parameters in the gamma distribution. In this section, these relationships will be investigated by use of the concentration distributions measured in natural streams and laboratory. The selected data are listed in Table 7.3.1. The 9 data sets in 6 natural streams/canal are from Godfrey and Frederick (1970); they conducted "Pulse Tracer Test" by a line source injection of tracer, but the concentration measurement was only done at a center of a flow-section at each of 5 to 6 sections downstream. The behavior of the temporal moment for the concentration distributions measured at a center is different from those for the cross-sectional averaged concentration as described in **Chapter 4**, therefore, the 4 data sets selected from author's experiments are also examined, and listed in Table 7.3.1.

7.3.1 Concentration Time of Centroid

The relationship between various concentration times and the distance from the insertion point is presented in Fig. 7.3.1 (a) for Run 921 in laboratory, and (b) for Test

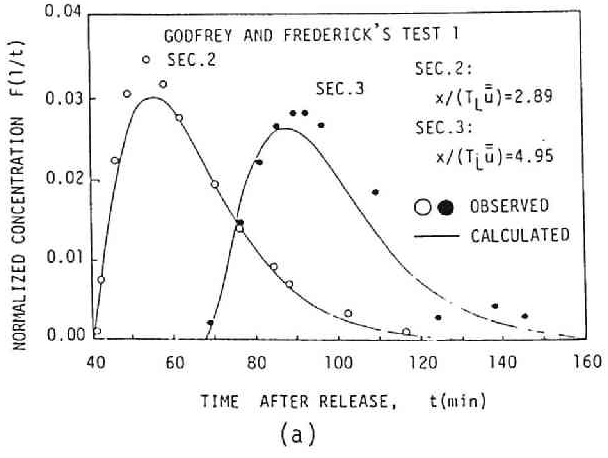

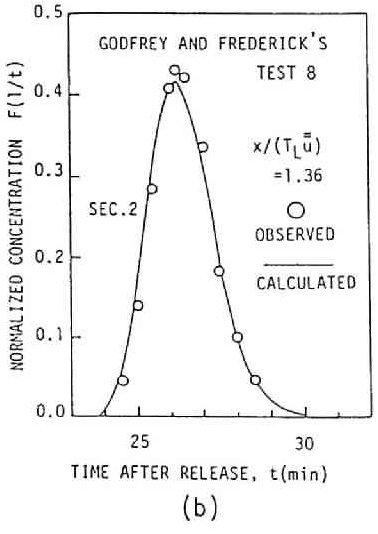

Figure 7.2.4: Concentration distributions in the time coordinate. Comparison of the calculated distributions by use of the gamma distribution with the distribution observed in natural streams are made. (a) Test 1 in Copper Creek below gage near Gate City, (b) Test 8 in Coachella Canal near Hotvill

Table 7.3.1: Summary of hydraulic variables in selected measurements in laboratory and natural streams.

Investigator	(1) Run -Number	(2) Velocity $\bar{v}$(cm/s)	(3) Width B(m)	(4) Depth d(cm)	(5) Shear -Velocity u_*(cm/s)	(6) Re. x10^3	(7) Fr.	(8) B/d	(9) $\bar{v}/u_*$	(10) J_A x10^{-2}	(11) D/du_*	(12) $T_L^{3)}/(d/u_*)$	(13) $A/\bar{A}$	(14) River
(1) ┐	Run-1	32.2	0.10	3.12	1.94	9.56	0.58	3.21	16.6	5.57	28.9 [1]	1.88	1	┐
(2) Author	Run-3	27.4	0.10	2.05	1.69	4.70	0.71	4.88	16.2	5.23	47.6 [1]	3.47	1	Lab. Flume (St.)
(3) ┘	Run-4	36.5	0.25	2.69	2.18	8.38	0.71	9.29	16.7	2.46	46.0 [1]	6.68	1	┘
(4) ┐	Test-1	21.9	15.94	44.80	7.83	99.00	0.11	35.6	2.80	25.5	555.9 [2]	277.9	1.385	Copper Creek (St.)
(5)	Test-2	22.2	48.46	93.30	6.71	222.0	0.08	51.9	3.31	18.8	222.0 [2]	107.9	1.688	Clinch River (St.)
(6) Godfrey	Test-3	14.1	18.65	38.40	11.46	54.80	0.07	48.6	1.23	12.8	211.1 [2]	1089.0	1.026	Copper Creek (Cr.)
(7) -Frederick	Test-4	13.2	35.36	86.90	5.18	124.0	0.05	40.7	2.55	10.1	210.7 [2]	321.4	1.119	Powell River (Cr.)
(8)	Test-5	13.5	29.57	69.50	4.88	221.0	0.11	42.6	2.77	19.0	238.3 [2]	163.8	0.644	Clinch River (St.)
(9)	Test-6	53.3	18.29	80.80	10.27	329.0	0.19	22.6	5.19	45.1	258.0 [2]	21.2	1.079	COpper Creek (St.)
(10)	Test-7	82.3	59.43	216.70	9.84	1171.0	0.18	27.4	8.36	14.1	252.7 [2]	25.5	1.379	Clinch River (St.)
(11)	Test-8	65.8	24.69	157.30	3.96	1052.0	0.17	15.7	16.6	2.34	153.7 [2]	23.8	1.037	Coachella Canal (St.)
(12) ┘	Test-10	65.5	51.21	251.20	10.15	1633.0	0.13	20.4	6.45	15.4	182.0 [2]	28.4	1.784	CJinch River (St.)

Note [1]: By means of moment method [2]: By means of routing method by Fischer

[3]: $T_L = D/(J_A \cdot \bar{v}^2)$

Abbreviations: Lab., Laboratory; St., Straight; Cr., Crooked

1 in Copper Creek. In Fig. 7.3.1 (a), the open circles denote $\bar{t}$: the concentration time for the centroid of the cross-sectional averaged concentration distributions $C_n(t;x)$, the closed circles $\bar{t}_c$: that for the concentration distributions $\bar{c}_{cn}$ measured at a center of flow-section, and the half closed circles t_i; that for the top edge of the distributions. The reciprocal of the slope of the solid lines is equal to the cross-sectional averaged velocity, and that of the dashed line to the celerity of the top edge of distributions. It is clearly demonstrated that the relationship:

$$u_c \equiv \frac{x}{\bar{t}} = U \tag{7.3.1}$$

is established, that is, the convective velocity u_c is confirmed to be equal to the cross-sectional average velocity U as already shown in **Chapter 4**. It is also demonstrated that the convective velocity for $\bar{c}_{cn}$ is also equal to U The dimensionless time difference between $\bar{t}_c$ and $\bar{t}$ is plotted against the distance in Fig. 7.3.2. The difference becomes constant as the distance from the injection point increases. On the contrary, $\bar{t}$ is smaller than $t = x/U$ in 7 data sets out of 9 data sets in natural streams. The convective velocity u_c and the celerity of the peak concentration in Test 4 are equal to U after a long travel time, but it is commonly larger than U as shown in column 13 in Table 7.2.1. ($A/\bar{A}$ in the column 13 is equal to u_c/U.) Thus, the concentration distribution at a center of flow-section is commonly transported faster than by the average velocity U in natural stream.

7.3.2 Variance

The variances for C_n, and $\bar{c}_{cn}$ are plotted against the distance in Fig. 7.3.3 for Run 921. The open circles denote the variance σ_t^2 for C_n, and the closed circles denote the variance σ_{ct}^2 for $\bar{c}_c$. The behavior of σ_{ct}^2 is different from that of σ_t^2; the magnitude of σ_{ct}^2 is smaller than that of σ_t^2, and the required length for linear growth of σ_{ct}^2 is longer than that for σ_t^2, but the slope of each two curves becomes the same for a longer travel time. These facts observed in laboratory confirm the results in the numerical experiments in 2-D flows by Yotsukura and Fiering (1964). Thus, the moment method for $\bar{c}_c$ can be usable for determining the dispersion coefficient in stead of that for C, but the required length for linear growth of the variance is much longer than that for C.

The growth of the variance is sometimes approximated by

$$\frac{\sigma_t^2}{2J_A T_{SL}^2} = \exp(-\chi) + \chi - 1 \tag{4.4.5}$$

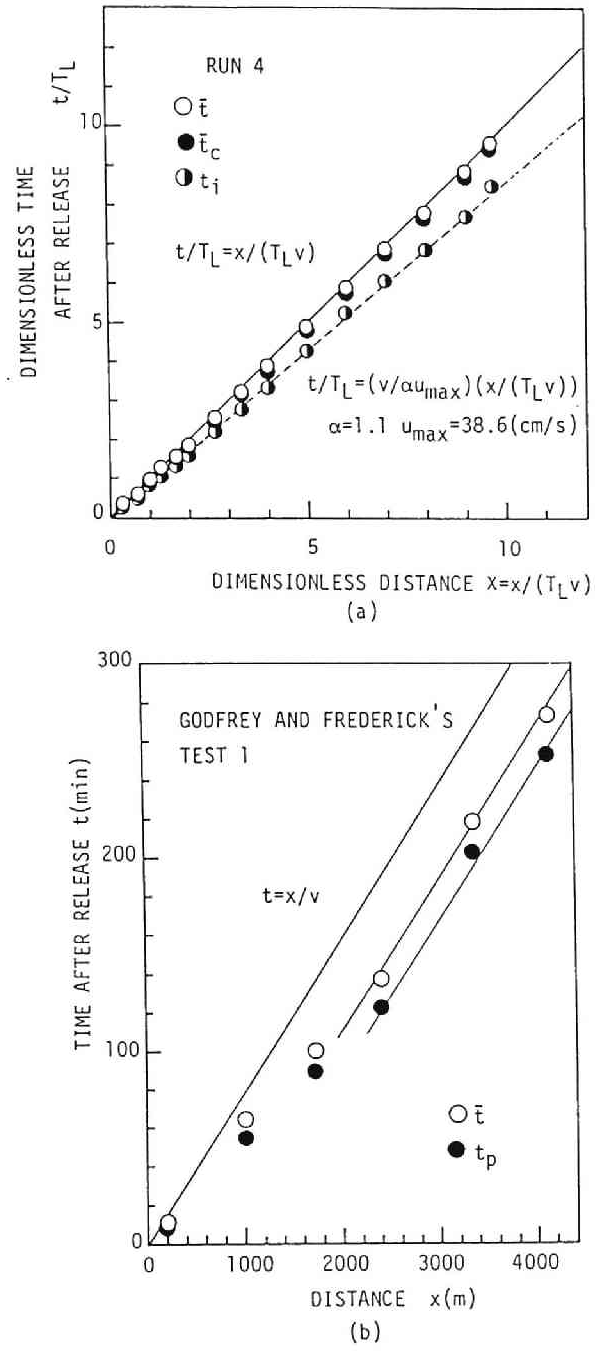

Figure 7.3.1: Various concentration times measured at selected sections. (a) Laboratory measurements, and (b) Measurements in natural streams.

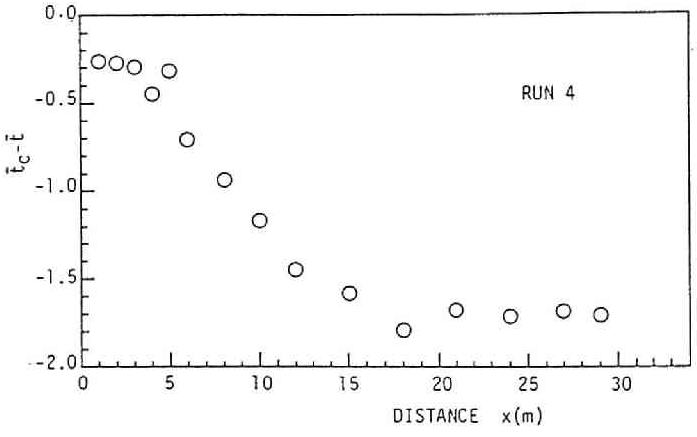

Figure 7.3.2: Time difference between concentration time $\bar{t}$, and $\bar{t}_c$ in laboratory.

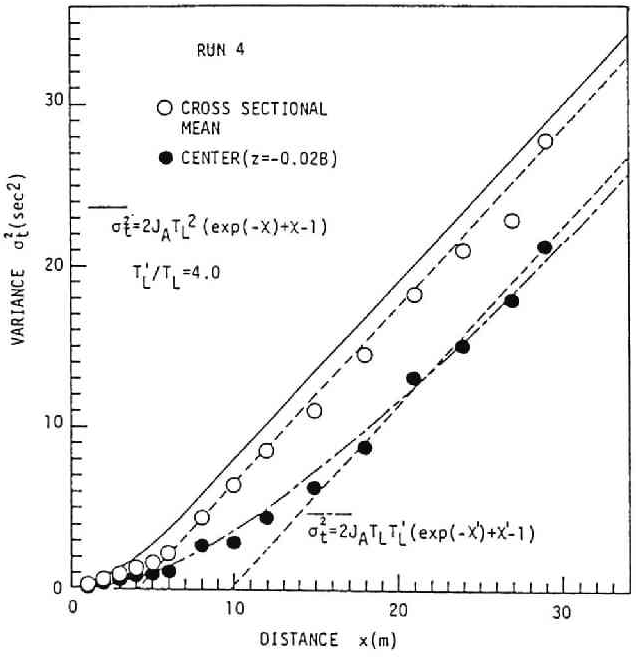

Figure 7.3.3: Variances for C_n, and $\bar{c}_{cn}$ at selected sections measured in Run 921. Open circles denote the variance σ_t^2 for C_n, and closed circles denote the variance σ_{ct}^2 for $\bar{c}_{cn}$. Solid line denotes Eq. 4.4.5, and dash-dotted line Eq. 7.3.2.

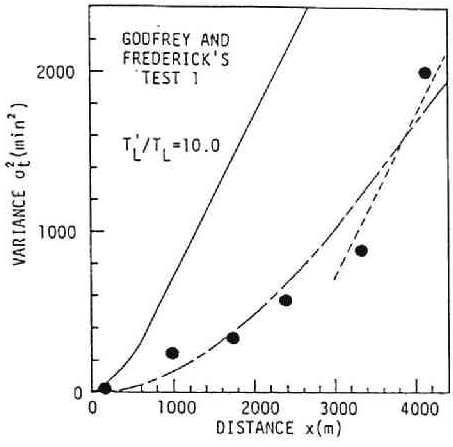

Figure 7.3.4: Variances for $\bar{c}_c$ at selected sections measured in Test 1 in Copper Creek. Closed circles denotes the variance σ_{ct}^2 for $\bar{c}_c$, and dash-dotted lines Eq. 7.3.2.

and the similar modeling for the growth of σ_{ct}^2:

$$\frac{{\sigma_t}^2(\chi')}{2J_A T_{SL} {T_L}'} = \exp(-\chi') + \chi' - 1 \qquad (\chi' = x/T_L' U) \tag{7.3.2}$$

where T_L' is the parameter which describes the delayed growth of σ_{ct}^2, is examined for Run 921 in Fig.7.3.3. The dash-dotted line in Fig. 7.3.3 denotes the relationship of Eq. 7.3.2, where T_L' was determined by the try and error method, and the magnitude of T_L'/T_{SL} is 4.0. Eqs. 4.4.5 and 7.3.2 are also examined in Test 1 in Copper Creek, and the results are presented in Fig. 7.3.4, where the magnitude of T_L'/T_{SL} is 10.0. Further applications of Eq. 7.3.2 to selected data in laboratory and natural streams are presented in Fig. 7.3.5 and fine agreements between Eq. 7.3.2 and σ_{ct}^2 measured is demonstrated. The relationship between T_L' and hydraulic variables are illustrated in Fig. 7.3.5, and it is stated as:

$$\frac{{T_L}'}{T_L} = 0.3\frac{B}{d} \tag{7.3.3}$$

Thus, the growth of the variance for the concentration distributions measured at a center of a cross-section in natural streams as well as laboratory was formulated.

7.3.3 Peak Concentration

The time difference between $\bar{t}$ and t_P for C_n in laboratory is presented in Fig. 7.3.7. It

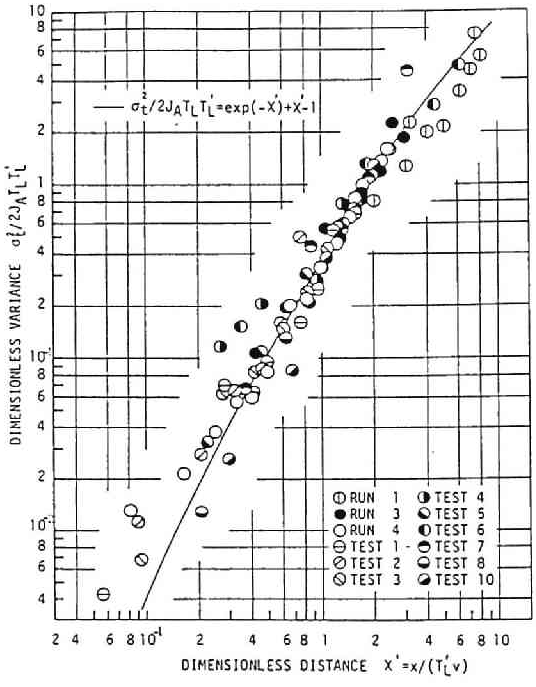

Figure 7.3.5: Variances for $\bar{c}_c$ at selected sections measured in laboratory and natural streams. Circles denote the variance σ_{ct}^2 for $\bar{c}_c$, and a solid line Eq. 7.3.2.

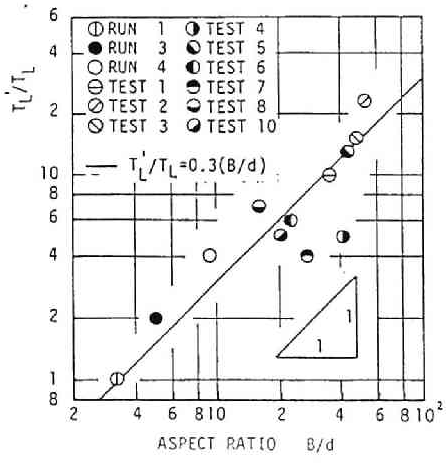

Figure 7.3.6: T_L'/T_{SL} and B/d in laboratory and natural streams.

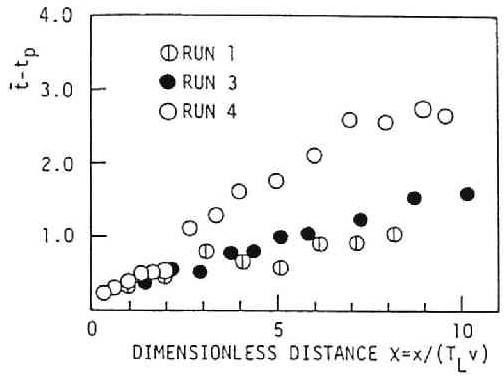

Figure 7.3.7: The time difference between $\bar{t}$ and t_P for C_n in laboratory.

is realized that the celerity of C_P is shorter than the convective velocity of the centroid u_c for a short travel time, and this is equivalent to the fact that a concentration distribution is skewed. It is also realized from Fig. 7.3.7 that the time difference between $\bar{t}$ and t_p becomes constant with the increase of the travel time, and this is also presented in Fig. 7.3.1 (b) for natural stream. This fact assures that λ in the PDF of the gamma distribution is constant for a long travel time as shown in Eq. 7.2.9.

Fig. 7.3.8 shows the time difference $\bar{t} - t_P$ at selected sections in natural rivers, and it is disclosed that the time difference in natural streams is much bigger than that in laboratory. Assuming the concentration distributions can be approximated by the gamma distribution, the relationship between t_P and $\bar{t}$ is stated as

$$\frac{1}{\lambda T_{SL}} = \frac{\bar{t}}{T_{SL}} - \frac{t_P}{T_{SL}} \tag{7.3.4}$$

and Eq. 7.3.2 leads to the following relationship

$$\frac{1}{\lambda T_{SL} J_A} = \frac{2}{\beta} \frac{-1 + \chi' + \exp(-\chi')}{\chi'} \tag{7.3.5}$$

and

$$\beta = \frac{U}{u_c} \left(1 - \frac{u_c}{\alpha u_{maxc}} \right) \tag{7.3.6}$$

where αu_{maxc} is the celerity of the top edge of the concentration, and equal to $1.1 u_{max}$. The magnitude of β defined by Eq. 7.3.6 is estimated at $0.1 \sim 0.3$ from Fig. 7.3.8.

Assuming Eqs. 7.3.2 and 7.3.6 are established, the parameters in the gamma distributions are rewritten as:

$$\lambda T_{SL} = \frac{\beta}{2 J_A} \frac{\chi'}{-1 + \chi' + \exp(-\chi')} \tag{7.3.7}$$

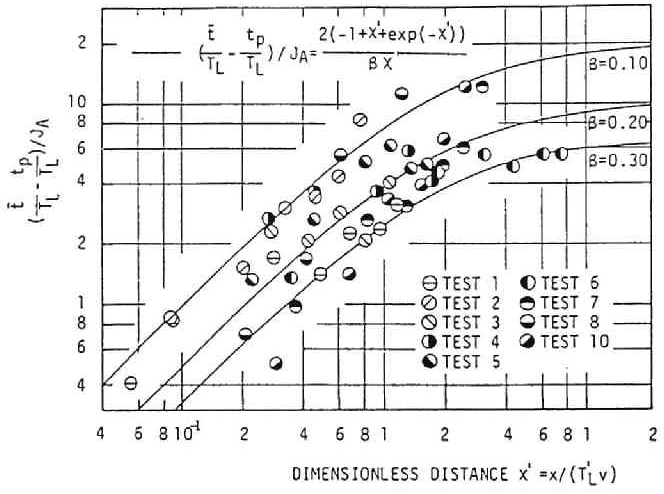

Figure 7.3.8: The time difference between $\bar{t}$ and t_P for $\bar{c}_c$ in natural streams. Plottings are on log-log sheet.

$$k = \frac{\beta^2}{2J_A}\left(\frac{T_L'}{T_{SL}}\right)\frac{\chi^2}{-1+\chi'+\exp(-\chi')} \tag{7.3.8}$$

and the normalized peak concentration is obtained by Eq. 7.2.5. Therefore,

- For $\chi' \ll 1$,

$$\frac{1}{\lambda T_{SL}} = \frac{\bar{t}}{T_{SL}} - \frac{t_P}{T_{SL}} = \frac{J_A}{\beta}\chi' \tag{7.3.9a}$$

$$k = \frac{\beta^2}{J_A}\left(\frac{T_L'}{T_{SL}}\right) \qquad (n \geq 1) \tag{7.3.9b}$$

$$C_{nP} = \frac{\beta}{J_A T_{SL}}\left(\frac{T_L' U}{T_{SL} u_c} - \frac{J_A}{\beta}\right)\frac{(k-1)^{(k-1)}e^{-(k-1)}}{\Gamma(k)}\left(\frac{t_P}{T_{SL}}\right)^{-1} \tag{7.3.9c}$$

Thus, $\bar{t} - t_P$ increases in proportion to the distance x, and C_{nP} decreases in inverse proportion to t_P/T_{SL}.

- For $\chi' \gg 1$

$$\frac{1}{\lambda T_{SL}} = \frac{2J_A}{\beta} \tag{7.3.10a}$$

$$k = \frac{\beta^2}{2J_A}\frac{T_L'}{T_{SL}}\chi' \tag{7.3.10b}$$

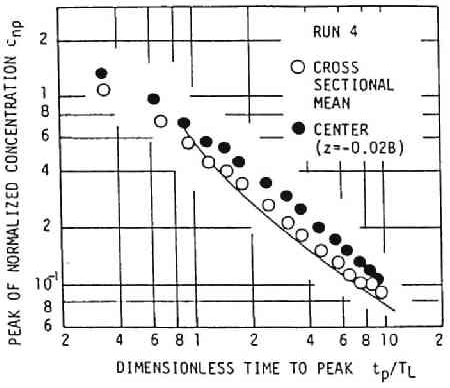

Figure 7.3.9: C_{nP} and $\bar{c}_{cnP}$ observed in Run 921 against t_P and the predicted ones by use of Eqs. 7.2.5, 7.2.6, 7.3.7, and 7.3.8 denoted by solid lines. Plottings are on log-log sheet.

$$C_{nP} = \frac{1}{2\sqrt{\pi J_A T_{SL}{}^2}} \left(\frac{U}{u_c}\right)^{\frac{1}{2}} \left(\frac{t_P}{T_{SL}}\right)^{-\frac{1}{2}} \tag{7.3.10c}$$

Thus, $\bar{t} - t_P$ is constant and C_{nP} decreases in proportion to $(t_P/T_{SL})^{-1/2}$. (Aya, Iwasa, Toda, 1981).

Fig. 7.3.9 shows C_{nP} and $\bar{c}_{cnP}$ observed in Run 921 against t_P and the predicted ones by use of Eqs. 7.2.5, 7.2.6, 7.3.7, and 7.3.8 denoted by solid lines. The fine agreement between two results are demonstrated for $t_P/T_{SL} \geq 1$.

7.3.4 Predicting Concentration Distributions

The gamma distribution approximation for the concentration distributions in laboratory and natural streams has already demonstrated in **Chapter 6**, and **Section 7.2**. Determining U and u_{max} is difficult in non-uniform natural flows which has irregular cross-section, therefore, the other parameter estimation method should be developed.

One of them is the use of β defined by Eq. 7.3.6, that is, t_P can be determined by β. Fig. 7.3.10 shows the comparison of concentration distributions measured in Test 1 and calculated by use of Eq. 7.3.2 for σ_{ct}^2, Eqs. 7.3.4 and 7.3.5 and β for t_P, and measured $\bar{t}$. The fine agreement is observed in the concentration distributions for a longer travel time, and the models proposed above were verified to be usable for predicting concentration distributions in natural streams.

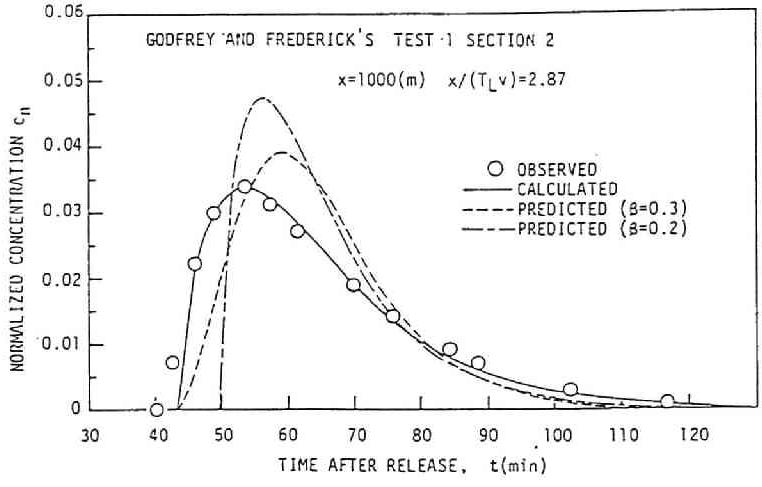

(a)

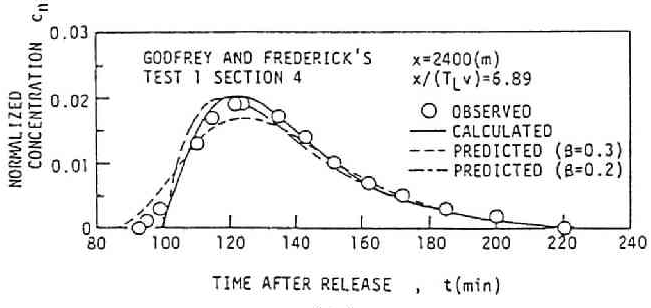

(b)

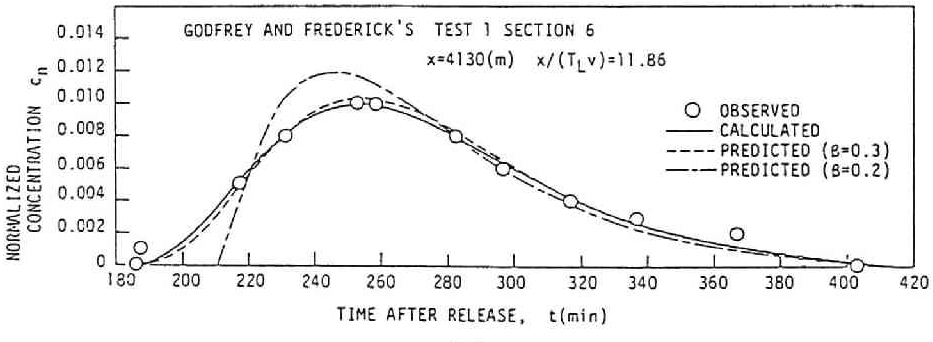

(c)

Figure 7.3.10: Comparison of concentration distributions measured in Test 1 and calculated by use of Eq. 7.3.2 for σ_{ct}^2, Eqs. 7.3.4 and 7.3.5 and β for t_P, and measured $\bar{t}$. (a) $x = 1\,000$ m, (b) $x = 2\,400$ m, and (c) $x = 4\,130$ m.

7.4 Conclusions

This chapter is concerned with the concentration distributions observed in "Pulse Tracer Test" in natural streams and laboratory. They are commonly skewed from the Gaussian distribution. The skewed distribution is sometimes explained to be caused by the trapping of tracer cloud in the dead zone in riverbed or channel-side, but more commonly and clearly explained by the convective transport by the temporal averaged velocity, that is, the Lagrangian turbulent velocity of a particle, of which the **PDF** is described by a non-Gaussian distribution in **Chapter 6**. Such skewed distributions were examined and approximately described by use of the gamma (Pearson's Type III) distribution in this chapter.

In **Section 7.2**, the possibility of the gamma distribution approximation were successfully examined and demonstrated for the concentration distributions measured in rectangular or trapezoidal cross-section laboratory flumes, and natural streams.

The main descriptors of the concentration distributions measured, that is, the concentration times of the centroid (the average), the peak-concentration time (the modal value), the top of leading limb, the variance, and the peak concentration were investigated in **Section 7.3**. The concentration time of the centroid of the distribution $\bar{t}$ is commonly longer than that of the peak concentration t_P, but the celerities of the centroid and the peak concentration is the same as the mean velocity U for the cross-sectional averaged concentration curves C in laboratory. On the contrary, $\bar{t}_c$ of $\bar{c}_c$: a point-measured concentration curves at a center of flow-section is shorter than $\bar{t}$ of C, but its celerity is the same as the mean velocity U for laboratory data, but 1.2 times larger than U for natural streams. That is, the convective velocity for $\bar{c}_c$ and C is equal to U in laboratory, but the convective velocity for $\bar{c}_c$ in natural streams is larger than U. (Compare the result in **Chapter 8**.)

The behavior of the variance for $\bar{c}_c$ is quite different from that for C. That is, the magnitude of the variance σ_{ct}^2 is smaller than σ_t^2 for C and the growth of σ_{ct}^2 is slower than that of σ_t^2, but the slope of σ_{ct}^2 - x in a normal sheet is the same as that of σ_t^2 x. Therefore, it is concluded that the Moment Method for $\bar{c}_c$ gives the same dispersion coefficient as for C, but the required time for the linear growth of σ_{ct}^2 is much larger than that of σ_t^2. This delayed growth of the variance was described by the introduction of the parameter T_L', and the relationship of T_L' with the width to depth ratio B/d, Eq. 7.3.3 was obtained.

The relationship between the peak concentration C_P and its concentration time t_P was also investigated by being based on the gamma distribution approximation, and the new parameter β which links the celerities of the centroid and the top edge

of the distributions with U was introduced. The value of β for $\bar{c}_c$ in natural streams is $0.1 \sim 0.3$. The gamma distribution approximation by use of $\bar{t}$, $\sigma_c t^2$, and β was also successfully demonstrated.

Chapter 8

MASS TRANSPORT IN THE FLOWS OVER PERMEABLE BOUNDARIES

8.1 Introduction and Objectives

The actual streams under natural environment commonly flow over permeable boundary consisting of silts, sands, gravels and so on, and it is well known that there exist the sub-surface flow under permeable boundaries and the inter-flow between surface and sub-surface flows through the permeable beds. Therefore, the associated momentum and mass transfer between two kinds of flow influences the characteristics of flow and the mass transport in the surface flow and the sub-surface flow. Yamada and Kawabata (1982) reported that the velocity distribution of the surface flow is still stated by the log-law, but should be shifted, and the friction factor is larger than that in impervious flows; the velocity distribution in the sub-surface flow is described by the exponential function and becomes constant with the increase of the depth.

This inter-flow also influences the longitudinal and depth-wise transports of the mass contained in surface and/or sub-surface flows. Einstein (1968), and Ashida, Egashira, Kanayashiki and Ogawa (1980) reported that the concentration of fine particles in the flows over sand or gravel beds decreases in the longitudinal direction. Nagaoka and Ohgaki (1990) investigated the depth-wise dispersion coefficient in such a porous boundary in view of the water quality improvement works. Adrian and Martel (1990) measured the longitudinal dispersion coefficient in overland flow of wastewater on the grass covered slopes and reported the magnitude of the dispersion coefficient at $(2. \sim 30.) \times 10^{-2}$ m^2/s.

This chapter is concerned with the mass transport of solute in the vertical and longitudinal directions in the flows over permeable boundaries, because the mecha-

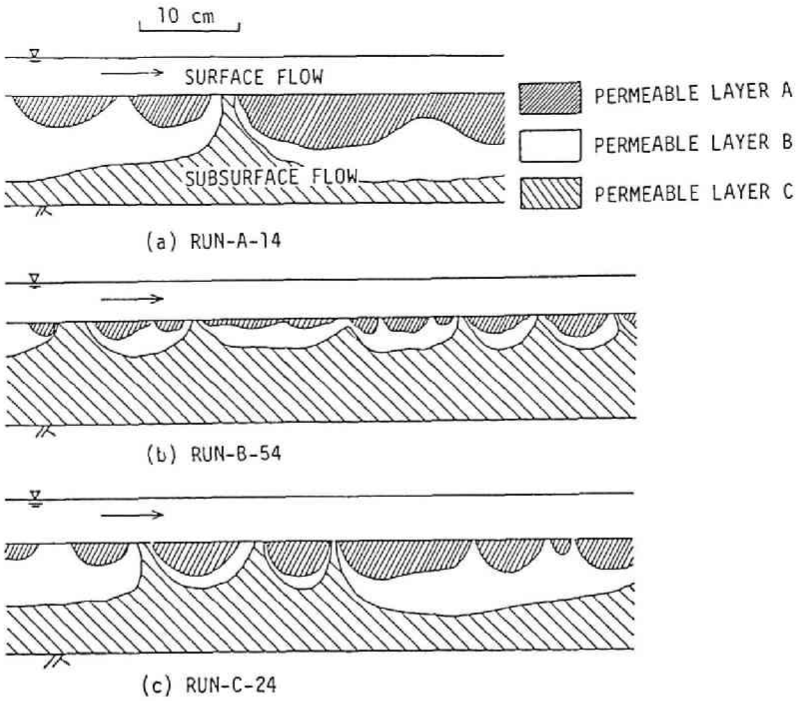

Figure 8.2.1: Classification of permeable boundary measured by flow visualizatfion.

nism of the depth-wise mass transport has not yet been clarified, and its effects on the longitudinal transport have not yet been investigated. The study focuses on the convective velocity and the dispersion coefficient of tracer clouds in the flow over permeable boundaries. Theoretical analysis will show that the convective velocity and the dispersion coefficient are quite different from those in the flow over impermeable boundaries by the effect of vertical mass transport between the surface and the sub-surface flows.

8.2 Results of Preliminary Experiment

8.2.1 Classification of Permeable Boundary in View of Mass Transport

Iwasa, Aya and Nakai (1986) made the dye tracer study in the flows over porous beds made by 4 kinds of sorted sands. The flow visualization with dye solution disclosed the inter-flow. Figs. 8.2.1 (a), (b), (c) show the permeable boundary is classified into

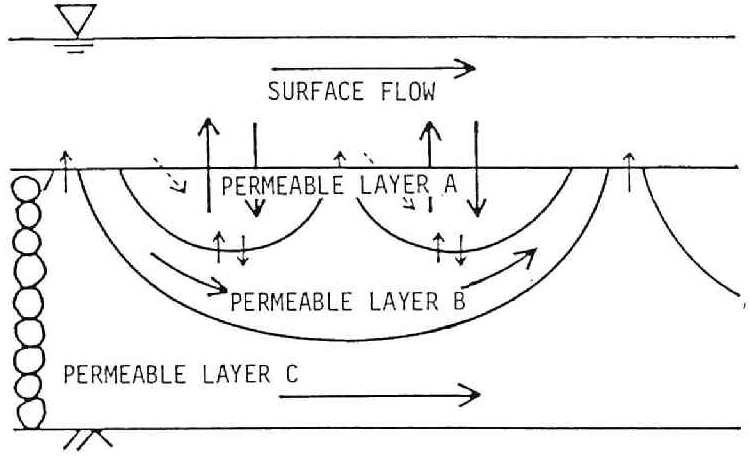

Figure 8.2.2: Schematic illustration of flows in permeable boundary. The hatched region is the mixing layer which consists of the mixing cell where the mass transfer between surface and sub-surface flows is the most active.

three layers; the layer A is rapidly dyed by Rhodamine B solution inserted in the surface flow and the intruded dye returns to the surface flow soon after stopping the insertion of the dye solution, the layer B can also be dyed, but more slowly, and the layer C is not dyed by the dye solution from the surface flow. The interface between the layers B and C is clear and stable. The Methylene Blue solution inserted at the bottom of the permeable boundary does not intrude the layer B and the interface observed by two methods of dye insertion is the same one.

The eddy flow is observed in the layer A, and it is realized that the depth-wise mass and momentum transports exist between two flows because of large velocity difference.

8.2.2 Geometrical Features of Mixing Layer/Mixing Cell

The permeable boundary is schematically classified into three regions as shown in Fig. 8.2.2. The permeable layer A is the most active region for the vertical mass transport and the interaction between surface and sub-surface flows, and it is called the "Mixing Layer" hereafter. It consists of the mixing cells as shown in Fig. 8.2.2. Geometrical features of the mixing cell are described by the average thickness y_b, the thickness to length ratio η, and the length ratio ξ of the active surface length L' to

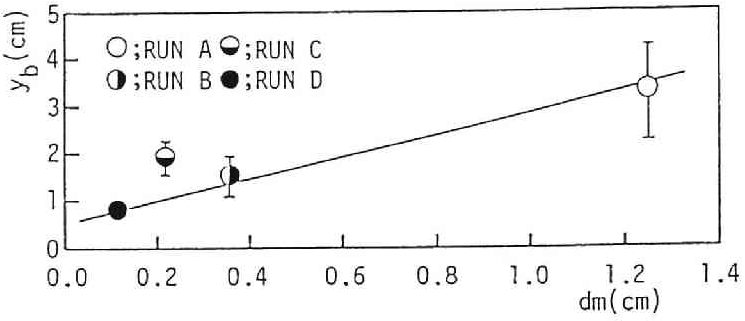

Figure 8.2.3: Thickness of the mixing cell and the mean grain size of permeable boundaries.

the total length L, and they are respectively defined by

$$y_b = \frac{\sum_{i=1}^{n} a_i}{\sum_{i=1}^{n} l_i} = \frac{A}{L'} \tag{8.2.1}$$

$$\eta = \frac{n y_b}{L'} \tag{8.2.2}$$

$$\xi = L'/L \tag{8.2.3}$$

where a the area of the mixing cell, A the total area of the mixing cells observed in the length L, l the surface length of the mixing cell, L' the total length of the surface length of the mixing cells observed in the length L, n the number of the mixing cell observed in the length L.

20 dye tracer experiments in 4 kinds of beds by Iwasa, Aya and Nakai (1986) disclosed the geometrical features of the mixing cell. The relationship of y_b with the mean grain size d_m of the bed is presented in Fig. 8.2.3, and it is stated by

$$y_b = 2.35 d_m + 0.53 \qquad \text{(unit in cm)} \tag{8.2.4}$$

ξ and η were not found to be related with the hydraulic variables and the grain size of the beds, but as shown in Fig. 8.2.4, their magnitude are commonly

$$\xi \approx 0.825$$

$$\eta \approx 0.25$$

Therefore, the number of the mixing cells observed in the unit length is stated by

$$n/L = 0.206/y_b \tag{8.2.5}$$

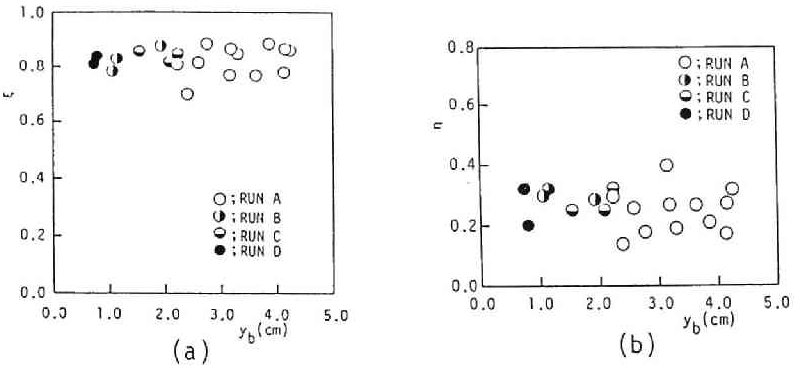

Figure 8.2.4: Dimensions of the mixing cell. (a) Mixing cell length, and (b) Mixing cell thickness.

8.2.3 Characteristic Time for Concentration Decay

The concentration decay in the mixing layer after stopping the tracer injection are presented in Fig. 8.2.5 on log-normal sheet, and it is clearly stated by use of the exponential function. The dimensional analysis disclosed the relationship between the characteristic time of the decay T_{10} and the hydraulic variables of the surface and the sub-surface flows as shown in Fig. 8.2.6. The relationship is described by

$$\frac{d_m}{T_{10}U_A} = C\left(\frac{K}{U_A}\right)\left(\frac{h}{d_m}\right)^{3/5}\left(\frac{U_A}{\sqrt{gh}}\right)^{7/10} \tag{8.2.6}$$

where U_A the average velocity of the surface flow, h the depth of the surface flow, K the permeability coefficient of the porous beds, d_m the mean grain size of the beds, and g the gravitational acceleration. The subscript $_{10}$ denotes the base of the decay is 10.

The mass exchange velocity k between the surface and the sub-surface flow is related with the characteristic time T_{10} as

$$k = (\ln 10)y_b/T_{10} \tag{8.2.7}$$

and the magnitude of k is calculated at

$$k/U_A \approx (2.0 \sim 9.0) \times 10^{-3}$$

The vertical dispersion coefficient D_y in porous beds is described by

$$D_y \approx \frac{4\ln 10}{\pi^2}\frac{y_b^2}{T_{10}} \tag{8.2.8}$$

and its magnitude is

$$D_y/hu_* = (0.6 \sim 16) \times 10^{-2}$$

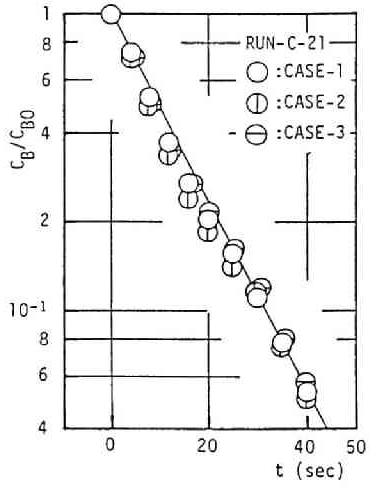

Figure 8.2.5: Example of concentration decay measured in the mixing cell.

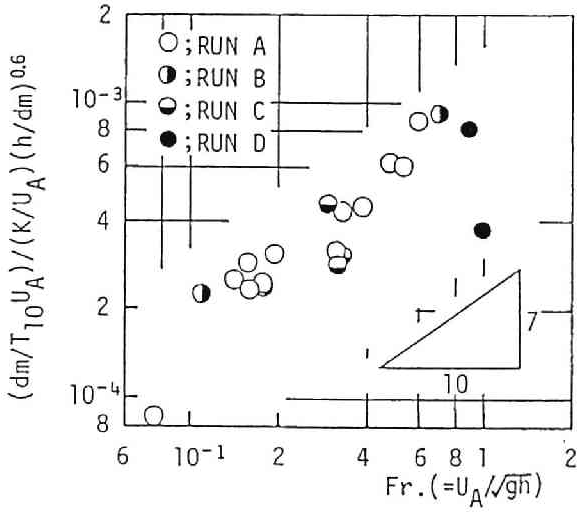

Figure 8.2.6: Characteristic time and hydraulic variables.

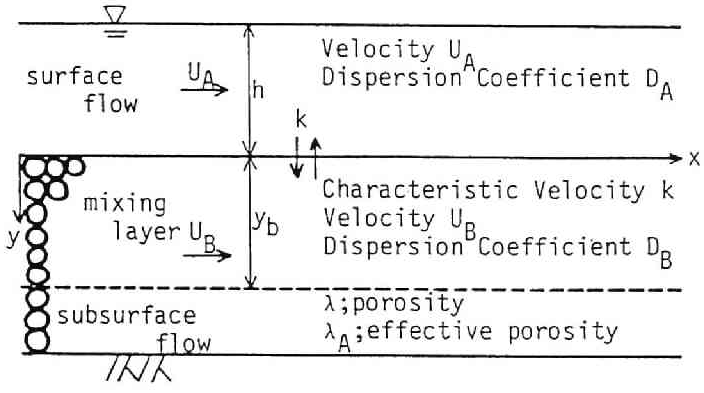

Figure 8.3.1: Definition sketch of variables for the longitudinal mass transport.

or

$$D_y/U_b d_m = 0.9 \sim 25$$

The order of the magnitude of D_y is the same as the depth-wise turbulent diffusion coefficient of the surface flow, and much larger than the lateral dispersion coefficient in porous media. Thus, it was disclosed that there is the mass exchange between the surface and the sub-surface flows, and the vertical mixing in porous beds are affected by the surface flows.

8.3 Longitudinal Dispersion in Flows over Permeable Boundary

8.3.1 Mathematical Models

This section is concerned with the effects of the vertical mass transport described in Section 8.2 on the longitudinal convection and the dispersion of tracer clouds. Mathematical models are similar to those of the "Dead Zone Models" for the longitudinal mixing in open channel flows with dead zone (Okubo, 1973, and Muramoto, Michiue and Nakagawa, 1976). The flows are idealized as shown in Fig. 8.3.1, in which the mixing layer is identified by the layer A.

Supposing the uniform surface flow over a saturated permeable boundary and referring to the definition sketch of Fig. 8.3.1, the mass conservation equations of unit width in two flows can be written as follows:

Mass conservation equation in the surface flow,

$$\frac{\partial C_A}{\partial t} + U_A \frac{\partial C_A}{\partial x} = D_A \frac{\partial^2 C_A}{\partial x^2} - \frac{\lambda_A k}{h}(C_A - C_B) \qquad (8.3.1a)$$

Mass conservation equation in the mixing layer,

$$\frac{\partial C_B}{\partial t} + U_B \frac{\partial C_B}{\partial x} = D_B \frac{\partial^2 C_B}{\partial x^2} - \frac{\lambda_A k}{\lambda y_b}(C_B - C_A) \qquad (8.3.1b)$$

where C_i is the average concentration in the flow i, U_i the average velocity, D_i the dispersion coefficient for the cross-section Bh, h the depth, y_b the thickness of mixing layer, k the characteristic velocity for mass exchange, λ the porosity, λ_A the effective porosity for mass exchange, x the distance, and t the time. The subscript i denotes the variables for the surface flow ($i = A$), and the sub-surface flow ($i = B$).

Eqs. 8.3.1 can be rewritten in the non-dimensional form by use of the friction velocity u_*, and the depth of the surface flow h as:

$$\frac{\partial C_A}{\partial t^*} + {U_A}^* \frac{\partial C_A}{\partial x^*} = {D_A}^* \frac{\partial^2 C_A}{\partial {x^*}^2} - \frac{k^*}{{s_A}^*}(C_A - C_B) \qquad (8.3.2a)$$

$$\frac{\partial C_B}{\partial t^*} + {U_B}^* \frac{\partial C_B}{\partial x^*} = {D_B}^* \frac{\partial^2 C_B}{\partial {x^*}^2} - \frac{k^*}{{s_B}^*}(C_B - C_A) \qquad (8.3.2b)$$

where $s_A^* = 1/\lambda_A$, $s_B^* = 1/\lambda_A \times \lambda y_b/h$, and $*$ denotes the non-dimensional variables, but it will be neglected hereafter.

The above system of partial differential equations under the specified initial conditions is easily solved in the form of characteristic function of concentration distribution by use of the Fourier-Laplace transformation:

$$\overline{C}_i(m,t) = \int_{-\infty}^{\infty} e^{jmx} C_i(x,t)dx \qquad (j^2 = -1) \qquad (8.3.3)$$

The n-th moment of concentration distribution defined by following equation:

$$M_{in}(t) \equiv \int_{-\infty}^{\infty} x^n C_i(x,t)dx \Big/ \int_{-\infty}^{\infty} C_i(x,t)dx \qquad (8.3.4)$$

is obtained by use of the characteristic function as follows,

$$M_{in}(t) = \frac{1}{j^n}\frac{\partial^n}{\partial m^n}\overline{C}_i(m,t)\Big|_{m=0} \Big/ \overline{C}_i(0,t) \qquad (8.3.5)$$

8.3.2 Solving the Equations under Special Initial Conditions

The special case in which the tracer of mass $W_0 = \rho h$ is inserted at $x = 0$ and $t = 0$ in the surface flow will be considered. Initial conditions are written as;

$$C_A(x,0) = \delta(x) \qquad (8.3.6a)$$

$$C_B(x,0) = 0 \tag{8.3.6b}$$

where $\delta(x)$ is the Dirac's distribution. By using the Fourier-Laplace transform of Eq. 8.3.3, Eqs. 8.3.2 are transformed into the following forms.

$$\frac{\partial \overline{C}_A}{\partial t} = jmU_A\overline{C}_A - D_Am^2\overline{C}_A - \frac{k}{s_A}(\overline{C}_A - \overline{C}_B) \tag{8.3.7a}$$

$$\frac{\partial \overline{C}_B}{\partial t} = jmU_B\overline{C}_B - D_Bm^2\overline{C}_B - \frac{k}{s_B}(\overline{C}_B - \overline{C}_A) \tag{8.3.7b}$$

and the initial conditions of Eq. 8.3.6 are transformed as

$$\overline{C}_A(m,0) = 1 \tag{8.3.8a}$$

$$\overline{C}_B(m,0) = 0 \tag{8.3.8b}$$

The solutions of Eqs. 8.3.7 under the initial conditions of Eq. 8.3.8 are easily obtained as:

$$\overline{C}_A = \left(\frac{1}{2} + \frac{\alpha-\beta}{2\sqrt{Q}}\right)e^{\gamma_1 t} + \left(\frac{1}{2} - \frac{\alpha-\beta}{2\sqrt{Q}}\right)e^{\gamma_2 t} \tag{8.3.9a}$$

$$\overline{C}_B = \frac{k}{s_B\sqrt{Q}}(e^{\gamma_1 t} - e^{\gamma_2 t}) \tag{8.3.9b}$$

where

$$\alpha = -\left(m^2D_A + \frac{k}{s_A}\right) + jmU_A$$

$$\beta = -\left(m^2D_B + \frac{k}{s_B}\right) + jmU_B$$

$$P = \alpha + \beta$$

$$Q = (\alpha-\beta)^2 + 4k^2/s_As_B$$

$$\gamma_1 = (P + \sqrt{Q})/2$$

$$\gamma_2 = (P - \sqrt{Q})/2$$

The n-th moment is given by use of Eq. 8.3.5 for Eq. 8.3.9. The concerned transport characteristics in the longitudinal direction are the total amount of mass, the convective velocity and the dispersion coefficient in each flow. Therefore, the zero-th, the first, and the second moment are obtained as:

The zero-th moment,

$$M_{A0} = \theta + (1-\theta)e^{-st} \tag{8.3.10a}$$

$$M_{B0} = \theta(1 - e^{-st}) \tag{8.3.10b}$$

where

$$\theta \equiv h/(h+\lambda y_b) \tag{8.3.11}$$

$$s \equiv (h+\lambda y_b)k/y_b u_* \tag{8.3.12}$$

The first moment,

$$\mu_A = \left\{ \frac{2\theta(1-\theta)}{s}(U_A - U_B)(1-e^{-st}) + \theta u t + (1-\theta)\tilde{u}te^{-st} \right\} / \, M_{A0} \tag{8.3.13a}$$

$$\mu_B = \left\{ \frac{(1-\theta)(2\theta-1)}{s}(U_A - U_B)(1-e^{-st}) + \theta(ut - \tilde{u}te^{-st} \right\} / \, M_{B0} \tag{8.3.13b}$$

where

$$u = \frac{h}{h+\lambda y_b}U_A + \frac{\lambda y_b}{h+\lambda y_b}U_B$$

$$\tilde{u} = \frac{\lambda y_b}{h+\lambda y_b}U_A + \frac{h}{h+\lambda y_b}U_B$$

The second moment moment,

$$\begin{aligned}
{\sigma_A}^2 &= -\frac{a_0}{M_{A0}} - \left(\frac{\Omega_A}{M_{A0}}\right)^2 + \frac{2a_1}{M_{A0}}t + \left(1 - \frac{\theta}{M_{A0}}\right)\frac{\theta}{M_{A0}}u^2t^2 \\
&+ \left\{ \frac{a_0}{M_{A0}} + 2\left(\frac{\Omega_A}{M_{A0}}\right)^2 + \frac{2}{M_{A0}}\left(a_2 - \frac{a_3}{M_{A0}}\right)t + \left(\tilde{u} - \frac{2\theta u}{M_{A0}}\right)\frac{1-\theta}{M_{A0}}\tilde{u}t^2 \right\} e^{-st} \\
&- \left\{ \frac{\Omega_A - (1-\theta)\tilde{u}t}{M_{A0}} \right\}^2 e^{-2st}
\end{aligned} \tag{8.3.14a}$$

$$\begin{aligned}
{\sigma_B}^2 &= -\frac{b_0}{M_{B0}} - \left(\frac{\Omega_B}{M_{B0}}\right)^2 + \frac{2b_1}{M_{B0}}t + \left(1 - \frac{\theta}{M_{B0}}\right)\frac{\theta}{M_{B0}}u^2t^2 \\
&+ \left\{ \frac{b_0}{M_{B0}} + 2\left(\frac{\Omega_B}{M_{B0}}\right)^2 + \frac{2}{M_{B0}}\left(b_2 + \frac{b_3}{M_{B0}}\right)t - \left(\tilde{u} - \frac{2\theta u}{M_{B0}}\right)\frac{\theta}{M_{B0}}\tilde{u}t^2 \right\} e^{-st} \\
&+ \left\{ \frac{\Omega_B + \theta\tilde{u}t}{M_{B0}} \right\}^2 e^{-2st}
\end{aligned} \tag{8.3.14b}$$

where

$$\begin{aligned}
a_0 &= -4\theta(1-\theta)(D_A - D_B)/s - 6\theta(1-\theta)(1-2\theta)(U_A - U_B)^2/s^2 \\
a_1 &= \theta D + \Omega_A u(1 - \theta/M_{A0}) \\
a_2 &= (1-\theta)\tilde{D} - \Omega_A\tilde{u} \\
a_3 &= \Omega\{(1-\theta)\tilde{u} - \theta u\} \\
b_0 &= -2\theta(1-2\theta)(D_A - D_B)/s - 2\theta\{(1-2\theta)^2 - 2\theta(1-\theta)\}(U_A - U_B)^2/s^2 \\
b_1 &= \theta D + \Omega_B u(1 - \theta/M_{B0}) \\
b_2 &= -(\theta\tilde{D} + \Omega_B\tilde{u})
\end{aligned}$$

$$
\begin{aligned}
b_3 &= \Omega_B \theta(u+\tilde{u}) \\
D &= \theta D_A + (1-\theta) D_B + \theta(1-\theta)(U_A - U_B)^2/s \\
\tilde{D} &= (1-\theta) D_A + \theta D_B - \theta(1-\theta)(U_A - U_B)^2/s \\
\Omega_A &= 2\theta(1-\theta)(U_A - U_B)/s \\
\Omega_B &= \theta(1-2\theta)(U_A - U_B)/s
\end{aligned}
$$

8.4 Results

The amount of mass W_i, the convective velocity U_{ci}, and the dispersion coefficient D_i are stated/defined by the following relationships:

Total amount of mass,

$$W_A \equiv \rho h M_{A0} \tag{8.4.1a}$$

$$W_B \equiv \rho \lambda y_b M_{B0} \tag{8.4.1b}$$

Convective velocity,

$$U_{ci} \equiv \frac{dM_{i1}}{dt} \qquad \text{for} \qquad i = A, B \tag{8.4.2}$$

Dispersion Coefficient measurable;

$$\overline{D_i} \equiv \frac{1}{2}\frac{d\sigma_i^2}{dt} \equiv \frac{1}{2}\frac{d}{dt}(M_{i2} - M^2{}_{i1}) \qquad \text{for} \qquad i = A, B \tag{8.4.3}$$

These transport characteristics are found as functions of the travel time of cloud and the time-dependent behavior are illustrated in Figs. 8.4.1 for (a) Total amount of mass, (b) Convective velocity, and (c) Dispersion coefficient, where the parameter s defined by Eq. 8.3.12 is equal to a reciprocal of the characteristic time scale. For a larger travel time, they converge on constant values respcetively, and they are described bellow.

Total amount of mass

By use of Eqs. 8.4.1, Eqs. 8.3.10 derive the mass existing in each flow in final stage as

$$W_A|_{t\to\infty} = \theta W_0 \tag{8.4.4a}$$

$$W_B|_{t\to\infty} = (1-\theta) W_0 \tag{8.4.4b}$$

The total amount of mass in two flows are

$$W_A + W_B = W_0$$

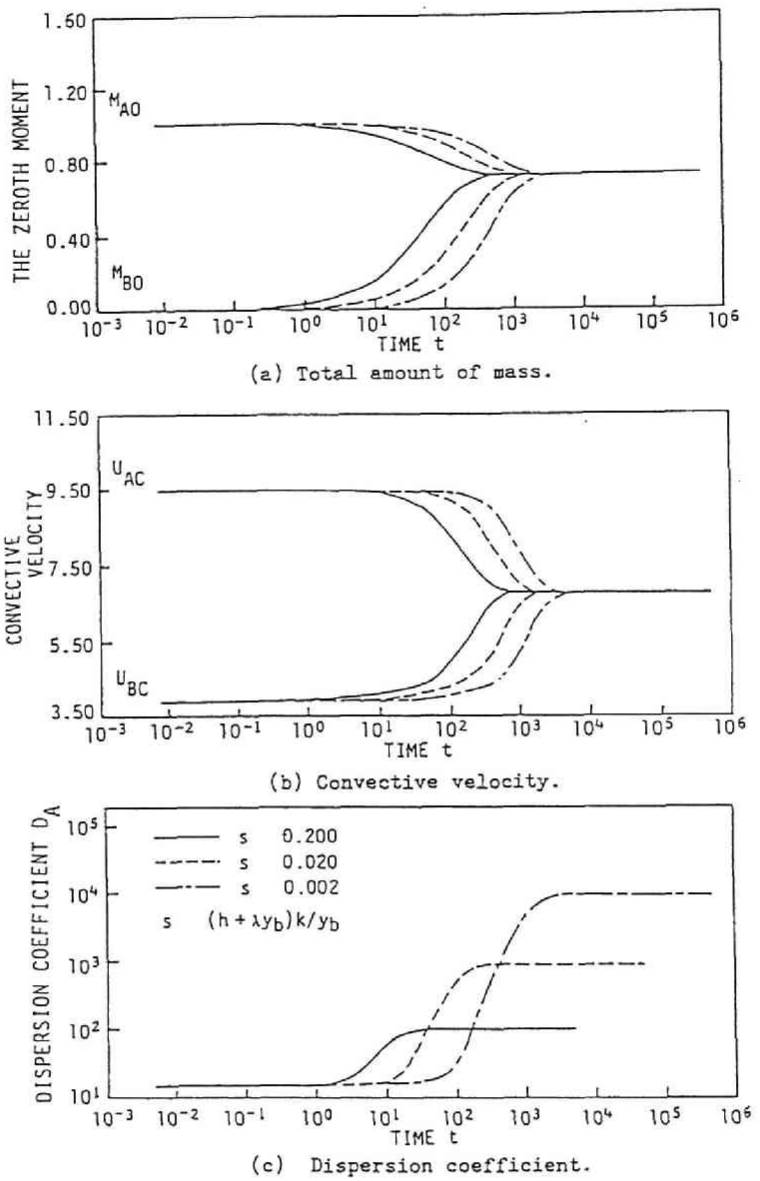

Figure 8.4.1: Time dependent behavior of transport characteristics. The parameter $s = (h + \lambda y_b)k/y_b u_*$ is equal to a reciprocal of the characteristic time scale. (a) The zero-th moment, (b) Convective velocity, and (c) Dispersion coefficient.

at arbitrary time and equal to W_0. The amount of mass inserted in the surface flow at $t = 0$ is $W_A(0) = W_0$, and that in the sub-surface flow is $W_B(0) = 0$. Traveling in the longitudinal direction, the tracer spreads in the longitudinal and vertical directions in both of two flows mainly by the vertical mass exchange characterized by the velocity k. For a large travel time, the amount of mass in each flow becomes constant, and the ratio of mass existing in each flow is equal to the ratio of each flow section as shown in Eqs. 8.4.4.

Convective velocity of tracer clouds

By use of Eq. 8.4.2, Eq.8.3.13 derives the convective velocity in a final stage as

$$U_{cA}|_{t\to\infty} = U_{cB}|_{t\to\infty} = \frac{h}{h+\lambda y_b}U_A + \frac{\lambda y_b}{h+\lambda y_b}U_B \tag{8.4.5}$$

During a short travel time, the inserted tracer is convected by the surface flow and the velocity of tracer cloud is equal to the average velocity of the surface flow. However, the convective velocity of cloud in the surface flow becomes slower and that in the sub-surface flow becomes higher. For a large travel time, both convective velocities become the same as described in Eq. 8.4.5 and equal to the weighted average of the velocity of two flows, while the average flow velocity in each flow is quite different from each other. This interesting phenomenon can be explained as follows;

1. Real mass transport processes are the vertical mass transport between surface and sub-surface flows, that is, in the leading limb the tracer convected by the surface flow intrudes into the sub-surface flow and in the falling limb the intruded tracer returns into the surface flow.

2. The convective velocity in the final stage is given by Eq. 8.4.5. Its value is equal to the weighted average of velocities of two flows, and the flow section of each flow is used as the weighting factor.

Dispersion coefficient

By use of Eq. 8.4.3, Eqs.8.3.14 derive the dispersion coefficient measured in a final stage as:

$$\begin{aligned}\overline{D}_A|_{t\to\infty} &= \overline{D}_B|_{t\to\infty} \\ &= \frac{h}{h+\lambda y_b}D_A + \frac{\lambda y_b}{h+\lambda y_b}D_B + \frac{(\lambda y_b)^2 h}{(h+\lambda y_b)^3}\cdot\frac{h}{k}(U_A - U_B)^2\end{aligned} \tag{8.4.6}$$

The mass transport mechanism explained in the above paragraph is much more effective on the dispersion coefficient. For a large travel time, the dispersion coefficient is

given by Eq. 8.4.6 and stated by the sum of three terms. The first two terms are the weighted average of the dispersion coefficient in each flow with use of the flow section as the weighting factor. The last term shows the effect of vertical mass transport between the surface and the sub-surface flows, and the velocity difference between two flows. This term is sometimes much larger than the first two terms. Eq. 8.4.6 also shows that the measurable dispersion coefficients in both flows have the same value.

Thus, results obtained by mathematical models indicate that the mass exchange between the surface and sub-surface flows play an important role in the longitudinal mass transport. Under special hydraulic conditions, the convective velocity is much smaller and the dispersion coefficient much larger than those in the flow over impermeable boundaries.

8.5 Discussions on Dispersion Coefficient

The time dependent growth of the variance σ_A^2 described by Eq. 8.3.14a is shown in Fig. 8.5.1 (a) on log-log sheet, and (b) on normal sheet. σ_A^2 rapidly increases during $1 \leq st \leq 10$, and has the linear relationship with st for $st \geq 10$. Thus, the required length for linear growth of the variance depends on the parameter s, and commonly much larger than that in impervious channels.

The third term of the dispersion coefficient given by Eq. 8.4.6 is the function of k, h, y_b, λ, U_A and U_B. Preliminary studies in the experimental flume with sand beds show that the magnitude of the characteristic velocity k is of the order of 10^{-2} cm/s, and the thickness of mixing layer y_b a few times of the grain size of permeable boundary, and that they are dependent on hydraulic conditions. The relationship between $\gamma \equiv (h\lambda y_b)^2/(h + \lambda y_b)^3$ and y_b/h is presented in Fig. 8.5.2. γ is strongly affected by y_b/h and has the maximum value at $y_b/h = 2/\lambda$. Therefore the value of the dispersion coefficient is the maximum at $y_b/h = 2/\lambda$. Thus, the longitudinal mass transport in the flows over permeable boundaries is strongly affected by the thickness of the mixing cell y_b, and the characteristic velocity of mass exchange k.

The results obtained by the dispersion experiment made in the laboratory flumes with sand bed (Iwasa, Aya and Nakai, 1986) are summarized in Table 8.5.1. The convective velocities U_{cA} and U_{cB} of surface and sub-surface flows agrees each other, and commonly slower than the discharge velocity U_A in the surface flows as described in Eq. 8.4.5. The dispersion coefficient D_{ob} measured in the surface flows by the

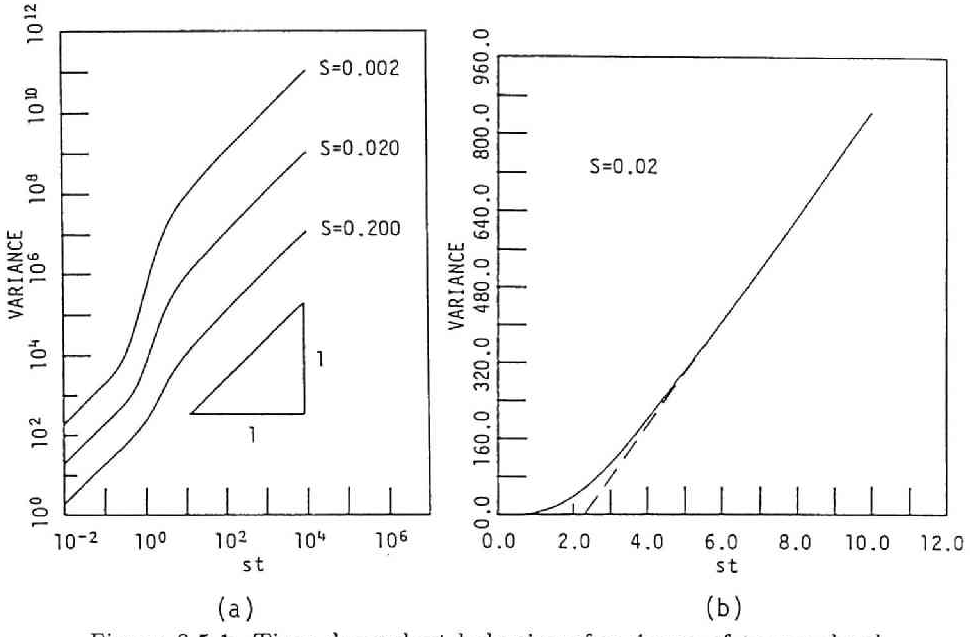

Figure 8.5.1: Time dependent behavior of variance of tracer cloud. (a) on log-log sheet, and (b) on normal sheet.

moment method are listed in the column 6, and its order of the magnitude is much bigger than those of D_A which are estimated by Eq. 4.5.15. It is of the same order measured in the flows on the glass covered slope by Adrian and Martel (1990). Thus, the mathematical results obtained in **Section 8.4** were verified.

In natural streams with the large aspect ratio B/h, the third term can be extremely smaller than the first term, because the dispersion coefficient D_A is dependent on B/h as described in **Chapter 5**, and much larger in these streams. However, it would be important in the shallow, narrow, and steep streams flowing over the bed composed by large gravels in mountainous areas.

The discussion obtained above will be extended to the "Dead Zone Model". In the condition of $U_B = 0$, $D_B = 0$, and $h/y_b =$ *flow zone volume / dead zone volume*, these results are found to be equivalent ones in the models with dead zone in channel bed (Valentine and Wood, 1977), and in channel sides (Muramoto, Michiue and Nakagawa, 1976). They are concerned with the transport processes only in the main flow, and the interesting results described above are not indicated. The dead zone modeling should be carefully examined in view of not only the dispersion coefficient, but also the convective velocity of tracer cloud and the behavior of the variance which

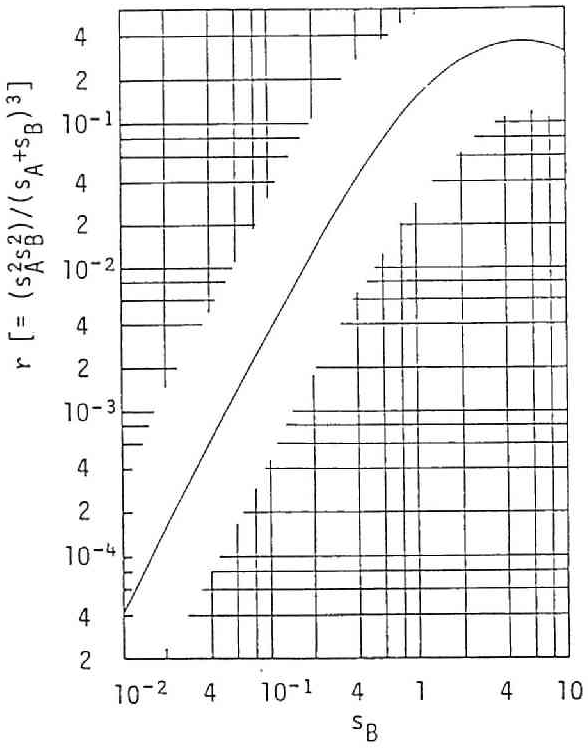

Figure 8.5.2: Relationship between γ and y_b/h.

Table 8.5.1: Summary of dispersion experiments in laboratory flume with sand bed.

(1) RUN NO.	(2) U_{CA}	(3) U_{CB}	(4) U_{CP}	(5) U_A	(6) D_{ob}	(7) D_A	(8) B/h	(9) D_B	(10) k/u_*	(11) k_{10}/u_*
		(cm/sec)			hu_*	hu_*		hu_*	($\times 10^{-2}$)	
A1	13.0	12.0	11.5	14.8	178	13.1	2.10	8.06	7.54	3.27
A2	5.31	5.35	6.19	10.6	1204	26.2	4.20	11.3	1.97	0.856
B1	15.5	15.2	13.6	19.8	663	14.5	2.33	8.29	2.68	1.16
B2	10.7	10.8	9.28	16.9	1454	21.1	3.38	8.43	1.71	0.743
C1	24.5	21.2	22.0	34.3	1039	13.2	2.13	5.44	2.57	1.12
C2	20.0	19.4	18.4	30.4	1023	17.9	2.88	4.89	2.75	1.19

requires a much more longer period for the linear growth.

8.6 Conclusions

The vertical and the longitudinal mass transports in the flow over permeable boundaries were investigated in this chapter. Preliminary dye tracer study in **Section 8.2** disclosed the features in the sub-surface flows which have the surface flow over the permeable boundary. That is,

1. The sub-surface flow is classified into three kinds of flows/regions in view of the vertical mass transport between surface and sub-surface flows. The strong mass transport is observed in the upper two layers, and it is influenced by the surface flow.

2. The mass transport is the most active in the mixing cell in the first upper layer. It covers 80% of the surface of the permeable boundary; its thickness is a few times of the mean grain size of the porous media, and the thickness to length ratio is 0.25.

3. The vertical mass transport between two flows and/or in the sub-surface flow was examined by use of the characteristic time scale T_{10}, the characteristic velocity of mass exchange k, and the vertical dispersion coefficient D_y in the mixing layer. T_{10} is described by Eq. 8.2.6, the order of the magnitude of k/U_A is 10^{-3}, and that of D_y is the vertical turbulent diffusion coefficient in the surface flows.

The longitudinal mass transport in the flows over permeable boundary was investigated by the theoretical analysis in **Sections 8.3** and **8.4**. Results obtained disclosed that the mass exchange between the surface and sub-surface flows play an important role in the longitudinal mass transport. That is,

1. The convective velocity in the surface flow is equal to the weighted average of two velocities in the surface and the sub-surface flows, when the cross-sectional areas are used as a weighting factor. The convective velocity in the sub-surface flow is the same values as that in the surface flow.

2. The dispersion coefficient in the surface flow is a sum of three terms; the first two terms are the weighted average of dispersion coefficient in each flow, when cross-sectional areas are used as a weighting factor, and the last term is caused by the velocity difference and the mass transport between two flows. The value

of the dispersion coefficient in the sub-surface flow is the same as that in the surface flow.

3. These characteristics are strongly dependent on the ratio of the thickness of the mixing layer to the depth, and the characteristic velocity of mixing. They play an important role in the torrential flow.

These theoretical results were verified by use of the experimental results for the longitudinal dispersion in the flows over sand bed in Section 8.5.

The results obtained in this chapter are easily extended to the dead zone model for longitudinal mixing in the channel flow with dead zone in channel bottom and/or sides. They will also be useful in the research of the deposition/transport of fine particles over gravel beds, the groundwater pollution caused by the contaminants from the surface water, and the longitudinal mass transport in the flows over hill slopes.

References in Part II

Adrian, D. D., and Martel, C. J. (1990). Longitudinal dispersion in overland flow of wastewater, *Proc. Int'l Conf. on Physical Modeling of Transport and Dispersion*, IAHR-ASCE, 14A.15–16.

Ashida, K., Egashira, S., Kanayashiki, T., and Ogawa, Y. (1980). Yield processes of wash load in stream channels, *Annuals*, Disaster Prevention Research Instituite, Kyoto University, Vol. 23, No. B-2, 413–431, (in Japanese).

Aya, S., Iwasa, Y., and Toda, T. (1981). Analysis of some longitudinal dispersion experiments in natural streams, *Proc. 25th Japanese Conference on Hydraulics*, JSCE, 423–432, (in Japanese).

Einstein, H. A. (1968). Deposition of silt particles in a gravel bed, *J. Hydraulic Division, Proc. ASCE*, Vol. 94, No. HY5, 1197–1205.

Elder, J. W. (1959). The dispersion of marked fluid in turbulent shear flow, *J. Fluid Mechanics*, Vol. 5, 544–560.

Fischer, H. B. (1966). Longitudinal dispersion in laboratory and Natural streams, Report No. KH-R-12, California Institute of Technology, Pasadena, California.

Godfrey, R. G., and Frederick, B. J. (1963). Dispersion in natural streams, Open file report, U. S. Geological Survey.

Hay, J. R., (1966). Mass transport mechanics in open channel flow, Dissertation presented to Vanderbilt University, Nashville, Tennessee., in partial fulfillment of the requirements for the degree of Doctor of Philosophy.

Iwasa, Y., Aya, S., and Nakai, T. (1986). Mass transport between turbulent surface and subsurface flows over permeable boundaries and its effect on the longitudinal dispersion, *Annuals*, Disaster Prevention Research Institute, Kyoto University, Vol. 29, B–2, 511–527, (in Japanese).

McQuivey, R. S., and Keefer, T. N. (1976). Convective model of longitudinal dispersion, *J. Hydraulic Division, Proc. ASCE*, Vol.102, No. HY10, 1409–1424.

Monin, A. S., and Yaglom, A. M. (1971). "Statistical Fluid Mechanics" translated from the Russian by Scripta Technica, Inc., and edited by J. L. Lumley, MIT Press, Cambridge, Massachusetts.

Muramoto, Y., Michiue, M., and Nakagawa, H. (1976). Longitudinal dispersion in open-channel flows, *Proc. 20th Japanese Conference on Hydraulics*, JSCE, 133-139, (in Japanese).

Nagaoka, H., and Ohgaki, S. (1990). Mass transfer mechanism in a porous riverbed, *Water Research*, Vol. 24, No. 4, 417–425.

Okubo, A. (1975). Effect of shoreline irregularities on streamwise dispersion in estuaries and other embayments, *Netherlands J. Sea Research*, 6(1-2), 213–224.

Petersen, F., Bo (1977). Prediction of longitudinal dispersion in natural streams, Series Paper No. 14, Institute of Hydrodynamics and Hydraulic Eng., Technical University of Denmark.

Sayre, W. W. (1969). Dispersion of silt particles in open channel flow, *J. Hydraulic Division, Proc. ASCE*, Vol. 95, No. HY3, 1009–1039.

Sayre, W. W. (1977). Discussion on "Convective model of longitudinal dispersion" by McQuivey and Keefer (1976), *J. Hydraulic Division, Proc. ASCE*, Vol. 103, No. HY7, 820–823.

Shimada, S. (1980). Stochastic analysis of longitudinal dispersion, *Proc. 24th Japanese Conference on Hydraulics*, JSCE, 1–6, (in Japanese).

Taylor, G. I. (1953). Dispersion of soluble matter in solvent flowing slowly through a tube, *Proc. Royal Society of London*, Series A, Vol. 219, 186–203.

Thakston, E. L. and Schnelle, K. B., (1970). Predicting Effects of Dead Zones on Stream Mixing, *J. Sanitary Engineering Division, Proc. ASCE*, Vol. 96, No. SA2, 319-331.

Valentine, E. N., and Wood, I. R. (1977). Longitudinal dispersion with dead zones, *J. Hydraulic Division, Proc. of ASCE*, Vol. 103, No. HY. 9, 975–990.

Yamada, T., and Kawabata, N. (1982). A thoretical study on the resistance law of the flow over porous layer, *Proc. JSCE*, JSCE, No. 325, 69–80, (in Japanese).

Yotsukura, N., and Fiering, M. (1964). Numerical solution to a dispersion equation, *J. Hydraulics division, Proc. ASCE*, Vol. 90, No. HY5, 83–104.

PART III:

TRANSVERSE MIXING IN RIVERS

Chapter 9

NUMERICAL MODELING OF FLOWS AND TRANSVERSE MIXING IN A RIVER

9.1 Introduction

9.1.1 Objectives

Contaminants discharged into a river spread in the longitudinal, the transverse and the depth-wise directions by convection and turbulent transports. The flows in rivers is uni-directional and the magnitude of the length scale in the longitudinal direction is much larger than those in other two directions, and one-dimensional models have been the most usable. In case the transverse distribution of the concentration is of interest, the depth-averaged two-dimensional models are required. The stream tube models by Yotsukura and Sayre (1976) is one of the most famous 2-D models and they are successfully applied to the analyses of transverse mixing in many river channels (Lau and Krishnappan, 1981, Holly and Nerat, 1983, and so on), and its recent application to Yodo River was made by Li, Yagi and Sueishi (1987).

It is well known that the hydrodynamic transport processes, that is, the convection plays an important part in the mixing in the river, therefore the 2-D models for the flows and the mixing is required in case the flow field is not simple or unsteady, while the contaminant itself is passive. The development of the electronic computer system and the software in the last two decades makes these analysis possible and the 2-D mathematical models in the Cartesian coordinate system have mostly been used and solved by Finite Difference Method (FDM) or Finite Element Method (FEM).

During the last decade, the numerical analysis by use of the mathematical models in the curvilinear coordinate system with FDM has been developed, so that it saves computer resources and makes the handling of the computation codes much easier

especially in the flow analysis in the complicated domains. A river confluence forms such kind of complicated domains, and this chapter will show the 2-D mathematical models for flow behavior and associated mixing in a river in generalized curvilinear coordinate system, and it will be applied to Yodo River System.

9.1.2 Yodo River System

It is common that effluents from sewerage systems are discharged into rivers, therefore the water quality in a receiving river is usually worse than that in the upstream part of a river. In case river waters are used repeatedly for the source of the service water, the water quality problem in receiving rivers is serious, and the analysis of spreading of the effluent by use of refined models is required in view of water quality aspect as well as quantity aspect.

The area selected in this study is the Yodo River System, which is one of the most important rivers in Kinki metropolitan area, Japan. Its catchment area is 8,240 km^2 and the population in the riverbasin is 16 million. Its riverbasin is roughly divided into four portions, that is, three sub-riverbasins of three main tributaries; Uji River , Kizu River , Katsura River , and the lower sub-riverbasin from the confluence of three tributaries to the rivermouth. The Yodo River System, and its water systems are illustrated in Figs. 9.1.1, and 9.1.2 respectively. The status of the water utilization is summarized that water used in the upstream region from the confluence flows back into the Yodo River and it causes the qualitative problems to water utilization in the downstream region.

Water quality in the Yodo River system is not bad in general; the water in Uji River is relatively clean and it has the highest flow rate amongst three tributaries, Kizu River has the highest water quality because the population in its sub-riverbasin is small, and the water quality in the upstream part of Katsura River is clean but it is worse above the confluence of the Yodo River system, because it receives the waste water discharged from Kyoto City. In the lower riverbasin from the confluence, the Osaka metropolitan-area has been developed and the amount of the service water tapping this lower reach is more than 40 m^3/s and it is distributed to more than 10 million persons in the metropolitan area.

The flow regimes in the Yodo River as of 1980 are listed in Table 9.1.1. The main tributary, Uji River shares more than 60% to the total amount in discharge throughout all of flow regimes. In the flow regimes of the annual average, the discharge of each of Kizu River and Katsura River is nearly equal to 60 m^3/s and each share is about 20%. This share is changed as the total discharge is decreased. For example, in the flow regime of the drought water discharge, the discharge of Kizu River is 30

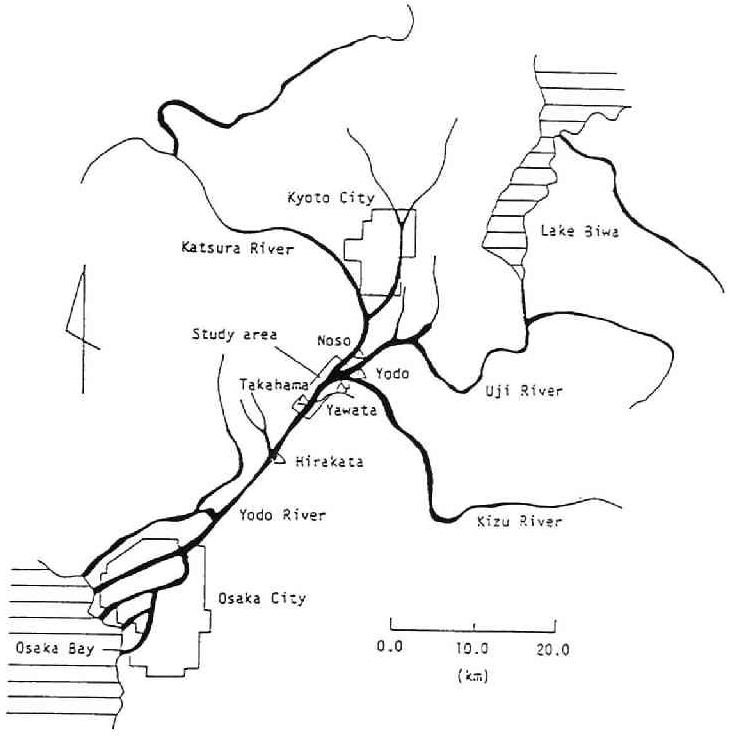

Figure 9.1.1: The Yodo River System.

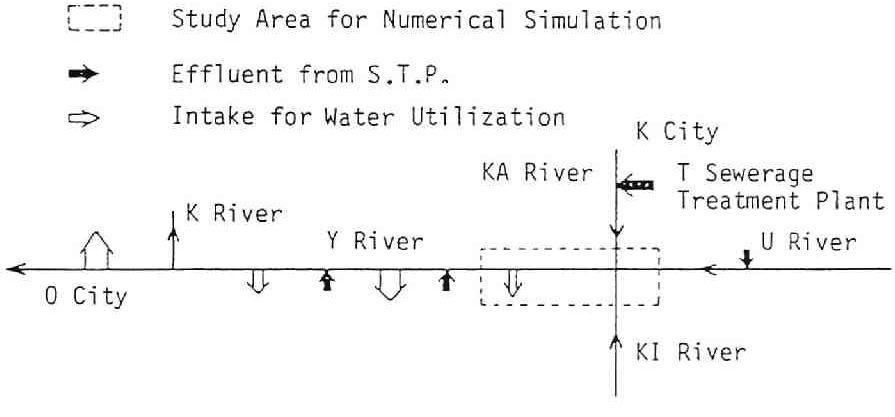

Figure 9.1.2: Outline of water system in the Yodo riverbasin.

m^3/s and its share 25%, while the discharge of Kizu River is 18 m^3/s and its share 15%, because the discharge in Katsura River includes the constant effluent from the sewerage treatment plants in Kyoto City, and it is estimated about 5 m^3/s at present. After completion of the sewer systems, it will increase up to 15 m^3/s.

Table 9.1.1: Flow regimes in the Yodo River system.

Regime	Discharge (m^3/s)			
	Katsura R.	Uji River	Kizu River	Total
Annual average	62.(19.3)	203.(63.2)	56.(17.5)	321.
185: Ordinary water discharge	50.(20.2)	160.(64.5)	38.(15.3)	248.
275: Low water discharge	35.(20.6)	108.(63.5)	27.(15.9)	170.
355: Drought discharge	30.(24.4)	75.(61.0)	18.(14.6)	123.

Figures in the parentheses denote the ratio to total discharge in per cent.

A lot of research works and field measurements have been made because of the importance of Yodo River and scientific interests in the mixing below the confluence since 1950's. At present, the most convenient method investigating the water quality in the Yodo River system will be the mathematical simulation. The mathematical models are required to express the complicated geometry of the confluence, flow behaviors and associated dispersion, therefore those described in the curvilinear coordinate system will satisfy the above requirements.

9.2 2-D Numerical Modeling of flows and Mixing in Yodo River System

9.2.1 2-D Numerical Models in Curvilinear Coordinate System

(1) 2-D Mathematical Models

The basic hydraulic principles applied to describing the flow behavior and the associated mixing of concentration are the conservation laws of momentum, water and mass of dispersion materials as stated in **Section 3.3** in **Part I**. The length scale in the depth-wise direction is much smaller than those in the transverse and the longitudinal directions in rivers, and therefore the mixing time scale in the depth-wise direction does. In case the river water is not stratified, the concentration distributions in the depth-wise direction are commonly almost uniform, and the 2-D mathematical models in the horizontal plane will be usable.

The basic 3-D mathematical models for turbulent shear flows and concentration mixing are:
Momentum equations,

$$\frac{\partial \bar{u}_i}{\partial t} + \frac{\partial \bar{u}_i \bar{u}_j}{\partial x_j} = F_i - \frac{1}{\bar{\rho}} \frac{\partial \bar{p}}{\partial x_i} + \frac{\partial \overline{\tau_{ij}}}{\partial x_j} \qquad (i = 1, 2, 3) \tag{9.2.1}$$

Continuity equation,

$$\frac{\partial \bar{u}_i}{\partial x_i} = 0 \tag{9.2.2}$$

Turbulent diffusion equation:

$$\frac{\partial \bar{c}}{\partial t} + \frac{\partial \bar{u}_j \bar{c}}{\partial x_j} = \frac{\partial \bar{s}_j}{\partial x_j} \tag{9.2.3}$$

where $\bar{u}_i$ is the ensemble average of velocity in the x_i direction, $\bar{p}$ the ensemble average of pressure, $\bar{\rho}$ the ensemble average of density of water, F_i the body force in the x_i direction, $\overline{\tau_{ij}}$ the x_i directional shear stress acting on the control surface element perpendicular to the x_j direction caused by the turbulent motion, $\bar{c}$ the ensemble average of concentration, $\bar{s}_i$ the x_i component of the gradient type mass transport vector caused by the turbulent motion, x_i the Cartesian coordinate $(i = 1, 2, 3)$, x_1, x_2 the horizontal coordinate respectively, x_3 the vertical coordinate, and t the time. (Hereafter, $\bar{}$ (overbar) denoting the ensemble averaged values will be neglected.)

The 2-D mathematical models are obtained by integrating each of the basic 3-D partial differential equations of Eqs. 9.2.1 to 9.2.3 from the bottom $-z_b$ to the water surface ζ assuming the hydrostatic pressure distribution. Its procedures are well-known and the final results in the Cartesian coordinate system are written as:

$$\frac{\partial}{\partial t}\begin{pmatrix} M_1 \\ M_2 \\ h \\ N \end{pmatrix} + \frac{\partial}{\partial x_i}\begin{pmatrix} U_i M_1 \\ U_i M_2 \\ U_i h \\ U_i N \end{pmatrix} = \frac{\partial}{\partial x_i}\begin{pmatrix} h\tau'_{1i}/\rho \\ h\tau'_{2i}/\rho \\ 0 \\ hS_i \end{pmatrix} + \begin{pmatrix} -gh \cdot \partial\zeta/\partial x_1 \\ -gh \cdot \partial\zeta/\partial x_2 \\ 0 \\ 0 \end{pmatrix} + \begin{pmatrix} -\tau'_{1b}/\rho \\ -\tau'_{2b}/\rho \\ 0 \\ 0 \end{pmatrix} \tag{9.2.4}$$

and

$$U_i \equiv \int_{-z_b}^{\zeta} \bar{u}_i dx_3/h \qquad (h = \zeta + z_b) \tag{9.2.5}$$

$$M_i \equiv \int_{-z_b}^{\zeta} \bar{u}_i dx_3 = U_i h \tag{9.2.6}$$

$$C \equiv \int_{-z_b}^{\zeta} \bar{c} dx_3/h \tag{9.2.7}$$

$$N \equiv \int_{-z_b}^{\zeta} \bar{c} dx_3 \tag{9.2.8}$$

$$\frac{\tau'_{ij}}{\rho} \equiv -\frac{1}{h}\{\int_{-z_b}^{\zeta} \overline{(u_i - \bar{u}_i)(u_j - \bar{u}_j)}dx_3 + \int_{-z_b}^{\zeta} (\bar{u}_i - U_i)(\bar{u}_j - U_j)dx_3\} \tag{9.2.9a}$$

$$\frac{\tau'_{ij}}{\rho} \equiv \nu' \left(\frac{\partial U_i}{\partial x_j} + \frac{\partial U_j}{\partial x_i}\right) \tag{9.2.9b}$$

$$\frac{\tau_{ib}}{\rho} \approx \frac{gn^2 M_i \sqrt{M_1^2 + M_2^2}}{h^{7/3}} \tag{9.2.10}$$

$$S_i \equiv -\frac{1}{h}\{\int_{-z_b}^{\zeta} \overline{(c - \bar{c})(u_j - \bar{u}_j)}dx_3 + \int_{-z_b}^{\zeta} (\bar{c} - C)(\bar{u}_j - U_j)dx_3\} \tag{9.2.11}$$

$$S_i \equiv D_{ij}\partial C/\partial x_j \tag{9.2.12}$$

$$\left(D_{ij} \right) = \begin{pmatrix} D_{11} & D_{12} \\ D_{21} & D_{22} \end{pmatrix} = \begin{pmatrix} cos^2\theta D_L + sin^2\theta D_T & sin\theta cos\theta\,(D_L - D_T) \\ sin\theta cos\theta\,(D_L - D_T) & sin^2\theta D_L + cos^2\theta D_T \end{pmatrix} \tag{9.2.13}$$

where U_i is the x_i component of the depth averaged velocity vector, M_i the x_i component of the momentum flux vector, h the water depth $(= \zeta + z_b)$, ζ the water surface elevation, z_b the bottom elevation, C the depth-averaged concentration, N the depth-integrated concentration, τ'_{ij} the x_i directional shear stress acting on the control surface element perpendicular to the x_j direction and it includes the turbulent and dispersion effects, ν' the viscosity coefficient including turbulent and dispersion effects, τ_{ib} the frictional shear stress acting on the bottom and Eq. 9.2.10 is equivalent to Manning's formula for 1-D flows, n Manning's roughness coefficient, S_i the x_i component of the gradient type mass transport vector including the turbulent diffusion and the dispersion, D_L the longitudinal dispersion coefficient, D_T the transverse dispersion coefficient, and θ the angle between Cartesian coordinates and the principal axes of diffusion and dispersion. Note that D_{ij} is equivalent to $D2_{ij}$ in **Part I**. The definition sketch of variables, and the Cartesian coordinate systems are shown in Fig. 9.2.1.

Viviand (1974) shows the transformation of a conservation form equation; Eq. 9.2.14 in the Cartesian coordinate system x_i can be transformed into Eq. 9.2.15 in the generalized curvilinear coordinate system ξ_i.

$$\frac{1}{J}\left(\frac{\partial f}{\partial t} + \frac{\partial F_i}{\partial x_i}\right) = 0 \tag{9.2.14}$$

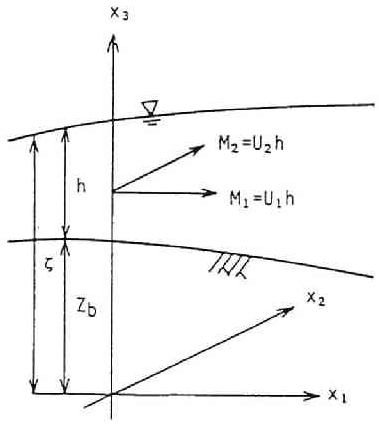

Figure 9.2.1: Definition sketch of variables and the Cartesian coordinate systems.

$$\frac{\partial}{\partial t}\left(\frac{f}{J}\right)+\frac{\partial}{\partial \xi_j}\left(\frac{\partial \xi_j}{\partial x_i}\frac{F_i}{J}\right)=0 \tag{9.2.15}$$

where

$$\xi_i=\xi_i(x_1,x_2) \qquad (i=1,2) \tag{9.2.16}$$

$$J\equiv\left|\frac{\partial \xi_i}{\partial x_j}\right| \tag{9.2.17}$$

Therefore, by application of the relationships described above to each component of the set of Eq. 9.2.4 in the Cartesian coordinate system, they are rewritten into the set of partial differential equations in the non-orthogonal curvilinear coordinate system as:

$$\begin{aligned}&\frac{\partial}{\partial t}\left(\frac{1}{J}\right)\begin{pmatrix}M_1\\M_2\\h\\N\end{pmatrix}+\frac{\partial}{\partial \xi_i}\left(\frac{1}{J}\right)\begin{pmatrix}U^iM_1\\U^iM_2\\U^ih\\U^iN\end{pmatrix}\\&\quad=\frac{\partial}{\partial \xi_i}\left(\frac{1}{J}\right)\begin{pmatrix}h\tau^{r1i}/\rho\\h\tau^{r2i}/\rho\\0\\hS^i\end{pmatrix}+\frac{1}{J}\begin{pmatrix}-gh\cdot\partial\xi_i/\partial x_1\cdot\partial\zeta/\partial\xi_i\\-gh\cdot\partial\xi_i/\partial x_2\cdot\partial\zeta/\partial\xi_i\\0\\0\end{pmatrix}+\frac{1}{J}\begin{pmatrix}-\tau_{1b}/\rho\\-\tau_{2b}/\rho\\0\\0\end{pmatrix}\end{aligned} \tag{9.2.18}$$

and

$$U^i\equiv\frac{\partial \xi_i}{\partial x_j}U_j \tag{9.2.19}$$

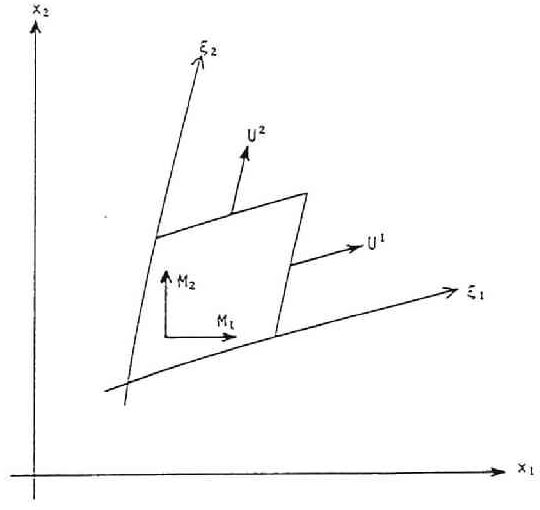

Figure 9.2.2: Cartesian coordinate systems and generalized coordinate system.

$$\tau'^{ij} = \frac{\partial \xi_j}{\partial x_k} \tau'_{ik} \tag{9.2.20}$$

The shear stress τ'_{ij} and the gradient type mass transport S^i can be written:

$$\frac{\tau'_{ij}}{\rho} = \nu' \left(\frac{\partial \xi_k}{\partial x_j} \frac{\partial U_i}{\partial \xi_k} + \frac{\partial \xi_k}{\partial x_i} \frac{\partial U_j}{\partial \xi_k} \right) \tag{9.2.21}$$

$$S^i = D^{ij} \frac{\partial C}{\partial \xi_j} \tag{9.2.22}$$

$$D^{ij} = \frac{\partial \xi_i}{\partial x_k} \frac{\partial \xi_j}{\partial x_l} D_{kl} \tag{9.2.23}$$

Followings are notable on the set of Eq. 9.2.18;

1. The first equation of Eq. 9.2.18 is the momentum conservation equation in the x_1 direction, the second one that in the x_2 direction, the third one the continuity equation and the forth one the mass conservation equation for the contaminant.

2. The dependent variables are the same as those in the Cartesian coordinates system, but only the independent variables are transformed into the non-orthogonal curvilinear system.

3. They are as simple as those in the Cartesian coordinate system.

4. The space coordinate system is non-orthogonal curvilinear system, therefore it is much easier to generate the grids for calculation in the physical domain.

(2) Boundary Conditions

The set of Eq. 9.2.18 can be solved under certain boundary and initial conditions. Boundary condition for flows adopted at the closed boundary is "non-slip condition", then the following relationship will be specified:

$$M_1 = M_2 = 0 \tag{9.2.24}$$

At open boundary, the distributions of momentum flux vector $\boldsymbol{M}$ or water surface elevation ζ can be specified. In case the distribution of momentum flux vector in the ξ_2 direction is specified, assuming that the coordinate system is orthogonal near the boundary, M_i is obtained as:

$$M_i = \frac{1}{\sqrt{g_{11}}}\frac{\partial x_i}{\partial \xi_1}M^1 + \frac{1}{\sqrt{g_{22}}}\frac{\partial x_i}{\partial \xi_2}M^2 \tag{9.2.25}$$

where g_{ii} is the metric tensor defined by

$$g_{ii} = \left(\frac{\partial x_1}{\partial \xi_i}\right)^2 + \left(\frac{\partial x_2}{\partial \xi_i}\right)^2 \quad (i = 1, 2) \tag{9.2.26}$$

and M^i the contravariant vector component of momentum flux vector specified. In usual flow analysis in a river, the measured data of discharge Q is available. Assuming M^2 is equal to zero, M^1 distribution can be obtained as:

$$M_J^1 = Q h_J^{5/3} \Big/ \sum_{I=1}^{n} h_I^{5/3} \tag{9.2.27}$$

where J denotes the J-th lattice in the ξ_2 direction.

For the conservation equation of concentration, the condition of "no-mass transport" at the closed boundary gives:

$$\frac{\partial C}{\partial \xi_i} = 0 \tag{9.2.28}$$

and in case the concentration is specified at the upstream open boundary,

$$N = Ch \tag{9.2.29}$$

can be used.

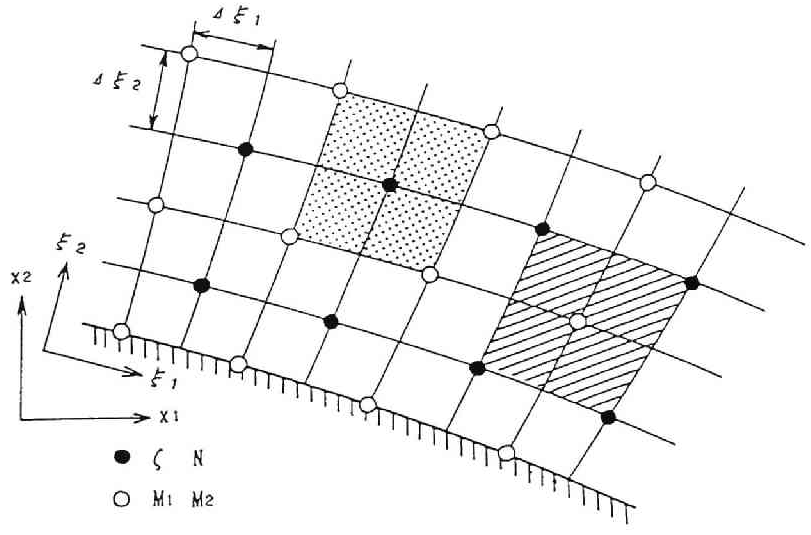

Figure 9.2.3: Definition points of variables and domains for integrating the mathematical models in a physical plane. Open circles denote the points for M_1 and M_2, and solid circles for ζ and N. Dotted domain is for the equations for mass and concentration, and hatched domain for the momentum equations.

(3) Numerical Procedures

The system of the partial differential equations of Eq. 9.2.18 can numerically be solved by FDM. The definition points of variables is shown in Fig. 9.2.3 and the finite difference forms of Eq. 9.2.18 are obtained by integrating the each of equations in the hatched or dotted domains in Fig. 9.2.3. The final finite difference form of each of Eq. 9.2.18 is obtained by use of Adams-Bashforth scheme for the local derivative, Donor-cell scheme in 2-D plane for convection terms, and the application of the central difference scheme for gradient type transport. The finite difference form of the convective terms usually includes the numerical effects which causes the numerical dispersion and dissipation. The third order finite difference scheme as QUICK (Leonard, 1978) and its extension to 2-D phenomena by Takemoto et al, (1986), Kawamura (1985) 's scheme and so on are possible. Iwasa et al (1988) showed that the Donor-cell scheme of the second order accuracy gives the same results as the QUICK scheme, if the coordinate system would be selected in accordance with the flow direction.

Write the momentum equation in the x_1 direction as:

$$\frac{\partial}{\partial t}\left(\frac{\phi}{J}\right)+L_1(\phi)=L_2(\phi)+L_3(\phi)+L_4(\phi) \tag{9.2.30}$$

The finite difference representation for each terms of Eq. 9.2.30 is shown as:
Local time derivative term,

$$\begin{aligned}\phi^{n+1}\approx\phi^n+J\Delta t\Big\{&-\frac{3}{2}L_1(\phi^n)+\frac{1}{2}L_1\left(\phi^{n-1}\right)+\frac{3}{2}L_2(\phi^n)-\frac{1}{2}L_2\left(\phi^{n-1}\right)\\&+\frac{3}{2}L_3(\phi^n)-\frac{1}{2}L_3\left(\phi^{n-1}\right)+\frac{3}{2}L_4(\phi^n)-\frac{1}{2}L_4\left(\phi^{n-1}\right)\Big\}\end{aligned} \tag{9.2.31}$$

Convective terms,

$$L_1(\phi)\equiv\frac{\partial}{\partial\xi_i}\left(\frac{1}{J}U^i\phi\right) \tag{9.2.32a}$$

is approximated as

$$\begin{aligned}\frac{1}{2\Delta\xi_1 2\Delta\xi_2}\iint L_1(\phi)d\xi_1 d\xi_2{}_{I,J}\approx\frac{1}{2\Delta\xi_1 2\Delta\xi_2}\Bigg\{&\int\left(\frac{U^1}{J}\phi\right)d\xi_2{}_{I+1,J}-\int\left(\frac{U^1}{J}\phi\right)d\xi_2{}_{I-1,J}\\&+\int\left(\frac{U^2}{J}\phi\right)d\xi_1{}_{I,J+1}-\int\left(\frac{U^2}{J}\phi\right)d\xi_1{}_{I,J-1}\Bigg\}\end{aligned} \tag{9.2.32b}$$

and

$$\begin{aligned}&\int\left(\frac{U^1}{J}\phi\right)d\xi_2{}_{I,J}\\&\quad\approx\frac{1}{J_{I,J}}\frac{1}{2}\left\{U^1_{I,J}\left(\phi_{I-1,J}+\phi_{I+1,J}\right)+\mid U^1_{I,J}\mid\left(\phi_{I-1,J}-\phi_{I+1,J}\right)\right\}2\Delta\xi_2\end{aligned} \tag{9.2.32c}$$

$$\begin{aligned}&\int\left(\frac{U^2}{J}\phi\right)d\xi_1{}_{I,J}\\&\quad\approx\frac{1}{J_{I,J}}\frac{1}{2}\left\{U^2_{I,J}\left(\phi_{I,J-1}+\phi_{I,J+1}\right)+\mid U^2_{I,J}\mid\left(\phi_{I,J-1}-\phi_{I,J+1}\right)\right\}2\Delta\xi_1\end{aligned} \tag{9.2.32d}$$

hereafter, subscript I, J and so on denote the variables at the lattice point $(I\Delta\xi_1, J\Delta\xi_2)$ or the center of the integration.
Turbulent and dispersive viscosity terms,

$$L_2(\phi)\equiv\frac{\partial}{\partial\xi_i}\left(\frac{h}{J}\frac{\tau^{ij}}{\rho}\right) \tag{9.2.33a}$$

is approximated as

$$\frac{1}{2\Delta\xi_1 2\Delta\xi_2}\iint L_2(\phi)\,d\xi_1 d\xi_2{}_{I,J}$$
$$\approx \frac{1}{2\Delta\xi_1 2\Delta\xi_2}\left\{\left(\frac{h}{J}\frac{\tau^{i1}}{\rho}\right)2\Delta\xi_2{}_{I+1,J} - \left(\frac{h}{J}\frac{\tau^{i1}}{\rho}\right)2\Delta\xi_2{}_{I-1,J}\right.$$
$$\left. + \left(\frac{h}{J}\frac{\tau^{i2}}{\rho}\right)2\Delta\xi_1{}_{I,J+1} - \left(\frac{h}{J}\frac{\tau^{i2}}{\rho}\right)2\Delta\xi_1{}_{I,J-1}\right\} \quad (9.2.33b)$$

Pressure terms,

$$L_3(\phi) \equiv -\frac{gh}{J}\left(\frac{\partial\xi_i}{\partial x_j}\frac{\partial\zeta}{\partial\xi_i}\right)_{I,J} \quad (9.2.34a)$$

is approximated as

$$\frac{1}{2\Delta\xi_1 2\Delta\xi_2}\iint L_3(\phi)\,d\xi_1 d\xi_2{}_{I,J} \approx -g\left(\frac{h}{J}\right)_{I,J}\left\{\left(\frac{\partial\xi_1}{\partial x_j}\right)_{I,J}\frac{1}{2\Delta\xi_1}(\zeta_{I+1,J}-\zeta_{I-1,J})\right.$$
$$\left. + \left(\frac{\partial\xi_2}{\partial x_j}\right)_{I,J}\frac{1}{2\Delta\xi_2}(\zeta_{I,J+1}-\zeta_{I,J-1})\right\} \quad (9.2.34b)$$

τ^{ij} is calculated by the relationship of Eqs. 9.2.20 and 9.2.21, and the space derivative of the depth averaged velocity can be approximated by the central difference scheme. Bottom shear-stress term,

$$L_4(\phi) \equiv -\frac{1}{J}\frac{\tau_{ib}}{\rho} \quad (9.2.35a)$$

is approximated as

$$\frac{1}{2\Delta\xi_1 2\Delta\xi_2}\int\int L_4(\phi)\,d\xi_1 d\xi_2{}_{I,J} \approx -\left(\frac{1}{J}\frac{\tau_{ib}}{\rho}\right)_{I,J} \quad (9.2.35b)$$

In case the variable not at its definition points are required, it is calculated by the method of linear interpolation.

9.3 Verification of the Numerical Models

The developed models are applied to the Yodo River system. As stated in Section 9.1, it has the three main tributaries of different flow characteristics and concentration fields. They merge into Yodo River and the confluence has complicated flow behaviors as well as geometry. A lot of research works and the field measurement on the mixing

in the Yodo River system have been made because of the importance of the river and scientific interests in the mixing below the confluence since the 1950's. Recently Li, Yagi and Sueishi(1987) investigated the mixing process in the river by the stream tube model (Yotsukura and Sayre, 1976) and estimated the transverse dispersion coefficient at $0.6 \sim 2.0hu_*$, however hydraulic characteristics of the mixing have not yet clarified.

9.3.1 Outlines of Simulations for Verification

The segments of the Yodo River System selected for the study area includes the confluences, so that it is suitable for examining the models developed in view of topographic aspects. Its downstream boundary is 32.0 km from the reference point near the rivermouth and the upstream boundary 36.2 km at Katsura River, 36.2 km at Uji River and 0.4 km at Kizu River. (See Fig. 9.1.1.) The concerned river channels are limited only within the low flow channel, because the study focuses on the spreading of the contaminant and the water quality problem usually becomes serious during the low-flow condition.

Generated grids made by use of the geographical survey data in Yodo River and their numerical interpolation by Akima (1970) are shown in Fig. 9.3.1 (a). Non-orthogonal curvilinear grids of about 25 m in length and 5 m in width cover the study area of about 4 km in length in the longitudinal direction and about 100 m in width in the transverse direction. Its general topography made by use of the geographical river survey data and its interpolation is illustrated in Fig. 9.3.1 (b).

Selected study area includes two confluences, that is, Kizu River merges into Uji River at the upper confluence located at the 35.2 km section and Katsura River merges into Uji River at the lower confluences located at the 34.4 km section. The non-uniform distributions of riverbed elevation and the existence of concavities and convexity are observed. There is a big concavity along the right bank-side between two confluences and a convexity below the concavities. There are also some concavities along the right or the left bank-side below the lower confluence.

The flow discharge and the concentration distribution, i.e., the transverse distributions of the flow rate per unit width and concentration of the contaminants, for example, NH_3-N are specified according to the results of the field measurements at the upstream boundaries of the three tributaries. The uniform water surface elevation is also specified at the downstream boundary in the main stream.

The values of the parameters used in the mathematical models are: Manning's roughness coefficient $n = 0.02$: the turbulent and dispersive viscosity coefficient $\nu' = 0.01$ m^2/s: the longitudinal dispersion coefficient $D_L = 5.93hu_*$ according to

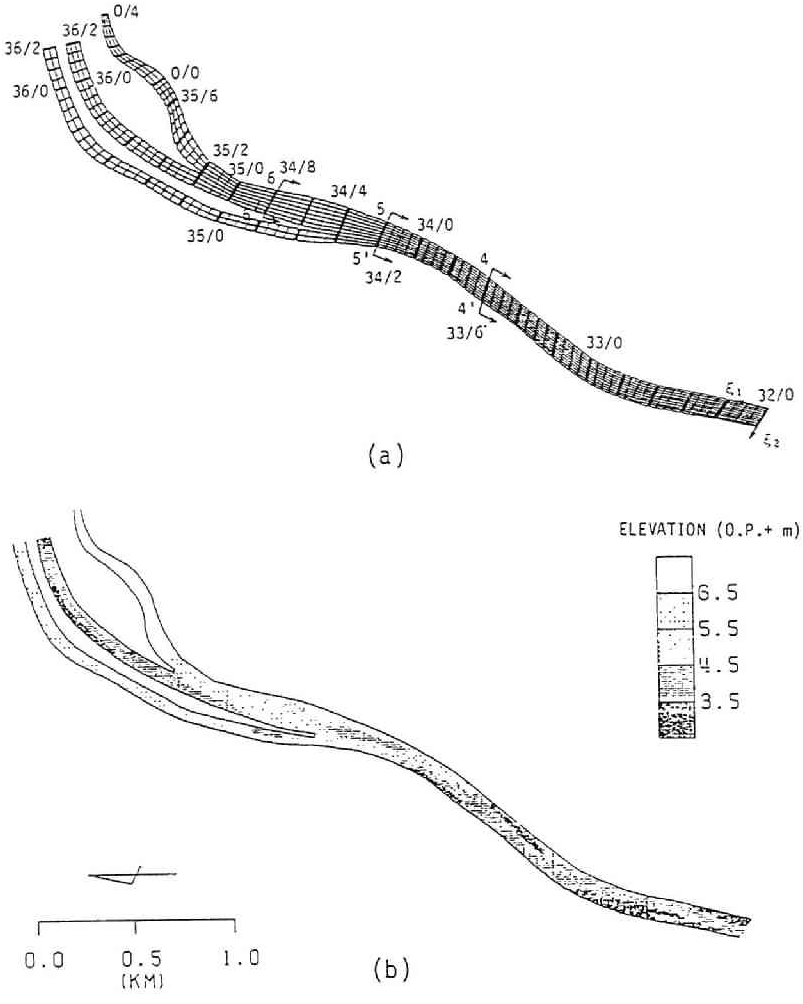

Figure 9.3.1: Yodo River confluence selected for study area. (a) Generated curvilinear grids, and (b) bathymetric map (in O.P. + m).

Table 9.3.1: Summary of boundary conditions for 62-0904, and 61-1028 Tests.

Test	Item		Katsura R.	Uji R.	Kizu R.	Yodo R.
	Discharge	$Q(m^3/s)$	19.0	120.4	11.2	—
62-	Stage	ζ(O.P. + m)	—	—	—	5.13
0904	NH_3-N Conc.	C(ppm)	3.39	0.24	0.13	—
	Discharge	$Q(m^3/s)$	18.4	60.5	11.4	—
61-	Stage	ζ(O.P. + m)	—	—	—	5.75
1028	NH_3-N Conc.	C(ppm)	3.03	0.35	0.14	—
	SiO_2 Conc.	C(ppm)	9.00	2.27	13.21	—

Elder (1959): the transverse dispersion coefficient $D_T = 0.2hu_*$.

The transverse dispersion coefficient was measured in laboratory by Elder (1959), Okoye (1970), Iwasa, Hosoda and Noguchi (1982), Webel and Schazmann (1988), and so on, and in rivers by Yotsukura et al (1970), and so on. Their results are summarized in Yotsukura and Nakamura (1988), and many texts as Fischer (1979) and Holly (1985), and its magnitude is of the order of $0.1 \sim 0.2hu_*$ in laboratory, and $0.4 \sim 0.8hu_*$ in straight rivers. The detailed discussion on the transverse dispersion coefficient in Yodo River System will be given in **Sub-section 9.3** and **Chapter 10**.

Two sets of verification test, that is, 62-0904 Test and 61-1028 Test were conducted. Field measurements for 62-0904 Test were made by Kinki Regional Bureau, Ministry of Construction on September 4, 1987 and that for 61-1028 Test by Osaka Prefectural Government on October 28, 1986. They were done in the period of the low or drought water discharge, and flow and concentration fields were confirmed to be almost steady-state. 2-D models described in the previous subsections can calculate unsteady behavior of flow and concentration, however by specifying the steady-state boundary conditions, they give the steady flow and concentration fields.

The specified boundary conditions for two tests are summarized in Table 9.3.1. The selected water quality parameters are NH_3-N for 62-0904 Test, and NH_3-N and SiO_2 for 61-1028 Test. The transverse concentration distributions of these water quality parameters at each upstream boundary section of three rivers were almost uniform. NH_3-N concentration in Katsura River is the highest among three tributaries because it receives the effluent from sewerage treatment plants in Kyoto City, but SiO_2 concentration is the highest in Kizu River among three tributaries.

9.3.2 Simulation Results and Discussions

The simulation models calculate the unsteady behaviors of flow and spreading of contaminants, but only the results under the steady conditions will be presented.

(1) Steady-state flow behaviors

Water surface elevation contour map, the momentum flux vector distributions and the depth-averaged velocity vector distributions obtained in the simulation for 62-0904 Test are illustrated in Figs. 9.3.2 (a), (b) and (c).

Water surface contour lines are nearly perpendicular to channel boundaries. The increase of water surface elevation in the lower reach below the second confluence is very small and the water surface profile is backwater curves in a mild slope channel, however in the upper reach, the water-depth is shallow and the water surface profile is more influenced by the riverbed condition. The riverbed in Kizu River is the highest and the increase of the water surface elevation is the biggest, on the contrary the bed-slope in Uji River is nearly horizontal or partially adverse, therefore very small increase of the water surface elevation is obtained. The water surface in Katsura River is medium among the three tributaries, because its riverbed slope is medium.

The distributions of the momentum flux vector and the depth-averaged velocity vector distributions are shown in Figs. 9.3.2 (b) and (c) respectively. In the upper segments above each of the confluence, the transverse distributions are nearly uniform, because the riverbed elevation in the transverse direction is nearly uniform in Kizu River and Katsura River and the water depth in Uji River is deep. Below the upper confluence, Kizu River merges into Uji River. The riverbed elevation in Uji River is much lower than that in Kizu River, therefore the water of Kizu River flows into the right side of the channel below the upper confluence, and the momentum flux vector distributions in the transverse direction are quite different from that in each of the upper part, that is, it becomes quite non-uniform, because it is influenced by the deep concavities. As shown in the bathymetric map of Fig. 9.3.1 (b), there is a concavity in the central part of the channel just below the second confluence, and the flow concentrates the central part of the channel. In accordance with the existence of the concavity in the left bank-side following the concavity upstream, the flow concentrates on the left bank-side. Thus, below the second confluence, the flow changes its main route from the central part to the right bank-side, to the left bank-side and so on according to the distribution of the riverbed elevation. The depth-averaged velocity vector distributions are shown in Fig. 9.3.1 (c). Velocity vectors change their direction in accordance with channel configuration as in the momentum

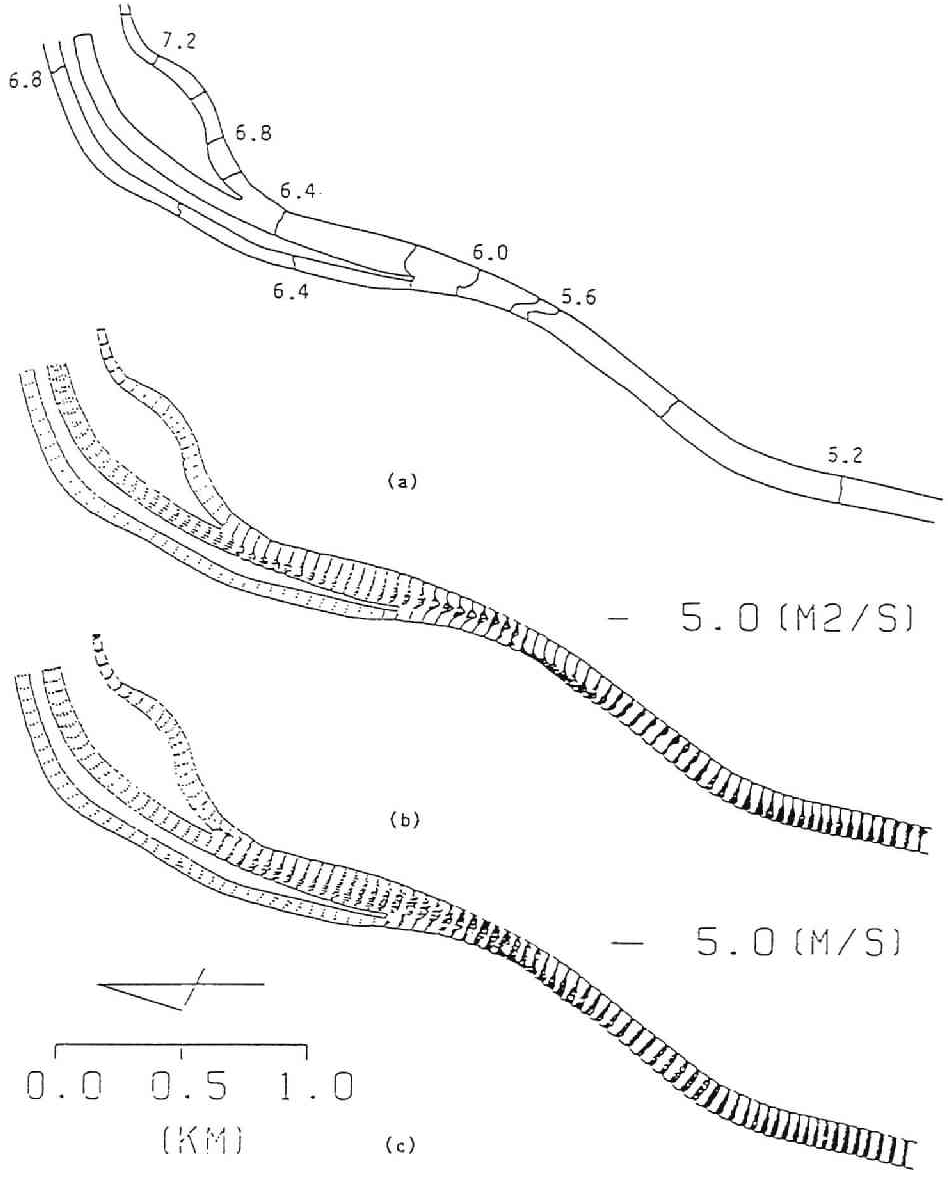

Figure 9.3.2: Simulated results under steady state conditions in 62-0904 Test. (a) Water surface elevation contour map, (b) momentum flux vector distributions, and (c) depth-averaged velocity vector distributions.

flux vector distributions of Fig. 9.3.1 (b), however its transverse distributions are more uniform than the momentum flux vector distributions.

The comparison of the simulated results with the observed ones are not able to made because of the lack of measured data, however simulated results give the rigorous and reasonable results for flow behavior.

(2) Steady-State Concentration Distributions

The spreading of NH_3-N concentration from Katsura River is shown in Fig. 9.3.3 (a) for 62-0904 Test and Fig. 9.3.3 (b) for 61-1028 Test. The high NH_3-N concentration from Katsura River merges into Yodo River at the lower confluence and mainly flows down along the right bank-side, but its spreading width becomes longer or shorter along the flow direction, because the flow concentrates on the central part at first, next the right bank-side, then the left bank-side as described in **Paragraph 9.3.2 (1)**. Thus, the change of the spreading width is correspondent with the longitudinal variation of the transverse distributions of the momentum flux vector.

(3) Flow Behavior and Mixing at the Confluences

The momentum flux vector distributions obtained in the simulation for 61-1028 Test and the bathymetry at the confluence are presented in Fig. 9.3.4 (a), and the velocity vector distributions and the iso-depth contour map in Fig. 9.3.4 (b). They are a part of the simulation results for whole of the test area, and demonstrate the flow behavior in more detail in the area including two confluences. According to the riverbed elevation distribution, the flow mainly goes down along the Uji River below the upper confluence, and on the central part of the channel below the lower confluence. The water from Kizu River merges into the water from Uji River at the upper confluence and a part of the merged water flows toward the right bank-side above the convexity between two confluences. The water from Katsura River flows into the main stream below the lower confluence.

The variations of the flow direction are more clearly demonstrated in the velocity vector distributions in Fig. 9.3.4 (b). The flow toward Uji River from other two tributaries is clearly observed in the portion of the shallow water below each of two confluences, and the divergence and convergence of flows are also clearly observed above/below the convexity located between two confluences.

Thus, the angle between Kizu River and Uji River at the first confluence, and

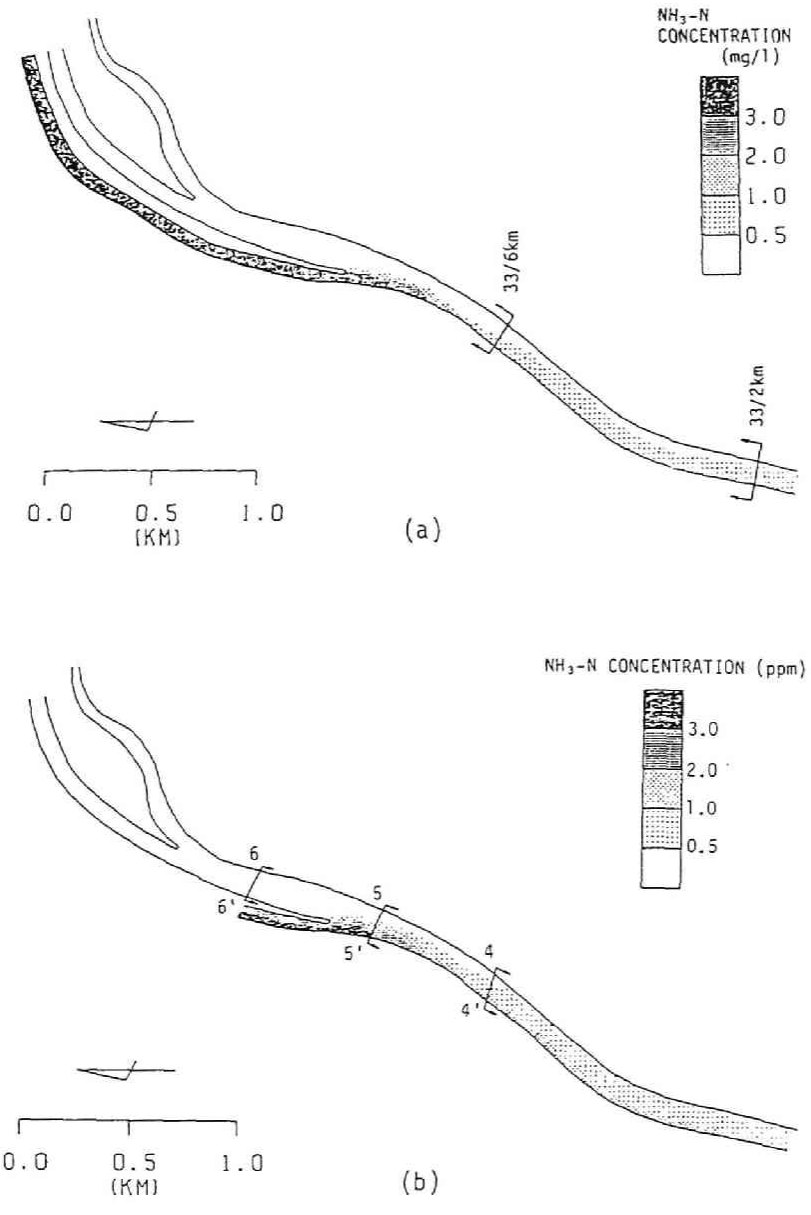

Figure 9.3.3: Spreading of NH_3-N concentration simulated in (a) 62-0904 Test, and (b) 61-1028 Test.

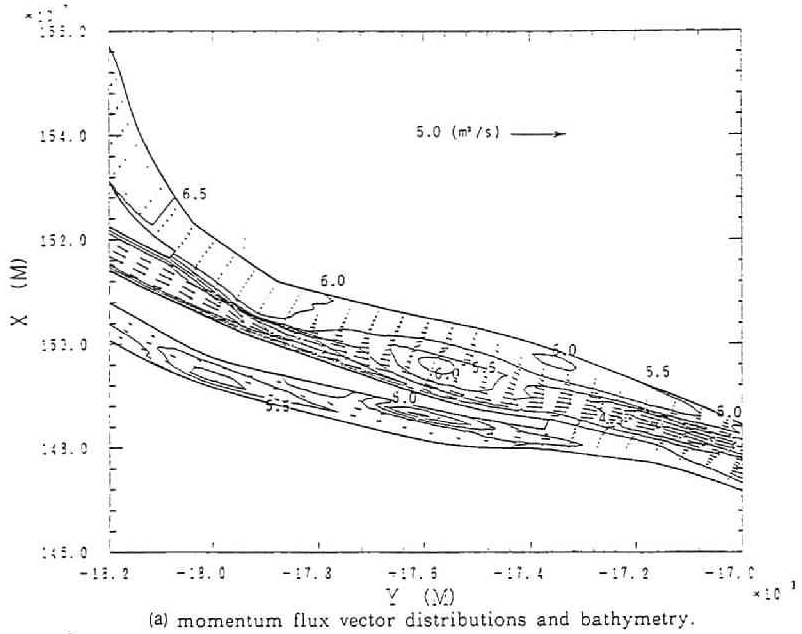

(a) momentum flux vector distributions and bathymetry.

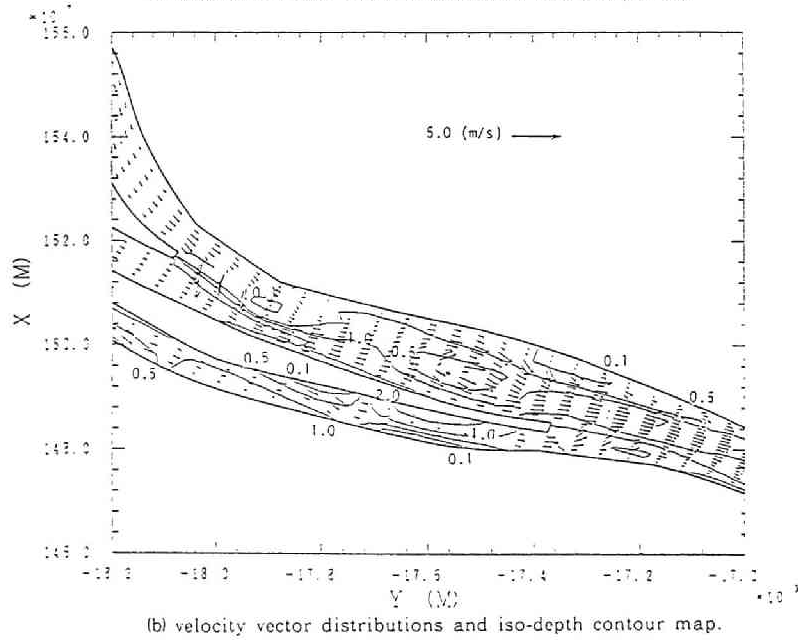

(b) velocity vector distributions and iso-depth contour map.

Figure 9.3.4: Flow behavior and mixing at the confluence simulated in 61-1028 Test. (a) Momentum flux vector distributions and the iso-contour map of the bottom elevation, and (b) Depth-averaged velocity vector distributions and the iso-contour lines of water depth.

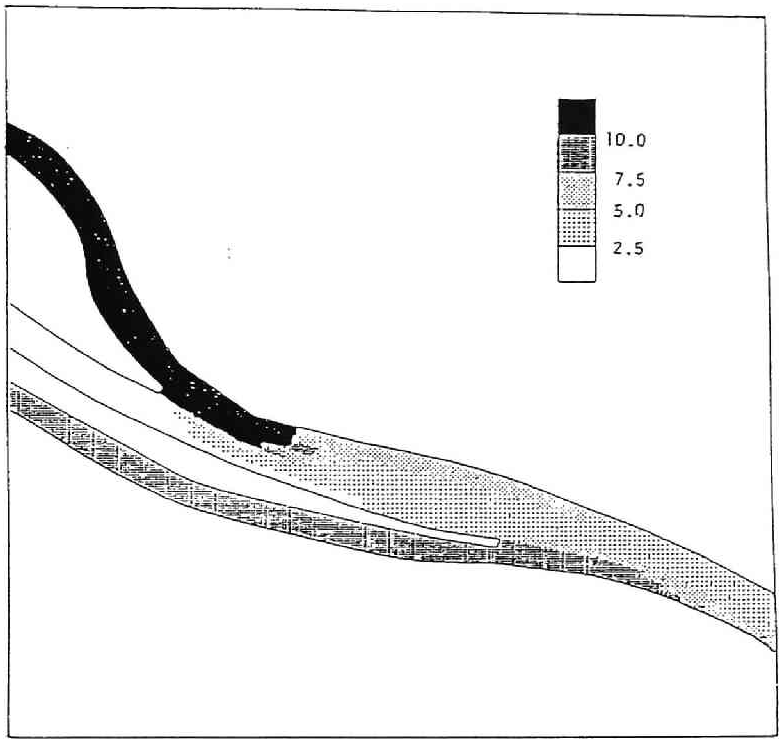

Figure 9.3.5: Spreading of SiO_2 concentration at the confluences simulated in 61-1028 Test.

that between Katsura River and Uji River at the second confluences are very small, however the strong mixing occurs below the confluence.

The mixing at the confluences is demonstrated in Fig. 9.3.5, which describes the spreading of SiO_2 concentration for 61-1028 Test. The high SiO_2 concentration water from Kizu River spreads widely just below the upstream confluence, being transported by the flow toward the Uji River, and it disperses channel-fully above the convexity by the flow diverged. The SiO_2 concentration from Katsura River also spreads into Uji River below the lower confluence, being transported by the flow into Uji River, however it is not so clearly shown as that below the upper confluence.

(4) Transverse Distributions of Concentration

The transverse distributions of NH_3-N concentration at the sections of 33.6 km and 36.1 km obtained in the simulation for 62-0904 Test under various dispersion coeffi-

cients are comparatively presented with the measured ones in Figs. 9.3.6 (a) and (b).

The influence of the magnitude of the transverse dispersion coefficient on the transverse concentration distribution is small at both sections of 33.6 km and 32.2 km, and the larger transverse dispersion coefficient causes the smaller decrease of NH_3-N concentration near the right bank-side. Simulated results under the non-dimensional dispersion coefficient $D_T/hu_* = 0.20$ and 2.00 have nearly the same concentration distribution and give fine agreements with observed one as shown in Fig. 9.3.6 (a).

This results show that the convective transport plays a more important role in the transverse mixing in the Yodo River Confluence than the gradient type mass transport, because the transverse distribution of the momentum flux vector is quite non-uniform and the mixing is mainly governed by the convection as described above. It is also concluded that the magnitude of the transverse dispersion coefficient at the confluence is of the same order as those measured in other straight laboratory flumes and river channels (Fischer et al, 1979).

The transverse distributions of NH_3-N concentration obtained in the simulation of 61-1028 Test are comparatively presented with field-measured distributions in Figs. 9.3.7 (a), (b), and (c). NH_3-N concentration from Uji River and Kizu River mixes well and its distribution is almost uniform at 6-6′ (34.8 km) section which is 400. m below the confluence of two tributaries, as shown in Fig. 9.3.7 (a). This is caused by the strong mixing of the flow from Kizu River with the flow from Uji River and the divergence of diluted Uji River water as stated earlier in **Paragraph 9.3.2 (3)**. Simulated results have quite good agreement with the observed concentration distribution.

Observed and simulated NH_3-N concentration distributions at 5-5′ (34.2 km) section are presented in Fig. 9.3.7 (b). The test section locates at 200. m below the confluence of Uji River and Katsura River, and the water of Katsura River containing high NH_3-N concentration merges into Uji River water as described in **Paragraph 9.3.2 (3)**, but a part of water from Katsura River flows down along the right bank side below the confluence, therefore concentration near the right bank-side is still high. The river width is so long and the distance from the confluence is so short, therefore the NH_3-N concentration near the left-bank side is still low.

At the section of 4-4′ (33.6 km), the concentration distribution is more uniform, that is, the concentration near the right bank-side becomes much lower and it becomes a little higher near the left bank-side, because as described in **Paragraph 9.3.2 (1)**, the flow concentrates at the center part of the channel at the 5-5′ section but near the

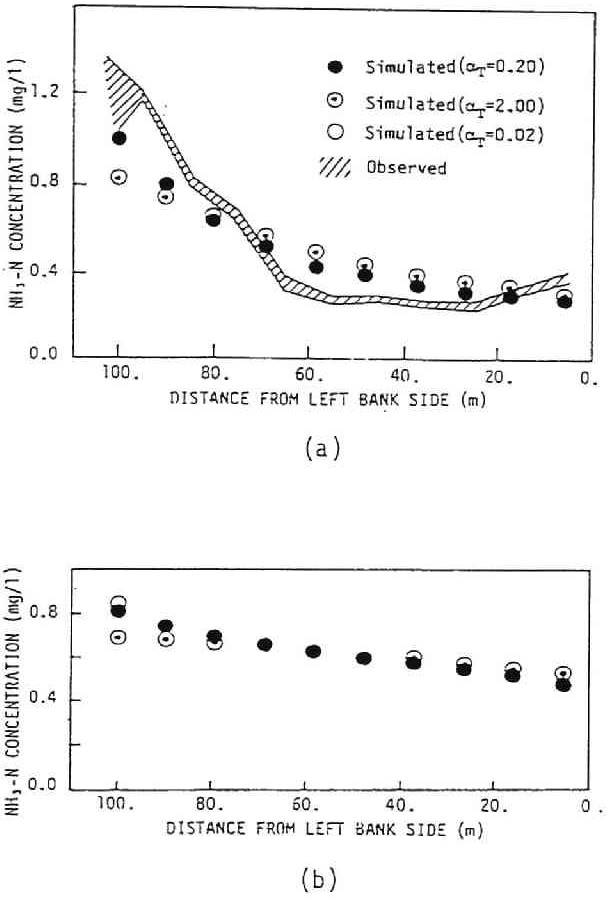

Figure 9.3.6: Transverse distributions of NH_3-N concentration simulated in 62-0904 Test and measured ones. (a) 33.6 km section, and (b) 32.2 km section. Circles denote simulated values under various dispersion coefficients, and the hatched area shows the observed concentration distribution.

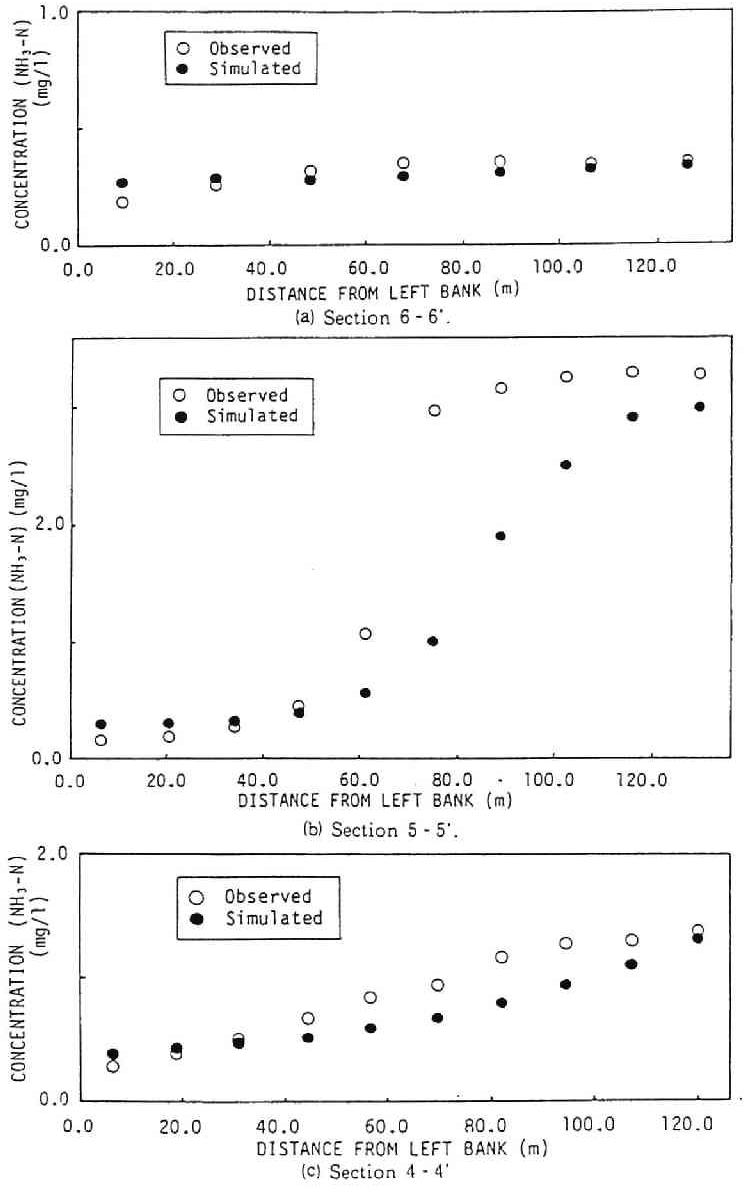

Figure 9.3.7: Transverse distributions of NH_3-N concentration simulated in 61-1028 Test and measured ones. (a) 6-6′ (34.8 km) section, (b) 5-5′ (34.2 km) section, and (c) 4-4′ (33.6 km) section.

right-bank side at the 4-4′ section. This change of the flow rate distribution causes the strong mixing of water, that is, the low NH_3-N concentration water at the center part of the channel dilutes the high concentration water near the right bank side. The dispersion transport makes the concentration near the left bank-side a little higher. The agreement between observed and simulated concentration distributions at both 5-5′ and 4-4′ sections are not so bad, and small difference between them are observed near the center part of the channel.

The simulated results of SiO_2 concentration for 61-1028Test are also comparatively illustrated with field-measurement concentration distributions at 6-6′, 5-5′ and 4-4′ sections in Figs. 9.3.8 (a), (b) and (c). Simulated results at the 6-6′ section have not so good agreement with observed one but those at the 5-5′ and 4-4′ sections are much better. A special feature observed through three results is the difference between measured and simulated concentration near the left bank-side, but two results at the 5-5′ and 4-4′ sections have very fine agreements each other except this portion. It is thought to be caused by the insufficient upstream boundary condition in Kizu River, or the entrainment from the bottom, and/or inflow of SiO_2 which is not included in the numerical models between the upstream boundary and the 6-6′ section, because the results for NH_3-N has very good agreement with observed ones near the left bank-side as shown in Figs. 9.3.7 (a), (b), and (c).

Two sets of simulation for verifying the mathematical models described in **Section 9.2** were carried out in the Yodo River System which includes the confluences of three tributaries. The simulated flow behavior was not compared with field data, because they were not measured; however the water surface elevation contour lines, the momentum vector distributions, and the velocity vector distributions simulated are reasonable ones, and their features are discussed in details with relation to the bathymetry of the study area. The simulated concentration distributions were successfully compared with the distributions obtained in 62-0904 and 61-1028 field measurements. The estimated transverse mixing coefficient is less than $2.0hu_*$, and it is supposed that the convective transport play a more important role than the dispersive transport. The mechanism of mixing in the Yodo River Confluence are discussed in detail with relation to flow behavior, and they are summarized as;

1. The river bed of Yodo River is not uniform, and the river water mainly flows down in the lower part of the riverbed,

2. Therefore, the main stream changes its route from one side to the opposite side of the channel in flowing down,

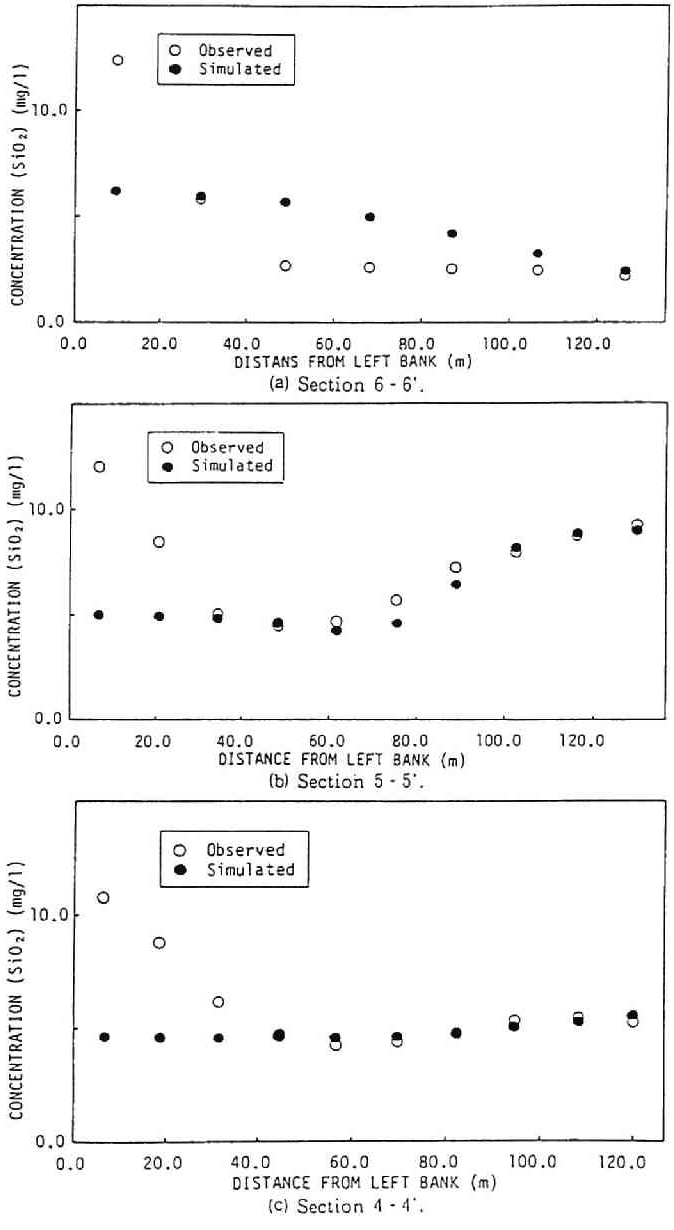

Figure 9.3.8: Transverse distributions of SiO_2 concentration simulated in 61-1028 Test and measured ones. (a) 6-6′ (34.8 km) section, (b) 5-5′ (34.2 km) section, and (c) 4-4′ (33.6 km) section.

3. This change of the water-route within the low-flow channel makes the mixing accelerated and the concentration distribution more uniform.

9.4 Conclusions

The 2-D mathematical models describing the flow behavior and associated mixing for the river system was presented in the generalized curvilinear coordinate system and the validity of the developed numerical models was successfully examined by comparing the simulated results with field data.

In **Section 9.1**, objectives of the study in this chapter was stated, and its necessity was also described in the Yodo River system which has the three main tributaries, and receives effluents from sewerage treatment plants in the middle part; its water is used for service water in the lower riverbasin.

The 2-D mathematical models in the generalized curvilinear coordinate system were derived from common 2-D plain hydraulic models in the Cartesian coordinate system in **Sub-section 9.2.1**. Their dependent variables are the same as those in the Cartesian coordinates system and only the independent variables are transformed into the non-orthogonal curvilinear system. They are as simple as those in the Cartesian coordinate system. The space coordinate system is non-orthogonal curvilinear system, therefore it is much easier to generate the grids for calculation in the physical domain. The finite difference forms of the mathematical models in the curvilinear coordinate system were obtained by the integration method in **Sub-section 9.2.2**. They have the second order accuracy in space coordinate and time coordinate, and the numerical models were also developed.

The proposed models was applied to the confluence of the Yodo River System case study and its validity was examined in **Section 9.3**. The simulated flow behaviors were not compared with field data, however the water surface elevation distributions, the momentum flux vector distributions and the depth-averaged velocity vector distributions simulated were reasonable and their features were discussed in detail with relation to its bathymetry. It was disclosed that the water-depth was shallow in low/drought discharge conditions, and the flows in channels were very affected by the riverbed elevation which is non-uniformly distributed in the longitudinal direction as well as the transverse direction. The simulated concentration distributions were successfully compared with the measured ones. The concentration distributions of contaminants were mostly affected by the convective transport of the flows, and the transverse mixing coefficient is estimated at less than $2.0hu_*$.

The mixing processes of the waters from Katsura River or Kizu River below the

confluences were also discussed in detail with the relation to the flow behavior. It was suggested that the convective transport plays a more important role in the transverse mixing in the Yodo River Confluence than the gradient type mass transport.

Chapter 10

MECHANISM OF TRANSVERSE MIXING IN YODO RIVER SYSTEM

10.1 Introduction

10.1.1 Objectives and Outlines of Experiments

As described in **Sub-section 9.1.2**, the investigation on the mechanism of the mixing at/below the confluence of the Yodo River System is urgently required in terms of environmental view points, as well as very interested in terms of environmental hydraulics on the mixing in open-channel flows. This chapter will study the mixing at/below the confluence of Yodo River System under various hydraulic conditions and disclose the mechanism of mixing in terms of the aspects stated above by the numerical methods developed and examined in **Chapter 9**,

The hydraulic conditions affective on the mixing at/below the confluence can be expected to be:

1. The magnitude of the transverse dispersion/mixing coefficient,
2. Flow regimes of rivers of which the confluence is consisted,
3. Distributions of the riverbed elevation at/below the confluence,
4. Flow rate of each of tributaries to the total discharge below the confluence,
5. Geometrical features of the confluence as an angle between each of tributaries and the main stream, and
6. Water surface elevation at the lower boundary.

Therefore, the first series of the numerical experiment for the mixing in Yodo River system was conducted under the various flow regimes listed in Table 10.2.1 in **Section 10. 2.** It covers the flow regime between the annual average discharge and the drought discharge during which the water quality pollution problem is the most serious. The second series was also done under the same boundary conditions of the first series, but with hypothetical cross-section channels, that is, Model river (a): the rectangular cross-section channel, and Model river (b): the river-channel dredged along the right bank side, while the alignment of both model rivers is similar to the actual river. The influence of the magnitude of the transverse mixing coefficient will also be examined through these two set of numerical experiments. The other possible influence of the item 4, 5, and 6 were examined in Iwasa and Aya (1990), and Oue, Iwasa and Aya (1990).

The numerical simulation models and their procedures are similar to those described in **Chapter 9**, so that they are not mentioned, but the results of the numerical experiments under various hydraulic conditions will be described in this chapter. The numerical simulation models can disclose the unsteady behavior of flow and the spreading of tracer cloud, but only the results under the steady conditions will be presented.

Additionally, the simplified hydraulic model experiment for the dispersion in the downstream part from the Yodo River confluence was also conducted to confirm the results obtained in numerical experiments.

10.2 Numerical Experiments in an Actual River System

10.2.1 Conditions of Numerical Experiments

The numerical experiments were conducted under four different hydraulic conditions listed in Table 10.2.1. The discharge of each tributary was from "Annual Report for 1980: Discharge Measurements in Important Rivers in Japan" (River Bureau, Ministry of Construction, 1982), and the water surface elevation at the downstream boundary was calculated by use of those measured at Takahama stage-observatory and listed in "Annual Report for 1980: Stage Measurements in Important Rivers in Kinki Region, Japan" (Kinki Regional Bureau, Ministry of Construction, 1982). The concentration at upstream boundary of each tributary is hypothetical, and two sets of conditions were given, that is, $C = 100\%$ at Katsura River and $C = 0$ at Uji River and Kizu River for the first set, and $C = 100\%$ at Kizu River and $C = 0$ at Katsura River and Kizu River for the second set. The each value of turbulent viscosity, roughness

Table 10.2.1: The flow regimes used in the numerical experiment.

Regime	Discharge Q (m^3/s)				Stage at D. B.
	Katsura R.	Uji R.	Kizu R.	Total	(m + O.P.)
Annual average discharge	62. (19.3)	203. (63.2)	56. (17.5)	321. (100.)	6.475
Ordinary water (185) discharge	50. (20.2)	160. (64.5)	38. (15.3)	248. (100.)	6.190
Low water (275) discharge	35. (20.6)	108. (63.5)	27. (15.9)	170. (100.)	5.890
Drought (355) discharge	30. (24.4)	75. (61.0)	18. (14.6)	123. (100.)	5.485

Figures in the parentheses denote the ratio to total discharge in per cent.

coefficient and the longitudinal mixing coefficient is the same as those in **Chapter 9**. The value of the transverse dispersion/mixing coefficient estimated in Yodo River was reported at $D_T = 0.05$ m^3/s by Nambu (1960), $D_T/hu_* = 0.6 \sim 2.0$ by Li, Yagi and Sueishi (1987), $D_T/hu_* = 2.2$ by Yoneda, Iwata and Inoue (1986), and so on. The magnitude of the transverse dispersion coefficient is larger than those summarized in **Sub-section 9.3.1**, while the lower dispersion coefficient $0.2hu_*$ was selected in this numerical experiments, but the different values of the coefficient were also examined.

10.2.2 Results and Discussions of Numerical Experiments

(1) Effects of Flow Regime

a. Flow fields

The water surface elevation contour maps, the momentum flux vector distributions and the depth-averaged velocity vector distributions are shown in Figs. 10.2.1, 10.2.2, and 10.2.3 respectively. Each of figures illustrates those obtained under different four flow conditions. The features of flow fields obtained under each hydraulic condition are nearly similar each other and to those described for verification tests in **Chapter 9**. The distinguishable features between four flow regimes are observed in the distributions of the momentum flux vector and the depth-averaged velocity, and they are summarized as:

1. The river water mainly flows down in the lower part of the riverbed elevation in the channel, and the water route in the channel was developed in accordance with the riverbed topography, that is, concavities and convexities as illustrated in the topographical map of Fig. 9.3.1 (b).

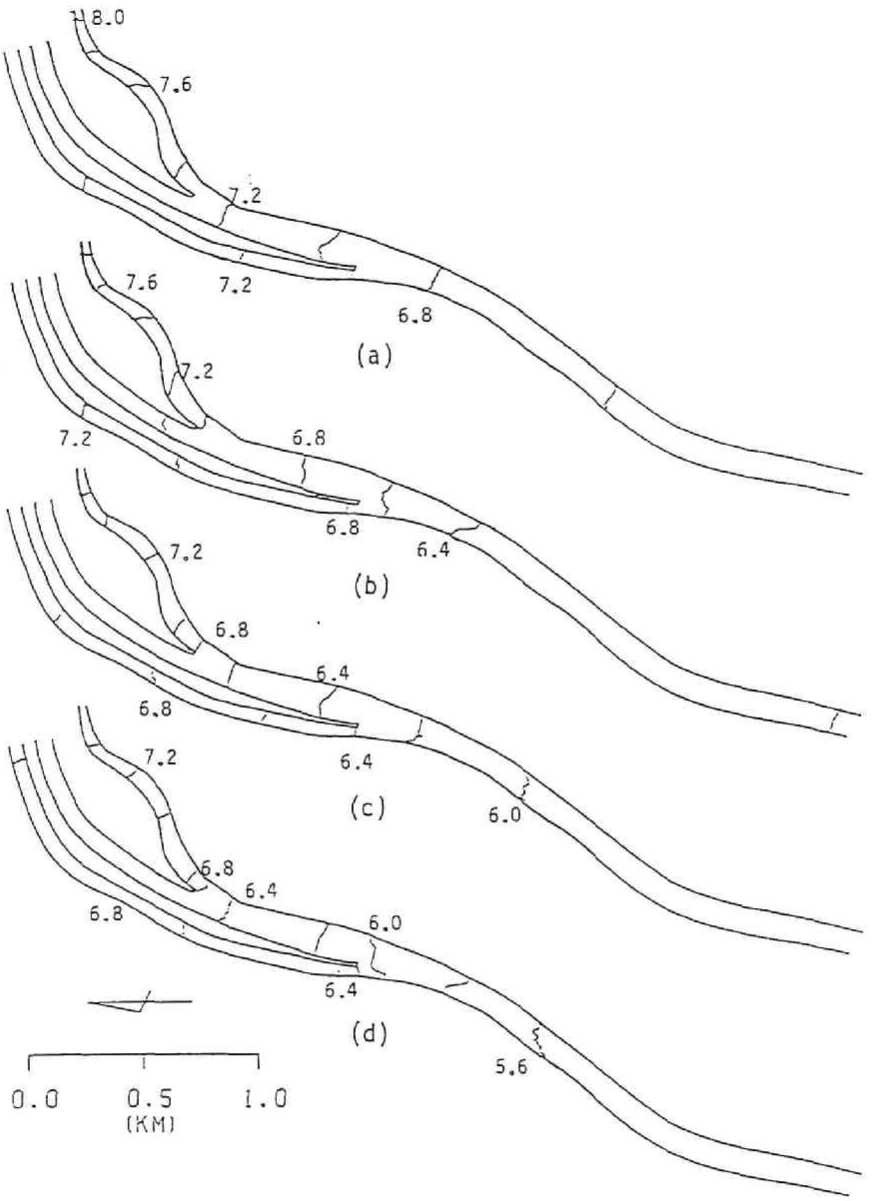

Figure 10.2.1: Water surface elevation contour maps in Yodo River system under various flow regimes. (a) Annual average discharge, (b) Ordinary (185) water discharge, (c) Low water (275) discharge, and (d) Drought (355) discharge.

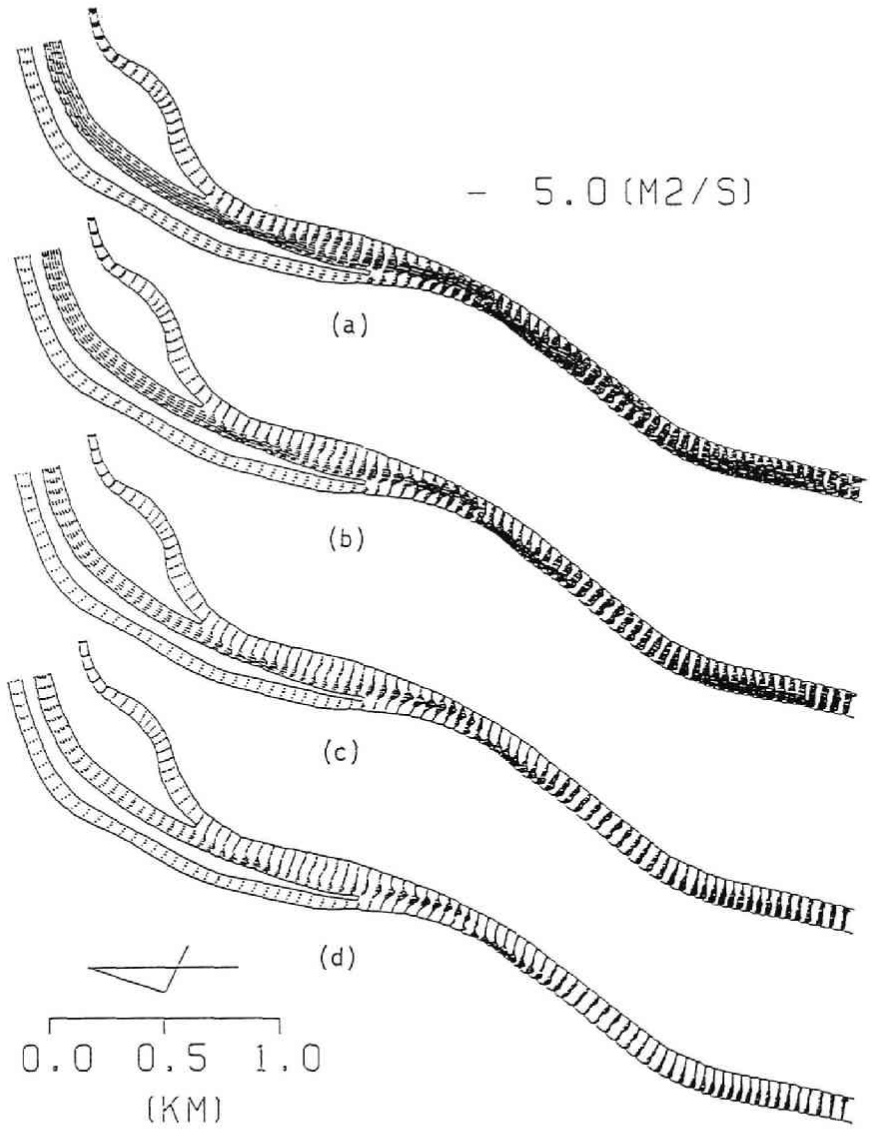

Figure 10.2.2: Momentum flux vector distributions in Yodo river system simulated under various flow regimes (a) Annual average discharge, (b) Ordinary (185) water discharge, (c) Low water (275) discharge, and (d) Drought (355) discharge.

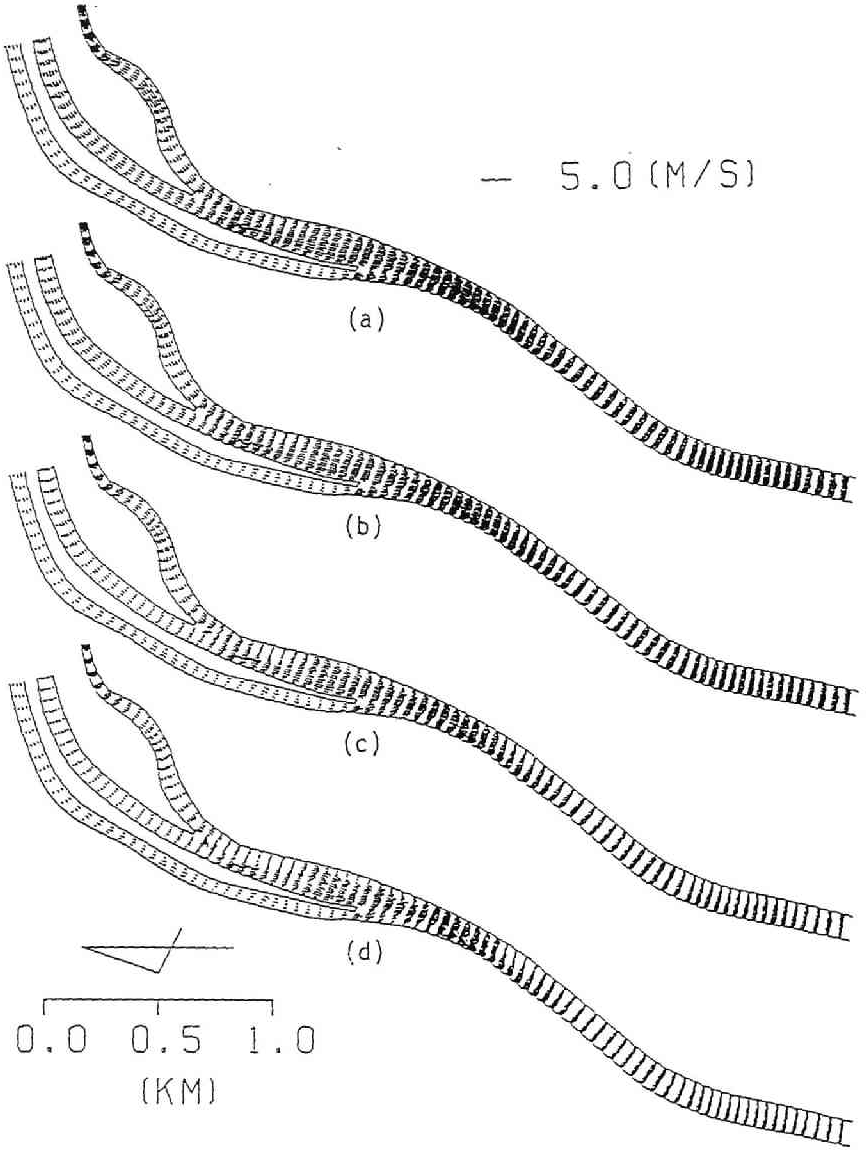

Figure 10.2.3: Depth-averaged velocity vector distributions in Yodo river system simulated under various flow regimes. (a) Annual average discharge, (b) Ordinary (185) water discharge, (c) Low water (275) discharge, and (d) Drought (355) discharge.

2. The momentum flux vector distributions are non-uniform in the transverse direction, and its transverse distributions are also varied in the longitudinal direction.

3. These distributions are influenced by flow regimes; that is, the non-uniformity becomes larger and larger as the discharge becomes smaller.

4. The distributions of the depth-averaged velocity vector are also affected by the riverbed topography and the flow regimes

5. These influence is definitely observed in the confluences, because the water-depth is shallow and the riverbed topography is more non-uniform, and the direction of the depth-averaged velocity vector is changed in the confluences.

6. But they are smaller below the second confluence, because the riverbed slope is very mild and the water surface profile is the backwater below the confluence.

These features are more definitely observed in closer illustrations of Fig. 10.2.4 in which the momentum flux vector and the depth-averaged velocity vector distributions are illustrated between two confluences under (a) Regimes of annual average discharge, and (b) drought discharge.

b. Concentration distributions

The steady state concentration distributions of tracer cloud from Katsura River under four flow regimes are shown in Figs. 10.2.5 (a),(b), (c) and (d). The tracer cloud from Katsura River merges into the main channel at the second confluence, and mainly flows down along the right bank-side. They disperse in the transverse direction, but the spreading width is changed in the longitudinal direction, that is, it becomes longer and/or shorter in flowing down as described in **Sub-section 9.3.2**. The distinguishable feature between four regimes is that the spreading width of tracer cloud is wider and wider with the decrease of discharge, that is the transverse concentration distributions are less uniform in Regime of annual average discharge, and more uniform in Regime of drought discharge. This feature is more clearly demonstrated in Fig. 10.2.6, which illustrates the transverse distributions of concentration at 33.6km section under four flow regimes in Figs. 10.2.6 for (a) the tracer from Katsura River, and for (b) the tracer from Kizu River. This notable characteristics of the transverse mixing is explained as:

1. The momentum flux vector distributions is less non-uniform in Regime of annual average discharge, and more non-uniform in Regime of drought discharge in both longitudinal and transverse directions.

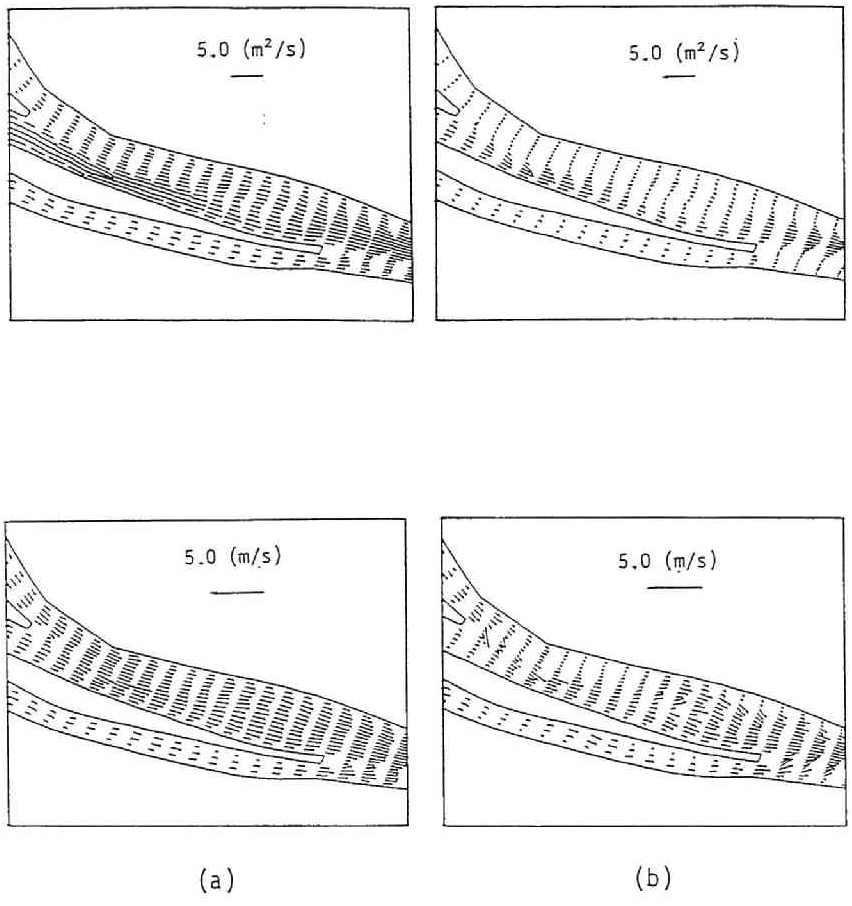

Figure 10.2.4: Distributions of the momentum flux vector and the depth-averaged velocity vector at the confluences of Yodo River System. (a) Annual average discharge, and (b) drought (355) discharge.

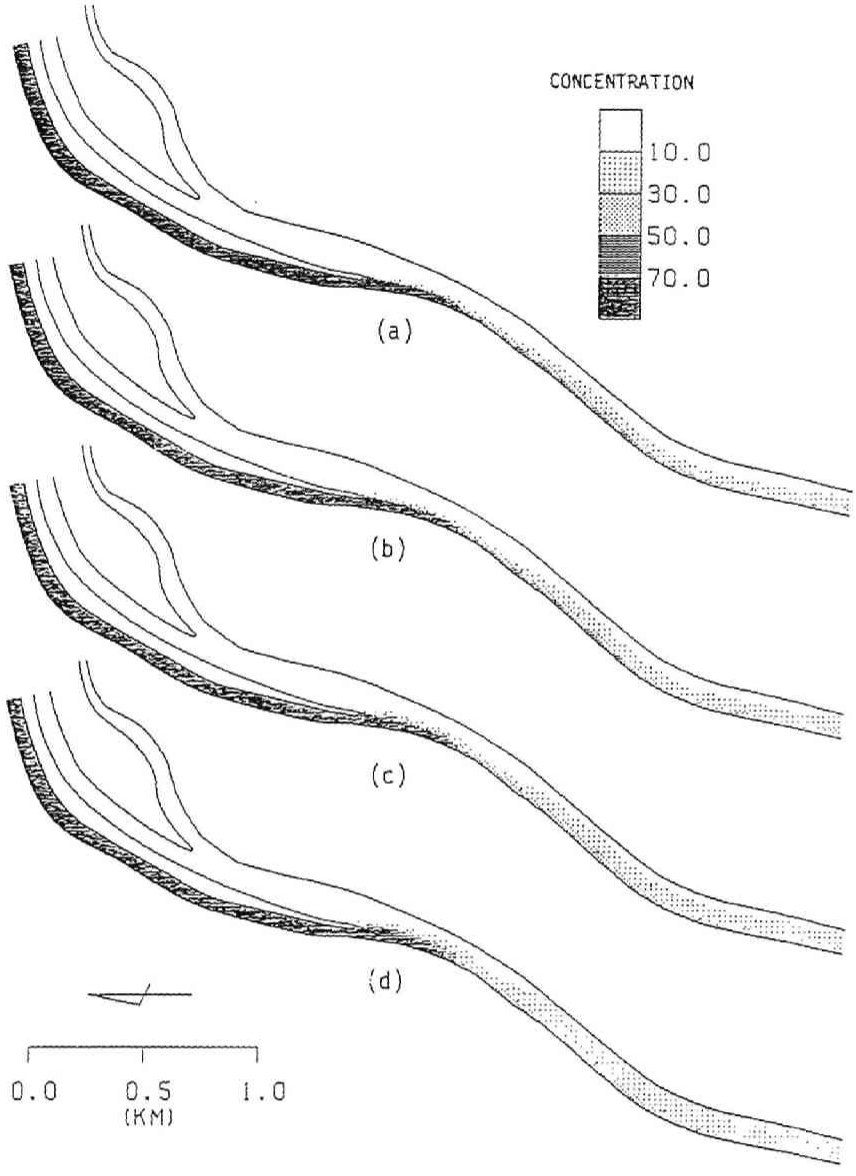

Figure 10.2.5: Distributions of concentration from Katsura River in Yodo river system simulated under various flow regimes. (a) Annual average discharge, (b) Ordinary (185) water discharge, (c) Low water (275) discharge, and (d) Drought (355) discharge.

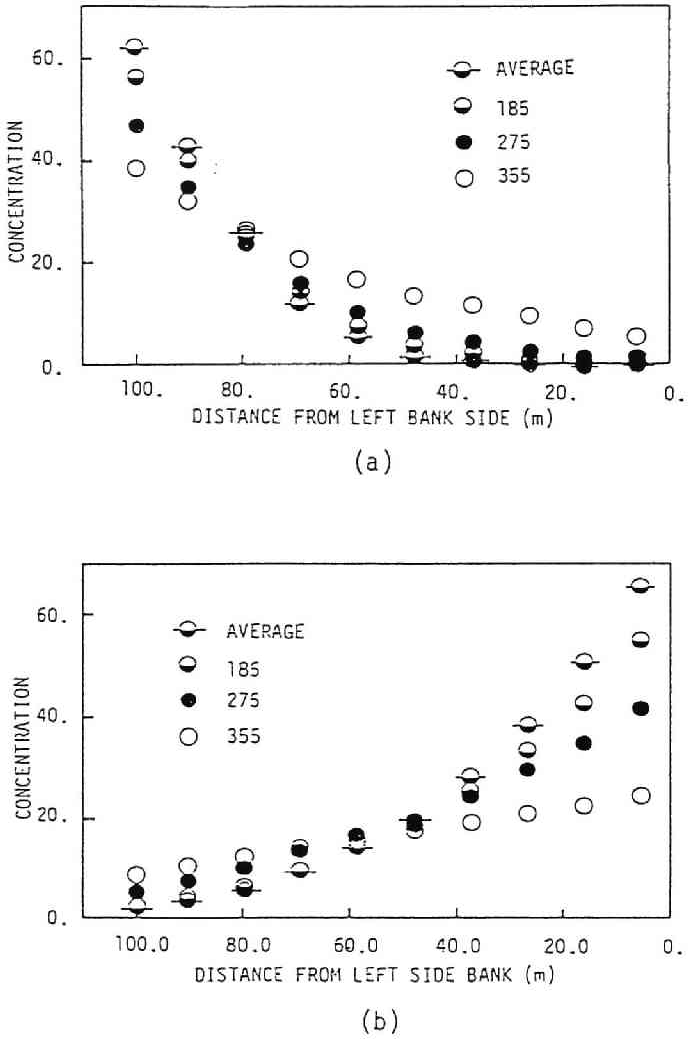

Figure 10.2.6: Transverse distributions of concentration at 33.6 km section simulated under under various flow regimes. (a) Tracer from Katsura River, and (b) Tracer from Kizu River.

2. These variations of the momentum flux vector distribution causes the transverse mixing of tracer cloud by the convective transport as well as the transverse dispersion.

3. The transverse distributions of the momentum flux vector are more varied in the longitudinal direction with decrease of discharge as described above, therefore, the transverse mixing is more accelerated.

4. Thus, as the discharge becomes smaller, the mixing of the tracer cloud in the transverse direction becomes more accelerated by the convective transport, therefore, the transverse distributions of the tracer becomes more uniform.

Figs. 10.2.7 (a) and (b) show close views of the momentum flux distributions between 34.0km section and 33.0km section below the confluences, and Figs. 10.2.8 (a) and (b) the corresponding concentration distributions of the tracer cloud from Katsura River. These figures more definitely demonstrate the mechanism of the transverse mixing in the downstream part from the Yodo River confluence.

(2) Effect of Transverse Dispersion

The influence of the transverse mixing coefficient was examined under Regime of Ordinary water (185) discharge, because it has already examined under 62-0904 verification test in **Section 9. 3**, and its discharges are between low water and drought discharges. The value of the transverse mixing coefficient is specified at $D_T/hu_* =$ 0.02, 0.2, and 2.00. The transverse distributions of tracer concentration from Katsura River are presented in Figs. 10.2.9 for (a) 33.6 km section, and (b) 32.08 km section. The variation of the concentration distributions is not so large, but the concentration distribution is more uniform, as larger transverse mixing coefficient is specified, comparing the results in 62-0904 Test, because it becomes more effective with increase of the discharge, as described in former **Sub-subsection 10.2.2 (1)**. However, its influence is less effective on the distributions, and the different flow regime causes much more varied concentration distributions as shown in Fig. 10.2.8.

Thus, it was disclosed that the transverse mixing was made by the transverse mixing coefficient as well as the convective transport caused by the change of water-route in the channel, and the latter one is more dominant in Yodo River System, which has non-uniform distributions of the riverbed elevation in the longitudinal and the transverse direction.

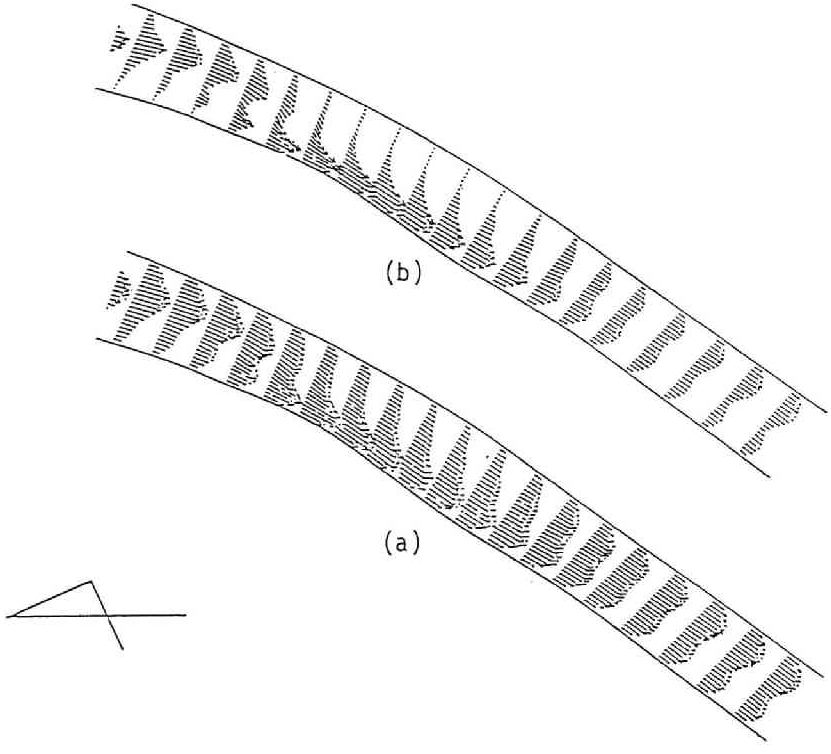

Figure 10.2.7: Momentum flux vector distributions between 33.0 km and 34.0 km sections in Yodo River System simulated in (a) annual average discharge, and (b) drought (355) discharge.

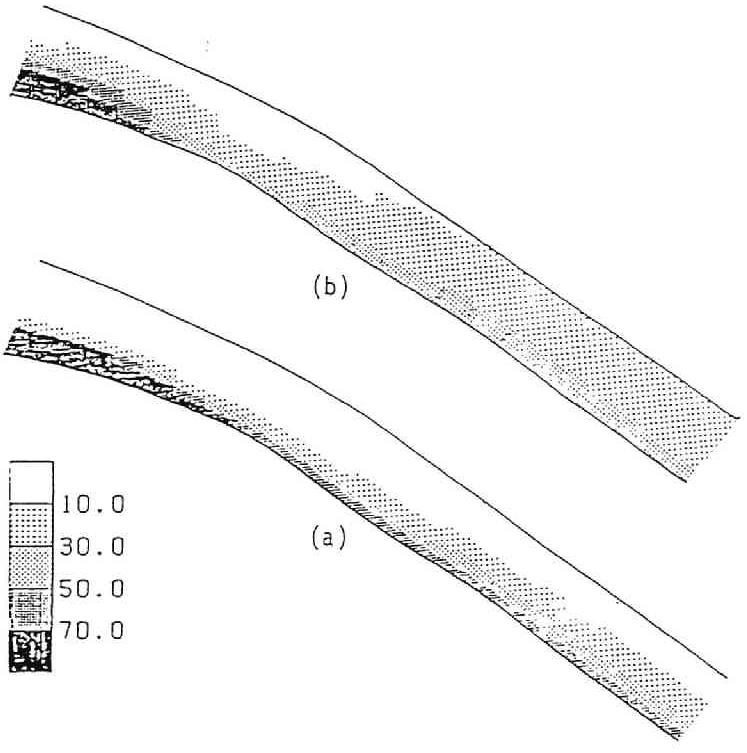

Figure 10.2.8: Distributions of concentration from Katsura River between 33.0 km and 34.0 km sections in Yodo River System simulated in (a) annual average discharge, and (b) drought (355) discharge.

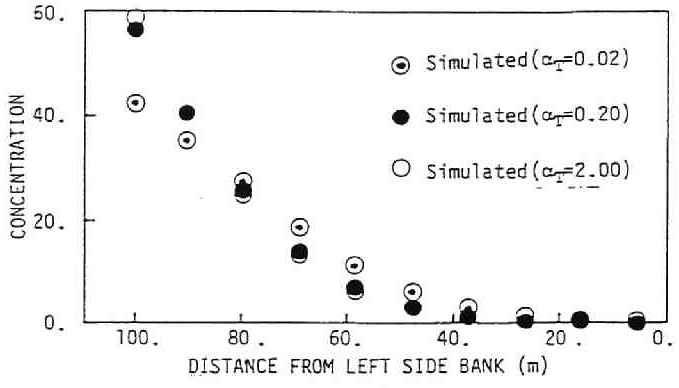

(a)

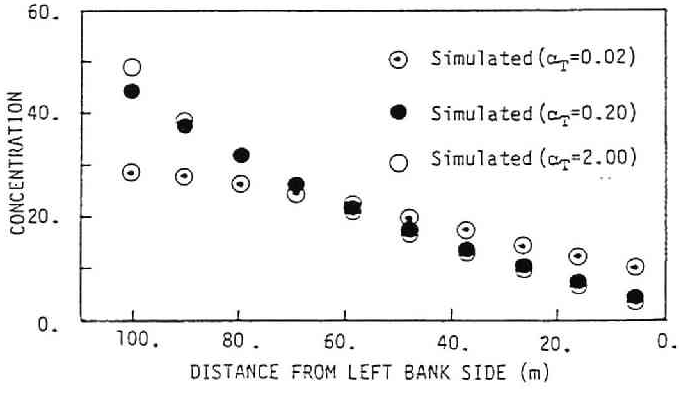

(b)

Figure 10.2.9: Transverse distributions of tracer concentration from Katsura River under various transverse mixing coefficients simulated in ordinary (185) discharge condition. (a) 33.6 km section, and (b) 32.08 km section.

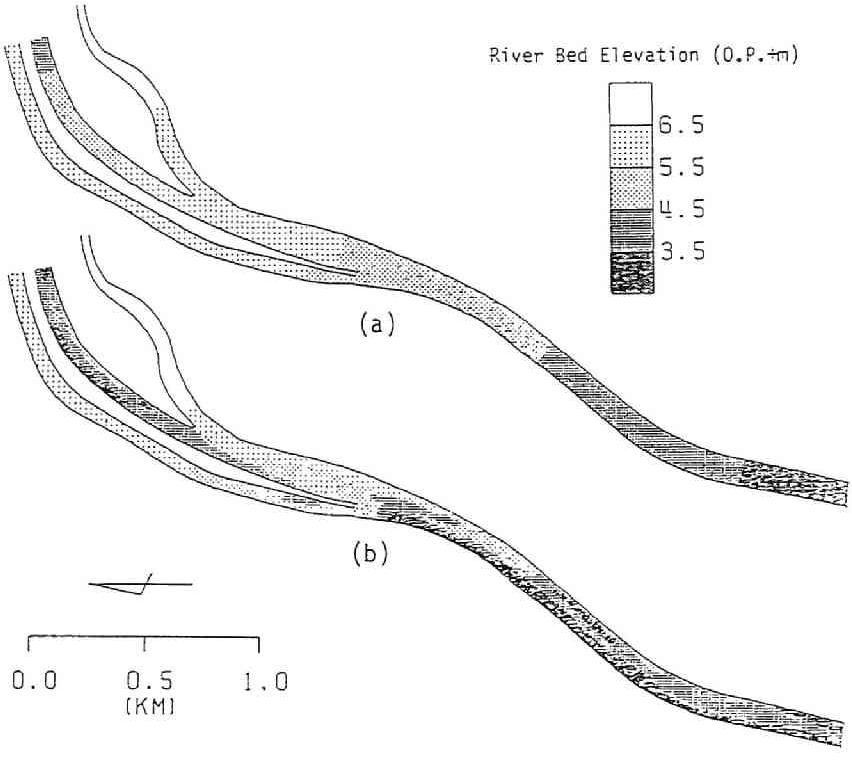

Figure 10.3.1: Bathymetric maps of model rivers. (a) Model river (a), and (b) Model river (b).

10.3 Numerical Experiments in a River System of Various Cross-Section Channels

10.3.1 Outlines of Experiments

The first numerical experiment disclosed that the non-uniform distributions of the riverbed elevation is more effective on the transverse mixing in Yodo River System, and this section will investigate the mixing in two kinds of the model channel of Yodo River System, that is, Model river (a) which has the rectangular cross-section, and Model river (b) in which the river channel was dredged along the right bank-side. The bathymetry of two model rivers are illustrated in Figs. 10.3.1 for (a) Model river (a), and (b) Model river (b). These channel geometries are hypothetical ones, but happened to be in/after river improvement works. The simulation conditions are similar to those in 62-0904 Test in Section 9.3 and in the first set of numerical experiments in Subsection 10.2.

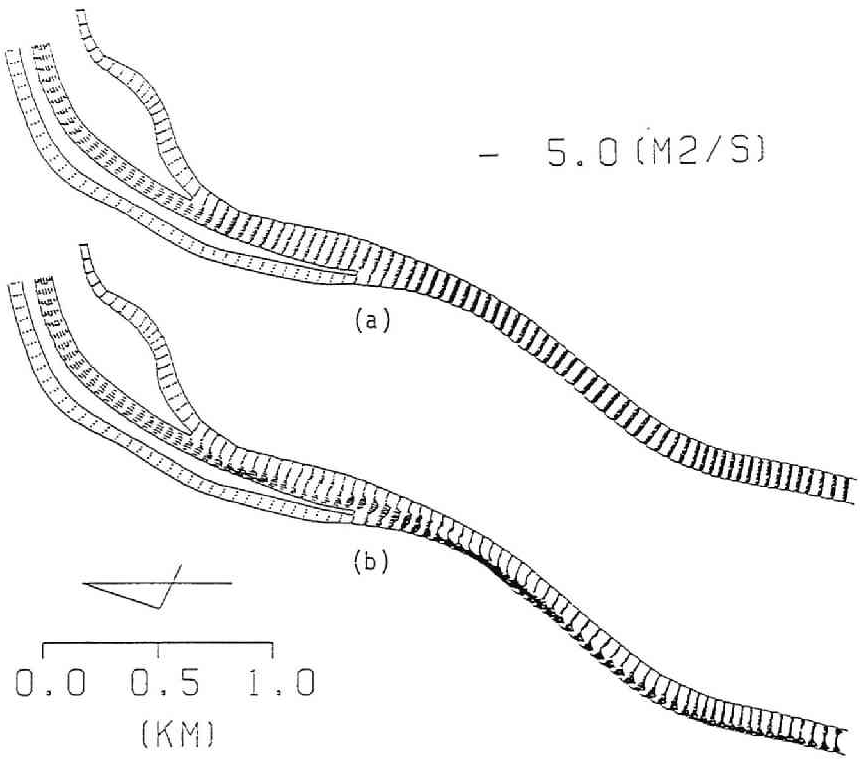

Figure 10.3.2: The momentum flux vector distributions under Regime 62-0904 in model rivers. (a) Model river (a), and (b) Model river (b).

10.3.2 Results and Discussion on Experiments under Various Channel Geometries

(1) Effects of Channel Geometry

a. Flow fields

The momentum flux vector distributions are presented in Fig. 10.3.2 for (a) model river (a), and (b) model river (b). Comparing the results in actual river channel presented in Fig. 9.3.2 in Chapter 9, the momentum flux vector distributions in the lateral direction are quite uniform in Model river (a), and its longitudinal variations are very small. On the contrary, the momentum flux vector distributions in Model river (b) is quite non-uniform in the transverse direction, but uniform in the longitudinal direction. The flows from three tributaries converge and concentrates on the right side of channel and flows down along the right bank-side. Thus, the channel geometry is quite effective on the flow fields.

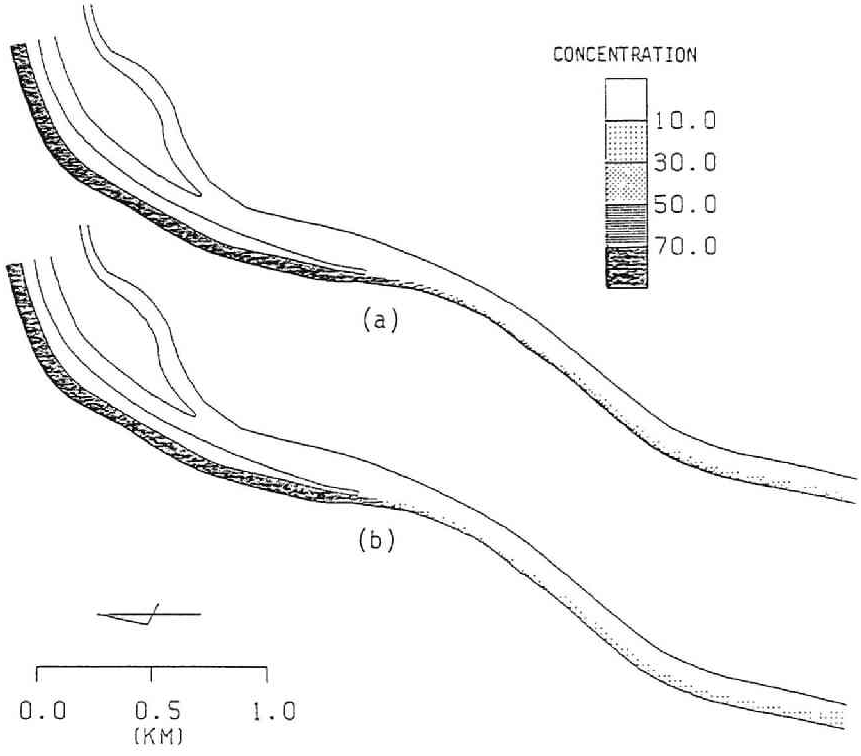

Figure 10.3.3: Spreading of tracer concentration from Katsura River in various channel geometry under Regime 62-0904. (a) Model river (a), and (b) Model river (b).

b. Concentration distribution

Spreading of the tracer from Katsura River are also illustrated in Fig. 10.3.3 for (a) Model river (a), and (b) Model river (b). Comparing the concentration distributions obtained in an actual river channel presented in Fig. 9.3.3 in Chapter 9, the spreading width of tracer are limited and much smaller than those in actual ones. The transverse concentration distributions at 33.6 km section under three different channel conditions in Regime 62-0904 are comparatively presented Fig. 10.3.4. The concentration distribution is quite non-uniform in Model river (a), and the mixing is controlled, because the momentum flux vector distributions are uniform in the longitudinal direction, and, therefore the convective transport in the transverse direction is very small and the mixing is only caused by the transverse dispersion. The spreading width is also limited in Model river (b), but its peak concentration is as

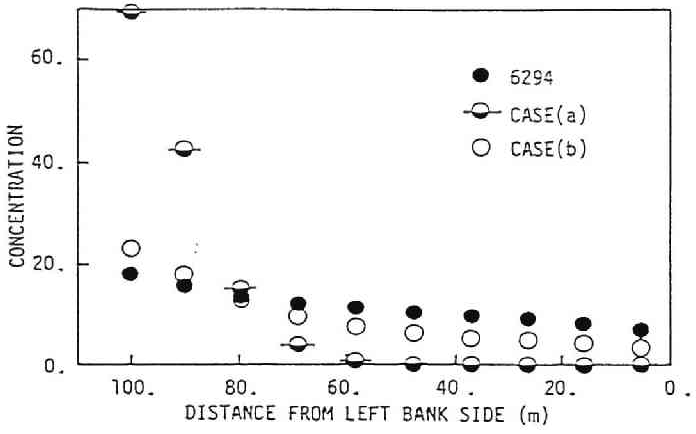

Figure 10.3.4: Transverse distributions of tracer concentration at 33.6 km section in various channel geometry under Regime 62-0904. Solid circles denotes distributions for the actual river cross-section, half closed circles for the model river (a), and open circles for the model river (b).

small as that in the actual river, because the flows from three tributaries strongly merge together below the confluence, therefore the high concentration from Katsura River was diluted by the waters from Uji and Kizu Rivers. Below the confluence, the momentum flux vector distributions are non-uniform in the transverse direction, but uniform in the longitudinal direction, and the spreading width is limited. Thus, the channel geometry is quite effective on the spreading of the concentration, because the flow fields are affected by the channel geometry.

10.3.3 Results and Discussions on Experiments in Rectangular Cross-Section Channels

(1) Flow Fields

The water surface elevation contour maps, the momentum flux vector distributions and the depth-averaged velocity vector distributions under various discharge conditions are shown in Figs. 10.3.5, 10.3.6, and 10.3.6 respectively. The features of flow fields obtained under each hydraulic condition are nearly similar each other, but quite different from those obtained in actual river channels. That is, the water surface elevations in Fig. 10.3.5 are quite uniform in the transverse direction. The momentum flux vector distributions, and the depth-averaged velocity vector distributions are quite uniform in the transverse direction except near the side-boundaries, and in

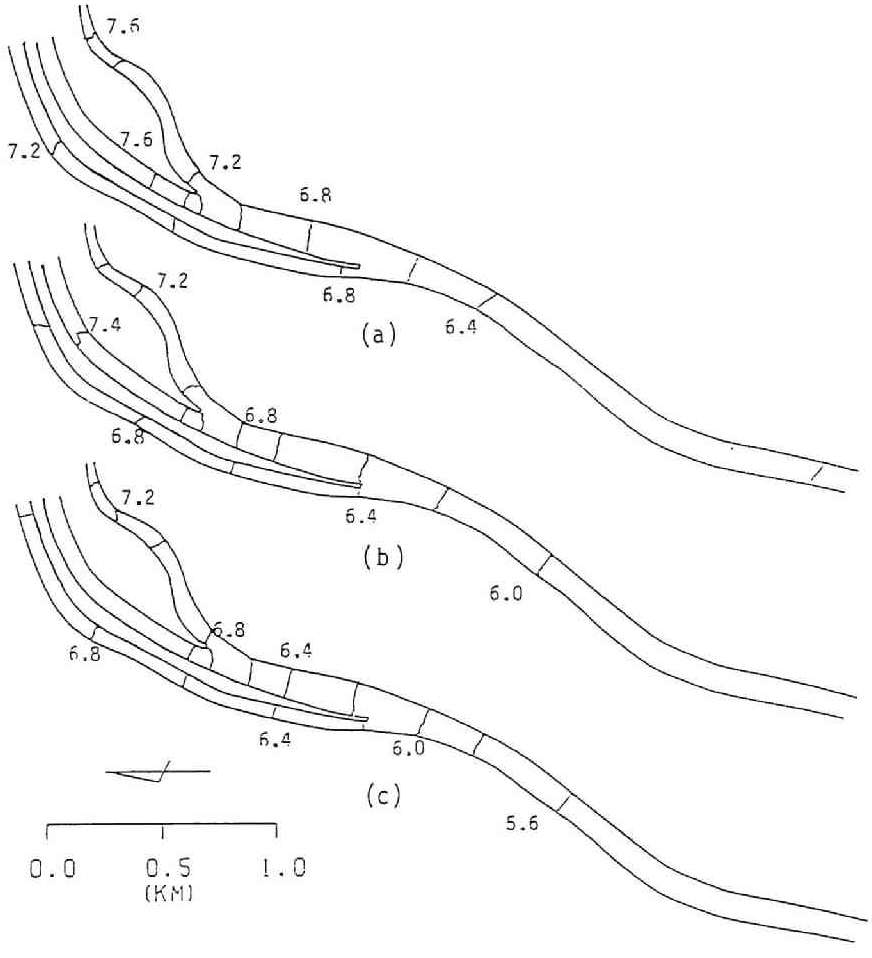

Figure 10.3.5: Water surface elevation contour maps in rectangular cross-section channels under various flow regimes. (a) Ordinary (185) water discharge, (b) Low water (275) discharge, and (c) Drought (355) discharge.

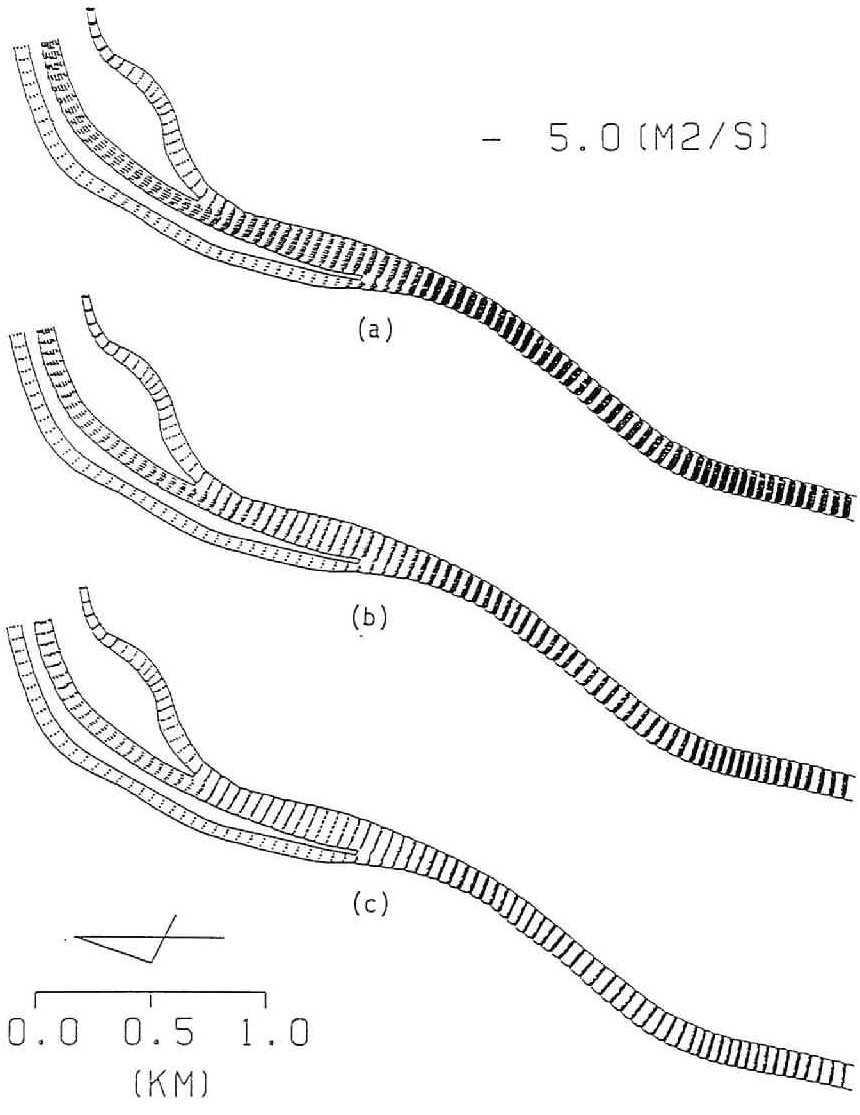

Figure 10.3.6: Momentum flux vector distributions in rectangular cross-section channels under various flow regimes. (a) Ordinary (185) water discharge, (b) Low water (275) discharge, and (c) Drought (355) discharge.

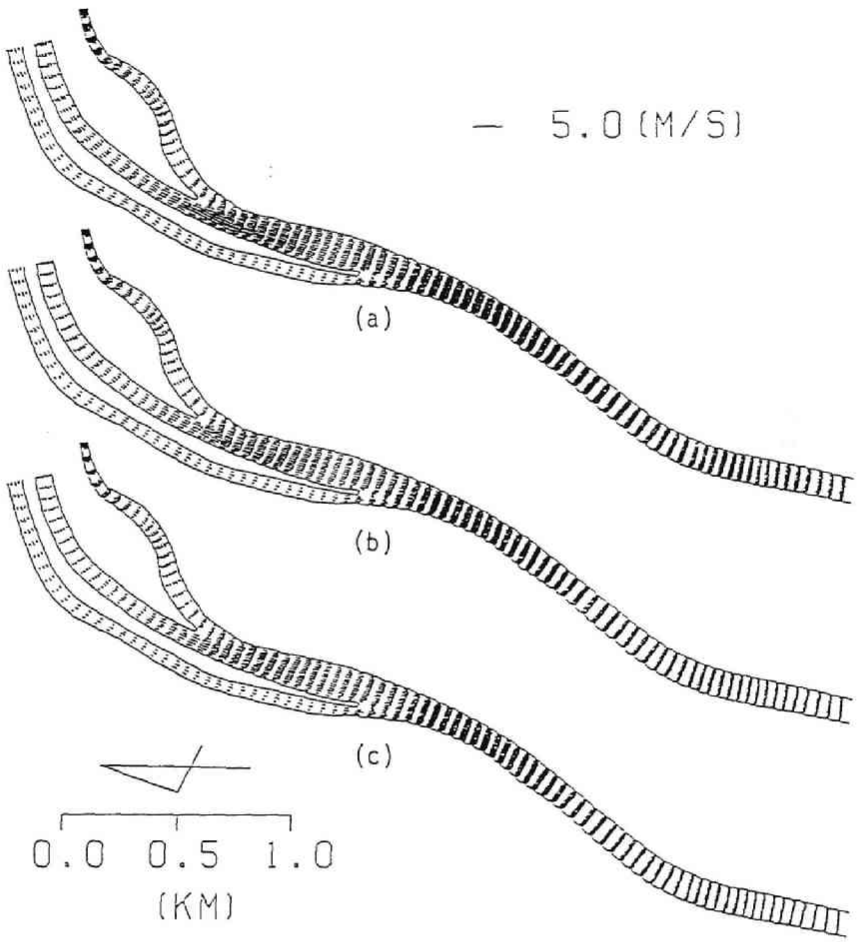

Figure 10.3.7: Depth-averaged velocity vector distributions in rectangular cross-section channels under various flow regimes. (a) Ordinary (185) water discharge, (b) Low water(275) discharge, and (c) Drought (355) discharge.

the longitudinal direction. It is because that the riverbed elevation is uniform in the lateral direction.

(2) Concentration Distributions

The spreading of tracer concentration in various flow regimes is presented in Fig. 10.3.8 for (a) Regime of the ordinary water discharge, (b) Regime of the low water discharge, and (c) Regime of the drought water discharge. The transverse concentration distributions are also presented in Fig. 10.3.9 at (a) 33.6 km section, and (b) 32.05 km section.

Comparing the results in actual river channels presented in Figs. 10.2.5, and 10.2.6, the spreading width is controlled and limited and the concentration distributions are much more non-uniform, and only a little difference of concentration distributions between various flow regimes are observed. It is because the momentum flux vector distributions are uniform in the longitudinal direction, and, therefore the convective transport in the transverse direction is very small and the mixing is only caused by the transverse dispersion as described in **Subsection 10.2.**

The transverse concentration distributions under various transverse dispersion coefficients in Regime of the low water discharge are also presented in Fig. 10.3.10 at (a) 33.6 km section, and (b) 32.08 km section. The results under the transverse dispersion coefficient of $D_T/hu_* = 0.02$ and 0.2 are similar each other at 33.6 km section and 32.08 km section, but under the dispersion coefficient of $D_T/hu_* = 2.0$, its effect is more obvious and the high concentration at the right bank-side becomes lower.

Thus, the transverse spreading are hardly affected by the flow regimes, but mainly governed by the transverse dispersion transport, because the riverbed elevation is distributed uniformly, and the momentum flux vector distributions are also uniform in the longitudinal direction, so that the convective transport is minor. Therefore, the estimation of the magnitude of the transverse dispersion coefficient is more important in rectangular cross-section channels than in actual river channels.

10.4 Laboratory Flume Experiment

10.4.1 Simplified Hydraulic Model Experiment

A series of hydraulic experiment by use of the laboratory flume was conducted in order to verify the characteristics of the mixing obtained in the numerical experiment. The straight flume of 25.0 cm in width has the series of rectangular-shaped depressions on the bottom alternately located beside a right or left channel-side. Its dimensions

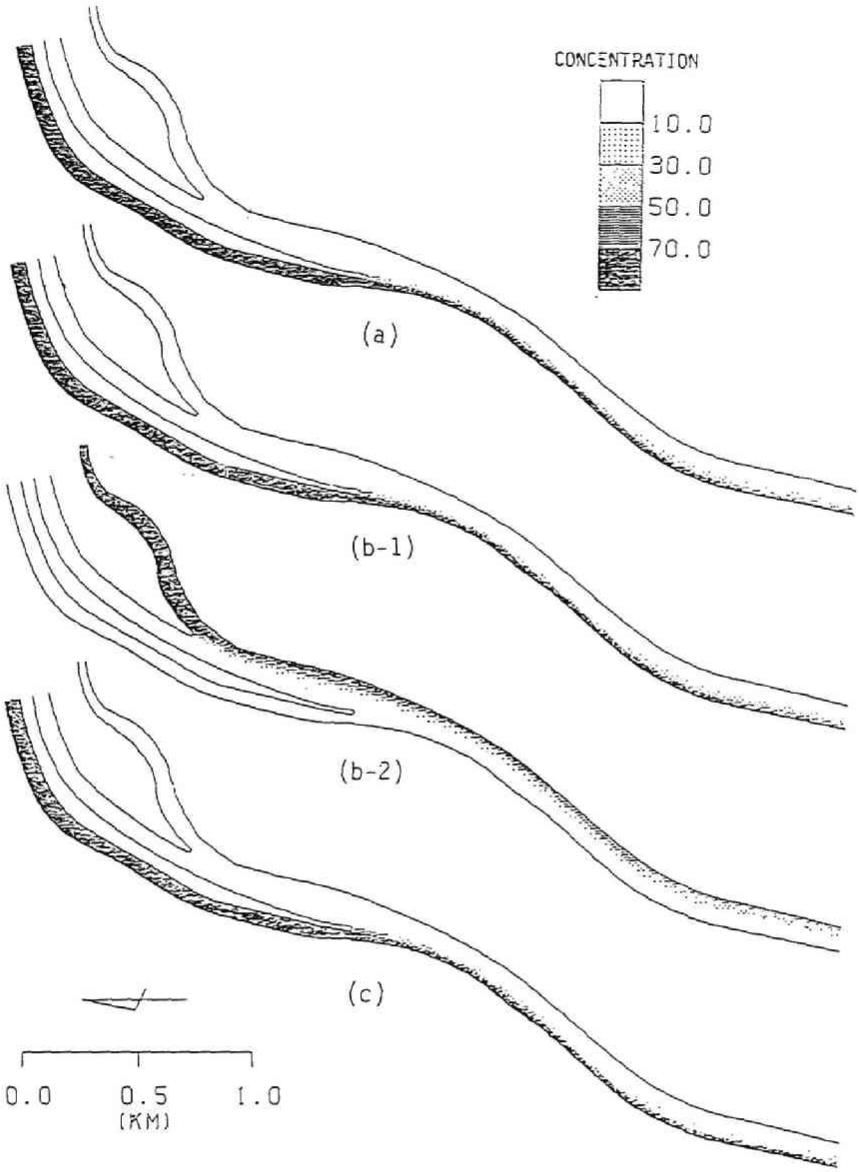

Figure 10.3.8: Spreading of concentration in rectangular cross-section channels under various flow regimes. (a) Annual average discharge, (b) Low water (275) discharge, and (c) Drought (355) discharge.

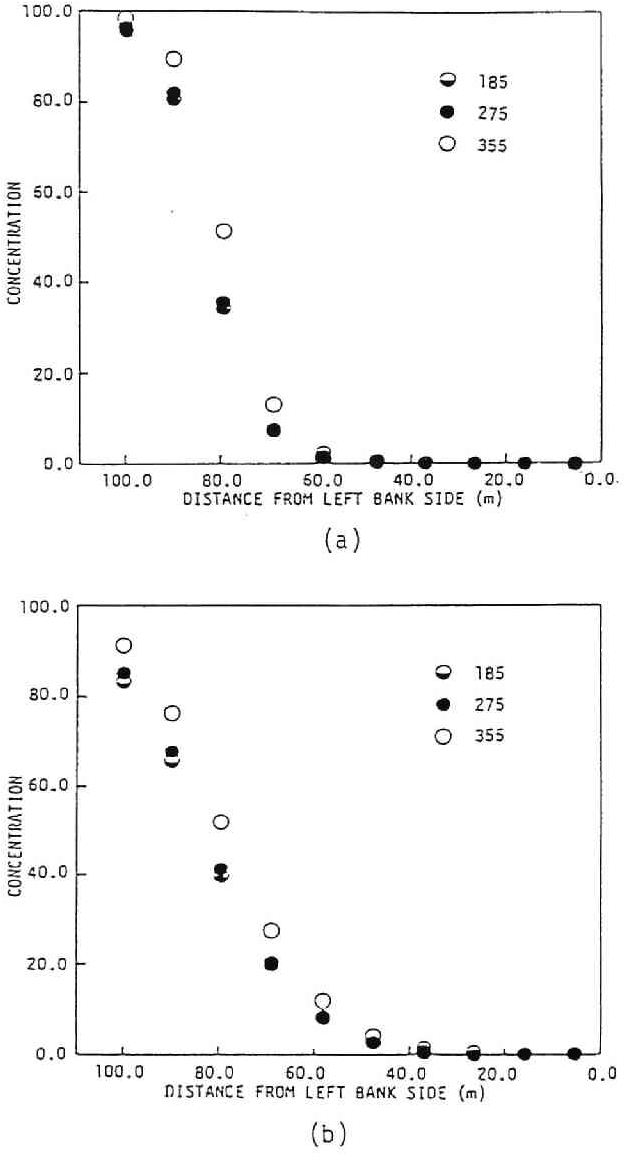

Figure 10.3.9: Transverse distribution of tracer concentration in rectangular cross-section channels under various flow regimes. Open circles denote the distribution for drought water (355) discharge, solid circles for low water (275) discharge and half-closed circles for ordinary (185) discharge. (a) 33.6 km section, and (b) 32.05 km section

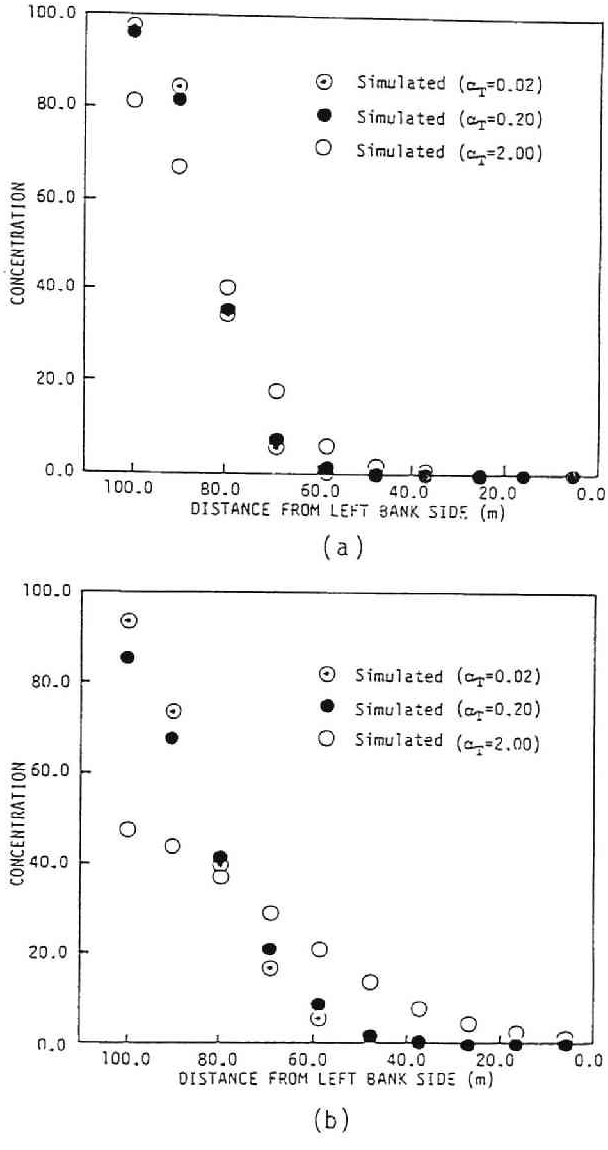

Figure 10.3.10: Transverse concentration distributions under various transverse dispersion coefficients in Regime of the low water discharge. Circles with dot denote the results under the transverse dispersion coefficient of $D_T/hu_* = 0.02$, solid circles under $D_T/hu_* = 0.2$, and open circles under $D_T/hu_* = 2.0$, (a) 33.6 km section, and (b) 32.08 km section.

Table 10.4.1: Summary of conditions of simplified hydraulic model experiment.

Run No.	Depth h(cm)	Discharge Q(l/s)	Velocity U(cm/s)	Flume
1	0.610	0.239	15.7	rectangular
2	0.696	0.263	15.1	simplified model
3	1.040	0.536	20.6	simplified model

are 75.0 cm long, 5.0 cm wide and 1.0 cm deep. This flume was used as a simplified hydraulic model for the Yodo River System below the confluence, and its scale is about 1/400 in the horizontal plane and 1/200 in the vertical direction. A rectangular cross-section channel was also used. The hydraulic conditions in the experiments are summarized in Table 10.4.1 and the discharge in Run 1 is equivalent to the annual average discharge in the prototype.

The dye-solution used as the tracer was continuously injected as a point source at the upstream section of the flume. The tracer spread in the transverse and the longitudinal directions and its dispersion cloud was observed and recorded by a photo-camera, but quantitative measurements were not made.

10.4.2 Results and Discussions on Hydraulic Experiment

The spreading of the tracer cloud observed in a rectangular cross-section flume test is illustrated in Fig. 10.4.1 in (a) a rectangular cross-section flume test, and Figs. 10.4.1 in (b), (c) and (d) a flume with depressions. The tracer injected near the channel-side spreads in the transverse direction in flowing down, but the width of tracer cloud is smaller on depressions and larger below the ends of depressions. The transverse mixing is the largest in Run 2, the second one in Run 3 and the third one in Run 1, and these results are in accordance with the results obtained in numerical experiments. That is, the spreading width becomes larger as the discharge decreases. Fig. 10.4.1 (d) shows the spreading of the tracer cloud injected at the half-width (the center of the flume). The meandering of the dye cloud suggests the flow also meanders and it is caused by the existence of the depressions; the flow concentrating on depressions spreads in the transverse direction below the downstream end of them, because the flow depth becomes shallower, and at the upstream end of depressions, the flow again converges and concentrates on them. Thus, the spreading and convergence of flow caused by depressions make the transverse mixing accelerated. This effect is stronger as discharge and/or average depth is smaller as shown in Figs. 10.4.1 (b) and (c).

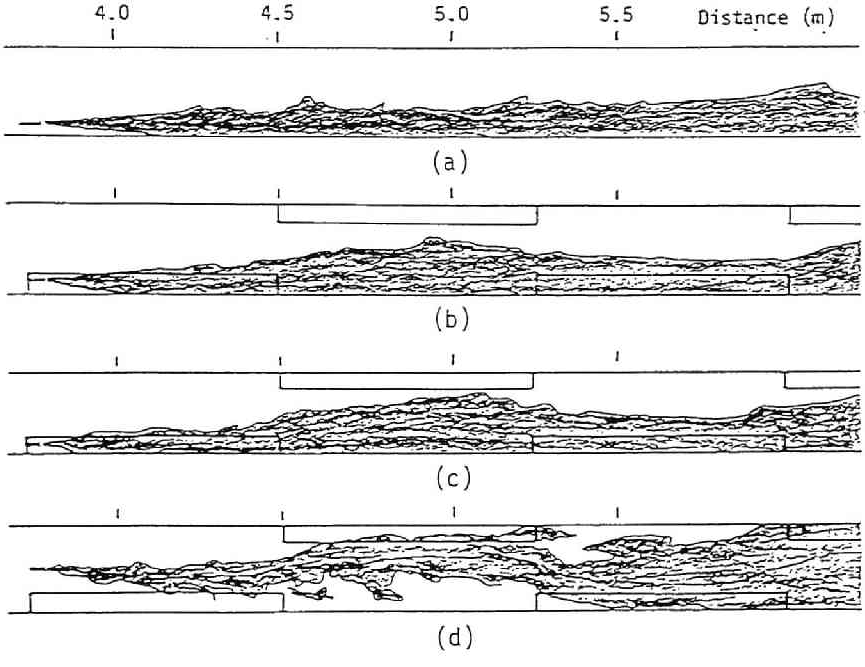

Figure 10.4.1: Spreading of continuously injected dye solutions. (a) Run 1: rectangular cross-section flumes, and side injection, (b) Run 3: simplified model with depressions, and side injection, (c) Run 2: simplified model with depressions, and side injection, and (d) Run 2: simplified model with depressions, and center injection.

10.5 Conclusions

The characteristics of the flow behavior and the associated mixing at/below the confluence in the Yodo River system were investigated by the mathematical and the hydraulic modeling. The mixing investigated by numerical experiments under various hydraulic conditions in **Section 10.2** was summarized as:

1. The riverbed in Kizu River is the highest and that in Uji River is the lowest in the elevation, and the waters in Kizu River and Katsura River merge into the water in Uji River at the confluences.

2. Below the confluence, the river water mainly flows down in the lower part of the riverbed and the main water-stream changes its route from one side to the opposite side of channel according to the non-uniform riverbed topography.

3. The spreading width of the tracer cloud changes in the longitudinal direction in accordance with the divergence and the convergence of flows caused by the non-uniform riverbed topography.

4. The tracer cloud spreads more widely as total discharge is smaller.

The mechanism of the mixing in the Yodo River System was also investigated by the numerical experiments under various channel geometries, dispersion coefficient, and discharge conditions in **Section 10.3**. The features obtained by numerical experiments were verified by the simplified hydraulic experiments in **Section 10.4**, and they are itemized as:

1. The flow behaviors are influenced by the riverbed topography and flow regimes,

2. The spreading of tracer cloud in the transverse direction is wider as discharge is lower, and this is caused by the existence of concavity/depression in the bottom.

The mechanism of the transverse mixing in the Yodo River system below the confluence can be explained as;

1. The riverbed is not uniform and the river water mainly flows down in the lower part of the riverbed.

2. And the main stream meanders within the channel in accordance with riverbed topography.

3. This meandering causes spreading and convergence of tracer cloud and makes concentration distributions more uniform.

4. In case the total discharge is larger or the cross-section of channel is rectangular, the longitudinal variation of the transverse distribution of the momentum flux vectors is smaller and the transverse mixing is also smaller.

Thus, the transverse convective transport caused by the longitudinal variation of the transverse distributions of the momentum flux vector plays an important role in the transverse mixing as well as the dispersive transport. The convective transport is more dominant than the turbulent and dispersion transport in an actual river which has the non-uniform riverbed elevation in the longitudinal and the transverse directions, but the dispersive transport is more important in the channel which does not have the longitudinal variation of the riverbed and the momentum flux vector distributions.

References in Part III

Akima, H. (1970). A new method of interpolation and smooth curve fitting base on local procedure, *J. Assoc. Computational Machinery*, Vol. 17, No. 4, 589–602.

Elder, J. W. (1959). The dispersion of marked fluid in turbulent shear flow, *J. Fluid Mechanics*, Vol. 5, 544–560.

Fischer, H. B. et al (1979). "Mixing in Inland and Coastal Waters", Academic.Press, New York. .

Holly, Jr., F. M. (1985). Dispersion in rivers and coastal waters— 1. Physical principles and dispersion equations in "Developments in Hydraulic Engineering–3" edited by Novak, P., Elsevier, London. .

Holly, Jr. F. M., and Nerata, G. (1983). Field calibration of stream-tube dispersion model, *J. Hydraulic Division, Proc. ASCE*, Vol. 109, No. HY11, 1455–1470.

Iwasa, Y., and Aya, S. (1990). Spreading of effluent in receiving river waters, *Proc. 5th Int'l Conference on Urban Storm Drainage*, Vol. 1, 541–546.Iwasa, Y., Aya, S.

and Baba, H. (1989) Flow Behavior And Associated Dispersion of Contaminants at a River Confluence by Means of the Depth-Averaged Mathematical Models, Proc. of the third Symposium on Computational Fluid Mechanics, 563-566, (in Japanese).

Iwasa, Y., Aya, S., and Baba, H. (1990) 2-D numerical analysis of flow and associated transverse mixing of contaminants in the Yodo River Stem, *Proc. 7th Congress of APD-IAHR*, Beijing-China, Vol. III, 207–212.

Iwasa. Y., Aya, S. Tsuchiya, T., and Nishiuch, Y. (1988). 2-D numerical simulation of flow and associated dispersion by means of generalized curvilinear coordinate system, *Annuals*, Disaster Prevention Research Institute, Kyoto University, Vol. 31, B-2, 589–600, (in Japanese).

Iwasa. Y., Hosoda, T., and Noguchi, Y. (1982). Transverse mixing coefficient in open-channel flows, *Annuals*, Disaster Prevention Research Institute, Kyoto University, Vol. 25, B-2, 557–572, (in Japanese).

Kawamura, T. (1985). Direct simulation of flows at high Reynolds number using a third-order upwind scheme, "Recent studies on turbulent phenomena" edited by Tatsumi, T., Maruo, H., and Takami, Assoc. Science Documents Information, Tokyo, 117–149.

Lau, L., and Krishnappan, B. G. (1981), Modeling transverse mixing in natural streams, *J. Hydraulic Division, Proc. ASCE*, Vol. 107, No. HY2, 209–226.

Leonard, B. P. (1979). A stable and accurate convective modelling procedure based on quadratic interpolation, *J. Computational Methods in Applied Mechanics and Engineering*, No. 19, 59–98.

Li, S., Yagi, S., and Sueishi, T. (1987). Transverse dispersion of water quality in the Yodo river and its effect to the source of water supply. *Proc. 31th Japanese Conference on Hydraulics*, JSCE, 311–316, (in Japanese).

Nambu, S. (1960). Analysis of concentration distribution of contaminants in a polluted river, *J. Water Supply Eng. Assoc.*, No.304, 29–37, (in Japanese).

Okoye, J. K. (1970). Characteristics of transverse mixing in open-channel flows, Report No. KH-R-23, California Institute of Technology, Pasadena, California.

Oue, M., Iwasa, Y. and Aya, S (1990). Numerical experiments of flows and mixing at a confluence, *Proc. Annual Conference of JSCE*, Vol. 2, ... (in Japanese).

Takemoto, et al. (1986). A curvilinear coordinate method for the solution of incompressive Navier-Stokes equations using the third-order upwind difference scheme, Transaction of JSIDRE, No. 121, 57– 65.

Viviand, H. (1974). Formes conservatives des equations de la dynamique des gaz, *La Recherche Aérospatiale*, No. 1, 65–66.

Yoneda, N. Iwata, K., and Inoue, Y. (1986). Estimation of transverse dispersion coefficient by use of water quality data measured in a river, *Proc. 8th Kyoto Univ. Symposium on Environmental Engineering*, 103–110, (in Japanese).

Yotsukura, N., Fischer, H., and Sayre, W. W. (1970). Mixing characteristics of the Missouri river between Sioux city Iowa, and Plattsmouth Nebraska, Water–supply paper, 1899–G, U. S. Geological Survey.

Yotsukura, N., and Nakamura, S. (1988). The stream-tube model for the transport of dissolved materials in natural rivers, *Proc. JSCE*, No.399, II-10, 85–94.

Yotsukura, N., and Sayre, W. W. (1976). Transverse mixing in natural streams, *Water Resources Research*, Vol. 12, No. 4, 695–704.

Chapter 11

CONCLUSIONS

The longitudinal and transverse mixing of mass in turbulent shear flows in open-channels was investigated by various methods in this report. The work focused on the basic studies, but aims to apply its results to actual problems in river engineering, because the longitudinal and the transverse mixing of fine particles and contaminants discharged into a river is quite interested in terms of environmental aspects in the field of river hydraulics.

The report consists of three portions. The **Part I** is concerned with the longitudinal dispersion coefficient which is the most important parameter for describing the longitudinal mixing in open-channel flows. The **Part II** studied the other topics related with the longitudinal mixing in open-channel flows, that is, concentration distributions and the mixing in the flows on permeable boundaries, which is common under natural environment. The **Part III** is the investigation of the transverse mixing in an actual river by use of the numerical modeling. The contributions of the present study are summarized bellow.

11.1 Contributions of Part I

In **Part I**, the one-dimensional longitudinal dispersion in confined turbulent shear flows was studied by theoretical, experimental and empirical methods.

(1) Contributions of Chapter 2

Chapter 2 investigated the longitudinal dispersion of continuous movements of a particle by use of the method of Lagrangian modeling. The movements of a particle is stated by Lagrangian descriptions, and the theoretical models for the Lagrangian auto-correlation function in 3-D turbulent shear flows were presented and the longitudinal dispersion coefficient was obtained in **Section 2.2**. The 3-D numerical

simulation models for a particle dispersion were developed in **Section 2.3**, and they were successfully examined by 2-D numerical experiments, comparing the theoretical results obtained by previous studies in **Sections 2.4** and **2.5**. 3-D numerical experiments were conducted in **Section 2.6**, and the theoretical results and assumptions introduced in **Section 2.2** were successfully examined and verified by the results of numerical experiments in **Sections 2.7** and **2.8**. Thus, the dispersion processes and the longitudinal dispersion coefficient in 2-D and 3-D turbulent shear flows were disclosed as:

1. The dispersion processes in open-channel flows can be decomposed into three components, that is, the Eulerian turbulent transport, the dispersion caused by the vertical non-uniformity of the velocity distributions, and the dispersion by the lateral non-uniformity of the velocity distributions.

2. The Lagrangian auto-correlation function is also decomposed into three components, and each of them is stated by the exponential function.

3. The Lagrangian integral time scale is quite different from the mixing time scale in 3-D turbulent flows, and described by the weighted average of the mixing time scales for the three components of the Lagrangian turbulent velocity.

4. The intensity of the non-uniformity of the velocity distributions in the lateral direction is smaller than that in the vertical direction, but the mixing time scale in the lateral direction is much larger than that in the vertical direction.

5. Therefore, the dispersion coefficient is described as a product of the three components of the intensity of the Lagrangian turbulent velocity and the three components of the integral time scale. It is quite larger in open-channel flows which has the large width to depth ratio.

6. The non-uniformity of the velocity distributions in the lateral direction is the most dominant over the longitudinal dispersion in turbulent open-channel flows, and the dispersion coefficient depends on the width to depth ratio.

(2) Contributions of Chapter 3

The longitudinal dispersion coefficient was theoretically investigated by the method of Eulerian modeling in **Chapter 3**. In **Section 3.2**, the previous theoretical studies on the dispersion coefficient based on the turbulent diffusion equation were reviewed,

and the assumptions used were summarized. In **Section 3.3**, the 3-D turbulent diffusion equation, 1-D convective dispersion equation, and the definition of the longitudinal dispersion coefficient were stated in the orthogonal curvilinear coordinate system. The mathematical theory of the dispersion coefficient developed by the previous studies was presented in more general form by use of the 3-D turbulent diffusion equation in the orthogonal curvilinear coordinate system in **Section 3.4**. The distinguishable features of Fischer's modeling from others were disclosed in terms of the mixing time scale introduced in **Chapter 2**, and it was concluded that the longitudinal dispersion can be modeled in terms of 2-D plain phenomena in wide open-channel flows, but should be done in terms of 3-D phenomena in ordinary laboratory flumes. In **Section 3.5**, the locally time-averaged velocity and concentration were respectively decomposed into three components, that is, the cross-sectional averaged values, the deviation of the depth-averaged values from the cross-sectional averaged values, and the deviation of the local temporal averaged-values from the depth-averaged values. The dispersion coefficient in 1-D models were also decomposed into three components, that is, the Eulerian turbulent diffusion term, the dispersion caused by the vertical non-uniformity of the velocity distributions, and the dispersion caused by the lateral non-uniformity of the velocity distribution. The third term is equivalent to Fischer's formula, and dependent on B/d. It is the major component of the dispersion coefficient in wide open-channel flows in laboratory and natural streams, but its magnitude is estimated to be of the same order in ordinary laboratory flumes.

(3) Contributions of Chapter 4

The longitudinal dispersion was also investigated by the detailed laboratory experiments in **Chapter 4**. The objectives of the experiment were to disclose the characteristics of time-dependent behaviors of the tracer cloud, and to verify the theoretical results in **Chapters 2** and **3** as stated in **Section 4.1**. The experimental apparatus and the method were stated in **Section 4.2**, that is, the experiments were conducted by injecting the salt solution as the tracer in the selected flows in the rectangular cross-section laboratory flumes, and measuring its concentration at selected points in selected sections by use of the conductivity meters. The methods of data processing and analysis were stated in **Section 4.3**. That is, the behaviors of the temporal moments for concentration distributions, and the characteristics of the velocity distributions was calculated. The dispersion coefficient was determined by three different methods.

The results of the experiments were stated in **Section 4.4**. The spreading of the injected tracer in 3-D space can be stated:

1. The tracer is stretched in the longitudinal direction by the longitudinal component of the flow velocity vector which has the strongly non-uniform distribution in the vertical direction and the weak one in the lateral direction. The concentration distributions becomes three-dimensionally non-uniform and highly skewed for a short travel time.

2. The vertical mixing makes the concentration distribution in the vertical direction uniform again.

3. The lateral mixing following the vertical mixing also makes the concentration distribution in the lateral direction uniform again for a long travel time, and the magnitude of the dispersion coefficient becomes much larger than that in 2-D shear flows.

The spreading of the tracer was also investigated by the behaviors of the first, the second and the third temporal moments and the peak concentration. They described the quite different concentration distributions from the Gaussian distribution, and highly skewed ones. The convergence on the Gaussian distribution was very slow. The difference of the temporal moment behavior between the cross-sectional concentration and those measured at points in a section was also disclosed.

The theoretical results obtained by use of the Lagrangian modeling in **Chapter 2**, and the Eulerian modeling in **Chapter 3** were successfully compared with the experimental results;

1. The convective velocity of the centroid of the tracer cloud is equal to the cross-sectional averaged velocity.

2. The growth of the variance of the tracer cloud can be stated by the proposed models of Eq. 4.5.5 and can be approximated by Eq. 4.5.14

3. The characteristics of the integral time scale in 3-D turbulent shear flows was examined and it was verified that the mixing time scale T_l in the lateral direction is quite different from the integral time scale T_{SL}, and T_l is good approximation for T_l^*

4. The definite agreement between the dispersion coefficients measured in the experiments and those predicted by Eq. 2.2.35 presented in **Chapter 2**, and Eq. 3.5.45 presented in **Chapter 3** was demonstrated.

The dimensional analysis also disclosed the empirical relationship of the dimensionless dispersion coefficient with the width to depth ratio and the velocity factor as described by Eq. 4.5.17.

Thus, it was concluded that the dispersion coefficient in rectangular cross-section open-channel flows is not predicted by Elder's formula, but can be predicted by Eqs. 2.2.35, 3.5.45, and/or 4.5.17.

(4) Contributions of Chapter 5

In **Chapter 5**, the applicability of the three formulae presented in the previous chapters was examined to river flows as well as to the various flows in laboratory flumes made by other investigators. The relationship between the dispersion coefficient and the hydraulic variables in rivers was also investigated by use of the screened data.

The results of the previous measurements for the longitudinal dispersion coefficient in various laboratory flumes and actual rivers were collected and carefully reviewed in **Sections 5.2** and **5.3**. A lot of experiments and field measurements have been done, but a few of them were satisfied with the requirements in the theory.

The dispersion coefficient obtained in terms of one-particle analysis in **Chapter 2** was successfully examined by the dispersion coefficient measured in rivers by use of Godfrey and Frederick's data in **Sub-section 5.4.1**, though its agreement was not so fine as that in laboratory. The magnitude of each of three components of the dispersion coefficient was also investigated by use of the velocity distribution data measured in rivers, and it was concluded that the 2-D approximation in the lateral direction can be possible for the dispersion in rivers. The characteristics of the velocity distributions in rivers were investigated in terms of Lagrangian dispersion theory, and it was concluded that the magnitude of the non-uniformity of the vertical direction is of the order of 1.0 to 10., and those of the lateral direction 10.. Therefore, they are comparable each other. The integral time scale and the mixing time scale were also studied, and the definite relationship of Eq. 5.4.7 for rivers was obtained.

In **Sub-section 5.4.2**, the dispersion coefficient obtained in terms of Eulerian analysis in **Chapter 3** was successfully examined by the dispersion coefficient measured in rivers by use of Godfrey and Frederick's data, though its agreement was less fine than that in laboratory. The dispersion coefficients calculated by Eqs. 2.2.35 and 3.5.43 by use of the velocity distributions measured in laboratory by the author and measured at each section in rivers by Godfrey and Frederick were compared. It was found that the magnitude of the dispersion coefficient calculated by both of the Lagrangian and the Eulerian modeling are of the same order, though the theoretical proof was difficult for the agreement between two results by the Lagrangian and Eulerian modeling.

The dimensional analysis of the dispersion coefficient was also conducted in **Sub-section 5.4.3**, and the definite relationship between D/du_* and B/d described by

Eq. 5.4.12 was obtained by using 62 data in laboratory and 79 data in rivers.

11.2 Summary of Dispersion Coefficient

The longitudinal mixing and the dispersion coefficient in open-channel flows were studied by theoretical methods by use of the Lagrangian and the Eulerian modeling. Theoretical results were verified by numerical and laboratory experiments, and field-measured data. Both of results by the Lagrangian and Eulerian modeling can describe the 1-D longitudinal mixing in not only laboratory flumes but also rivers, though the agreement between two results by two different modeling were not theoretically proved but experimentally done. The mechanism of the longitudinal mixing are described as:

1. The longitudinal dispersion in open-channel flows is 3-D. It can be decomposed into three components: the Eulerian turbulent diffusion: the dispersion caused by the vertical non-uniformity of the velocity distributions: the dispersion caused by the lateral non-uniformity of the velocity distributions.

2. The vertical and the lateral non-uniformity of the velocity distribution and the turbulent mixing in both directions causes the longitudinal dispersion.

3. The intensity of the vertical non-uniformity is commonly larger than the lateral one in laboratory flumes and rivers, but the mixing time/length scale in the lateral direction is much larger than that in the vertical direction in ordinary open-channel flows in laboratory and rivers.

4. Therefore, both are effective on the longitudinal dispersion in laboratory, but the influence of the vertical non-uniformity of the velocity distributions becomes relatively smaller with increase of the width to depth ratio, and it can commonly be neglected in the dispersion in rivers.

11.3 Contributions of Part II

The Part II investigated the particle dispersion by discontinuous movement, the concentration distributions in "Pulse Tracer Tests" in rivers and laboratory, and the mass transport in the flows on pervious beds is investigated.

(1) Contributions of Chapter 6

In **Chapter 6**, the convective dispersion processes in the longitudinal direction in confined flows were studied in view of the discontinuous movement of a particle. Assuming the Lagrangian turbulent velocity was independent each other in the sense of the probability, the probability density distribution of a particle location, which is equivalent to the concentration distribution, was presented by use of the probability density function (**PDF**) of the Lagrangian turbulent velocity in **Section 6.2**. The models for a particle movement were similar to those described in **Chapter 2**, however, it was assumed that the Lagrangian turbulent velocity v'_{1i} in the time step Δt_i was independent on v'_{1i-1} in the former time step Δt_{i-1}. Therefore, the models in **Chapter 6** deprive the dispersion processes of the features in **Chapter 2**, but following notable features were obtained:

1. The **PDF** of the Lagrangian turbulent velocity for longitudinal dispersion is not described by the Gaussian distribution, but by the exponential distribution for 2-D open-channel flow and for the flows in rectangular cross-section laboratory flume.

2. Therefore, the **PDF** of the particle displacement is different from the Gaussian for a short travel time, because it is influenced by the **PDF** of the Lagrangian turbulent velocity; for a longer travel time, it converges on the Gaussian by the "Central Limit Theorem" in probability and statistics.

3. Thus, the skewed concentration observed in the dispersion measurement is disclosed to be peculiar to the shear flow dispersion and the fundamental feature.

In **Section 6.3**, the **PDF** of the Lagrangian turbulent velocity v'_1 in the longitudinal dispersion phenomena was studied, assuming the influence of the Eulerian turbulent velocity was negligibly small. The **PDF** of v'_1 in 2-D open-channel flows under the logarithmic velocity distribution was described by the exponential distribution, and the concentration distributions during the asymptotic processes approaching the Gaussian distribution was described by the Earling/gamma distribution (Pearson's Type Ⅲ distribution).

The concentration distributions measured in "Pulse Tracer Test" in open-channel flows were studied in **Section 6.4** and **6.5**. The **PDF** of v'_1, and the magnitude of the time step Δt in in 3-D flows were discussed in view of the magnitude of the mixing time scale T_v in the vertical direction, and T_l in the lateral direction. Neglecting the effects of the Eulerian turbulence and the vertical non-uniformity of the velocity distributions on the longitudinal dispersion, the models for describing

the concentration distributions in 3-D flows were presented in **Section 6.4**. The direct verification of the proposed models was not made, but the gamma distribution approximation was successfully examined by use of the concentration distributions and the velocity distribution measured in the rectangular cross-section laboratory flume in **Section 6.5**. The non-uniform lateral distribution of the depth-averaged velocity, which is dominant component over the longitudinal dispersion, was stated by the logarithmic distribution. That is, the **PDF** of v_l' is described by the exponential distribution, and the concentration distribution by the gamma distribution for the flows in rectangular cross-section laboratory flumes.

(2) Contributions of Chapter 7

The actual concentration distributions observed in "Pulse Tracer Test" for the measurement of the dispersion coefficient in laboratory and natural streams were investigated in **Chapter 7**. They are commonly skewed from the Gaussian distribution, and the skewed distributions were examined and approximately described by use of the gamma (Pearson's Type Ⅲ) distribution in this chapter.

In **Section 7.2**, the possibility of the gamma distribution approximation was widely examined and successfully demonstrated for not only the cross-sectional averaged concentrations C but also the point-measured concentration distributions $\bar{c}_c$ at the center of flow-section in laboratory and natural streams.

The main descriptors of the distribution, such as the first moment, the variance, the modal value, and so on at each of measuring points were investigated with relation to the hydraulic variables of flows for C and $\bar{c}_c$ in **Section 7.3**.

1. The concentration time of the centroid of the distribution $\bar{t}$ is commonly longer than that of the peak concentration t_P, that is, the concentration distributions are commonly skewed.

2. The celerities of the centroid and the peak concentration is the same as the mean velocity U for C as well as $\bar{c}_c$ in laboratory for a longer travel time. It is 1.2 times larger than U for $\bar{c}_c$ in natural streams.

3. The magnitude of the variance σ_{ct}^2 is smaller than σ_t^2 for C and the growth of σ_{ct}^2 is slower than that of σ_t^2, but the slope of $\sigma_{ct}^2 - x$ in a normal sheet is the same as that of $\sigma_t^2 - x$.

4. Therefore, the Moment Method for $\bar{c}_c$ gives the same dispersion coefficient as for C, but the required time for the linear growth of σ_{ct}^2 is much larger than that of σ_t^2.

5. This delayed growth of the variance is described by the introduction of the parameter T_L', and T_L' has the relationship with the width to depth ratio B/d described by Eq. 7.3.3.

6. Being based on the gamma distribution approximation, the parameter β, which links the celerities of the centroid and the top edge of the distributions with U, was introduced. The concentration time t_p for the peak concentration C_P is described by the parameter β, and the value of β for $\bar{c}_c$ in natural streams is $0.1 \sim 0.3$.

The gamma distribution approximation for $\bar{c}_c$ in natural streams by use of $\bar{t}$, $\sigma_c t^2$, and β was also successfully demonstrated in **Section 7.4**.

(3) Contributions of Chapter 8

The vertical and longitudinal mass transports in the flows over permeable boundary, which are common in natural environment, were investigated in **Chapter 8**. Preliminary dye tracer study in **Section 8.2** disclosed the features of the vertical mass transport between the surface flows and the sub-surface flows under permeable boundary.

1. The sub-surface flow is classified into three flow regions in view of the vertical mass transport. The mass transport is observed in the upper two layers, and it is influenced by the surface flow.

2. The mass transport is the most active in the mixing cell in the first upper layer. It covers 80% of the surface of the permeable boundary; its thickness is a few times of the mean grain size of the porous media, and the thickness to length ratio is 0.25.

3. The vertical mass transport is characterized by the time scale T_{10}, the velocity of mass exchange k, and/or the dispersion coefficient D_y in the mixing layer. T_{10} is described by Eq. 8.2.6, the order of the magnitude of k/U_A is 10^{-3}, and that of D_y is the same as the vertical turbulent diffusion coefficient in the surface flows.

By using the mathematical models similar to those in "Dead Zone Modeling" for the longitudinal mixing in natural streams, the longitudinal mass transport in the surface and the sub-surface flows was theoretically investigated in **Sections 8.3** and **8.4**. Results obtained disclosed that the mass exchange between the surface and the sub-surface flows played an important role in the longitudinal mass transport.

1. The convective velocity in the surface flow is the same as that in the sub-surface flow, and equal to the weighted average of two velocities in the surface and the sub-surface flows.

2. The dispersion coefficient in the surface flow is the same as that in the sub-surface flow, and described by a sum of three terms; the first two terms are the weighted average of dispersion coefficient in each flow, and the last term is caused by the velocity difference and the mass transport between two flows.

3. These characteristics are strongly dependent on the ratio of the thickness of the mixing layer to the flow-depth, and the characteristic velocity of mixing. They play an important role in the torrential flow.

These theoretical results were verified by use of the experimental results for the longitudinal dispersion in flows on sand bed in **Section 8.5**.

11.4 Summary of Mechanism of Longitudinal Dispersion

The studies on the longitudinal mass transport, the dispersion coefficient, and the concentration distributions in **Part I** and **Part II** disclosed the mechanism of the one-dimensional mass transport in the longitudinal direction in open-channel flows as;

1. The non-linear growth of the variance observed in "Pulse Tracer Test" is caused by the dispersion by continuous movements. The required travel length/time for the linear growth of the variance are determined by the mixing time scale in the lateral direction in open-channel flows, because the width to depth ratio is commonly large in open-channel flows.

2. The skewed concentration distribution commonly measured in the longitudinal dispersion experiments in laboratory and natural streams is peculiar to the phenomena in shear flow dispersion, and the fundamental feature, because the **PDF** of the Lagrangian turbulent velocity is commonly different from the normal distribution. The skewed concentration distribution converges on the Gaussian distribution for a longer travel time by the "Central Limit Theorem", but the required travel time is dependent on the **PDF** of the Lagrangian turbulent velocity, and its order of the magnitude is longer than $20T_l$, in case the

PDF of v_l' is described by the exponential distribution.

11.5 Contributions of Part III

The **Part III** investigated the longitudinal/transverse mixing in a river system which had the complicated geometry by numerical analysis.

(1) Contributions of Chapter 9

In **Chapter 9**, 2-D mathematical models for flows and associated mixing were presented in the generalized curvilinear coordinate system, and the numerical models with use of FDM were developed. They were successfully examined by their application to the Yodo River system.

The 2-D mathematical models for flows and the associated longitudinal and transverse mixing of mass were derived in the generalized curvilinear coordinate system from the common 2-D mathematical models in the 2-D hydraulic analysis for shallow water in the Cartesian coordinate system in **Section 9.2**. Their dependent variables are the same as those in the Cartesian coordinates system; only the independent variables, that is, the space coordinates were transformed into the non-orthogonal curvilinear system, therefore, it is much easier to generate the grids for calculation in the physical domain. They are as simple as those in the Cartesian coordinate system, and the finite difference forms of the mathematical models were presented by the integration method in **Section 9.2.**. They have the second order accuracy in the space and the time coordinates, and the simulation codes were developed.

The proposed models were applied to the confluence of the Yodo River System case study and its validity was examined in **Section 9.3**. The simulated flow behaviors were not compared with field data because of the lack of data, however they were reasonable ones, and their features were discussed in detail with relation to its bathymetry. The water-depth is shallow in low water/drought discharge conditions, and the flows in channels are very affected by the riverbed elevation which is non-uniformly distributed in the longitudinal and the transverse directions. The simulated concentration distributions were successfully compared with the measured ones. The concentration distributions of contaminants were mostly affected by the convective transport of the flows, and the transverse mixing coefficient was estimated at less than $2.0hu_*$.

The mixing processes of the waters from Katsura River or Kizu River below the

confluences were also discussed in detail with the relation to the flow behavior. It was suggested that the convective transport played a more important role in the transverse mixing in the Yodo River Confluence than the gradient type mass transport.

(2) Contributions of Chapter 10

In **Chapter 10**, the flow behaviors and the transverse mixing at/below the confluence of the three rivers in the Yodo River system under various hydraulic and geometrical conditions were investigated by use of the mathematical models developed in **Chapter 9** and also by the simple physical modeling.

The characteristics of the flow behavior and the associated mixing were investigated by numerical experiments under various hydraulic conditions in **Section 10.2**, and described as;

1. The riverbed in Kizu River is the highest and that in Uji River is the lowest in the elevation, and the waters in Kizu River and Katsura River merge into the water in Uji River at the confluences.

2. Below the confluence, the river water mainly flows down in the lower part of the riverbed and the main water-stream changes its route from one side to the opposite side of channel according to the non-uniform riverbed topography.

3. The spreading width of the tracer cloud changes in the longitudinal direction in accordance with the divergence and the convergence of flows caused by the non-uniform riverbed topography.

4. The tracer cloud spreads more widely as total discharge is smaller.

The mechanism of the mixing in the Yodo River System was also investigated by the numerical experiments under the various channel geometries, the dispersion coefficient, and the discharge conditions in **Section 10.3**. The features obtained by numerical experiments were verified by the simplified hydraulic experiments in **Section 10.4**, and they are summarized as;

1. The flow behaviors are influenced by the riverbed topography and flow regimes.

2. The spreading of tracer cloud in the transverse direction is wider as discharge is lower, and this is caused by the existence of concavity/depression in the bottom.

11.6 Summary of Mechanism of Transverse Mixing in Yodo River System

The mechanism of the transverse mixing in the Yodo River system below the confluence can be explained as;

1. The riverbed is not uniform and the river water mainly flows down in the lower part of the riverbed.

2. The main stream meanders within the channel in accordance with riverbed topography, that is, the momentum flux vector distributions in the transverse direction have the longitudinal variations in accordance with the riverbed topography.

3. This meandering/longitudinal variation of the momentum flux distributions causes spreading and convergence of flows/tracer cloud and makes concentration distributions more uniform.

4. In case the total discharge is larger or the cross-section of channel is rectangular, the longitudinal variation of the transverse distribution of the momentum flux vectors is smaller and the transverse mixing is also smaller.

Thus, the transverse convective transport caused by the longitudinal variation of the transverse distributions of the momentum flux vector plays an important role in the transverse mixing as well as the dispersion transport. The convective transport is more dominant than the turbulent and dispersion transport in an actual river which has the non-uniform riverbed elevation in the longitudinal and the transverse directions, but the dispersion transport is more important in the channel which does not have the longitudinal variation of the riverbed and the momentum flux vector distributions.